Nanostructured Metal Electrodes for Wool Processing and Electroanalysis

---

A thesis

submitted in partial fulfilment

of the requirements for the Degree

of

Doctor of Philosophy in Chemistry

at the

University of Canterbury

by

Amy C. Cruickshank

November 2007

Abstract

The research presented in this thesis firstly concerns the use of electrochemical techniques to develop approaches to wool processing which have a lower impact on the environment than conventional chemical methods. Wool is a sulfur rich substrate and current methods used in wool processing often rely on sulfur-based reducing agents such as metabisulfite. However, due to increasing concern over the environmental impacts of metabisulfite, alternative methods are of interest. Electrochemical techniques have been applied to the process of wool setting in the presence of thiol setting agents. Wool disulfide bonds are reduced during this process and the thiol setting agent is converted to the disulfide. Efficient conversion of the disulfide back to the thiol setting agent would allow catalytic amounts of thiols to be used in wool setting. The electroreduction of cystine and 2-hydroxyethyl disulfide has been examined at a range of metal and carbon electrodes to find efficient methods of generating the corresponding thiols, cysteine and 2-mercaptoethanol respectively. Gold and silver were identified as the most efficient electrode materials. In industrial wool processing, the use of large-scale metal electrodes is expensive and therefore, high surface area gold and silver nanoparticle electrodes were fabricated by electrochemically depositing the metals onto low-cost carbon substrates. The most efficient electrochemical system for generating the thiol setting agent involved the electroreduction of cystine at the gold nanoparticle electrode and this system was used to successfully demonstrate that wool setting can be achieved using relatively low concentrations of cysteine.

Further research was carried out to investigate methods for the controlled preparation of metal nanoparticle electrodes and their utility for detecting hydrogen peroxide was examined. A simple and versatile approach for the preparation of tethered gold nanoparticle assemblies was developed by exploiting electrostatic interactions between citrate-capped gold nanoparticles and amine tether layers attached to carbon surfaces. The nanoparticle assemblies were optimised for the detection of hydrogen peroxide by selecting the size and density of electrostatically assembled nanoparticles. The number of amine functionalities on the surface and the assembly conditions controlled the nanoparticle density. Nanostructured palladium electrodes fabricated using vapour deposition methods to immobilise palladium nanoparticles directly onto carbon substrates were also examined for the electroanalysis of hydrogen peroxide.

Acknowledgements

I wish to extend my sincerest gratitude to my supervisor, Assoc. Prof. Alison Downard, for all the guidance and encouragement she has given me throughout my studies since without her support the completion of this thesis would not have been possible.

I would also like to thank the past and present members of the Downard group for making the laboratory an enjoyable and friendly working environment during the course of my research. Special thanks go to my fellow PhD comrades, Emelyn Tan, Jared Panther and Sam Yu (we have made it!), whose friendships are gratefully acknowledged and are integral to the fond memories I take with me of my time at the University of Canterbury. Thanks also to Dr Paula Brooksby from whom I have learnt so much during my research. I have greatly enjoyed my time in the Chemistry Department at the University of Canterbury and for this I would like to acknowledge all the members of the Department and the many talented technical staff for their support over the years.

I am extremely grateful to Canesis Network Limited in conjunction with the Tertiary Education Commission for the award of an Enterprise Scholarship, giving me the opportunity to study towards a PhD degree. Special acknowledgement goes to Dr Alisa Roddick-Lanzilotta of Canesis Network Limited for all her support and guidance regarding the wool processing aspects of this research.

A huge thank you goes to my parents, Cary and Stuart, for encouraging me to fulfill my dreams and reminding me that the world is my oyster. Completion of this thesis would not have been possible without their love and support. Thanks also to my brothers, Sam, Callum and Matt, for their encouragement and to my partner, Matt Jones, for all his patience and support, especially over the last year.

Lastly, I would like to give special mention to Dr Jeanette Hickford, my high school chemistry teacher at Rangi Ruru Girls' School, whose enthusiasm for chemistry inspired me to embark on this journey.

Contents

Symbols and Abbreviations

Subscripts

a	anodic	T	total
c	cathodic	GC	glassy carbon
p	(a) peak	*j*	species
	(b) particle	ss	steady-state
m	metal		

Symbols

Symbol	Meaning	Typical Units
A	area	cm^2
d	thickness of the modifying layer	cm
E	potential of an electrode *versus* a reference	V
$E_{1/2}$	measured half wave potential in voltammetry	V
E_{app}	applied potential	V
E_p	peak potential	V
E_{pa}	anodic peak potential	V
E_{pc}	cathodic peak potential	V
ΔE_p	difference between anodic and cathodic peak potentials in cyclic voltammetry	V
F	the Faraday constant; charge on one mole of electrons (96485 C mol^{-1})	C mol^{-1}
i	current	A
i_p	peak current	A
i_{pa}	anodic peak current	A
i_{pc}	cathodic peak current	A
i_{ss}	steady-state current	A
j	flux of molecules to the electrode surface per unit time	mol cm^{-2} s^{-1}
j_p	peak current density	A cm^{-2}

Symbol	Meaning	Typical Units
j_{pc}	cathodic peak current density	A cm^{-2}
j_{ss}	steady-state current density	A cm^{-2}
k	rate constant	cm s^{-1}
k^0	standard heterogeneous rate constant	cm s^{-1}
k_{obs}	observed rate constant	cm s^{-1}
λ	wavelength	nm
m_j	mass of species j	g
M_j	molar mass of species j	g mol^{-1}
n	(a) stoichiometric number of electrons involved in an electrode reaction	none
	(b) sample size	none
N	number of binding sites	none
N_j	total amount of species j in a system	mol
Q	charge passed in electrolysis	C
Q_c	value generally accepted in the literature for the charge density required to reduce a monolayer of: (a) surface oxide	μC cm^{-2}
	(b) upd lead at a gold surface	
Q_m	cumulative charge passed during metal deposition	C
r	radius	cm
R_a	average surface roughness	nm
t	time	sec
V_h	volume of a hemisphere	cm^3
X	number of particles	none
β	tunneling parameter	$Å^{-1}$
Γ_j	surface excess of species j	mol cm^{-2}
θ_j	fractional surface coverage of an interface by species j	none
ρ_j	density of species j	g cm^{-3}
υ	scan rate	V s^{-1}
χ	standard deviation of least squares	none

NMR Symbol	Meaning	Typical Units
app t	apparent triplet	none
dd	double doublet	none
δ	chemical shift	ppm
J	coupling constant	Hz
m	multiplet	none

Abreviations

Abbreviation	Meaning
2-HED	2-hydroxyethyl disulfide
AFM	atomic force microscopy
Amp	amperometry
BQ	benzoquinone
CF	carbon fabric
CNTs	carbon nanotubes
CV	cyclic voltammetry
DMFC	direct methanol fuel cell
DOPAC	3,4-dihydroxyphenylacetic acid
DT	decanethiolate
DTNB	5,5'-dithio-bis(2-nitrobenzoic acid)
DTSP	dithiobis *N*-succinimidyl propionate
ED	ethylenediamine
EDTA	ethylenediamine tetraacetic acid
EI	electron impact
EIS	electrochemical impedence spectroscopy
EQCN	electrochemical quartz crystal nanobalance
FcOH	hydroxymethyl ferrocene
FI	flow injection amperometry
GC	glassy carbon
HD	hexamethylene diamine

Abbreviation	Meaning
HMDE	hanging mercury drop electrode
HOPG	highly ordered pyrolytic graphite
HPLC	high performance liquid chromatography
HRP	horseradish peroxidase
IRRAS	infrared reflection-absorption spectroscopy
IRS	infrared reflection spectroscopy
LSV	linear sweep voltammetry
MHCF	transition metal hexacyanoferrate complex
MPc	transition metal phthalocyanine complex
MTSPc	transition metal tetrasulfophthalocyanine complex
NanoAg/GC	silver nanoparticles electrochemically deposited onto glassy carbon
NanoAu/GC	gold nanoparticles electrochemically deposited onto glassy carbon
NanoAu/CF	gold nanoparticles electrochemically deposited onto carbon fabric
NanoAu/ED/GC	citrate-capped gold nanoparticles immobilised onto an ED-modified glassy carbon electrode
NanoAu/HD/GC	citrate-capped gold nanoparticles immobilised onto an HD-modified glassy carbon electrode
NanoPd/PPF	palladium nanoparticles deposited onto pyrolysed photoresist film
NDT	1,9-nonanedithiol
NMR	nuclear magnetic resonance
OPG	ordinary pyrolytic graphite
PB	phosphate buffer
PEG	polyethylene glycol
PPF	pyrolysed photoresist film
pzc	point of zero charge
RDE	rotating disk electrode
RMS	root-mean-square
RSD	relative standard deviation
SAMs	self-assembled monolayers
SCE	saturated calomel electrode

Abbreviation	Meaning
SEM	scanning electron microscopy
SERS	surface enhanced Raman spectroscopy
SMDE	static mercury drop electrode
STM	scanning tunneling microscopy
TEM	transmission electron microscopy
THEOS	tetrakakis(2-hydroxyethyl)orthosilicates
TNB	2-nitro-5-thiobenzoic acid
TSPP	tetrakis (4-sulfophenyl)-porphyrin
TTAPP	tetrakis (4-trimethylammoniumphenyl)-porphyrin
UHV	ultrahigh vacuum
upd	underpotential deposition
UV-Vis	ultraviolet-visible
WRONZ	Wool Research Organisation of New Zealand (Inc.)
XPS	X-ray photoelectron spectroscopy

Chapter 1

Introduction

The research presented in this thesis was initially focused on the development of an electrochemical approach for the regeneration of chemical reducing agents during wool setting. The motivation was to find a more environmentally friendly method for wool setting than those currently used in the wool processing industry. This work was carried out with the sponsorship of Canesis Network Limited. Using metal nanoparticle-based electrodes, the concept of electrochemical regeneration of the reducing agent during wool setting was demonstrated. However, further optimisation of this process for industrial purposes was halted by the commercial sponsor because the industry is not ready to adopt this technology at present. Research then turned to a broader examination of the preparation and characterisation of metal nanoparticle-based electrodes and finally their utility for hydrogen peroxide detection. The first part of this introduction chapter reviews the chemistry of wool setting and the methods used in industrial wool setting processes. The second part provides an overview of metal nanoparticles and discusses techniques for the synthesis and preparation of nanostructured metal materials. Other aspects of the research are reviewed in the introductions of the relevant chapters.

1.1 The Wool Setting Process

Wool is a sulfur rich substrate which contains a high content of cystine (~ 500 μmol g^{-1}).[1] The disulfide bonds of the cystine residues cross-link adjacent protein chains in the wool fibre and play an important role in stabilising wool fibres as they restrict conformational rearrangement. Many wool processing methods are based on sulfur chemistry as the disulfide bonds influence the properties of the wool fibre. These properties can be significantly altered by changing the conformation of the wool fibre. For example, the strength of a woollen yarn can be increased by imparting twist into the yarn or the diameter of a wool fibre can be decreased by stretching the fibre. In these situations the conformations of the wool proteins are very strained. In order to release the strain and stabilise the changes in shape, the process of wool setting is essential. This process

involves the cleavage of disulfide bonds from the strained cystine amino acids of the peptide chain and allows new bonds to form giving a stable conformation that is no longer strained. Small extents of disulfide reduction are required to produce useful changes in fibre properties. For example, reduction of 20 % of wool disulfide bonds imparts shrink resistance and is sufficient to impart set.[1,2] These applications require the reduction of a limited number of wool disulfide bonds as loss of fibre strength can occur if too many cross-links are reduced.

1.1.1 The Chemistry of Wool Setting

Wool setting involves the rearrangement of crosslinks in a wool fibre to alleviate externally imposed stresses when the native conformation of the fibre is changed. Rearrangement of both hydrogen bonds and disulfide crosslinks are necessary for wool setting. There are three types of setting processes that can be defined: (1) permanent setting, (2) semi-permanent setting and (3) temporary setting.

1.1.1.1 Permanent Setting

Permanent setting of wool introduces new stable crosslinks into wool fibres which will not undergo breakage and reformation. Hence, permanent setting is imparted into the wool at the molecular level for the lifetime of the product. New crosslinks are introduced into wool fibres by treatment with strong alkali[1,3,4] or in boiling water for prolonged time periods.[1,5] Under these conditions, the wool cystine residues **1** (Scheme 1.1) undergo a β-elimination reaction to yield a dehydroalanine residue **2**, a cysteine residue **3** and sulfur.[1,5,6] The dehydroalanine residue reacts with cysteine **4** or lysine residues **6** on nearby protein chains to form lanthionine **5** and lysinoalanine **7** (Nε-(2-amino-2-carboxyethyl)lysine) crosslinks respectively. In addition, new crosslinks can also be formed by deliberate chemical modification of wool, *e.g.*, through treatment of wool with formaldehyde.[1,7] The introduction of new crosslinks into wool fibres render the wool proteins less amenable to conformational change and therefore, wool crosslinked in this way sets less readily compared to untreated wool even when setting agents are used (see Sections 1.1.2.2 and 1.1.3). These reactions are avoided in industrial setting processes because the chemistry leading to permanent setting in wool fibres is difficult to control. Over-crosslinking decreases the tensile strength of the fibres and causes brittleness. In addition, the use of formaldehyde is not acceptable

for industrial processes as it has been shown to be toxic, allergenic and carcinogenic.[8] For these reasons, the permanent setting reactions are not considered further here.

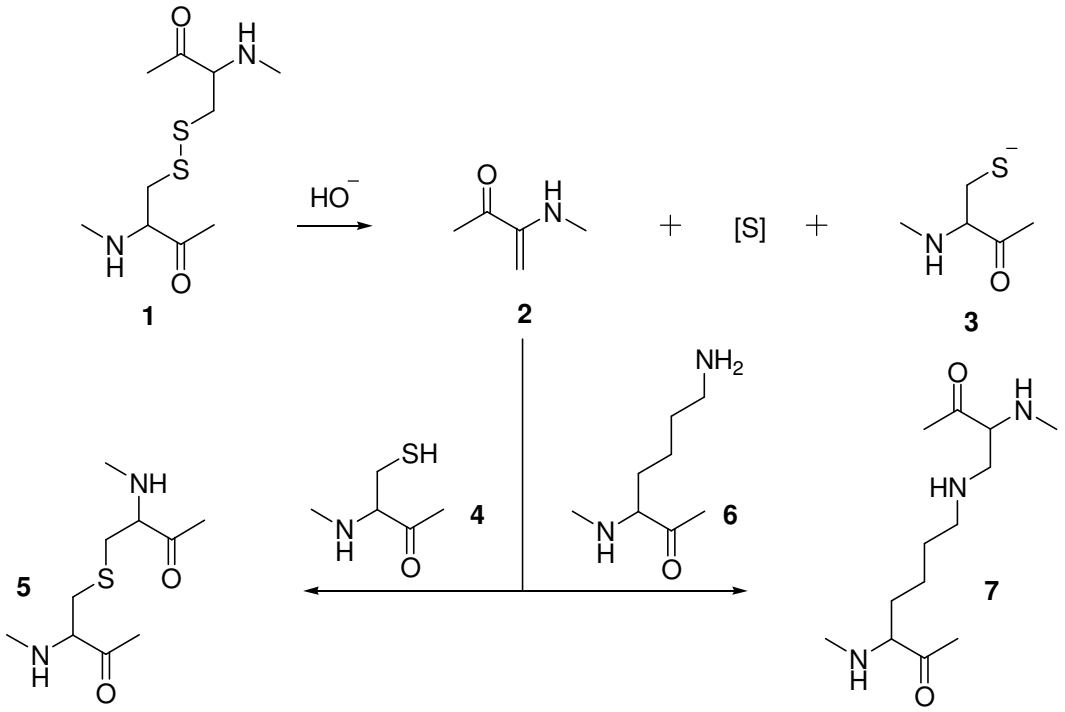

Scheme 1.1. The formation of lanthionine (**5**) and lysinoalanine (**7**) crosslinks between wool proteins after treatment with strong alkali or in boiling water.

1.1.1.2 Semi-Permanent Setting

Stabilisation of changes in the shape of wool fibres involving the cleavage and reformation of disulfide crosslinks is referred to as semi-permanent setting. Semi-permanent setting is responsible for setting achieved by all major industrial setting processes and is of most interest with respect to the work described in this thesis. When a wool fibre is bent, twisted or stretched the disulfide bonds that connect adjacent protein chains and give the fibre rigidity become stretched. To reduce the stress of stretched disulfide bonds the fibre naturally resists stretching trying to restore the fibre to its original shape and length. However, the fibre can be 'set' into the new shape by reducing the stress imposed on the fibre through cleavage and formation of new disulfide crosslinks. Cysteine residues within the wool fibre catalyse the rearrangement of the disulfide bonds from the

cystine amino acids of the peptide chain by initiating a thiol/disulfide interchange mechanism where each strained disulfide bond is replaced by an unstrained disulfide bond (Figure 1.1).[1,9,10]

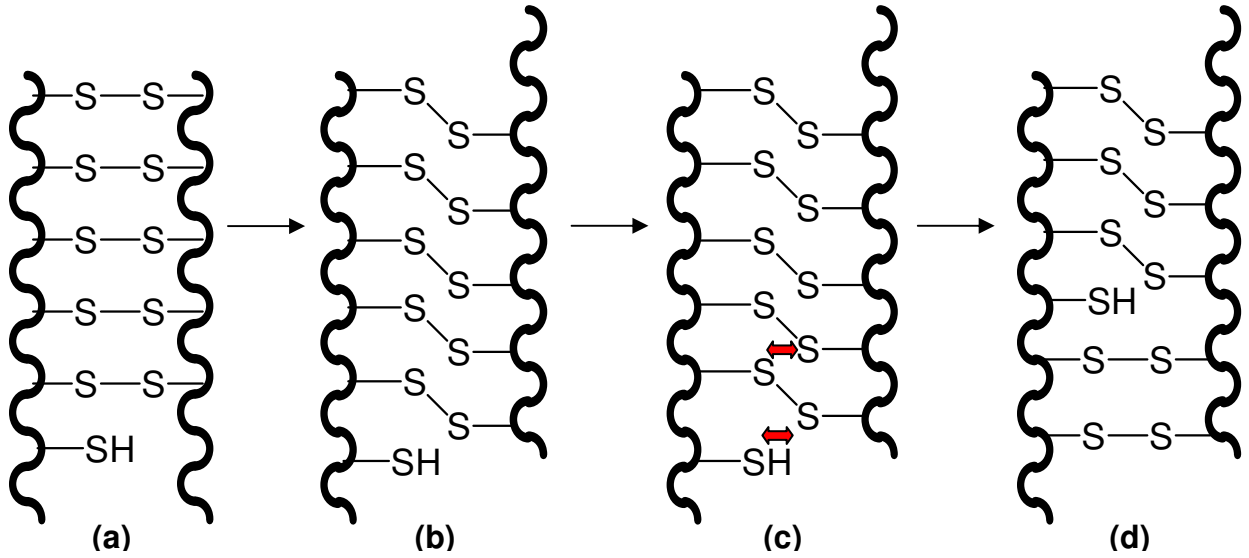

Figure 1.1. Representative illustration of the thiol-disulfide exchange mechanism in wool setting; (a) disulfide bonds connecting adjacent protein chains in an unstretched wool fibre, (b) extended disulfide bonds in a stretched wool fibre, (c, d) thiol-disulfide exchange interactions replace stretched disulfide bonds with unstretched disulfide bonds stabilising the wool fibre in the stretched conformation (note: reduction of 20 % of wool disulfide bonds is sufficient to impart semi-permanent set). Figure adapted from reference 1.

The thiol/disulfide interchange reaction is represented by the reaction in equation 1.1 where W-S-S-W represents the disulfide crosslinks between adjacent proteins of the wool fibre, WS^- represents the cysteine residues within the wool fibre and subscripts '1', '2' and '3' represent fragments of the wool protein chain.

$$\underset{\text{Stretched}}{W_1\text{-S-S-}W_2 + W_3S^-} \rightleftharpoons \underset{\text{Unstretched}}{W_1\text{-S-S-}W_3 + W_2S^-} \qquad (1.1)$$

The disulfide interchange reaction occurs as a result of nucleophilic attack on the S–S bond linking fragments of the protein chains W_1 and W_2 by the cysteine residue attached to W_3. A new disulfide bond is formed between W_1 and W_3 which is no longer under stress and another cysteine

residue appears on W_2. The rate of the reaction is dependent on the number of thiol groups and pH. The thiol anion is the species responsible for reducing the disulfide residues, therefore, reduction occurs most rapidly in alkaline solutions (pH > 8.0) when the cysteine residues (pK_a 8-10) are deprotonated.[1,11] The reaction in equation 1.1 is expressed as an equilibrium where the forward reaction is favoured to alleviate stress in the stretched disulfide bonds and reduce the overall stress of the fibre.[12] For this reason, wool setting is referred to as a chemical stress relaxation reaction as the stress imposed on the fibre leading to the change in conformation decays during the breakage and reformation of the disulfide crosslinks.[11]

1.1.1.3 Temporary Setting

Temporary setting involves the cleavage and reformation of hydrogen bonds which link coils of the protein chains in wool (Figure 1.2).[12-14] This reaction is promoted by the presence of heat and moisture as hydrogen bonds are relatively weak enabling wool molecules to move easily under these conditions. This allows the fibre to adopt a stretched, bent or creased shape. In temporary setting the disulfide crosslinks remain intact. Temporary setting is not as strong as permanent or semi-permanent setting as it can be rapidly and completely relaxed by immersion in warm water.

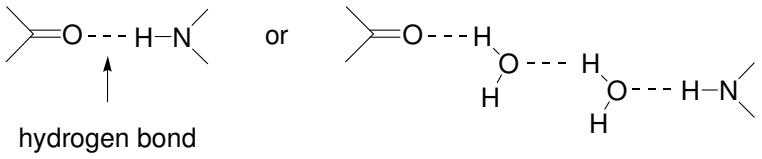

Figure 1.2. Hydrogen bond networks link the coils of protein chains in wool fibres. In the process of temporary setting these networks interchange in the presence of water and heat. Figure adapted from reference 14.

1.1.2 Industrial Methods for Wool Setting

Industrial processes for setting woollen materials involve the use of steam, immersion in boiling aqueous solutions for short periods of time or the use of chemical reducing agents. Under the conditions used in these methods, semi-permanent set is the major type of setting imparted into the

woollen material. Temporary setting involving hydrogen bonds also occurs, however, formation of lanthionine and lysinoalanine residues leading to permanent setting is negligible.

1.1.2.1 Steam Setting and Boil Setting

In steam setting and boil setting, the elevated temperatures increase the rate of the thiol/disulfide interchange reaction described for semi-permanent setting in Section 1.1.1.2. These processes are commonly used as batch methods.

Steam setting is typically carried out in an autoclave at 105-110 °C.[15] Before the wool is set, air is removed from the wool by exposing it to multiple cycles of vacuum followed by saturated steam for short periods of time (1 minute) so that steam may uniformly penetrate the wool. Setting of the wool is then performed by increasing the exposure time to steam to 10 minutes after which time the steam is removed from the autoclave. The level of set of autoclaved wool is dependent on moisture content. The wool itself is processed dry and it is important that it contains no wet spots as this can induce fibre damage, resulting in weak places on the yarn. Sources of water within the autoclave, *e.g.*, water entering the autoclave with the steam or condensation of the steam inside the autoclave, must be eliminated. A disadvantage of autoclave setting is that it can result in loss of fibre strength and lead to discolouration of the wool (yellowing) due to the degradation of aromatic amino acids, such as tryptophan and tyrosine, within the woollen fibre. A pH of 5.0-7.0 is desirable for wool to be set by steaming. At higher pH values excessive fibre damage and yellowing occurs.

Boil setting is carried out in water adjusted to pH 5.0 with acetic acid.[15] The yarn is put into water at 30 °C and the temperature is raised to the boil where it is maintained for 20 minutes. The temperature is then reduced, the wool is hydroextracted and dried. As with steam setting, this procedure also results in some yellowing of the wool.

Steam setting and boil setting processes are capable of imparting high levels of set into wool, however, they exhibit many disadvantages for use in industry because they are time consuming, damaging to wool fibres and great variability is observed between batches of wool treated.

1.1.2.2 Chemical Setting

The rate of the thiol/disulfide interchange reaction involved in semi-permanent setting can be accelerated by treatment of wool with reducing agents to convert the cystine crosslinks to cysteine residues. In contrast to steam setting and boil setting, chemical setting processes are carried out quickly, no yellowing of the wool is observed and simple and reliable control procedures can be adapted to continuous industrial processes.[12] Many reducing agents can be used for chemical setting processes but in industry the cheapest and most efficient reducing agent used is sodium metabisulfite ($Na_2S_2O_5$). Practical setting operations are performed at pH 7.0 when solid sodium metabisulfite exists as the bisulfite ion (HSO_3^-) in solution.[11] It is this anion which is responsible for reducing wool disulfide bonds *via* oxidative sulfitolysis (equation 1.2) to yield the cysteine residues necessary for catalysing the thiol/disulfide interchange mechanism involved in semi-permanent setting (equation 1.3).

$$W_1\text{-S-S-}W_2 + HSO_3^- \rightleftharpoons W_1\text{-S-S-}O_3^- + W_2\text{-}S^- + H^+ \qquad (1.2)$$

$$W_3\text{-S-S-}W_4 + W_2\text{-}S^- \rightleftharpoons W_3\text{-S-S-}W_2 + W_4\text{-}S^- \qquad (1.3)$$

Wool setting in the presence of sodium metabisulfite was used in the development of the yarn processing system commonly known as CHEMSET. This process was designed by the Wool Research Organisation of New Zealand (Inc.) (WRONZ) primarily for the processing of carpet yarns for cut-pile carpets.[11] Effective setting of the yarn used to manufacture carpets is very important as it promotes good retention of the twist imparted into the yarn after it is cut to form the carpet. If the yarn is not set effectively, the free end of the cut carpet tufts can untwist during wear or with vigorous cleaning, giving the carpet an ill-defined or fuzzy appearance which is undesirable. The CHEMSET process was designed as a continuous process where the wool, in the form of a thick coiled blanket, is transported on a conveyor belt and passed through a series of four solution baths. The first bath contains a detergent at 60-65 °C to clean the wool by removing contaminants from the yarn such as sand, dirt, wool wax (*i.e.*, lanolin), suint (natural grease formed from dry perspiration) and processing lubricant. This process is referred to as scouring. Wool setting occurs in the second bath which contains sodium metabisulfite (5-10 g L^{-1}) brought to pH 7.0 by the addition of anhydrous sodium carbonate. The effects of bisulfite concentration, temperature and treatment

time have all been investigated[16-18] and the setting reaction is normally carried out at 85 °C for an immersion time of 2 minutes. The wool is then rinsed twice in the third and fourth baths by immersion in water for 2 minutes at 85 °C. This process removes any residual bisulfite from the yarn. The rinsing procedure is a very important step of the setting process. If residual reducing agent is left in the wool then the set may be released by the application of stress or through a set-release process whereby the thiol/disulfide interchange reaction is reversed. Therefore, it is necessary to remove any excess reducing agent and thiol groups need to be oxidised to form disulfides upon completion of the setting reaction. Reducing agents can be eliminated by treatment of the set wool with an oxidising agent such as hydrogen peroxide[19] or through adequate rinsing. For the CHEMSET process, rinsing of the yarn with water at 85 °C followed by air oxidation of the cysteine residues was found to be sufficient for reversing the sulfitolysis reaction on wool and reforming the disulfide bonds between the protein chains (equations 1.2 and 1.3).[11,17]

In today's society, increasing concern about the environmental impacts of chemical processes has led to a need for the minimisation and control of waste. Evaluation of the waste waters produced during industrial setting of carpet yarns using the CHEMSET process showed that the effluent is only mildly toxic but is non-biodegradeable.[20] The use of sodium metabisulfite contributes significantly to the toxicity of the process. In solution sodium metabisulfite is converted to bisulfite and sulfite is a potentially corrosive substance. Sulfate is also present in the waste waters as a result of easy oxidation of sulfite. While sulfate is relatively harmless, large discharges may eliminate oxygen in receiving waters or sewage systems and interfere with biochemical oxidation which is undesirable. Hence, due to increasing concern over the environmental impacts of sodium metabisulfite used in industrial setting processes, alternative reducing agents are of interest.

1.1.3 Thiol Setting Agents

Thiol reagents such as cysteine,[21] 2-mercaptoethanol,[22] thioglycollic acid,[23] and toluenethiol[24] have been shown to be capable of reducing wool disulfide bonds.[1] Although there are many other reducing agents which can be used to reduce disulfide bonds, *e.g.*, sodium borohydride,[25,26] phosphines[27-29] and sulfites,[1,11,16-18] the advantage of using thiol reducing agents is that they have the required reactivity and specificity under conditions which do not cause protein damage within the wool fibres.[1] During reduction of wool disulfide bonds the thiol reducing agents

($R\text{-}S^-$) are converted to disulfides (R-S-S-R) (equation 1.4). After the wool is removed from the reducing conditions, the adjacent wool thiol groups can be re-oxidised in air to form disulfide bonds giving the wool a more stable conformation without being strained (equation 1.5).

$$\underset{\text{Strained}}{W\text{-}S\text{-}S\text{-}W} + 2R\text{-}S^- \longrightarrow 2W\text{-}S^- + R\text{-}S\text{-}S\text{-}R \qquad (1.4)$$

$$2W\text{-}S^- \longrightarrow \underset{\text{Unstrained}}{W\text{-}S\text{-}S\text{-}W} \qquad (1.5)$$

The effectiveness of the thiol setting agent for reducing wool disulfide bonds depends on the pK_a of the thiol, the redox potential and the extent of absorption by the wool.[1] Reduction of wool disulfide bonds occurs most rapidly in alkaline solutions. However, harsh alkaline conditions at elevated temperatures are undesirable for the setting process as cystine residues degrade under these conditions and are converted in part to lanthionine residues. Disulfide reduction can also be achieved using neutral or acidic conditions if a large excess of the thiol reducing agent is present. At present the use of thiol reducing agents is economically inefficient for an industrial process because of the large excess required and they react in an irreversible way. However, by utilising electrochemical methods it may be possible to regenerate thiol reducing agents by reduction of the disulfide product (equation 1.6). Hence, the electroreduction of disulfides is a focus of this research. The advantage of using electrochemical methods instead of chemical methods is that they require lower levels of reagents and they allow a degree of controllability to be added to the reaction.

$$R\text{-}S\text{-}S\text{-}R + 2e^- \xrightarrow{\text{Electrode}} 2R\text{-}S^- \qquad (1.6)$$

1.2 Methodologies for the Preparation of Nanostructured Metal Materials

Particles in the nanometer size range are stimulating considerable interest across a wide range of scientific disciplines because of their novel chemical and physical properties which originate from their small dimensions and differ from those of the bulk material.[30] The ratio of surface atoms to interior atoms increases as the particle dimensions get smaller giving rise to unique structural, electronic, magnetic, optical and catalytic properties.[31]

Many researchers are interested in the use of nanoparticles in terms of both the synthesis of nano-sized materials and exploitation of their novel properties through the fabrication of nanostructures. The key steps involved in fabricating nanostructures are the synthesis of nanoparticles and their assembly into complex structures by a variety of methods. Nanoparticles can be prepared from a range of materials.[30,32] The most common metals used are noble metals such as gold, silver, platinium and palladium. Transition metals including rhodium and ruthenium have also been employed. Nanoparticles synthesised from semiconducting materials (commonly referred to as quantum dots) such as cadmium sulfide and titanium dioxide are of considerable interest for the fabrication of nanoelectronic devices.[33,34] In addition, non-metallic nanoparticles made, for example, from clays are used in bioengineering applications.[35]

The work presented in this thesis concerns the use of noble metal nanoparticles namely gold, silver and palladium; methods for their synthesis and organisation on solid supports are reviewed in the following sections.

1.2.1 Synthesis of Metal Nanoparticles

The methods employed for preparing metal nanoparticles can be divided into two distinct categories: chemical and physical (Figure 1.3).[31] Chemical methods build the nanoparticle by controlled-aggregation of metal atoms formed after reducing metal ions. In contrast physical methods often involve vapour deposition and consist of the principle of subdividing bulk materials to nanoparticles. The properties of nanoparticles generally depend on their size, shape and

stabilising agents, which are determined by the preparation conditions. A brief overview of the methods used in this thesis to synthesise metal nanoparticles is given in Sections 1.2.1.1 and 1.2.1.2.

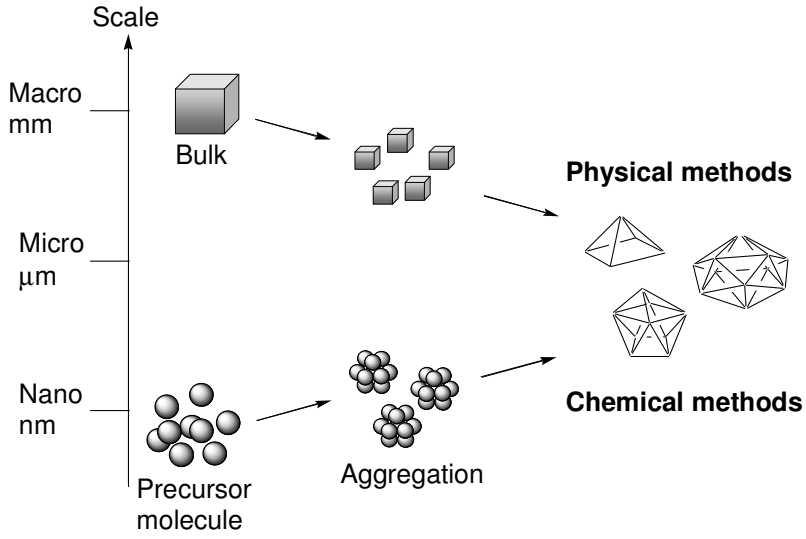

Figure 1.3. Schematic representation of the two distinct methods used to prepare nanoparticles: physical and chemical methods. Figure adapted from reference 31.

1.2.1.1 Chemical Methods

The most common method for the chemical synthesis of metal nanoparticles involves the reduction of metal complexes in dilute solution yielding a colloidal metal dispersion. The simplest and most widely used method for preparing gold nanoparticles is the aqueous reduction of $HAuCl_4$ by sodium citrate.[36,37] Nanoparticles of other noble metals such as silver, palladium and platinum can also be prepared by sodium citrate reduction of $AgNO_3$,[38,39] H_2PdCl_4[40] and H_2PtCl_4[41] respectively. Furthermore, mixed-metal particles can be synthesised which may have different functionality to the individual metals.[42] In addition to sodium citrate, other common reducing agents employed for the preparation of metal colloids include sodium borohydride,[43,44] citric acid and hydroxylamine hydrochloride.[45,46]

Nanoparticle size can be varied by changing the synthesis conditions. In general, a strong reducing agent promotes a fast reaction rate and favours the formation of smaller nanoparticles whilst a weak reducing reagent induces a slow reaction rate and relatively larger particles form.[45]

The effect of changing the synthesis conditions has been illustrated for the preparation of gold nanoparticles. The size of gold nanoparticles produced by sodium citrate reduction is controlled by varying the sodium citrate to gold ratio. Turkevich and co-workers showed that the particle diameter decreased as the concentration of sodium citrate is increased.[36] The addition of sodium borohydride, a strong reducing agent, to the citrate/gold solution gave even smaller particles with an average diameter of 2.6 nm.[37] A 'seeding' approach has also been developed for preparing large gold colloids to improve the monodispersity of the particles. For example, small citrate-capped gold nanoparticles (2.6 nm diameter) are grown to larger sizes by addition of a boiling solution of $HAuCl_4$ and sodium citrate.[47] Seeding growth allows the nanoparticle size to be manipulated by varying the ratio of seed to metal salt. The choice of reducing reagent has also been shown to influence the morphology of gold colloidal particles, *e.g.*, the use of sodium citrate or hydrogen peroxide as reducing agents yields spherical particles whereas faceted colloidal gold particles are formed when hydroxylamine hydrochloride (cubical with Au(100) facets) and citric acid (particles with trigonal symmetry containing Au(111) facets) are used under otherwise similar synthesis conditions.[46] The concentration of reducing agents and pH value also influence particle morphology. Upon lowering the pH value, particles with trigonal symmetry developed along with spherical gold particles grown in the presence of hydrogen peroxide.[46]

Colloidal methods are relatively simple and inexpensive, however, nanoparticles tend to be unstable in solution due to an increase in surface energy as the particle size decreases and special precautions have to be taken to prevent aggregation.[31] For instance, glassware needs to be cleaned thoroughly and the reagent solutions and solvents need to be filtered and of the highest purity. Synthesis of colloidal metal nanoparticles usually requires the use of a stabilising agent which associates with the surface of the particle imparting charge or solubility properties to keep nanoparticles suspended and prevent aggregation. For example, during sodium citrate reduction of metal salts, a weakly bound negatively charged layer of citrate-capping groups is formed on the nanoparticle surface and stabilises the colloids in solution as electrostatic repulsion between neighbouring particles inhibits aggregation.[48,49] Polymers such as polyethyleneimine and sodium polyacrylate have also been used to stabilise metal nanoparticles and are attached to the nanoparticle surface *via* electrostatic interactions.[45]

The synthesis of nanoparticles that contain surface functionality is desirable for the construction of functional architectures (see Section 1.2.2) and can be achieved during synthesis by the addition of a suitable agent to the reaction vessel. As nanoparticles form, the surface functionalisation agent attaches to the nanoparticles and also imparts enhanced stability and gives additional control over particle size.[30] Colloidal metal nanoparticles with surface functionality such as carboxylic acids have been prepared by sodium borohydride reduction in the presence of thiols under aqueous conditions.[50] When the surface functionalisation agent is not water soluble, a two-phase (water-toluene) synthesis can be used. This method has been employed in the preparation of long chain alkanethiol-coated surfaces on gold colloids.[43]

An alternative to using chemical reduction methodologies for the preparation of metal colloid dispersions is reduction of the metal salt at an applied potential. This electrochemical technique is typically carried out in aqueous electrolyte solutions and requires a conductive substrate onto which the metal nanoparticles are deposited. The same metal salt precursors used for preparing colloidal metal nanoparticles are also employed in electrochemical deposition methods. The overall surface area of the metal as well as nanoparticle size, density and shape can be controlled to some extent by varying the deposition conditions such as electrolyte composition, deposition time and/or overpotential.[51,52] A detailed discussion of the nucleation and growth mechanism for metal nanoparticles electrochemically deposited onto conductive substrates is given in Chapter 4, Section 4.1.2.

1.2.1.2 Physical Methods

Physical vapour deposition involves the conversion of solid material into a gaseous phase by physical processes; this material is then cooled and re-deposited on a substrate. Examples of physical vapour deposition conversion processes include thermal evaporation, laser ablation, spark erosion and sputtering.[31] For the research presented in this thesis palladium nanoparticles were prepared using magnetron sputtering (see Chapter 7, Section 7.2.4).[31,53] This method involves applying a direct current (dc) voltage between two electrodes to create an ionised gas discharge (also referred to as plasma). The gas used in sputtering is generally inert such as argon or xenon. For dc sputtering a negative voltage is applied to the electrically conductive target. High density dc plasma in low sputtering gas pressure is confined to the vicinity of the sputtering target by application of a

static magnetic field near the target (Figure 1.4). Accelerated ions from the high density gas bombard the target and subsequently eject atoms from surface layers which are deposited onto the substrate. The use of ionised gases during vapour deposition is advantageous because the final materials deposited are of a higher purity than those prepared by other physical vapour deposition methods. In addition, the magnetic field prevents secondary electrons produced by the target from bombarding the substrate and causing uncontrolled heating or damage. Large deposition rates can be achieved and multiple targets can be rotated to produce a multilayered coating on the substrate.

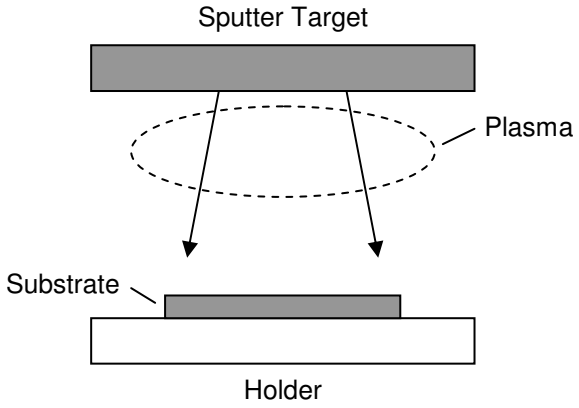

Figure 1.4. Schematic representation of plasma sputtering where accelerated ions of an inert gas (plasma), generated by applying a magnetic field, bombard the target and subsequently eject atoms from surface layers which are deposited onto a substrate. Figure taken from reference 53.

1.2.2 Preparation of Metal Nanostructures and their Applications

The emergence of nanotechnology, and research into nanoparticles has led to a variety of applications which include electronic nanodevices,[34,54] molecular catalysts[55-57] and chemical and biosensors.[58,59] Much of this interest was generated to take advantage of the unique chemical, optical and electrical properties that metal nanoparticles exhibit as a result of their very small size. Metal nanoparticles need to be immobilised onto solid supports to have any real application in practical devices and a variety of methods have been developed to organise nanoparticles into complex surface-bound structures.[30] As discussed in the previous section metal nanoparticles can be directly immobilised onto solid substrates by electrochemical and vapour phase deposition methods. This section focuses on techniques for the assembly of colloidal metal nanoparticles onto surfaces.

Applications of this technology are also discussed below. Illustrative examples of the uses for electrochemically deposited metal nanostructures are given in Chapter 4, Section 4.1.3.

A promising route for the fabrication of surface bound metal nanostructures is the assembly of metal colloids *via* electrostatic or covalent interactions onto suitably functionalised surfaces usually containing amine or thiol terminal groups allowing chemical reactivity to direct assembly (Figure 1.5). A wide variety of substrates including metals, silicon, glass and carbon have been used.[30] The general method for the formation of a colloid monolayer on a modified surface involves placing the surface-functionalised substrate into the solution of nanoparticles, which adsorb onto the surface and assemble over time. Ohsaka and co-workers used amine-terminated cysteamine self assembled monolayers (SAMs) attached to gold substrates to anchor citrate stabilised gold nanoparticles (2.3 nm diameter) *via* electrostatic interactions.[60] This electrode was investigated for the development of a dopamine sensor and exhibited greater sensitivity for the detection of dopamine (detection limit 0.13 μM) in the presence of ascorbate than a solid gold electrode. Well-separated voltammetric peaks were observed for dopamine and ascorbate at the gold nanoparticle electrode and the high sensitivity of this electrode could be attributed to the greater combined surface area of gold nanoparticles compared to the solid gold electrode.

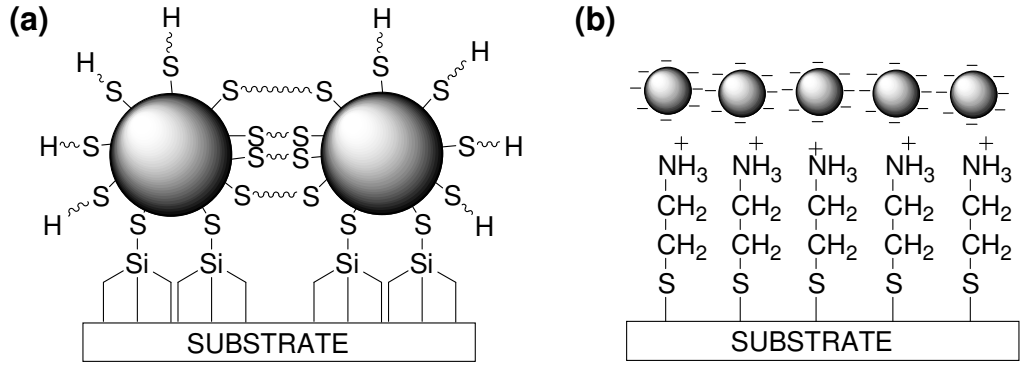

Figure 1.5. Schematic representation of gold nanoparticles assembled onto functionalised solid substrates by (a) covalent and (b) electrostatic interactions. Figure adapted from references 54 and 60.

Silicon is an important material in modern technology and there has been strong interest in the attachment of nanoparticles to modified silicon and glass surfaces. Functionalisation of the surface has been achieved using alkyloxysilanes. Three-dimensional nanostructures fabricated by electrostatically assembling citrate-capped gold nanoparticles (40 nm diameter) onto amine-terminated silanised indium tin oxide glass and silicon surfaces have attracted significant research interest towards the preparation of substrates for surface-enhanced Raman spectroscopy (SERS).[61] Atomic force microscopy showed that the gold nanoparticles self assembled on the silanised surface in such a way that the final assemblies were rough yet compacted. These characteristics related to the SERS activity of the substrate and a strong Raman signal towards the molecular probe bi-ethlyene-pyridine was observed at very low concentrations. An alternative route to the preparation of gold nanoparticle assemblies on glass substrates involved covalently attaching thiol-stabilised colloidal nanoparticles (2.2 nm diameter) onto thiol-terminated alkyloxysilane-modified surfaces.[54] This material exhibited conductivities that mimic the behaviour of semiconductors and depend markedly on the structure of the dithiol used to link the gold particles together. Proposed applications for these electrodes include uses in sub-microelectronic devices and circuitry including switches, diodes and photovoltaics.

An alternative method for constructing colloidal metal nanostructures is to assemble functionalised metal nanoparticles directly onto the solid support. Zhong *et al*. developed a strategy for preparing thin film network assemblies of thiolate encapsulated gold or gold-platinum alloy nanoparticles on glassy carbon electrodes by an exchange-cross-linking-precipitation route (Figure 1.6).[55-57] This involved immersion of the glassy carbon substrate into a hexane solution containing decanethiolate (DT)-encapsulated metal nanoparticles and 1,9-nonanedithiol (NDT) cross linking agent. In this solution, the DT capping agents were exchanged for NDT groups at the nanoparticle surface which facilitated cross linking of the functionalised metal nanoparticles and growth of a thin film on the electrode. These nanoparticle assemblies showed catalytic activity towards the electro-oxidation of carbon monoxide[55] and methanol[56,57] which are important reactions for fuel-cell development. Encapsulation of the nanoparticle surfaces with thiolates is advantageous to prevent aggregation and reduce carbon monoxide poisoning of the nanoparticle surface.[55,56]

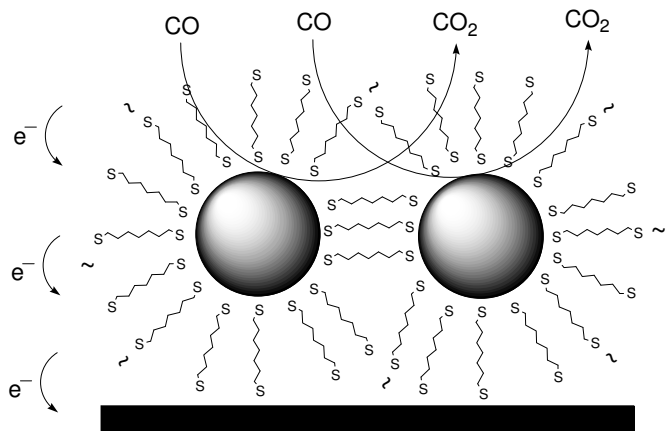

Figure 1.6. Schematic representation of catalytic sites for carbon monoxide oxidation at thiolate-capped, networked gold nanoparticles on a glassy carbon surface. Figure adapted from reference 55.

1.3 Statement of Aims

The work presented in this thesis falls into two main areas:

1. *Development of an Electrochemical Approach to Wool Setting*

The overall aim of this part of the research is to use electrochemical techniques to develop alternative approaches to the wool setting process which have a lower impact on the environment than current chemical methods and could be economically viable for an industrial process. In particular, the goal is to find efficient electrochemical methods for reducing the disulfide bonds of compounds such as cystine and 2-hydroxyethyl disulfide (2-HED) to form the corresponding thiols (cysteine and 2-mercaptoethanol respectively) which can subsequently act as reducing agents for the cleavage of wool disulfide bonds in the process of wool setting. These compounds are investigated because the electrolytic reduction of wool disulfide bonds in the presence of low concentrations of 2-mercaptoethanol has been previously reported in 1965[22] and cysteine is an environmentally favourable alternative because it is a readily available natural amino acid. Additional advantages of using cysteine are that it has a low odour and is less expensive compared to other thiols such as 2-mercaptoethanol, thioglycollic acid and toluenethiol. To achieve this goal, the following objectives were addressed:

- To survey the reduction of cystine and 2-HED at a range of metal and carbon electrodes to identify electrode materials where cleavage of the S–S bond occurs at mild potentials with high current densities.

- To fabricate high surface area metal nanoparticle electrodes for the electroreduction of cystine and 2-HED using the most promising electrode materials identified.

- To demonstrate the ability of a small amount of catalytically generated thiol to reduce wool disulfide bonds using electrochemistry.

2. Tailoring of Metal Nanoparticle Electrodes for the Electroanalysis of Hydrogen Peroxide

Expanding on the research described in the section above regarding the fabrication of high surface area metal nanoparticle electrodes, further work is carried out to investigate methods for the controlled preparation of metal nanoparticle assemblies. Their potential use in electroanalysis is examined by studying the electro-oxidation and reduction of hydrogen peroxide. Carbon substrates are employed for assembling metal nanoparticles. This material has a wide potential window, is generally low-cost, highly conducting, and mechanically stable and is available in a variety of forms suitable for different applications such as felts and cloths, pyrolysed photoresist films, high surface area carbon powders and carbon fibers.[62-64] These characteristics make carbon an interesting material for the assembly of metal nanoparticles. Gold and palladium nanoparticles are employed in this part of the research which aims to achieve the following objectives:

- To characterise gold and palladium nanoparticle electrodes fabricated using various methods including electrochemical deposition, vapour deposition and immobilisation by electrostatic interactions.

- To develop a method for the controlled assembly of gold nanoparticles onto amine tether layers attached to carbon surfaces by exploiting electrostatic interactions between anionic citrate-capping groups on the gold nanoparticles and cationic amine sites within the tethered layer.

- To control the size and density of metal nanoparticles assembled either directly onto carbon substrates or onto amine tether layers attached to carbon surfaces in order to optimise the electrode response towards the electro-oxidation and reduction of hydrogen peroxide.

1.4 Structure of Thesis

General experimental details relevant to the work described in this thesis are given in **Chapter 2**. The results for the two main research areas are organised as follows:

Chapters 3 to **5** are focused on the development of an electrochemical approach to wool setting. Direct reduction of cystine and 2-HED is examined in **Chapter 3** at a range of metal and carbon electrodes. The use of transition metal phthalocyanine complexes immobilised onto glassy carbon electrodes as mediators for disulfide reduction is also investigated. The fabrication of high surface area metal nanoparticle electrodes for the electroreduction of cystine and 2-HED is described in **Chapter 4** and the ability of a small amount of catalytically generated thiol for reducing wool disulfide bonds is investigated in **Chapter 5** using the most promising electrochemical system.

Chapters 6 and **7** are focused on the preparation and characterisation of metal nanoparticle electrodes and examines their use for the electrochemical detection of hydrogen peroxide. Specifically, **Chapter 6** investigates the electrochemically assisted covalent modification of carbon substrates with an amine film and the stability of these films in solution is examined using electrochemistry, atomic force microscopy and X-ray photoelectron spectroscopy. The controlled preparation of gold and palladium nanoparticle electrodes for the electro-oxidation and reduction of hydrogen peroxide is explored in **Chapter 7.**

Finally, **Chapter 8** provides a summary of the general conclusions that can be drawn from this work and discusses possible future directions for further research.

1.5 References for Chapter 1

1. Maclaren, J. A.; Milligan, B., In *Wool science: The chemical reactivity of the wool fibre;* Science Press: Marrickville, NSW, Australia, 1981.

2. Farnworth, A. J. Shrinkproofing of wool with reducing agents. *Journal of the Society of Dyers and Colourists* **1961**, *77*, 483-488.

3. Ziegler, K. L. The influence of alkali treatment on wool. *Proceedings of the International Wool Textile Research Conference, Paris,* **1965**, *2*, 312-323.

4. Corfield, M. C.; Wood, C. The formation of lysinoalanine during the treatment of wool with alkali. *The Biochemical Journal* **1967**, *103*, 15C-16C.

5. Robson, A.; Williams, M. J.; Woodhouse, J. M. The formation of lysinoalanine and lanthionine in wool fibres stretched in boiling water, and their relation to pemanent set. *Journal of the Textile Institute* **1969**, *60*, 140-151.

6. Swan, J. M. Mechanism of alkaline degradation of cystine residues in proteins. *Nature* **1957**, *179*, 965.

7. Caldwell, J. B.; Leach, S. J.; Milligan, B.; Delmenico, J. Formaldehyde treatments for stabilising set in wool. *Textile Research Journal* **1968**, *38*, 877-878.

8. *Formaldehyde*; MSDS No. F5522 [online]; Mallincrokrodt Baker: Phillipsburg, NJ, May 4, 2007. http://www.jtbaker.com/msds/englishhtml/f5522.htm (accessed Sept 16, 2007).

9. Caldwell, J. B.; Leach, S. J.; Meschers, A.; Milligan, B. The role of thiol groups in the setting of wool. *Textile Research Journal* **1964**, *34*, 627-634.

10. Crewther, W. G. Thiol-disulfide interchange reactions in the setting of single wool fibres. *Journal of the Society of Dyers and Colourists* **1966**, *82*, 54-58.

11. McKinnon, A. J. Package-to-package carpet yarn wet processing: The CHEMSET technology. *Wool Science Review* **1990**, *66*, 3-43.

12. Wood, E. J. Get set, stay. In *Tangling with wool*; Wool Research Organisation of New Zealand (Inc.), Chaucer Press Ltd: Christchurch, New Zealand, 2000; p 10.1-10.7.

13. Rouette, H.-K.; Kittan, G. Setting. In *Wool fabric finishing*; Crawshaw, G. H., Eds., Wool Development International Ltd.: Ilkley, UK, 1991; p 155-182.

14. McKinnon, A. J., *Carpet yarn quality enhancement: Setting reactions in wool carpet yarns - a brief explanation*, Wool Research Organisation of New Zealand (Inc.), Carpet Technical Seminar, **1999**, *Unpublished report*.

15. Wools of New Zealand. *Yarn finishing and chemical treatments: 4.2 Twist setting of wool carpet yarns.* Carpet Technical Information, **1994**.

16. Forbes, E. A.; Dittrich, J.-H. Bisulfite setting of woollen-spun carpet yarns. *Journal of the Society of Dyers and Colourists* **1980**, *96*, 10-14.

17. Dittrich, J.-H.; Forbes, E. A. Continuous bisulfite setting of wool carpet yarn - some exploratory experiments. *Textil-Praxis International* **1981**, *36*, 874-876, 1019-1021.

18. Forbes, E. A.; Dittrich, J.-H.; Wemyss, A. M.; White, M. A. Further aspects of bisulfite setting of wool carpet yarns in a tape scouring machine. *Journal of the Society of Dyers and Colourists* **1982**, *98*, 59-60.

19. Watson, A. A.; Page, C. T. In *Chemical aspects of setting and set release in wool carpet yarns*, 8th International Wool Textile Research Conference, Christchurch, New Zealand, **1990**, p 502-511.

20. Robinson, P. W. *Characteristics of effluent from wet processing of yarns.* Wool Research Organisation of New Zealand (Inc.), Report R183, **1991**.

21. Kubu, E. T.; Montgomery, D. J. The stress relaxation of fibrous materials. II. Kinetics of the reduction of wool keratin by cysteine. *Textile Research Journal* **1952**, *22*, 778-782.

22. Leach, S. J.; Meschers, A.; Swanepoel, O. A. The electrolytic reduction of proteins. *Biochemistry* **1965**, *4*, 23-27.

23. Asquith, R. S.; Puri, A. K. The Formation of mixed disulfides by the action of thioglycollic acid on wool-cystine and its relationship to wool setting. *Textile Research Journal* **1970**, *40*, 273-280.

24. Maclaren, J. A. Extent of reduction of wool proteins by thiols. *Australian Journal of Chemistry* **1962**, *15*, 824-831.

25. Brown, W. D. Reduction of protein disulfide bonds by sodium borohydride. *Biochimica et Biophysica Acta* **1960**, *44*, 365-367.

26. Kotsira, V. P.; Clonis, Y. D. Chemical modification of barley root oxalate oxidase shows the presence of a lysine, a carboxylate, and disulfides, essential for enzyme activity. *Archives of Biochemistry and Biophysics* **1998**, *356*, 117-126.

27. Sweetman, B. J.; Maclaren, J. A. The Reduction of wool keratin by tertiary phosphines. *Australian Journal of Chemistry* **1966**, *19*, 2347-2354.

28. Burns, J. A.; Butler, J. C.; Moran, J.; Whitesides, G. M. Selective reduction of disulfides by tris(2-carboxyethyl)phosphine. *Journal of Organic Chemistry* **1991**, *56*, 2648-2650.

29. Maclaren, J. A.; Sweetman, B. J. Preparation of reduced and S-alkylated wool keratins using tri-n-butylphoshine. *Australian Journal of Chemistry* **1966**, *19*, 2355-2360.

30. Shipway, A. N.; Katz, E.; Willner, I. Nanoparticle arrays on surfaces for electronic, optical, and sensor applications. *Chemphyschem* **2000**, *1*, 18-52.

31. Brydson, R. M.; Hammond, C. Generic methodologies for nanotechnology: Classification and fabrication. In *Nanoscale science and technology*; Kelsall, R.; Hamley, I.; Geoghegan, M., Eds; Jon Wiley & Sons Ltd.: Chichester, West Sussex, England, 2006; p 1-55.

32. Poole, C. P. J.; Owens, F. J., *Introduction to nanotechnology;* John Wiley & Sons, Inc.: Hoboken, NJ, USA, 2003; p 277-280.

33. Chua, J. B. Y.; Pan, C. K.; Ng, K. Y.; Tan, K. L.; Baroky, T. A. Device and method for emitting output light using quantum dots and non-quantum fluorescent material. U.S. Patent 7102152 B2, September 5, 2006.

34. Goldhaber-Gordan, D.; Montemerlo, M. S.; Love, J. C.; Opiteck, G. J.; Ellenbogen, J. C. Overview of nanoelectronic devices. *Proceedings of the IEEE* **1997**, *85*, 521-540.

35. Rohrbaugh, R. H.; Jordan IV, G. T.; McDonald, M. R.; Carter, J. D.; Gosselink, E. P.; Liddle, H. A. Coating composition for modifying surfaces. U.S. Patent 7112621 B2, September 26, 2006.

36. Turkevich, J.; Stevenson, P. C.; Hillier, J. The nucleation and growth processes in the synthesis of colloidal gold. *Discussions of the Faraday Society* **1951**, *No. 11*, 55-75.

37. Grabar, K. C.; Freeman, R. G.; Hommer, M. B.; Natan, M. J. Preparation and characterisation of au colloid monolayers. *Analytical Chemistry* **1995**, *67*, 735-743.

38. Bright, R. M.; Musick, M. D.; Natan, M. J. Preparation and characterisation of Ag colloid monolayers. *Langmuir* **1998**, *14*, 5695-5701.

39. Zheng, J.; Li, X.; Gu, R.; Lu, T. Comparison of the surface properties of the assembled silver nanoparticle electrode and roughened silver electrode. *Journal of Physical Chemistry B* **2002**, *106*, 1019-1023.

40. Turkevic.J; Kim, G. Palladium - preparation and catalytic properties of particles of uniform size. *Science* **1970**, *169*, 873-879.

41. Rampino, L. D.; Nord, F. F. Preparation of palladium and platinum synthetic high polymer catalysts and the relationship between particle size and rate of hydrogenation. *Journal of the American Chemical Society* **1941**, *63*, 2745-2749.

42. Toshima, N.; Yonezawa, T. Bimetallic nanoparticles - novel materials for chemical and physical applications. *New Journal of Chemistry* **1998**, *22*, 1179-1201.

43. Brust, M.; Walker, M.; Bethell, D.; Schiffrin, D. J.; Whyman, R. Synthesis of thiol-derivatised gold nanoparticles in a 2-phase liquid-liquid system. *Journal of the Chemical Society-Chemical Communications* **1994**, 801-802.

44. Hostetler, M. J.; Wingate, J. E.; Zhong, C. J.; Harris, J. E.; Vachet, R. W.; Clark, M. R.; Londono, J. D.; Green, S. J.; Stokes, J. J.; Wignall, G. D.; Glish, G. L.; Porter, M. D.; Evans, N. D.; Murray, R. W. Alkanethiolate gold cluster molecules with core diameters from 1.5 to 5.2 nm: Core and monolayer properties as a function of core size. *Langmuir* **1998**, *14*, 17-30.

45. Cao, G., *Nanostructure and nanomaterials: Synthesis, properties and applications;* Imperial College Press: London, UK, 2004.

46. Milligan, W. O.; Morriss, R. H. Morphology of colloidal gold - comparative study. *Journal of the American Chemical Society* **1964**, *86*, 3461-3467.

47. Brown, K. R.; Walter, D. G.; Natan, M. J. Seeding of colloidal Au nanoparticle solutions. 2. Improved control of particle size and shape. *Chemistry of Materials* **2000**, *12*, 306-313.

48. Turkevich, J. Colloidal gold. Part I: Historical and preparative aspects, morphology and structure. *Gold Bulletin* **1985**, *18*, 86-91.

49. Turkevich, J. Collodial gold. Part II: Colour, coagulation, adhesion, alloying and catalytic properties. *Gold Bulletin* **1985**, *18*, 125-131.

50. Abad, J. M.; Mertens, S. F. L.; Pita, M.; Fernández, V. M.; Schiffrin, D. J. Functionalisation of thioctic acid-capped gold nanoparticles for specific immobilisation of histidine-tagged proteins. *Journal of the American Chemical Society* **2005**, *127*, 5689-5694.

51. Finot, M. O.; Braybrook, G. D.; McDermott, M. T. Characterisation of electrochemically deposited gold nanocrystals on glassy carbon electrodes. *Journal of Electroanalytical Chemistry* **1999**, *466*, 234-241.

52. El-Deab, M. S.; Okajima, T.; Ohsaka, T. Electrochemical reduction of oxygen on gold nanoparticle-electrodeposited glassy carbon electrodes. *Journal of the Electrochemical Society* **2003**, *150*, A851-A857.

53. Chow, G.-M.; Zhang, J. Nanostructured films and coating by evaporation, sputtering, thermal spraying, electro- and electroless deposition. In *Handbook of nanophase and nanostructured materials*; Wang, Z. L.; Liu, Y.; Zhang, Z., Eds; Kluwer Academic/Plenum Publishers: New York, NY, USA, 2003; Vol. 1, p 246-277.

54. Bethell, D.; Brust, M.; Schiffrin, D. J.; Kiely, C. From monolayers to nanostructured materials: An organic chemist's view of self-assembly. *Journal of Electroanalytical Chemistry* **1996**, *409*, 137-143.

55. Maye, M. M.; Lou, Y. B.; Zhong, C. J. Core-shell gold nanoparticle assembly as novel electrocatalyst of CO oxidation. *Langmuir* **2000**, *16*, 7520-7523.

56. Lou, Y. B.; Maye, M. M.; Han, L.; Luo, J.; Zhong, C. J. Gold-platinum alloy nanoparticle assembly as catalyst for methanol electrooxidation. *Chemical Communications* **2001**, 473-474.

57. Luo, J.; Maye, M. M.; Lou, Y.; Han, L.; Hepel, M.; Zhong, C. J. Catalytic activation of core-shell assembled gold nanoparticles as catalyst for methanol oxidation. *Catalysis Today* **2002**, *77*, 127-138.

58. Hernández-Santos, D.; González-Garcia, M. B.; García, A. C. Metal-nanoparticles based electroanalysis. *Electroanalysis* **2002**, *14*, 1225-1235.

59. Luo, X. L.; Morrin, A.; Killard, A. J.; Smyth, M. R. Application of nanoparticles in electrochemical sensors and biosensors. *Electroanalysis* **2006**, *18*, 319-326.

60. Raj, C. R.; Okajima, T.; Ohsaka, T. Gold nanoparticle arrays for the voltammetric sensing of dopamine. *Journal of Electroanalytical Chemistry* **2003**, *543*, 127-133.

61. Seitz, O.; Chehimi, M. M.; Cabet-Deliry, E.; Truong, S.; Felidj, N.; Perruchot, C.; Greaves, S. J.; Watts, J. F. Preparation and characterisation of gold nanoparticle assemblies on silanised glass plates. *Colloids and Surfaces a-Physicochemical and Engineering Aspects* **2003**, *218*, 225-239.

62. McCreery, R. L.; Cline, K. K. Carbon electrodes. In *Laboratory techniques in electroanalytical chemistry*; Kissinger, P. T.; Heineman, W. R., Eds; Marcel Dekker, Inc.: New York, 1996; p 293-330.

63. Wang, J., *Analytical electrochemistry;* VCH: New York, 1994; p 83-85.

64. Ranganathan, S.; McCreery, R. L. Electroanalytical performance of carbon films with near-atomic flatness. *Analytical Chemistry* **2001**, *73*, 893-900.

Chapter 2

General Experimental Methods

2.1 General

Room temperature is defined as 20 °C. All temperatures quoted in this thesis have an error associated with temperature fluctuations of ± 4 °C.

2.2 Reagents and Solutions

The reagents employed in this research are given in Table 2.1, along with any abbreviation or formula used in the text, the supplier and the conditions for use. Unless otherwise stated, all reagents were of commercial grade. All aqueous solutions were prepared using Millipore Milli-Q water (>18 MΩ cm). Acetonitrile (HPLC grade) was used for non-aqueous electrochemistry and was dried over CaH_2 for 7 days and refluxed under nitrogen for 120 minutes prior to distilling in a nitrogen atmosphere. Tetrabutylammonium tetrafluoroborate ($[Bu_4N]BF_4$) was the electrolyte used for non-aqueous electrochemistry. This was prepared by mixing tetra-*n*-butylammonium hydroxide (8 % w/w aqueous solution) with fluoroboric acid (8 % w/w aqueous solution) (4:1 v/v) stirring vigorously. The resulting white precipitate was filtered, washed thoroughly with Milli-Q water and collected under vacuum suction. Following oven drying (45 °C) for 2 days, further drying was achieved using low pressure vacuum for 2 days (80 °C). The $[Bu_4N]BF_4$ electrolyte was stored under vacuum until use.

Table 2.1. Reagents and solvents used for the research described in this thesis.

Chemical	Formula/Abbreviation	Supplier	Use
5,5'-Dithio-bis(2-nitrobenzoic acid)	DTNB	Sigma	As received
Hexamethylenediamine	HD	Riedel-de Haën	As received
2-Hydroxyethyl disulfide	2-HED	Aldrich	As received
2-Mercaptoethanol	-	BDH	As received
Acetone (solvent grade)	-	Andrew Chemicals	As received
Acetonitrile (HPLC grade)	-	Ajax Finechem	Dried over CaH_2 for 7 days, refluxed and distilled
Ammonia	-	Wilsons Chemicals Ltd.	As received
Calcium hydride	CaH_2	Merck	As received
Cobalt (II) phthalocyanine	CoPc	Strem Chemicals	As received
Dimethyl sulfoxide	DMSO	Scharlau	As received
di-Sodium hydrogen orthophosphate (anhydrous) (AnalaR)	Na_2HPO_4	Fisons	Oven-dried at 45 °C overnight
Ethylenediamine	ED	Merck	As received
Fluoroboric acid (50 % w/w)	-	BDH	As received
Hydrochloric acid (33 %)	HCl	Orica Chemnet	As received
Hydrogen peroxide (50 % w/w)	H_2O_2	Wilsons Chemicals Ltd.	As received
Hydrogen terachloroaurate (III), ACS, 99.99 % (metals basis), Au 49.5 %	$HAuCl_4$	Alfa Aesar	As received, stored under nitrogen in the dark
Hydroxymethyl ferrocene	FcOH	Strem Chemicals	As received
Iron (II) phthalocyanine	FePc	Strem Chemicals	As received
Isopropyl alchol (solvent grade)	-	Shell Chemicals	As received
L-Cysteic acid	Cysteic acid	Aldrich	As received
L-Cysteine	Cysteine	AppliChem	As received
L-Cystine	Cystine	BDH	As received

Chemical	Formula/Abbreviation	Supplier	Use
Lead oxide (AnalaR)	PbO	BDH	As recieved
Leophen M[a]	Leophen M	BASF	As received
Manganese (II) phthalocyanine	MnPc	Strem Chemicals	As received, stored under vacuum
Methanol (solvent grade)	-	Australian Solvents and Chemicals Company	As received
Nitric acid (68 %)	HNO_3	Orica Chemnet	As received
p-Benzoquinone	BQ	May & Baker Ltd.	As received
Perchloric acid (70 %) (AnalaR)	$HClO_4$	BDH	As received
Potassium chloride (AnalaR)	KCl	BDH	As received
Potassium dihydrogen phosphate (AnalaR)	KH_2PO_4	Fisher Scientific Co.	As received or oven-dried at 45 °C overnight
Potassium nitrate	KNO_3	Ajax Chemicals	As received
Potassium nitrate (AnalaR)	KNO_3	Ajax Chemicals	As received
Potassium tetrachloroaurate (III), Premion, 99.99 % (metals basis)	$KAuCl_4$	Alfa Aesar	As received, stored under nitrogen in the dark
Silver nitrate	$AgNO_3$	BDH	As received, stored in the dark
Sodium borohydride	$NaBH_4$	Fisher Scientific Co.	As received
Sodium carbonate (anhydrous)	Na_2CO_3	BDH	As received
Sodium hydrogen carbonate (AnalaR)	$NaHCO_3$	BDH	Oven-dried at 200 °C overnight
Sodium hydroxide	NaOH	Merck	As received
Sodium metabisulfite (AnalaR)	$Na_2S_2O_5$	BDH	As received
Sodium perchlorate monohydrate	$NaClO_4$	Scharlau	As received
Sulfuric acid (95 %) (AnalaR)	H_2SO_4	Prolabo	As received
Tetrabutylammonium hydroxide (40 % w/w)	-	Acros Organics	As received
Tris(hydroxymethyl) aminomethane	Tris	Sigma	As received
tri-Sodium citrate	-	BDH	As received

[a] Neutral phosphoric acid ester with nonionic emulsifiers. Formula is unspecified. Leophen M is the name given in the Chemical Abstracts Service (CAS) Registry produced by the American Chemical Society.

2.3 Buffer Solutions

Two standard buffers (phosphate, pH 6.86 and carbonate, pH 10.01) were used to calibrate the pH meter (Hanna Instruments, Model H18314) (Table 2.2). Two phosphate buffers (pH 7.40 and pH 8.00) and Tris·HCl buffer (pH 9.00) were used as supporting electrolytes. The pH of these buffers was measured and the KH_2PO_4 buffer (pH 8.00) was adjusted with 0.1 M NaOH. The other buffers were used as prepared. All buffers were stored at 4 °C.

Table 2.2. Preparation of standard buffer solutions.

Buffer[a]	**Solution Concentration (M)**	**pH**	**Buffer substances**	**Mass of buffer substances (g)**	**Drying requirements**[b]
Phosphate[c]	0.025	6.86	KH_2PO_4	3.388	Oven-dried at 45 °C
			Na_2HPO_4	3.533	Oven-dried at 45 °C
Phosphate	0.040	7.40	KH_2PO_4	1.179	Oven-dried at 45 °C
			Na_2HPO_4	4.302	Oven-dried at 45 °C
Phosphate[d]	0.050	8.00	KH_2PO_4	6.805	Used as received
			NaOH	2.000	Used as received
Tris·HCl[e]	0.050	9.00	Tris	6.050	Used as received
			HCl	[f]	Used as received
Carbonate[c]	0.025	10.01	$NaHCO_3$	2.092	Oven-dried at 200 °C
			Na_2CO_3	2.640	Used as received

[a] Prepared by dissolving buffer salts in 1000 mL of Milli-Q water unless otherwise stated.

[b] Oven-dried salts were dried overnight prior to use.

[c] Prepared according to the methods of Taylor.[1]

[d] Prepared according to the method of Perrin and Dempsey.[2] In brief, buffer salts were dissolved individually into 500 mL of Milli-Q water. Then 461 mL of NaOH was added to 500 mL of KH_2PO_4 and made up to 1000 mL with Milli-Q water.

[e] Prepared according to the method of Perrin and Dempsey.[2] In brief, tris salt was dissolved in 500 ml of Milli-Q water to which 0.5 mL of concentrated HCl was added. Milli-Q water was added to give a final volume of 1000 mL.

[f] Final concentration of HCl was 6 mM.

2.4 Electrochemistry

Unless otherwise stated, all electrochemical measurements were performed at room temperature under a nitrogen atmosphere.

2.4.1 Instrumentation

Electrochemical measurements were performed using a computer-interfaced PAR Model 273A Potentiostat/Galvanostat with EG & G PAR Model 270/250 Research Electrochemistry Software (version 4.00). Alternatively, computer-controlled EG & G PAR Model 173 or Model 362 Potentiostats coupled to a Powerlab 4SP (ADInstruments) were employed. A variety of ADInstruments software was used in conjunction with the Powerlab 4SP and included Echem (version 1.5.2), Scope (version 3.6.13) and Chart (version 4.2.2). An EG & G PAR Model 616 rotating disc electrode (RDE) was utilised for steady-state voltammetry.

2.4.2 Carbon Electrodes

A wide variety of metal and carbon electrodes were used in this research. The majority of the work involved the use of carbon substrates for electrochemically grafting amines and fabricating metal nanoparticle electrodes. The different forms of carbon used for these purposes are described below. Experimental details regarding the construction of solid metal electrodes and the preparation of metal nanoparticle electrodes are described in the relevant chapters.

2.4.2.1 Glassy carbon Electrodes

Conventional-size glassy carbon electrodes were constructed by sealing glassy carbon rod (0.3 cm diameter, Tokai) in Teflon to give circular disk electrodes with a geometric area of 0.07 cm^2. Contact to the glassy carbon was made *via* a brass rod. Glassy carbon plates (15 mm × 15 mm) were also utilised. Prior to use, newly prepared glassy carbon electrodes were polished to a mirror finish using graded sanding papers followed by 3.0 μm diamond paste and then alumina slurries (1.0 and 0.05 μm) on polishing microcloth (LECO Lecloth). Between experiments, the

electrodes were polished with alumina slurries (1.0 and 0.05 μm) and rinsed with Milli-Q water. The glassy carbon plate electrodes were sonicated in Milli-Q water for 10 minutes to remove excess alumina.

2.4.2.2 Pyrolysed Photoresist Films (PPF)

Established methods were followed for preparing pyrolysed photoresist film (PPF);[3-5] however, the spin-coating step was altered due to the viscosity of the photoresist.[6] A silicon wafer (Si(100), N-type, Silicon Quest International) with a protective surface film (S1813 photoresist, Clariant) was precut into sections (13 mm × 13 mm) using a diamond scribe. The silicon samples were subsequently soniciated in successive baths of acetone, methanol and isopropyl alcohol to remove the protective film, and dried with nitrogen. A large drop of negative photoresist (AZ4620, Clariant) was spin-coated onto the wafers with a fast acceleration rate for 30 seconds at 3000 rpm to achieve a final thickness of ~ 6.5 μm. The spin-coating step was carried out in the dark using an EMS Ltd photoresist spinner. The photoresist-covered wafers were soft-baked at 95 °C for 20 minutes and left in an oven at 45 °C overnight before pyrolysis. Pyrolysis of the photoresist-coated wafers was performed in a furnace (Radatherm, Model 2216e) at 1060 °C for one hour to form a thin glassy carbon-like film on the silicon substrate. The photoresist-coated wafers were mounted on a silicon glass tube inside the furnace and the temperature was stepped in three stages to the maximum temperature required for pyrolysis: (1) room temperature to 550 °C over 20 minutes, (2) 550 °C to 750 °C over 30 minutes and (3) 750 °C to 1060 °C over one hour. The furnace was then allowed to cool to room temperature. A forming gas atmosphere (95% nitrogen and 5% hydrogen) was maintained inside the furnace during the heating and cooling phases of pyrolysis to avoid oxidation of the PPF (flow rate was 3.5 L min^{-1} during heating stages and then decreased to 0.3 L min^{-1} during cooling). After cooling to room temperature, the samples were removed from the furnace and briefly sonicated (10 seconds) in successive baths of acetone, methanol and isopropyl alcohol, dried with nitrogen and stored under vacuum. The average film thickness after pyrolysis was 1.5 μm as determined by scratching the photoresist film and profiling the scratch with a Sloan Dektak II profilometer. Sheet resistances were determined using gold conductive wires set in a square arrangement coupled with a spring tension device to provide reproducible downward pressure of the gold wires onto the PPF surfaces. PPF samples with sheet resistances of less than 30 Ω $\square^{-1}$ were used for electrochemistry. The typical root-mean-square

(RMS) surface roughness determined from AFM imaging of the surfaces was between 0.20 and 0.50 nm.

2.4.2.3 Carbon Fabric Electrodes

Woven carbon fabric is a low cost conducting carbon material available in large pieces and was used to support immobilised gold deposits for the bulk electrolysis of cystine (see Chapters 4 and 5). The carbon fabric used in this work was sourced from a local boat builder. It was woven from carbon fibers with a diameter of 6 μm and had a weight of 148 g m^{-2}. For developmental work (see Chapter 4, Section 4.3.2), carbon fabric disk electrodes were prepared from this material by sealing the edge of a circular area (1.67 cm diameter) with silicone sealant on both sides of the fabric. Once the silicone had cured, the electrode was cut from the bulk material leaving a small bundle of carbon fibers to form the electrical connection (Figure 2.1 (a)). The silicone sealant stopped the edges of the carbon fabric from fraying and prevented the movement of electrolyte solution, *via* capillary action, through the carbon fibers forming the electrode connection. For use in the electrochemical cell (see Section 2.4.3.4, Design 1), the electrode was mounted between two Teflon plates held together using nylon screws (Figure 2.1 (b)). The aperture (1.10 cm diameter) present in the Teflon holder exposed both sides of the carbon fabric electrode to the electrolyte solution leading to a geometric surface area of 0.95 cm^2 per side. A Viton O-ring (1.79 cm internal diameter) was also placed in between the Teflon plates to prevent leakage. For experiments involving the bulk electrolysis of cystine to generate the thiol reducing agent for wool setting (see Chapter 5, Section 5.3.3) a larger working electrode area was required. Cylindrical carbon fabric electrodes were prepared by firstly sealing the edge of a rectangle (4 cm × 11 cm or 9 cm × 11 cm) with silicone sealant on both sides of the bulk material. Once the silicone had cured, the electrode was cut from the bulk material, leaving a small bundle of carbon fibers to form the electrical connection, and the rectangle was rolled to form a cylinder which would fit into the inner compartment of the bulk electrolysis cell (see Section 2.4.3.4, Design 2 and 3). Silicone sealant was used to seal the two edges of the rectangle together and hold the electrode in the cyclindrical shape (Figure 2.1 (c) and (d)). The geometric area of the cylindrical carbon fabric electrodes was 44 cm^2 per side and 99 cm^2 per side (based on the size of the rectangle cut from the bulk material). All carbon fabric electrodes were sonicated in successive baths of acetone, methanol and isopropyl alcohol and dried with nitrogen prior to use.

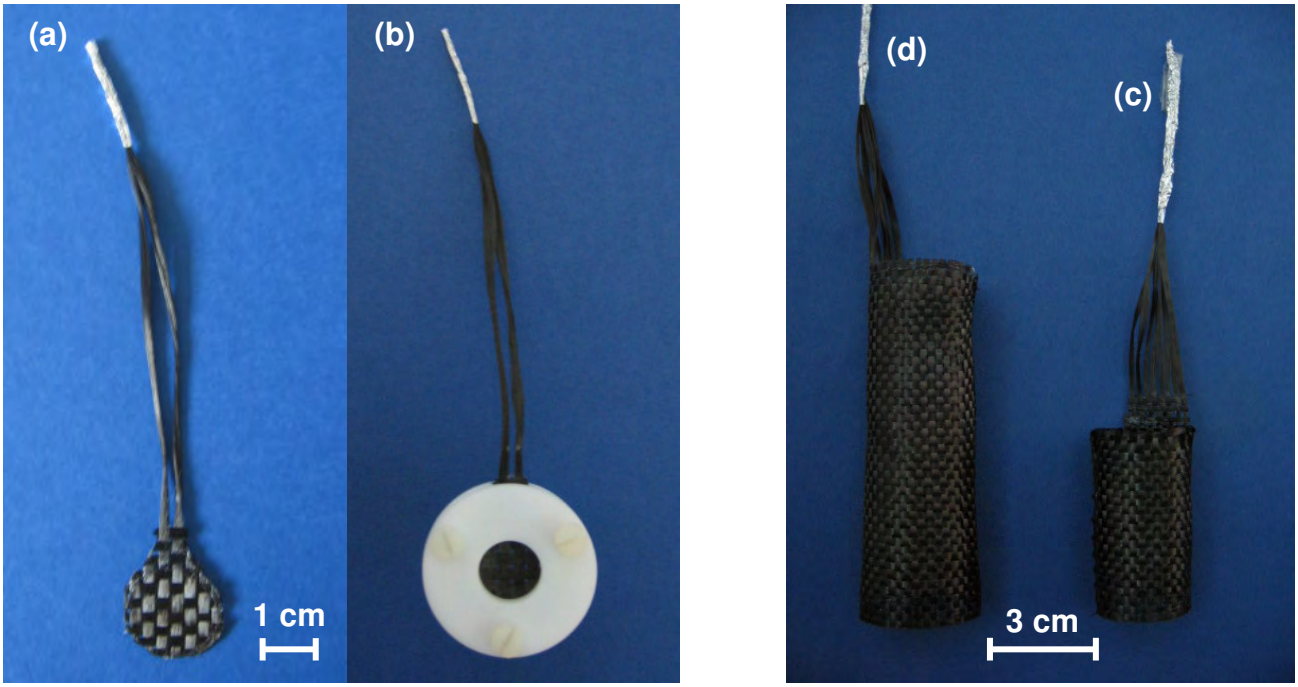

Figure 2.1. Carbon fabric electrodes used for bulk electrolysis: (a) carbon fabric disk electrode, (b) carbon fabric disk electrode mounted in Teflon holder and (c, d) cylindrical carbon fabric electrodes.

2.4.3 Electrochemical Cells

All electrochemical cells were made of glass and consisted of a three-electrode configuration. Unless otherwise stated, a platinum wire was used as the auxiliary electrode and the reference electrode was a saturated calomel electrode (SCE, saturated KCl) for aqueous solutions and Ag/Ag^+ (10^{-2} M $AgNO_3$ in 0.1 M $[Bu_4N]BF_4$-acetronitrile) for non-aqueous solutions. For the latter reference electrode, the silver wire was placed in a glass tube with a Vycor (porous glass) tip containing the $AgNO_3$ solution. This tube was separated from the solution in the electrochemical cell by placing it in a second glass compartment with a Vycor tip containing only electrolyte solution. The ferrocene/ferrocenium (Fc/Fc^+) couple appeared at $E_{1/2}$ = 0.034 V *vs*. Ag/Ag^+. All electrochemical cells were soaked in 10 % HNO_3 followed by rinsing in Milli-Q water and dried at 45 °C before use.

2.4.3.1 Circular Disk Electrodes

Experiments performed using glassy carbon disk electrodes (see Section 2.4.2.1) or metal electrodes insulated in glass or Teflon (see Chapter 3, Section 3.2.2) were carried out in a tapered cell (Figure 2.2). This allowed small sample volumes to be used. Metal electrodes assembled using a short metal plug, *e.g.*, copper and lead (see Chapter 3, Section 3.2.2) and gold and palladium (see Chapter 7, Section 7.2.2) were suspended in the electrochemical cell by the hanging meniscus method (Figure 2.3). This allowed the front of the electrode to contact the solution without requiring the sides to be insulated.

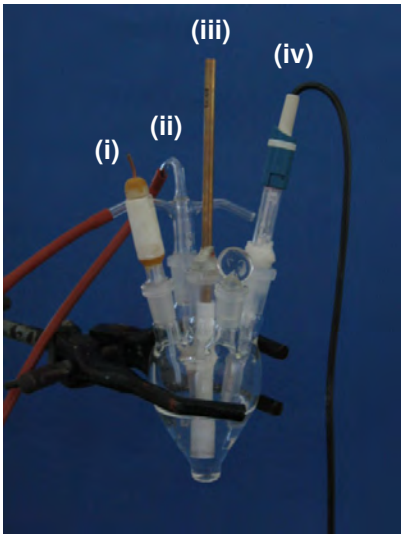

Figure 2.2. Electrochemical cell set-up used for disk electrodes: (i) auxiliary electrode (platinum wire), (ii) nitrogen bubbler, (iii) working electrode (glassy carbon disk electrode) and (iv) reference electrode (SCE).

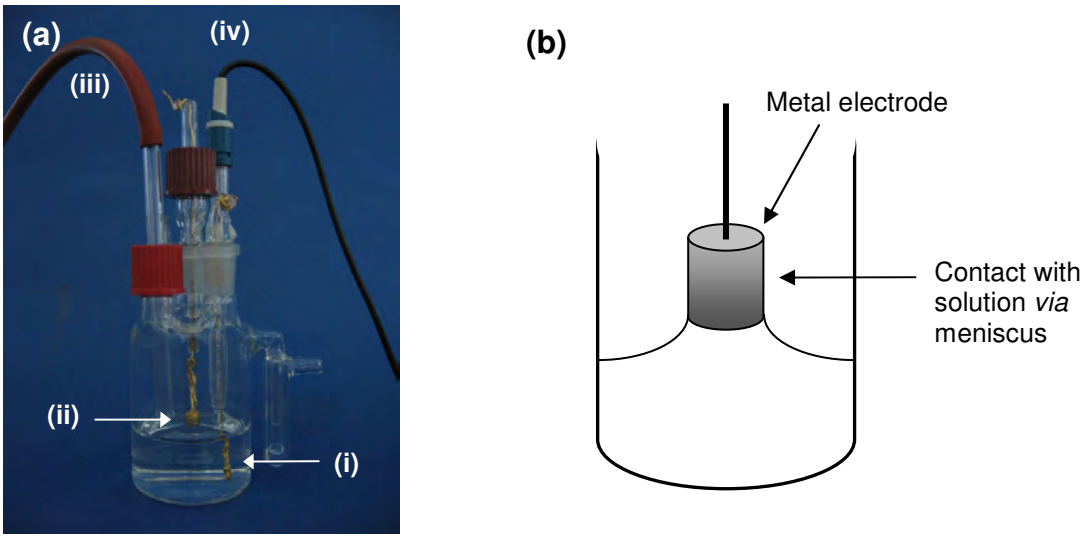

Figure 2.3. (a) Electrochemical cell set-up used for metal electrodes assembled using a short plug of metal: (i) auxiliary electrode (gold wire), (ii) working electrode (gold), (iii) nitrogen bubbler and (iv) reference electrode (SCE); (b) illustration of the hanging meniscus method used to suspend the working electrodes in the electrochemical cell.

2.4.3.2 PPF and Glassy Carbon Plates

Samples of PPF and glassy carbon plates were mounted horizontally on an insulated metal base plate under a glass cell held down by four springs (Figure 2.4). A Viton O-ring (size 008, internal diameter = 5.4 mm) between the sample and the glass cell sealed the solution above the surface. A larger Viton O-ring (size 012, internal diameter = 9.5 mm) was placed around the outside of the inner O-ring to stabilise the glass cell. Electrical contact was made to the working electrode using a copper strip externally connected to the sample.

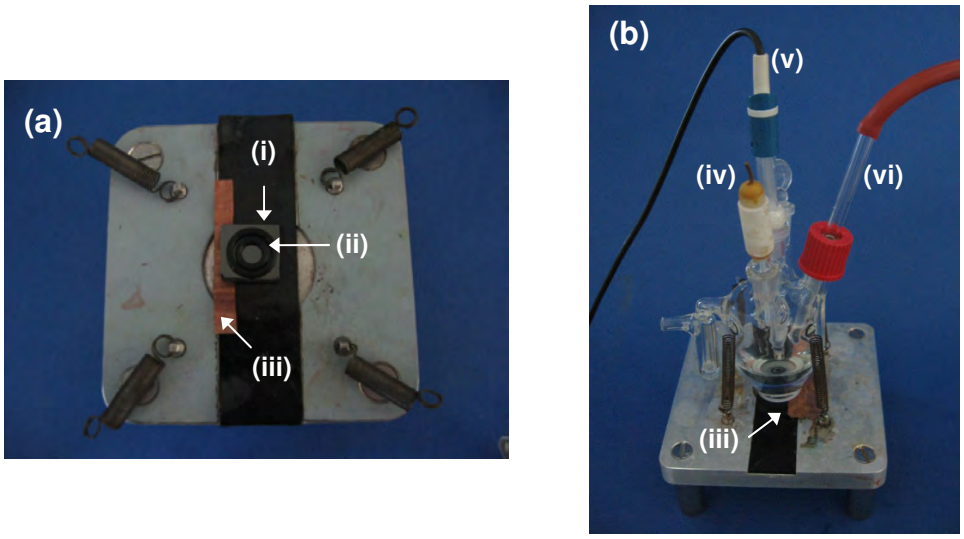

Figure 2.4. Electrochemical cell used for PPF and glassy carbon plate samples consisting of an insulated metal base plate (a) under a glass cell held down by four springs (b): (i) working electrode (glassy carbon plate), (ii) Viton O-rings to define electrode area and seal solution above electrode, (iii) copper electrical contact to the working electrode, (iv) auxiliary electrode (platinum wire), (v) reference electrode (SCE) and (vi) nitrogen bubbler.

The geometric area of the working electrode exposed to the solution in the cell set-up was defined by the inner O-ring. The cross-sectional view of the O-ring (Figure 2.5) depicts the O-ring contacting the surface at a point only. However, under the pressure of the glass cell and springs contact will be made over a greater area. Investigations carried out by Brooksby showed that the O-ring was not significantly deformed in the cell set-up[7] and hence, the active electrode area was assumed to be 0.31 cm^2 as calculated using equation 2.1 and the values: a = 1.8 mm and b = 5.4 mm (from Figure 2.5). The assumed diameter of the active electrode area is shown by 'd' in Figure 2.5. It is noted that the active surface area could be significantly different to that estimated, however, for the majority of the work reported in this thesis the absolute electrode area was not important. Instead, comparisons of the data obtained using this cell set-up were of more interest.

$$A = \pi\left(\frac{a}{4}+\frac{b}{2}\right)^2 \qquad (2.1)$$

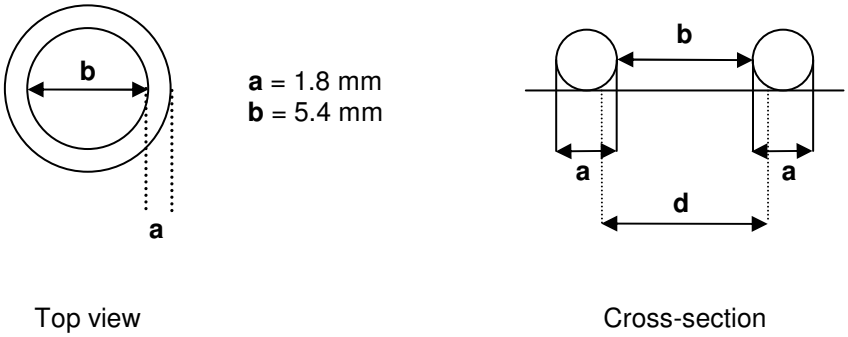

Figure 2.5. Illustration of a Viton O-ring (size 008) where **a** represents the diameter of the radial cross-section, **b** represents the internal diameter and **d** is the diameter used to estimate the active surface area of the working electrode.

2.4.3.3 Hydrodynamic Voltammetry

Hydrodynamic voltammetry was performed at stationary working electrodes consisting of a planar sheet of solid palladium or palladium nanoparticles immobilised on PPF substrates (see Chapter 7, Sections 7.2.2 and 7.2.4). The design of the electrochemical cell used for hydrodynamic voltammetry was based on that described in Section 2.4.3.2. The glass cell was manufactured to incorporate a rotating disc electrode (RDE) used to stir the solution above the working electrode mounted horizontally between the metal base plate and the glass cell (Figure 2.6).

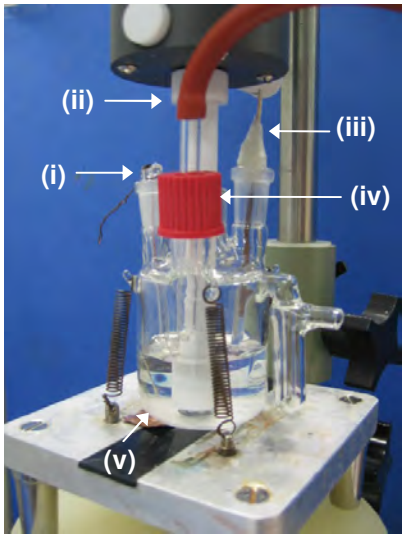

Figure 2.6. Electrochemical cell set-up used for steady-state voltammetry: (i) auxiliary electrode (platinum wire), (ii) glassy carbon RDE, (iii) reference electrode (Ag/AgCl), (iv) nitrogen bubbler and (v) copper electrical contact to working electrode.

2.4.3.4 Bulk Electrolysis

The bulk electrolysis of cystine at gold deposits immobilised on carbon fabric supports (referred to as nanoAu/CF, see Chapters 4 and 5) was carried out using the electrochemical cells shown in Figure 2.7. Three designs were used (Design 1, 2 and 3) which were all comprised of two glass compartments separated by a sintered glass frit (porosity 5). In addition, Design 3 was fitted with a water jacket around the outer compartment. Interchangeable Teflon lids were manufactured for Design 2 and 3 to allow wool to be mounted in the cell during wool setting experiments using the various methods described in Chapter 5 (Section 5.2.4). Cell Design 1 was used with carbon fabric disk electrodes. Cell Design 2 and 3 were used with cylindrical carbon fabric electrodes with a geometric area of 44 cm^2 and 99 cm^2 per side respectively (see Section 2.4.2.3). The cell set-up was the same for each of the cell designs. The carbon fabric support was suspended vertically in the inner compartment along with a saturated calomel electrode (SCE) as the reference. The auxiliary electrode was constructed from high surface area platinum gauze and was positioned in the outer compartment symmetrically around the carbon fabric electrode in the inner compartment of the cell to produce a uniform potential and current density across the carbon fabric electrode. During electrolysis, the solution was stirred and bubbled with nitrogen to achieve effective mass transfer.

2.5 Spectroscopic Techniques

Electron Impact (EI) Mass Spectra were recorded using a Kratos MS80RFA Mass Spectrometer operating at an accelerating potential of 4 kV and an ionisation energy of 70 eV. ^1H NMR spectra were obtained using a Varian Inova Spectrometer, operating at 500 MHz. All NMR spectra were recorded in D_2O solvent and a residual solvent signal was used as an internal standard. X-ray photoelectron spectroscopy (XPS) data were recorded using a Kratos Axis Ultra DLD spectrometer. The x-ray source was a monochromatic Al Kα source (1486.6 eV), operated at 150 W power. Operating conditions for recording XPS data are given in Chapter 6 (Section 6.2.2.3). UV-Vis spectroscopy was performed on a computer-interfaced Hewlett Packard Diode Array Spectrophotometer (Model HP 8452A). Quartz curvettes were used giving a path length of 1 cm.

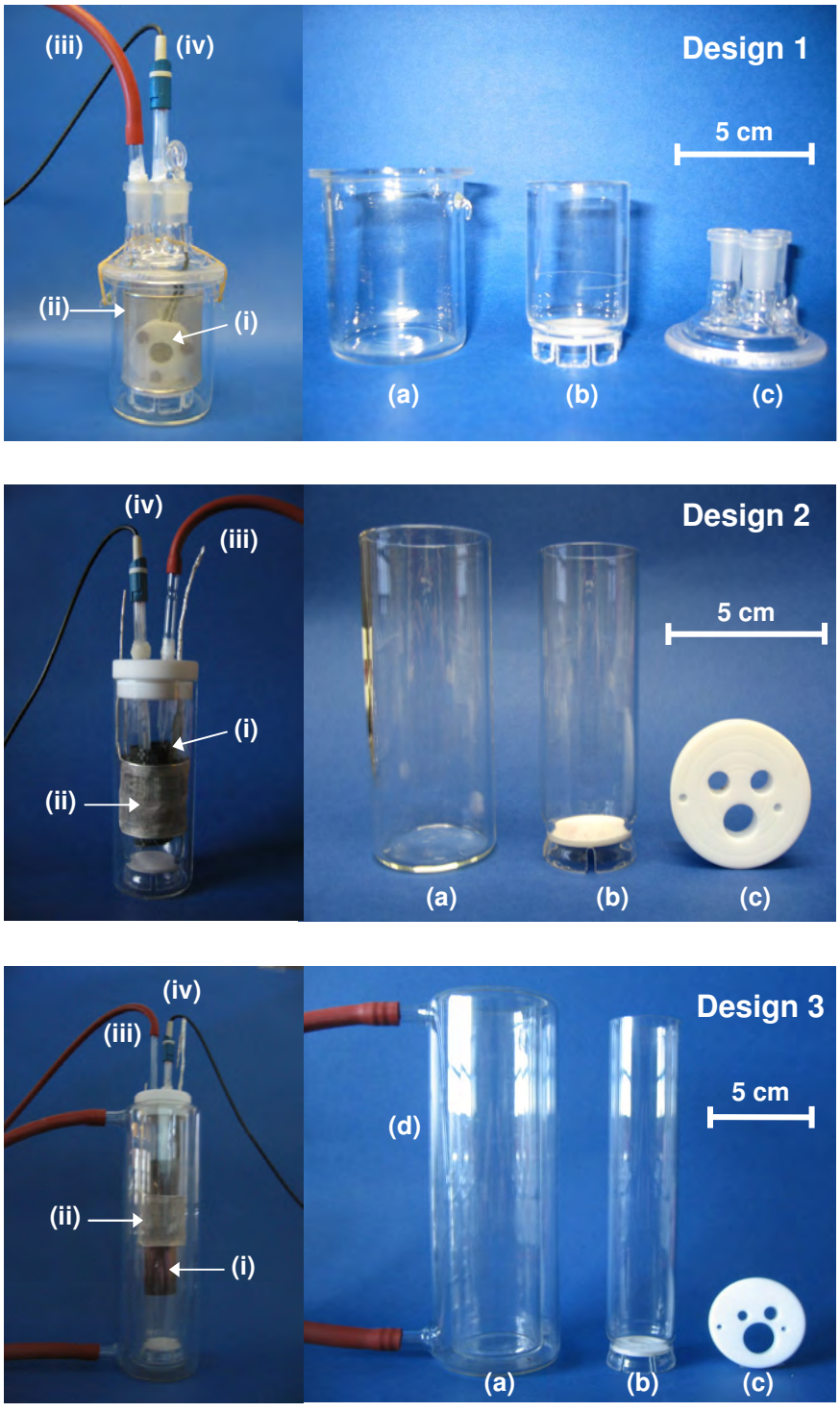

Figure 2.7. Bulk electrolysis cells Designs 1 to 3. (Left) Cell setup: (i) nanoAu/CF electrode, (ii) platinum gauze auxiliary electrode, (iii) nitrogen bubbler and (iv) reference electrode (SCE). (Right) Components of the bulk electrolysis cell: (a) outer and (b) inner compartment of bulk electrolysis cells, (c) glass or Teflon lid, (d) water jacket fitted to outer compartment for Design 3.

2.6 Microscopy

The atomic force microscope (AFM) consisted of a Nanoscope® Dimension™ 3100 controller coupled with a Nanoscope® IIIa scanning probe microscope controller from Digital Instruments. All measurements were carried out in non-contact tapping mode under ambient air conditions. Operating conditions for recording AFM topographical measurements are given in Chapter 6 (Section 6.2.2.2). Scanning electron microscopy (SEM) was performed using a Raith 150 e-beam lithography system operated at an accelerating voltage of 10 keV. Transmission electron microscopy (TEM) images were obtained using a Hitachi H600 transmission electron microscope operating at 75 keV. Sample preparation of TEM is described in Chapter 7 (Section 7.2.3.1).

2.7 Surface concentration of Species Immobilised at the Electrode Surface

The surface concentration of electroactive species immobilised at the electrode surface was determined according to equation 2.2,

$$\Gamma = \frac{Q}{nFA} \qquad (2.2)$$

where Γ represents surface concentration; Q is charge; n is the number of electrons; F is the Faraday constant and A is the geometric area of the working electrode.

Voltammetric peak analysis was performed by curve-fitting the data.[8] Mixed Lorentizian-Gaussian curves were fitted to the voltammetric peaks. Polynomial baselines can be fit during the least squares iteration or they can be solved for and subtracted from the voltammogram prior to the curvefit. A measure of the goodness of fit was made by minimising the standard deviation of least squares (χ). Values of $\chi > 10^{-6}$ were considered to be a good fit.

2.8 References for Chapter 2

1. Taylor, M. C. *Podzols: Aspects of their chemistry and development*. Ph.D. Thesis, University of Canterbury, Christchurch, New Zealand, 1980.

2. Perrin, D. D.; Dempsey, B., *Buffers for pH and metal ion control;* Chapman and Hall Ltd: London, UK, 1974; p 139, 143.

3. Kim, J.; Song, X.; Kinoshita, K.; Madou, M.; White, R. Electrochemical studies of carbon films from pyrolysed photoresist. *Journal of the Electrochemical Society* **1998**, *145*, 2314-2319.

4. Ranganathan, S.; McCreery, R. L. Electroanalytical performance of carbon films with near-atomic flatness. *Analytical Chemistry* **2001**, *73*, 893-900.

5. Ranganathan, S.; McCreery, R.; Majji, S. M.; Madou, M. Photoresist-derived carbon for microelectromechanical systems and electrochemical applications. *Journal of the Electrochemical Society* **2000**, *147*, 277-282.

6. Brooksby, P. A.; Downard, A. J. Electrochemical and atomic force microscopy study of carbon surface modification via diazonium reduction in aqueous and acetonitrile solutions. *Langmuir* **2004**, *20*, 5038-5045.

7. Brooksby, P. A., University of Canterbury, Christchurch, New Zealand, Personal Communication, 2007.

8. Loring, J. S. *Spectroscopic studies of ion solvation and ligand-metal coordination: Towards surface spectroscopy*. Ph.D. Thesis, University of California, Davis, USA, 2000.

Chapter 3

Electroreduction of Disulfides at Metal and Carbon Electrodes

3.1 Introduction

The focus of this research is to find efficient electrochemical methods for reducing the disulfide bonds of compounds such as cystine and 2-hydroxyethyl disulfide (2-HED) to yield the corresponding thiols which will subsequently act as reducing agents for the cleavage of wool disulfide bonds in the process of wool setting (see Chapter 5). This chapter describes the electrochemical reduction of cystine and 2-HED at metal and carbon electrodes.

3.1.1 The Electroreduction of Cystine at Metal Electrodes

Cystine and the corresponding thiol, cysteine, are very important biological amino acids and are widely used in the foodstuffs, cosmetics and pharmaceutical industries.[1] The electroreduction of cystine has been reported extensively in the literature and is currently the major industrial route to the thiol (Scheme 3.1).[2]

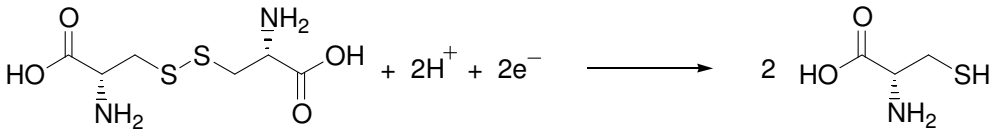

cystine cysteine

Scheme 3.1. Reduction of cystine to cysteine.

3.1.1.1 Mercury Electrodes

The electrochemistry of cystine and cysteine at mercury electrodes has been studied over a wide pH range (pH 1.0-13.0) by many authors.[3-8] Cystine has been shown to undergo a variety of interactions with mercury to form surface-bound complexes: mercury cystinates are produced when cystine is adsorbed onto the mercury surface *via* the carboxylate and amino groups of cystine; mercury cysteine thiolates are formed through surface bonding between cystine and mercury *via* the sulfur atoms of cysteine after cleavage of the S–S bond. A comprehensive study of the reactions of cystine at mercury electrodes has been published by Heyrovsḱy *et al.*[6] This study describes the mechanism for cystine reduction at mercury *via* two pathways that are (1) adsorption-controlled and (2) diffusion-controlled. The findings from this study are summarised in the following paragraphs.

At potentials positive of the point of zero charge (pzc) (~ -0.40 V (*vs*. SCE) at pH 9.9) the mercury surface has a net positive charge. Cystine from the bulk solution adsorbs onto the mercury surface to form mercury (I) cysteine thiolate (equation 3.1) at potentials just positive of the pzc. The reduction of this species to yield the corresponding thiol in solution is shown in equation 3.2,

$$(RSSR)_{ads} + [HgHg]_s \rightleftharpoons [RS\text{-}HgHg\text{-}SR]_s \qquad (3.1)$$

$$[RS\text{-}HgHg\text{-}SR]_s + 2e^- \longrightarrow 2RS^- + [HgHg]_s \qquad (3.2)$$

where RSSR represents cystine and RS^- represents the cysteine thiolate anion. The subscript ‘ads’ denotes the adsorbed state and the subscript ‘s’ and square brackets symbolise the groups of atoms forming part of the surface. In media with pH less than 9.0, the cysteine thiolate anion undergoes protonation (equation 3.3) and hence, cystine reduction is pH dependent.

$$RS^- + H^+ \rightleftharpoons RSH \qquad (3.3)$$

As the potential shifts more positive mercury reacts spontaneously with cystine to form a layer of surface-bound mercury (II) cysteine thiolate (equation 3.4). If the surface coverage of this species is not complete, unoccupied surface mercury atoms move closer together as the potential is

shifted less negative and mercury (II) cysteine thiolate undergoes a rapid spontaneous transformation to form mercury (I) cysteine thiolate (equation 3.5). However, if there is full surface coverage of mercury (II) cysteine thiolate, reaction 3.5 cannot occur and mercury (II) cysteine thiolate is reduced to give the thiol (equation 3.6).

$$(RSSR)_{ads} + [Hg]_s \longrightarrow [RS\text{-}Hg\text{-}SR]_s \quad (3.4)$$

$$[RS\text{-}Hg\text{-}SR]_s + [Hg]_s \rightleftharpoons [RS\text{-}HgHg\text{-}SR]_s \quad (3.5)$$

$$[RS\text{-}Hg\text{-}SR]_s + 2e^- \longrightarrow 2RS^- + [Hg]_s \quad (3.6)$$

At still more positive potentials, mercury is oxidised to form mercury (II) ions in solution which can interact with cystine *via* the carboxylate and amino groups. In solutions of pH 2.0-8.0 the carboxylic acid of cystine is in the dissociated state and the amino group is protonated, therefore, cystine is stable in the form of a double zwitterion ($^+R^-SS^-R^+$) and can form complexes with mercury (II) ions (equation 3.7 and 3.8). This complex also adsorbs strongly to the surface and over time, rearranges to give mercury (II) cysteine thiolate which is subsequently reduced by reaction 3.6.

$$Hg \rightleftharpoons Hg^{2+} + 2e^- \quad (3.7)$$

$$Hg^{2+} + {}^+R^-SS^-R^+ \rightleftharpoons Hg(RSSR)_{ads} + 2H^+ \quad (3.8)$$

At potentials more negative than that corresponding to the reduction of surface-bound mercury (I) cysteine thiolate the reduction of cystine is diffusion-controlled. Solution-based cystine undergoes direct reduction where electrons are transferred to the disulfide bond without any specific interaction with the mercury surface (equation 3.9):

$$(RSSR)_{soln} + 2e^- \longrightarrow 2RS^- \quad (3.9)$$

where the subscript ‘soln’ denotes solution-based cystine.

The oxidation of cysteine at mercury leads to the formation of mercury (II) cysteine thiolate. Reaction 3.2 has been expressed as an irreversible process because the cysteine anion (RS^-) does not react directly with metallic mercury to form surface-bound mercury (I) cysteine thiolate. Instead, the cysteine anions react with mercury (II) ions to form solution-based mercury (I) cysteine thiolate which is subsequently adsorbed onto the electrode surface (equation 3.10). This process is controlled by diffusion of the cysteine anions to the mercury electrode. At positive potentials, mercury (I) cysteine thiolate undergoes surface disproportionation to give mercury (II) cysteine thiolate and mercury (equation 3.11). There is no current produced as a result of reaction 3.11.

$$2RS^- + 2Hg \rightleftharpoons (Hg_2(SR)_2)_{ads} + 2e^- \quad (3.10)$$

$$(Hg_2(SR)_2)_{ads} \rightleftharpoons (Hg(SR)_2)_{ads} + Hg \quad (3.11)$$

The reduction of cystine at a mercury electrode occurs efficiently as the reaction takes place at low potentials and the rate of reaction is fast. However, mercury is very toxic and therefore, it has become desirable to find an alternative electrode material.

3.1.1.2 Alternative Metal Electrodes

Industrial production of cysteine is based on the electrochemical reduction of cystine in acidic electrolytes using lead or silver cathodes.[9,10] The mechanism for the electroreduction of cystine at these electrodes has been reported to be similar to that observed at mercury. Evidence of adsorption of cystine at silver electrodes was demonstrated by Watanabe *et al.* using surface-enhanced Raman spectroscopy (SERS) to monitor the change in intensity of the S–S stretching peak at 502 cm^{-1} during a potential sweep experiment.[11] During electroreduction, the disulfide is converted to two thiol fragments which, due to strong Ag–S bonding, are adsorbed at neighbouring silver sites. The mechanism for cystine reduction at a lead RDE electrode was observed to be similar to the direct reduction of cystine at a mercury electrode. Kinetic studies performed by Ralph *et al.*[12] were carried out in the presence of hydrochloric acid, and hence to avoid the formation of lead chloride and measure the disulfide reduction currents only, the RDE was maintained at potentials more negative than -0.70 V (*vs.* SCE). Under these conditions, the reduction was found to be

electrochemically irreversible and diffusion-controlled. Although there was no direct voltammetric evidence of adsorption of cystine onto lead, indirect support was obtained from the slope of the corresponding Tafel plot which was comparable with that obtained at mercury.[8] Direct evidence for the adsorption of cystine onto mercury has been reported as described in Section 3.1.1.1.

The disadvantage of using a lead cathode for the electroreduction of cystine is that the cysteine product can be contaminated with lead during the reduction process. When silver is used as the cathode material, the product is free from contamination with heavy metals, however, the current efficiency of the process is only 40-50 % which consequently results in higher energy consumption.[10] Alternative cathode materials that have been investigated include lead-silver alloy and lead-tin alloy, copper, zinc deposited on copper and tin deposited on copper, and graphite.[10] The reduction of cystine in hydrochloric acid was studied at these electrodes using a two compartment cell separated by a Nafion membrane. The anode consisted of a noble metal oxide coated titanium electrode. Electrolysis was carried out at elevated temperatures (36-45 °C) and a potential difference of between 3.8-4.3 V was applied between the anode and cathode. The major results from this study are summarised in Table 3.1.

Table 3.1. Effect of cathode materials on the electrochemical reduction of cystine to cysteine. Table adapted from reference 10.

Cathode	**Lead**	**Sn/Cu**	**Zn/Cu**	**Copper**	**Pb-Sn alloy**	**Pb-Ag alloy**	**Graphite**
Maximum current density of cell (A/dm^2)	30	12	12	12	36	16	13
Total current passed (A)	6.87	9.25	8.25	9.00	9.83	8.75	8.00
Excess current passed (%)	2.00	38.00	23.00	34.00	46.00	30.00	19.00
Cysteine formed (g)[a]	33.70	46.36	38.63	39.34	34.77	41.09	40.57
Metal ion content (ppm)	120.00	21.00	15.00	16.00	8.00	10.00	[b]

[a] 30 g of L-cystine was used.

[b] Not applicable.

High current efficiencies were achieved at a lead electrode, however, the metal ion content of the cysteine product was much higher compared to that observed at the alternative cathode materials. In comparison, the product yield for the electrode consisting of a thin film of tin deposited onto a copper electrode was very high and the metallic impurity was much lower. The zinc deposited copper electrode gave similar results to a bare copper electrode. The metallic impurity was less compared to the tin deposited copper electrode but the product yield was lower. Alloy electrodes and graphite gave the best results in terms of current efficiency, yield efficiency and quality of product due to low metal ion pick up during electrolysis. A restriction of using graphite or lead-silver alloy is that the cell can only be operated at low current densities whereas lead-tin alloy can be operated at much higher current densities.

Studies of the electroreduction of cystine have also been reported at platinum[13] and gold[14] electrodes under acidic conditions. Strong adsorption of cystine to gold and platinum electrodes was confirmed in these studies as a result of radiometric analysis using ^{35}S-cystine. At the platinum electrode the rate of adsorption of cystine is slow and the disulfide bond is not reduced electrochemically. However, the chemisorbed species is oxidised to cysteic acid, the corresponding sulfonic acid of cysteine (see Scheme 4.2, Chapter 4). At the gold electrode, less cystine is adsorbed but the rate of adsorption is faster in comparison to that at the platinum electrode.[13] As for platinum, the major product formed by reaction of cystine at the gold electrode is the oxidation of the disulfide to cysteic acid but the reduction of cystine to cysteine is also observed.[14]

3.1.2 The Electroreduction of Disulfides in the Presence of a Mediator

An alternative to the direct reduction of disulfides at the electrode surface is to use a mediator which shuttles electrons between the electrode and the disulfide. There have been two approaches for mediating the electroreduction of disulfide bonds: (1) immobilisation of the mediator onto a solid support and (2) use of water soluble mediators.

3.1.2.1 Transition Metal Phthalocyanine Complexes

Transition metal phthalocyanine complexes (MPc) (Figure 3.1) adsorbed onto graphite electrodes exhibit catalytic activity towards the electroreduction of cystine and 2-HED whilst unmodified graphite electrodes show very little activity for disulfide reduction over the same potential range.[15-17]

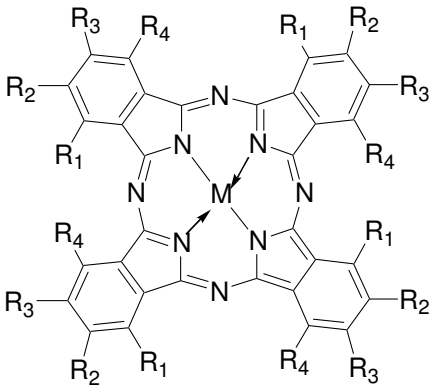

M: Co, Fe, Mn, Cu or Ni

$F_{16}Pc$: $R_1 = R_2 = R_3 = R_4 = F$

TsPc: $R_1 = R_2 = R_4 = H$, $R_3 = SO_3$

Pc: $R_1 = R_2 = R_3 = R_4 = H$

TAPc: $R_1 = R_2 = R_4 = H$, $R_3 = NH_2$

TNPPc: $R_1 = R_2 = R_4 = H$, $R_3 = O(CH_2)_2CH(CH_2)_2$

MeOPc: $R_1 = R_4 = H$, $R_2 = R_3 = OCH_3$

OEHPc: $R_1 = R_4 = H$, $R_2 = R_3 = OCH_2CH(CH_2CH_3)(CH_2)_3CH_3$

Figure 3.1. General structure of transition metal phthalocyanines. Figure taken from reference 17.

The effects of the central metal ion and substituents attached to the phthalocyanine ring on the reduction of disulfides have been investigated. Zagal and co-workers[15] investigated cystine reduction at various transition metal tetrasulfophthalocyanines (MnTSPc, FeTSPc, CoTSPc, CuTSPc and NiTSPc) adsorbed on ordinary pyrolytic graphite (OPG). The catalytic activity was shown to be dependent on the nature of the central metal ion. MnTSPc, FeTSPc and CoTSPc were

observed to catalyse the electroreduction of cystine whilst NiTSPc and CuTSPc were poor catalysts. A correlation between the electrocatalytic activity and the ability of the metal to bind axial ligands was expected, however, in the absence of a reliable measure of this ability, the authors used the number of *d* electrons on the metal to correlate the electrocatalytic activity for the reactions at each of the transition metal TSPc complexes. The activity was observed to decrease linearly with the number of *d* electrons in the metal.

The influence of substituents attached to the periphery of the phthalocyanine ligand on the reduction of 2-HED was investigated using a variety of cobalt phthalocyanine derivatives immobilised onto OPG.[17] The redox potential for the Co(II)/Co(I) couple influences the electrochemical oxidation and reduction of 2-mercaptoethanol and 2-HED respectively.[17,18] In turn, substituents attached to the phthalocyanine ligand are known to strongly influence the redox chemistry of this metal center (Table 3.2). The formal potential of the Co(II)/Co(I) redox couple is shifted to more positive values (compared to unsubstituted cobalt phthalocyanine) when electron-withdrawing groups are present on the ligand (–F and $–SO_3^-$) and to more negative values by electron-donating groups ($–NH_2$, methoxy, neopentoxy, and octaethylhexyloxy).

Table 3.2. Redox potentials of adsorbed cobalt phthalocyanine derivatives at pH 13.0.
Adapted from reference 17.

Compound	**Ligand**	**Co(II)/Co(I) redox potential (V *vs*. SCE)[a]**
$CoPcF_{16}$	hexadecafluorophthalocyanine	-0.345
CoTSPc	tetrasulfonatophthalocyanine	-0.518
CoPc	unsubstituted cobalt phthalocyanine	-0.605
CoTAPc	tetraaminophthalocyanine	-0.690
CoTNPPc	tetraneopentoxyphthalocyanine	-0.685
CoMeOPc	tetramethoxyphthalocyanine	-0.685
CoOEHPc	octaethylhexyloxyphthalocyanine	-0.725

[a] Obtained from cyclic voltammograms of phthalocyanines adsorbed on OPG in 0.2 M NaOH (pH 13.0) under nitrogen (υ = 100 mV s^{-1}). Potentials are from the average of anodic and cathodic peaks.

The effect of substituents present on the periphery of the phthalocyanine ligand on the activity for disulfide reduction could be seen when the Co(II)/Co(I) redox potential was plotted against the current density (log *i*) at a constant potential for each cobalt phthalocyanine derivative (Figure 3.2). A linear trend is observed indicating that the reaction rate increases with driving force, *i.e.*, for cobalt phthalocyanine derivatives that have a higher reductive power. These results suggest that the different adsorbed cobalt phthalocyanine derivatives behave like outer-sphere redox catalysts for the reduction of 2-HED and that the interaction of the disulfide with the cobalt center is weak. In contrast, the corresponding thiol, 2-mercaptoethanol, interacts strongly with the Co(II) center.[19,20] Oxidation of 2-mercaptoethanol in the presence of cobalt phthalocyanine complexes has been reported to occur *via* an inner-sphere mechanism where the rate of reaction decreases for cobalt phthalocyanine derivatives which have a higher oxidative power.[18]

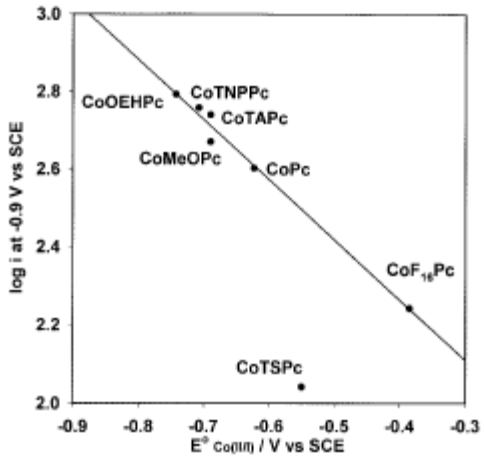

Figure 3.2. Plot of log *i* (current density) *versus* the Co(II)/Co(I) redox potential for the reduction of 2-HED in 0.2 M NaOH. Plot taken from reference 17.

Evidence of adsorption of cystine at the metal centers in transition metal phthalocyanines has been reported. In the presence of CoTSPc, FeTSPc and MnTSPc adsorbed onto ordinary pyrolytic graphite (OPG), Zagal *et al*. concluded that the electroreduction of cystine could proceed at reasonable rates only if the disulfide molecule adsorbed onto the surface.[15] Adsorption of the transition metal tetrasulfophthalocyanines was expected to be linked to the ability of the central metal ion to bind axial ligands. Studies with non-sulfur-containing amino acids revealed much less reactivity indicating that adsorption of cystine involved the metal center and the sulfur atoms of

cystine. Adsorption through a single sulfur atom was proposed.[21] The macrocyclic complexes are expected to adsorb with the ring parallel to the graphite surface, therefore, the metal centers in neighbouring tetrasulfophthalocyanines are too far apart to adsorb cystine *via* both sulfur atoms.

3.1.2.2 Polymer-Modified Electrodes

Polymer-modified electrodes have been used to immobilise metal ions and metal complex ions. Arai *et al.*[22] reported the modification of glassy carbon electrodes with conducting polymer films containing metal thiolates (platinum, palladium, copper, silver and mercury). The electrocatalytic activity of these films towards the electroreduction of cystine was compared to disulfide reduction at the corresponding bulk metals. All the metal thiolate films, except for mercury, exhibited catalytic activity towards disulfide reduction. Hydrogen evolution was observed to mask the reduction of cystine at solid platinum, palladium, silver and copper electrodes, however, this reaction was suppressed in the presence of the metal thiolate films. The reduction potential ranged from -0.90 to -1.05 V (*vs*. SCE, pH 7.0) and was observed to shift more positive from mercury < copper < silver < palladium < platinum. The current efficiency obtained at each of the electrodes was examined using constant-potential coulometry at -0.85 V (*vs*. SCE, pH 7.0). Cystine reduction proceeded with a current efficiency of 90-95 % at the copper thiolate film and 97-99 % at the other polymer modified electrodes. The current efficiencies achieved at the metal thiolate films were much higher compared to the corresponding bulk metals. In contrast, cystine reduction occurred at platinum and palladium with a current efficiency of less than 3 % and the current efficiency was only 10 % at a silver wire subjected to the same reduction conditions as the thiolate-modified electrodes.

3.1.2.3 Water Soluble Cobalt Porphyrins

An alternative approach to mediating the electroreduction of disulfide bonds is to use water soluble mediators such as cobalt porphyrins. In particular, the water soluble catalysts cobalt (II) tetrakis (4-sulfophenyl)-porphyrin (CoTSPP) and cobalt (II) tetrakis (4-trimethylammoniumphenyl)-porphyrin (CoTTAPP) show catalytic activity for the electroreduction of cystine at glassy carbon electrodes.[23] The irreversible, diffusion-controlled reduction of cystine in 0.2 M H_2SO_4 was observed at -0.74 V and -0.77 V (*vs*. SCE) for CoTSPP and CoTTAPP respectively. The catalytic

activity of the CoTSPP and CoTTAPP for cystine reduction was attributed to the central cobalt (II) ion complexing cystine. Disulfide reduction was not observed if the porphyrin ligand, H_2TTAPP, was solely present. The similar performance of CoTSPP and CoTTAPP indicated that the substituents on the porphyrin ring have no significant effect on the electrocatalytic activity of the cobalt porphyrins towards disulfide reduction.

3.1.3 Research Directions for Chapter 3

The work presented in this chapter assesses a range of electrodes for disulfide reduction. The focus of this research is to find electrode surfaces where cleavage of the S–S bond occurs at mild potentials with high current densities. This work has involved investigating the reduction of cystine and 2-HED at a variety of electrode surfaces including mercury, silver, gold, copper, nickel, lead, stainless steel, platinum and glassy carbon. Preliminary studies investigating the use of transition metal phthalocyanines immobilised onto a glassy carbon surface as a mediator for disulfide reduction have also been carried out. However, the use of molecular catalysts is unlikely to be practical for industrial processes due to progressive loss of the catalyst from the electrode, hence most of the work was carried out at solid metal electrodes. The electrochemical reduction of cystine and 2-HED was studied at pH 8.0-9.0 because the disulfide bonds in wool are reduced in this pH range during the process of chemical setting.

3.2 Experimental Methods

3.2.1 Preparation of 2-Hydroxyethyl Disulfide

2-Hydroxyethyl disulfide (2-HED) was prepared by air oxidation of 2-mercaptoethanol.[24] A solution containing 0.01 M 2-mercaptoethanol and 0.1 M ammonia (50 mL) was placed in a Dreschler bottle and connected to a vacuum pump. A second Dreschler bottle containing 0.1 M NaOH was connected in series with the 2-mercaptoethanol solution in order to facilitate fast oxidation. Air saturated with 0.1 M NaOH solution was passed through the solution of 2-mercaptoethanol for two days. The progress of the oxidation was monitored by the electrochemical response of small samples at a hanging mercury drop electrode (HMDE). Electron Impact Mass Spectroscopy was also used to analyse the product. Solutions of 2-HED were found to be stable for one week at room temperature.

3.2.2 Electrodes

A static mercury drop electrode (SMDE) (EG & G PAR Model 303A) was operated as a hanging mercury drop electrode (HMDE) with a medium drop size. Silver, gold, platinum, nickel, and stainless steel working electrodes were constructed by sealing metallic wire or rod into Teflon or glass to give circular disk electrodes. Glassy carbon disk electrodes were also prepared in this way by insulating glassy carbon rod in Teflon. Contact to the metal or glassy carbon was made *via* a brass rod or copper wire. The copper and lead working electrodes were assembled using a short plug of metal (copper: 0.38 cm diameter, 0.78 cm in length; lead: 0.39 cm diameter, 0.73 cm in length) welded to a copper wire on the back side. The copper and lead electrodes were suspended in the electrochemical cell by the hanging meniscus method (see Chapter 2, Section 2.4.3.1) allowing the front electrode surface to contact the solution without requiring the sides to be insulated. The geometric area of each electrode used in this study is given in Table 3.3.

Table 3.3. Specifications of the electrodes used for the electroreduction of cystine and 2-HED.

Electrode	Insulating material	Electrode material	Diameter (cm)	Geometric surface area (cm^2)
Silver	Teflon	wire[a]	0.18	0.025
Gold	Teflon	wire[a]	0.10	0.008
Platinum	Teflon	wire[a]	0.14	0.015
Nickel	Teflon	rod[a]	0.32	0.080
Stainless Steel	glass	rod[a]	0.39	0.119
Copper	[b]	plug[a]	0.38	0.113
Lead	[b]	plug[a]	0.39	0.119
Glassy carbon	Teflon	rod[a]	0.30	0.070
Mercury	[b]	HMDE	0.078	0.019

[a] The surface exposed to the solution was a polished disk of the material.

[b] No insulating material used for these electrodes.

3.2.2.1 Electrode Cleaning Procedures

The surface of the HMDE was renewed by dispensing a fresh mercury drop. For all other materials, newly prepared electrodes were polished to achieve a mirror finish using graded sanding papers followed by 3 μm diamond paste followed by alumina slurries (1.0 and 0.05 μm) on polishing microcloth (LECO Lecloth). Between experiments, the electrodes were polished with 1.0 and 0.05 μm alumina and rinsed with Milli-Q water. In addition, the glassy carbon and stainless steel electrodes were sonicated in Milli-Q water to remove excess alumina. All solid metal electrodes, except for lead, were subjected to potential cycling in order to reconstruct the surface to achieve the same surface starting-state at the beginning of each experiment. The details for each electrode are given in the Results and Discussion Section. The copper electrode was reconstructed in 0.1 M NaOH by applying a potential of -0.90 V (*vs*. SCE) for 10 minutes. A cyclic voltammogram was then recorded between -1.20 and 0.40 V (υ = 20 mV s^{-1}) to monitor the reconstruction process. This procedure was repeated until no successive changes were observed in the voltammogram.

3.2.3 Modification of Glassy Carbon Electrodes with Metal Phthalocyanine Complexes

Phthalocyanine complexes containing cobalt, manganese or iron metal centers were used. Adsorption of the metal-phthalocyanines onto glassy carbon was achieved by drop-coating the metal-phthalocyanine complex (1 mM dissolved in DMSO, one drop used) onto the electrode surface. Sufficient time was allowed for the adsorption equilibrium to be reached[15,18] and after 30 minutes the electrode was washed with ethanol followed by Milli-Q water. To remove the adsorbed metal-phthalocyanine, the electrode was polarised at potentials near hydrogen evolution. The surface was then renewed by polishing with alumina (1.0 μm and 0.05 μm).

3.2.4 Electrochemistry

3.2.4.1 Cyclic Voltammetry

Cyclic voltammetry of cystine and 2-HED was performed using a computer interfaced PAR Model 273A Potentiostat/Galvanostat. A standard three electrode cell was used containing a platinum wire auxiliary electrode and a SCE as the reference. For the experiments carried out at the HMDE, Ag/AgCl was used as the reference electrode, however, all potentials are reported with reference to SCE. All voltammetric data were obtained using scan rates of 50 mV s^{-1} or 100 mV s^{-1}. The potential corresponding to the cleavage of the disulfide bond was established by fitting a curved baseline and measuring the potential where the current is greatest *versus* the background. Experiments were carried out in either Tris·HCl buffer (0.05 M, pH 9.0) or KH_2PO_4 buffer (0.05 M, pH 8.0) with added electrolyte (0.1 M), as specified in the Results and Discussion Section.

3.3 Results and Discussion

3.3.1 The Electroreduction of Cystine at Metal and Carbon Electrodes

Efficient electrochemical methods for reducing the disulfide bond in cystine were examined by performing the reaction at a variety of electrode surfaces including mercury, silver, gold, copper, nickel, lead, stainless steel, platinum and glassy carbon.

3.3.1.1 Mercury

The complex nature of the reaction of cystine at a HMDE is reflected by the number of peaks observed in the cyclic voltammogram. Figure 3.3 shows the response for 1 mM cystine in Tris·HCl buffer (pH 9.0) recorded at a scan rate of 100 mV s^{-1}.

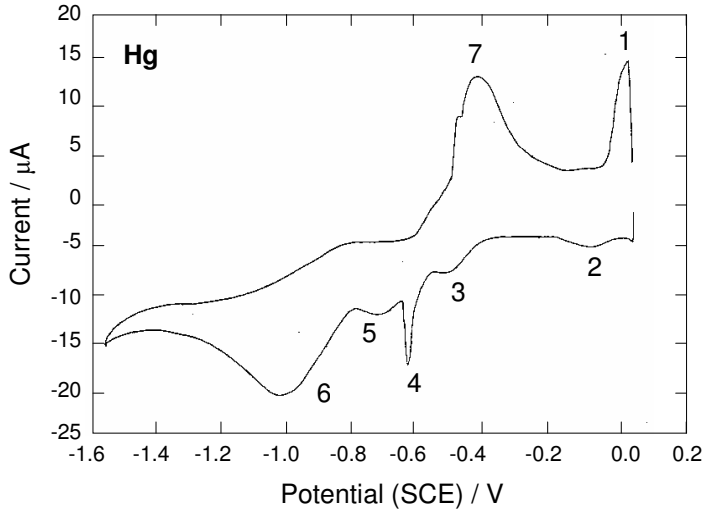

Figure 3.3. Cyclic voltammogram of 1 mM cystine in Tris·HCl buffer (pH 9.0) at a HMDE (υ = 100 mV s^{-1}). Supporting electrolyte is 0.1 M KNO_3.

This voltammogram is similar to those reported in the literature[4,6-8] and the peaks are assigned according to the reactions described in Section 3.1.1.1. At potentials positive of 0 V, cystine diffusing towards the electrode from the bulk solution reacts with mercury (II) ions, produced by dissolution of the mercury surface, to form mercury (II) cystinate (equation 3.7 and

3.8). This gives rise to the oxidation current at potentials more positive than -0.05 V (peak 1). The small reduction peak at -0.10 V (peak 2) most likely corresponds to the reduction of residual mercury (II) cystinate present at the electrode surface at the beginning of the potential scan. The reduction of mercury (II) cysteine thiolate (equation 3.6) is observed at -0.50 V (peak 3) whilst the reduction peaks at -0.64 V (peak 4) and/or -0.72 V (peak 5) are attributed to the reduction of mercury (I) cysteine thiolate (equation 3.2). It is proposed that peak 4 could be due to a non-Faradaic process but this was not investigated further. The main reduction peak at -1.02 V (peak 6) is due to the irreversible, diffusion-controlled reduction of cystine in solution which occurs without any specific interaction with the mercury surface (equation 3.9). The oxidation of cysteine to form mercury (I) cysteine thiolate (equation 3.10) is observed in the reverse scan at -0.43 V (peak 7). At potentials just positive of peak 7, mercury (I) cysteine thiolate undergoes surface disproportionation to give mercury (II) cysteine thiolate (equation 3.11). This reaction is not observed in the voltammogram as there is no associated current.

3.3.1.2 Gold

Chloride ions are known to adsorb to gold electrodes and cause dissolution of the gold surface. Therefore, the Tris·HCl buffer (pH 9.0) used to study the reduction of cystine at mercury is not suitable for use in the presence of a gold electrode. Instead, KH_2PO_4 buffer (pH 8.0) was chosen as the medium for investigating the reduction of cystine at a gold electrode. The response of 1 mM cystine in KH_2PO_4 buffer (pH 8.0) at a polycrystalline gold electrode is shown in Figure 3.4. This voltammogram is similar to that reported in the literature for the electroreduction of cystine at a gold electrode under acidic conditions.[14] Cystine has been shown to strongly adsorb onto gold, therefore, in our studies the peak at -0.86 V (peak 1) is attributed to the reduction of surface-bound gold (I) cysteine thiolate to yield solution-based cysteine. The thiol is oxidised back to the disulfide at 0.60 V (peak 2) and further oxidation of cystine to form cysteic acid occurs at 0.81 V (peak 3). The response of the polycrystalline gold electrode in blank KH_2PO_4 buffer (pH 8.0) is also shown in Figure 3.4 and the formation of gold surface oxide is observed at 0.81 V. Koryta and Pradáč[14] have proposed that surface oxides are involved in the oxidation of cystine (equation 3.12). The corresponding reduction of gold surface oxide is observed at 0.40 V (peak 4).

$$\dot{R}S_{ads} + 5OH_{ads} \longrightarrow RSO_3^- + 2H_2O + H^+ \qquad (3.12)$$

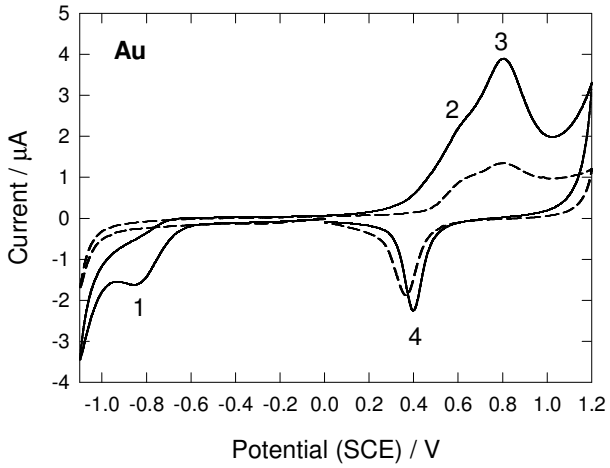

Figure 3.4. Cyclic voltammogram of 1 mM cystine in KH_2PO_4 buffer (pH 8.0) at a gold electrode (υ = 50 mV s^{-1}); in the absence (----) and presence (—) of 1 mM cystine. Supporting electrolyte is 0.1 M KNO_3. Prior to recording the cystine response, the gold electrode was electrochemically prepared by potential cycling between -0.45 and 1.45 V in 0.1 M $HClO_4$ for 3 hours.

Prior to recording cyclic voltammograms for the reaction of cystine at a gold electrode, the surface was subjected to potential cycling between -0.45 V and 1.45 V (υ = 50 mV s^{-1}) in 0.1 M $HClO_4$ for 3 hrs or until there was no change in successive cycles. This process is known as surface reconstruction.[25-27] It is well-established that for a clean gold electrode the top most atomic layer on the surface has a highly asymmetrical environment as they do not have neighbouring atoms above the plane of the surface.[25] This environment differs from that of atoms in the bulk material and changes in the position of the surface atoms often occur to account for the changed environment. In general, the bond lengths between atoms in the top layer and the second layer are contracted by a few percent relative to the bond length in the bulk material.[25,26] Furthermore, displacement of atoms away from their bulk lattice sites can also occur.[25] As the surface structure of an electrode can impact on the physical and chemical properties of the electrode, potential-induced reconstruction of the surface carried out in the current work is important as it leads to a rearrangement of the surface atom positions with time to give a well-ordered surface resembling that of the bulk material.

In the current work, changes were observed for the cyclic voltammogram of 1 mM cystine recorded at a gold electrode upon repetitive cycling. This indicated that the electrode could only be used for a short time to study the reactions of cystine at a gold electrode before the surface needs to be reconstructed. The reconstruction process carried out in 0.1 M $HClO_4$ described above is uneconomical for an industrial process as it is time consuming and therefore, expensive. As an alternative pretreatment method, the electrode was cycled in blank electrolyte within the potential region for the reduction of cystine (0 to -1.20 V). After seven cycles no changes in successive cyclic voltammograms were observed indicating that the surface had reached a steady state. The electrode was then transferred to the cystine solution and another scan was recorded over the same potential range to record the reduction response only (Figure 3.5). The reduction of cystine *via* the formation of surface-bound gold (I) cysteine thiolate shifted 60 mV more negative to -0.92 V. However, this potential is still positive of hydrogen evolution and allows the reduction of cystine to be distinguished clearly at a gold electrode. The shoulder seen at the solvent limit (~ -1.15 V) is likely to be due to the direct reduction of cystine. In the interests of a quick and inexpensive electrode pretreatment method for use in an industrial process, this pretreatment technique was used for subsequent investigations of the electroreduction of cystine at other metal electrodes.

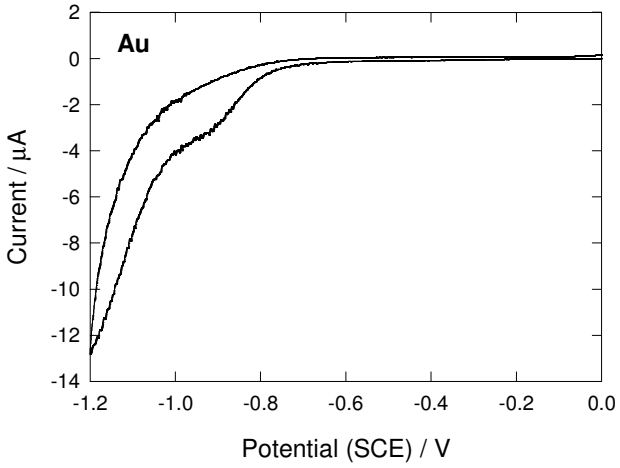

Figure 3.5. Cyclic voltammogram of 1 mM cystine in KH_2PO_4 buffer (pH 8.0) at a gold electrode (υ = 50 mV s^{-1}). Supporting electrolyte is 0.1 M KNO_3. Prior to recording the cystine response, the gold electrode was electrochemically prepared by potential cycling between 0 and -1.20 V in blank electrolyte for 7 cycles.

3.3.1.3 Silver

The response of silver towards cystine reduction was studied in KH_2PO_4 buffer (pH 8.0) containing 0.1 M $NaClO_4$. Prior to recording the cyclic voltammogram for cystine reduction, the electrode was electrochemically pretreated by cycling the potential between -0.40 and -1.20 V (υ = 50 mV s^{-1}) for 7 cycles. A cyclic voltammogram of 1 mM cystine was then recorded at the silver electrode over the same potential range (Figure 3.6). The small reduction peak observed at -0.88 V is attributed to the reduction of surface-bound silver (I) cysteine thiolate and the larger reduction peak at -1.15 V corresponds to the direct reduction of cystine in solution. These results are similar to those observed at a gold electrode. The small peak is assigned on the basis of the evidence of Watanabe *et al.,*[11] obtained using SERS, which demonstrated that cystine adsorbs onto a silver electrode to form the surface-bound cysteine thiolate. This result indicates that the mechanism for cleavage of the S–S group in cystine is analogous to that described for the reduction of cystine at a mercury electrode (equation 3.1 and 3.2).

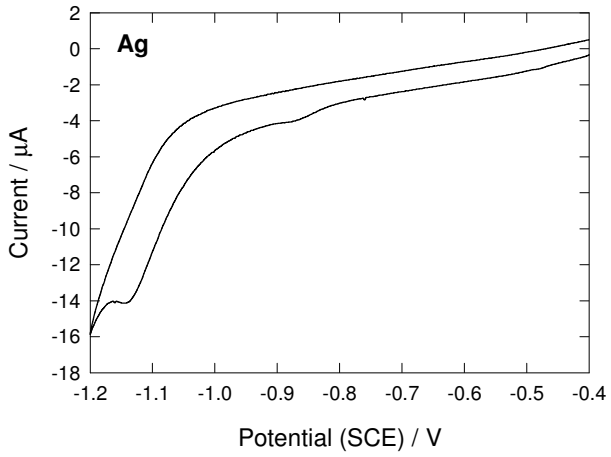

Figure 3.6. Cyclic voltammogram of 1 mM cystine in KH_2PO_4 buffer (pH 8.0) at a silver electrode (υ = 50 mV s^{-1}). Supporting electrolyte is 0.1 M $NaClO_4$.

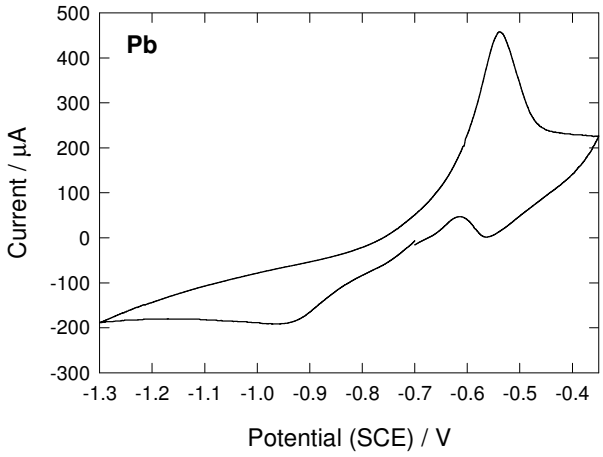

Figure 3.7. Cyclic voltammogram of 1 mM cystine in KH_2PO_4 buffer (pH 8.0) at a lead electrode (υ = 50 mV s^{-1}). Supporting electrolyte is 0.1 M KNO_3.

3.3.1.4 Lead

Industrial production of cysteine is performed by the electroreduction of cystine at a lead cathode in the presence of hydrochloric acid. However, corrosion of the lead electrode and subsequent formation of lead chloride at the electrode surface leads to product contamination.[28] In the present study, the electroreduction of cystine has been investigated using KH_2PO_4 buffer (pH 8.0) containing 0.1 M KNO_3 (Figure 3.7). The formation and reduction of lead surface oxides are observed at -0.53 V and -0.57 V respectively and the irreversible reduction of cystine is observed at -0.94 V. Cystine reduction occurs at least 350 mV less negative than the potential for hydrogen evolution. This is in contrast to the reduction of cystine in hydrochloric acid where hydrogen evolution occurs as a competitive reaction. Formation of lead surface oxide at the low potentials observed raises the possibility of product contamination with lead and therefore, potentials should be maintained below -0.70 V to observe the reduction of cystine only and eliminate contamination of the product.

3.3.1.5 Nickel

The reduction of cystine at a nickel electrode was studied in KH_2PO_4 buffer (pH 8.0). The electrode was subjected to the same pretreatment conditions as used for the silver electrode but potential cycling was performed between 0 and -1.20 V (υ = 50 mV s^{-1}). Figure 3.8 shows the response of 1 mM cystine at a nickel electrode. A small reduction peak is observed at the onset of hydrogen evolution at -0.97 V. Hence, hydrogen evolution and cystine reduction occur as competitive reactions at a nickel electrode making the two processes difficult to separate. The reduction peak observed at -0.82 V is also present in the corresponding cyclic voltammogram for the background electrolyte, therefore, this peak is most likely due to the presence of electrolyte ions.

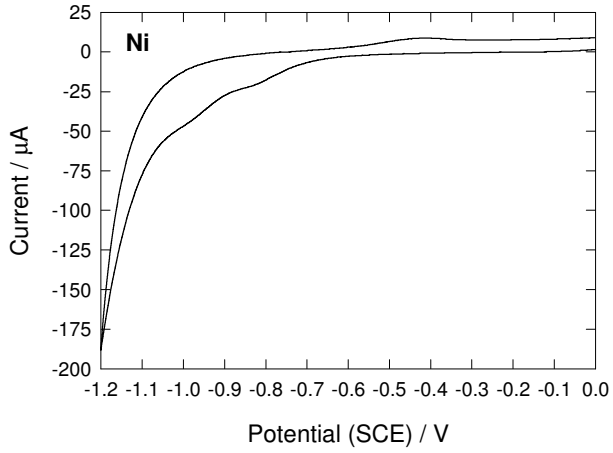

Figure 3.8. Cyclic voltammogram of 1 mM cystine in KH_2PO_4 buffer (pH 8.0) at a nickel electrode (υ = 50 mV s^{-1}). Supporting electrolyte is 0.1 M KNO_3.

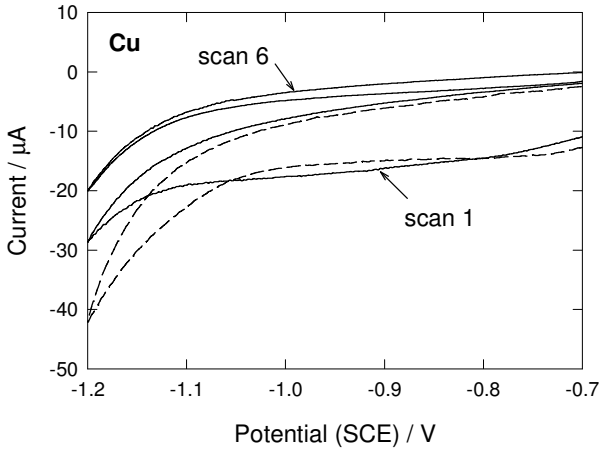

Figure 3.9. Cyclic voltammogram of 1 mM cystine in KH_2PO_4 buffer (pH 8.0) at a copper electrode (υ = 50 mV s^{-1}); in the absence (----) and presence (—) of 1 mM cystine. Supporting electrolyte is 0.1 M KCl.

3.3.1.6 Copper

The reduction of cystine is not observed at a copper electrode. Instead, evidence of a blocked electrode surface is obtained. The response of 1 mM cystine in KH_2PO_4 buffer (pH 8.0) at a copper electrode is shown in Figure 3.9. In blank electrolyte hydrogen evolution begins at -1.05 V, however, this process is suppressed in the presence of cystine. The current continues to decrease when the electrode is subjected to potential cycling between -0.70 and -1.20 V in 1 mM cystine indicating passivation of the surface (Figure 3.9, compare scan 1 and scan 6). As with most other metals, the reduction of cystine at a copper electrode is assumed to operate *via* adsorption of the disulfide onto the copper electrode to form surface-bound thiolates. However, the results obtained in this study indicate that these surface thiolates are not reductively cleaved off the surface before hydrogen evolution occurs and therefore, the surface remains blocked.

3.3.1.7 Platinum, Stainless Steel and Glassy Carbon

There was no evidence of disulfide reduction at platinum, stainless steel or glassy carbon electrodes. The response of platinum and glassy carbon electrodes towards the reduction of cystine was studied in KH_2PO_4 buffer (pH 8.0), whilst Tris·HCl buffer (pH 9.0) was used to study the response at a stainless steel electrode. Reduction of cystine was masked by hydrogen evolution at platinum (Figure 3.10) and stainless steel making it impossible to distinguish the two processes. These metals are referred to as low hydrogen overpotential metals as the onset of hydrogen reduction occurs at very low potentials: -0.90 V for platinum and -1.00 V for stainless steel in these experiments. In comparison, the overpotential for hydrogen evolution at glassy carbon is much larger. However, the reaction kinetics for the reduction of cystine are inherently slow at this electrode material and no evidence of disulfide reduction was observed (Figure 3.11).

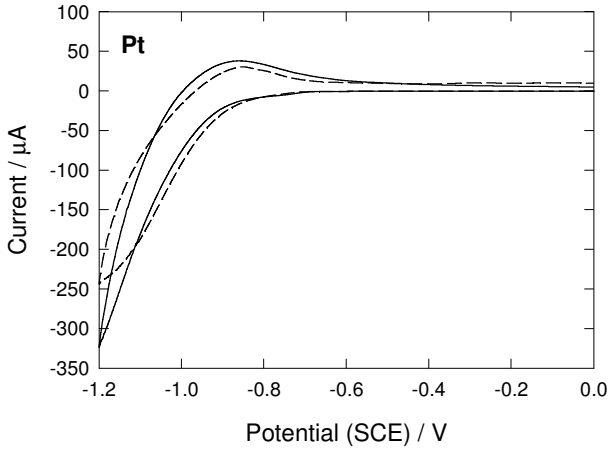

Figure 3.10. Cyclic voltammogram of 1 mM cystine in KH_2PO_4 buffer (pH 8.0) at a platinum electrode (υ = 50 mV s^{-1}); in the absence (----) and presence (—) of 1 mM cystine buffer. Electrolyte is 0.1 M KCl.

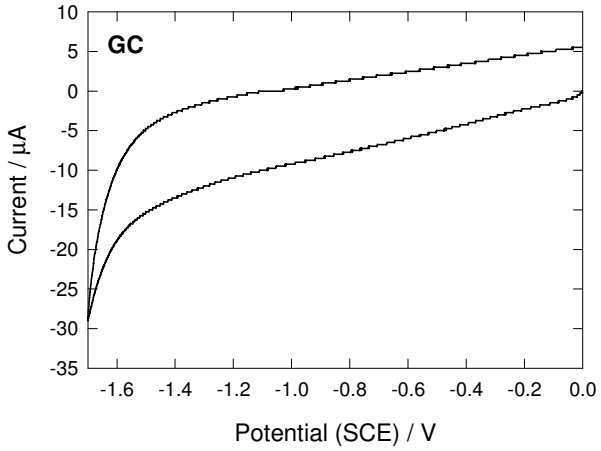

Figure 3.11. Cyclic voltammogram of 1 mM cystine in KH_2PO_4 buffer (pH 8.0) at a glassy carbon electrode (υ = 100 mV s^{-1}). Supporting electrolyte is 0.1 M KNO_3.

3.3.2 The Electroreduction of 2-Hydroxyethyl Disulfide at Metal and Carbon Electrodes

2-Mercaptoethanol has been reported to be effective in catalysing the electrolytic reduction of the disulfide bonds in wool proteins.[29] Therefore, the electroreduction of the corresponding disulfide, 2-HED (Scheme 3.2) at various solid electrodes has been investigated as an alternative to using cystine for the purposes of the application proposed in this project.

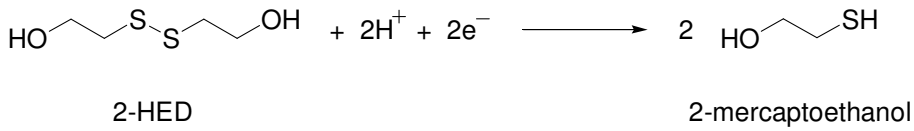

Scheme 3.2. Reduction of 2-HED to 2-mercaptoethanol.

The reduction potential for 2-HED at a mercury electrode was similar to that observed for cystine. Consideration of the reduction mechanism described for cystine in Section 3.1.1.1 suggests that the energy required to cleave the disulfide bond is similar for both compounds. Therefore, it was expected that the electrodes which showed activity towards the electroreduction of cystine would also show activity towards the reduction of 2-HED. Hence, the electroreduction of 2-HED was examined at silver, gold and nickel electrodes. In addition, the response obtained at a platinum electrode was investigated because although the reduction of cystine could not be observed at this electrode, platinum is commonly used in industrial processes. The response at glassy carbon was also studied because this material is commonly used as a support for mediators. The solid metal electrodes were electrochemically prepared prior to recording their response towards 2-HED using the same methods applied when investigating the reduction of cystine.

3.3.2.1 Mercury

As for cystine, the reduction of 2-HED at a mercury electrode is complicated by the formation of surface-bound thiolates. In the case of 2-HED, these complexes are referred to as mercury mercaptides and represent bonding between mercury and the sulfur atoms of 2-mercaptoethanol formed as a result of S–S bond cleavage. The response of 1 mM 2-HED in Tris·HCl buffer (pH 9.0) recorded at a scan rate of 100 mV s^{-1} is shown in Figure 3.12.

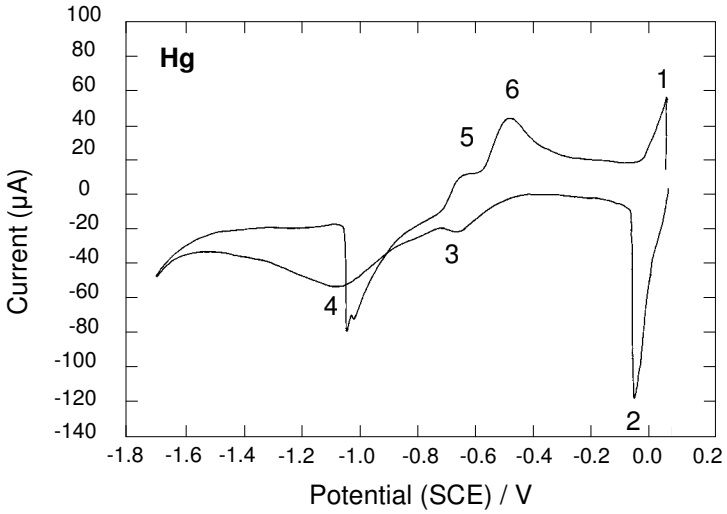

Figure 3.12. Cyclic voltammogram of 1 mM 2-HED in Tris·HCl buffer (pH 9.0) at a HMDE (υ = 100 mV s^{-1}). Supporting electrolyte is 0.1 M KNO_3.

The peaks in the voltammogram have been assigned by considering the reactions described in Section 3.1.1.1 for the electrochemistry of cystine at mercury electrodes as no reports of 2-HED reduction at mercury electrodes were found in the literature. At potentials greater than 0 V, the mercury surface is oxidised causing the dissolution of mercury (II) ions in solution (peak 1). Mercury (II) ions react with 2-HED through the deprotonated hydroxyl groups. Subsequently, the sharp reduction peak at -0.06 V (peak 2) corresponds to the reduction of this species. This reaction is proposed to occur in an analogous fashion to the reaction of cystine with mercury (II) ions through the carboxylate and amino groups (equation 3.7 and 3.8). Reduction of surface-bound mercury (I) mercaptide is observed at -0.69 V (peak 3) (equation 3.2). The main reduction peak at -1.11 V (peak 4) is due to the irreversible, diffusion-controlled reduction of 2-HED in solution (equation 3.9). On the reverse scan, the oxidation of the corresponding thiol, 2-mercaptoethanol, occurs in two stages.[30] The first step is the formation of a monolayer of mercury (I) mercaptide on the surface, observed at -0.66 V (peak 5) (equation 3.10). At more positive potentials, a one-electron charge transfer takes place and the mercury (I) mercaptide rearranges on the surface to form mercury (II) mercaptide (equation 3.11). This process is observed at -0.51 V (peak 6). The current spike at -1.06 V is only observed for high concentrations of 2-HED (it is not observed in the

voltammogram recorded for 0.25 mM 2-HED) and may correspond to a non-Faradaic current caused by desorption of 2-HED from the electrode surface.

3.3.2.2 Silver and Gold

The reduction of 1 mM 2-HED in KH_2PO_4 buffer was observed at silver (Figure 3.13) and gold (Figure 3.14) electrodes with the potentials of the reduction peak occurring at -0.96 and -1.00 V respectively.

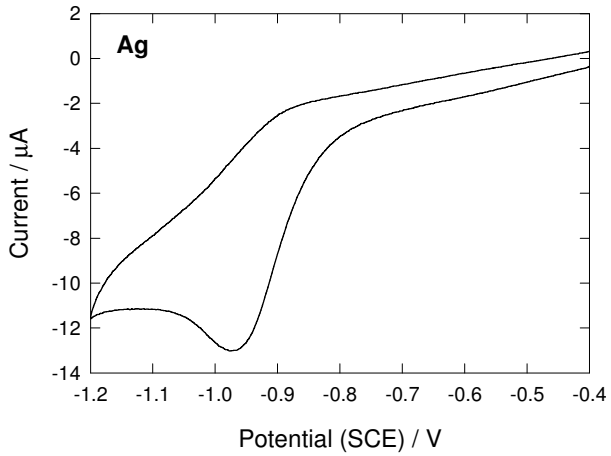

Figure 3.13. Cyclic voltammogram of 1 mM 2-HED in KH_2PO_4 buffer (pH 8.0) at a silver electrode (υ = 50 mV s^{-1}). Supporting electrolyte is 0.1 M KNO_3.

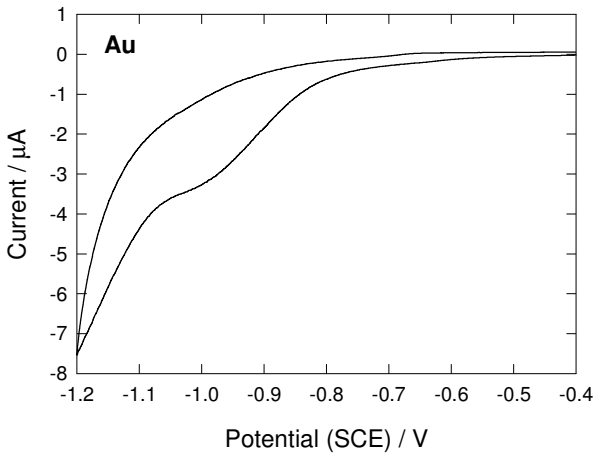

Figure 3.14. Cyclic voltammogram of 1 mM 2-HED in KH_2PO_4 buffer (pH 8.0) at a gold electrode (υ = 50 mV s^{-1}). Supporting electrolyte is 0.1 M KNO_3.

When the concentration of 2-HED was increased above 1 mM a second reduction peak appeared at -1.22 and -1.14 V at the silver and gold electrodes respectively (Figures 3.15 and 3.16, scans ii and iii). The magnitude of these peaks depended strongly on the concentration of the disulfide. It was proposed that this peak might correspond to the product of a bimolecular reaction involving the initial reduction product. However, the cyclic voltammograms of 2-mercaptoethanol at silver and gold electrodes did not show peaks at similar potentials, therefore, these peaks are not due to a bimolecular reaction involving 2-mercaptoethanol. Under basic conditions, thiols may also undergo oxidation to the corresponding sulfinic or sulfonic acid. Analysis of the 2-HED (> 1 mM) solution obtained by air oxidation of 2-mercaptoethanol using mass spectrometry indicated the

presence of 2-hydroxyethanesulfinic acid (*m/z* (EI): calculated for 2-HED ($C_4H_{10}O_2S_2$): 154; observed 154; calculated for 2-hydroxyethanesulfinic acid ($C_2H_6O_3S$): 110; observed 110). It is possible that the reduction of this species may give rise to the additional peaks observed in the presence of 2-HED, however, this was not investigated further.

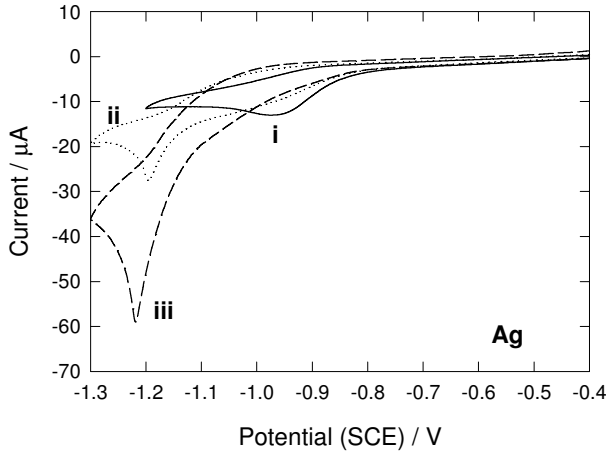

Figure 3.15. The effect of 2-HED concentration at a silver electrode; (i) 1 mM, (ii) 2 mM and (iii) 4 mM 2-HED in KH_2PO_4 buffer (pH 8.0) (υ = 50 mV s^{-1}). Supporting electrolyte is 0.1 M KNO_3.

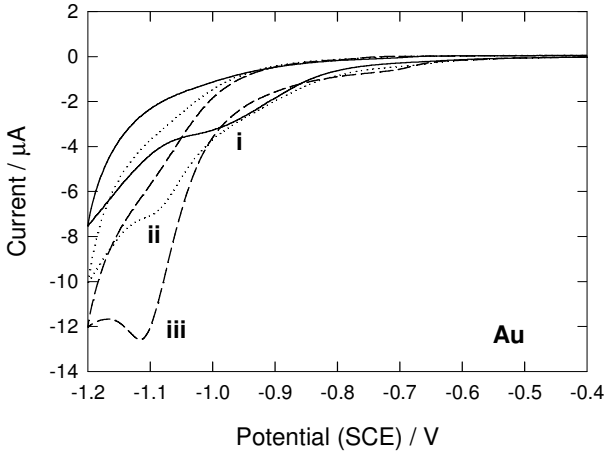

Figure 3.16. The effect of 2-HED concentration at a gold electrode; (i) 1 mM, (ii) 2 mM and (iii) 4 mM 2-HED in KH_2PO_4 buffer (pH 8.0) (υ = 50 mV s^{-1}). Supporting electrolyte is 0.1 M KNO_3.

3.3.2.3 Platinum, Nickel and Glassy Carbon

The response of platinum and nickel (Figure 3.17) electrodes towards the reduction of 2-HED was studied in KH_2PO_4 buffer (pH 8.0). The presence of 2-HED was observed to suppress hydrogen evolution at both electrodes and indicated that the surfaces were blocked. During disulfide reduction the thiolate formed adsorbs at the electrode surface. In order to observe the solution-based reduction of 2-HED electrochemically, the thiolate needs to be reductively cleaved from the surface. However, at the platinum and nickel electrodes this step does not occur and the reduction of 2-HED was not observed due to blocking of the electrode surface by the corresponding thiolate. In comparison, the response of 2-HED in Tris·HCl buffer (pH 9.0) at a glassy carbon electrode was analogous to that of cystine, *i.e.*, there was no evidence of disulfide reduction. This observation signified that the reaction was kinetically slow at this electrode material.

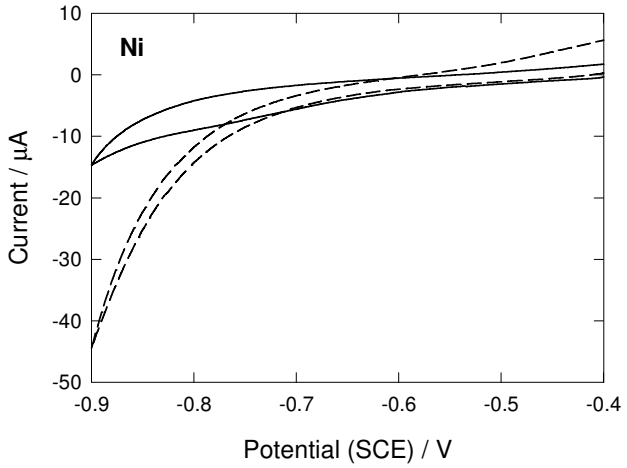

Figure 3.17. Cyclic voltammogram of 1 mM 2-HED in KH_2PO_4 buffer (pH 8.0) at a nickel electrode (υ = 50 mV s^{-1}); in the absence (----) and presence (—) of 1 mM 2-HED. Supporting electrolyte is 0.1 M KNO_3.

3.3.3 The Electroreduction of Cystine at Carbon Electrodes Modified with Metal Phthalocyanine Complexes

Transition metal phthalocyanines (MPc) adsorbed on graphite electrodes have been reported to exhibit electrocatalytic activity for the oxidation of thiols, including cysteine and 2-mercaptoethanol.[15,16,18-20] Reports of their use for disulfide reduction are less common.[15-17] In this work, preliminary studies were performed to evaluate the use of unsubstituted phthalocyanines containing transition metal centers of cobalt, iron and manganese for reducing the disulfide bond in cystine. These complexes will be referred to as CoPc, FePc and MnPc. Metal phthalocyanines act as a mediator to shuttle electrons between the electrode surface and cystine and therefore, offer an alternative to the direct reduction of cystine at solid electrodes.

The metal phthalocyanine complexes were immobilised onto glassy carbon. Whilst the reduction of cystine could not be observed at a bare glassy carbon electrode, it could be seen in the presence of all the metal phthalocyanines (Figure 3.18).

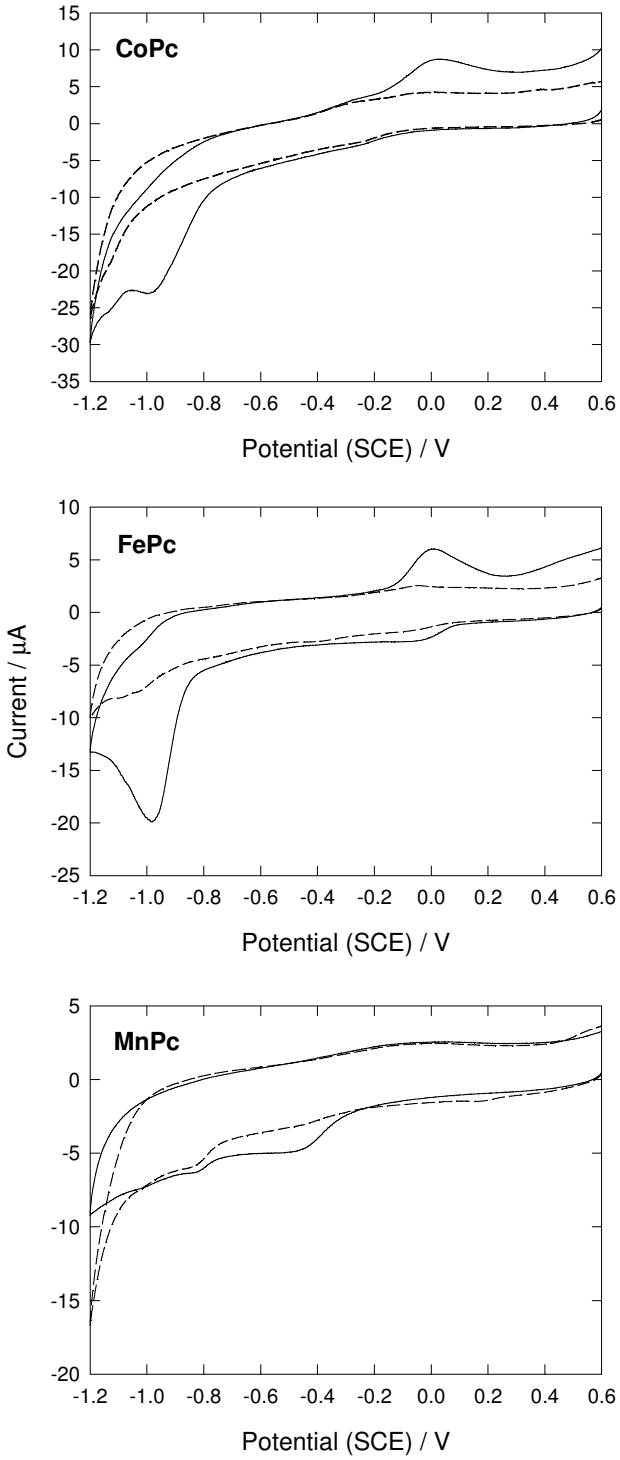

Figure 3.18. Cyclic voltammograms of 1 mM cystine in KH_2PO_4 buffer (pH 8.0) at glassy carbon electrodes modified with CoPc, FePc and MnPc (υ = 100 mV s^{-1}); in the absence (----) and presence (—) of 1 mM cystine. Supporting electrolyte is 0.1 M KNO_3.

The reduction peak varied with transition metal and occurred at -1.00, -0.96 and -0.50 V for CoPc, FePc and MnPc respectively. The subsequent oxidation of cysteine was observed in the reverse scan for CoPc and FePc at 0.07 and 0.10 V respectively. Oxidation of cysteine was not observed in the presence of MnPc. It has been suggested by Zagal *et al.* that cysteine oxidation is inhibited in the presence of manganese-centered phthalocyanines due to oxidation of the metal center from Mn(II) to Mn(III) and that the Mn(III) species is inactive for the electro-oxidation of cysteine.[15] In the literature, redox processes associated with the metal centers of transition metal phthalocyanine complexes have been reported.[31,32] In this work, only processes with very low currents were observed (-0.25 V for Co(II)/Co(I) and -0.035 V for Fe(II)/Fe(I)) presumably because the amount of complex adsorbed onto the glassy carbon electrode is very small. However, it is apparent that reduction of cystine occurs at the low oxidation state metal center (Co(I) and Fe(I)) and oxidation of the thiol occurs at the higher oxidation state metal center (Co(II) and Fe(II)). This observation is consistent with the literature reports.[17,33] Suppression of hydrogen evolution was observed at the MnPc modified electrode indicating that some inhibition is taking place at potentials negative of -1.00 V.

3.3.4 Comparison of Electrodes for the Electrochemical Reduction of Cystine and 2-Hydroxyethyl Disulfide

The results obtained for the electroreduction of cystine and 2-HED are summarised in Table 3.4. The best conditions overall for the electrochemical reduction of disulfides are achieved at lead and mercury electrodes. High currents are achieved and disulfide reduction is observed at potentials more positive than where proton reduction occurs. The disadvantage of employing lead and mercury electrodes is that they are highly toxic and therefore, other surfaces should be considered. Of the remaining electrodes, FePc/GC exhibited the best performance for the electroreduction of cystine as high currents were achieved at the energetically favourable potential of -0.96 V. However, the use of molecular catalysts for an industrial process is not practical due to loss of the catalyst from the electrode. Therefore, of the solid electrodes, gold is the most promising electrode for cystine reduction. Silver demonstrated the best performance for the electroreduction of 2-HED giving a high current density at the least negative reduction potential of -0.96 V. Platinum, stainless steel and nickel have low hydrogen overpotentials and as a consequence the reduction of cystine at these electrodes is masked by the evolution of hydrogen. Evidence of the electrode surface

being blocked by surface-bound thiolates is observed at copper in the presence of cystine and nickel and platinum electrodes used for the reduction of 2-HED. At these electrodes, hydrogen evolution is suppressed by the adsorbed thiolates and disulfide reduction is not observed.

Table 3.4. Summary of the electroreduction of cystine and 2-HED at metal and carbon electrodes.

Electrode	**Cystine**		**2-HED**	
	E_{pc} **(V)**	j_{pc} **(μA cm^{-2})**[a]	E_{pc} **(V)**	j_{pc} **(μA cm^{-2})**[a]
Mercury	-1.02	416	-1.11	1521
Gold	-0.92	88	-1.00	38
Silver	-1.15	64	-0.96	218
Lead	-0.94	621		
Nickel	-0.97	[b]	Blocked electrode	-
Copper	Blocked electrode	-		
Platinum	Masked by H_2 evolution	-	Blocked electrode	-
Stainless Steel	Masked by H_2 evolution	-		
Glassy carbon	Not observed	-	Not observed	-
CoPc/GC	-1.00	52[c]		
FePc/GC	-0.96	152[c]		
MnPc/GC	-0.50	18[c]		

[a] Based on the geometric area of the electrode.

[b] Could not be measured.

[c] Based on the geometric area of glassy carbon.

3.3.4.1 General Mechanism for the Electrochemical Reduction of Cystine and 2-Hydroxyethyl Disulfide

To account for the results observed in the current study, a general mechanism for the reduction of the disulfide bond in cystine and 2-HED at the various electrode surfaces has been derived based on that described in the literature as outlined in Section 3.1. The initial step involves adsorption of the disulfide from solution onto the electrode surface to give the corresponding thiolate (equation 3.13):

$$(RSSR)_{ads} + [MM]_s \rightleftharpoons [RS\text{-}MM\text{-}SR]_s \qquad (3.13)$$

where RSSR represents the disulfide and M represents the electrode material, *e.g.*, gold, silver, lead, nickel or mercury. Subscript 'ads' denotes the adsorbed state and subscript 's' along with square brackets indicates the groups of atoms forming part of the surface.

It is anticipated that during electroreduction, the disulfide is converted to two thiol fragments which are adsorbed at neighbouring metal sites, hence, the metal is predominantly present in the +1 oxidation state in the thiolate complex. Direct evidence for this proposal has been observed at silver electrodes and at transition metal phthalocyanine complexes (CoPc, FePc and MnPc) immobilised onto glassy carbon electrodes.[11,17] The thiolate is subsequently reduced off the electrode surface to yield the corresponding thiol in solution (equation 3.14):

$$[RS\text{-}MM\text{-}SR]_s + 2e^- \longrightarrow 2RS^- + [MM]_s \qquad (3.14)$$

where RS^- represents the thiolate anion. In this study, the electroreduction of cystine and 2-HED was investigated at pH 8.0-9.0. At pH 8.0 the thiolate anion will be protonated (equation 3.3). If the thiolate is not desorbed off the electrode surface the electrode is blocked and disulfide reduction cannot be observed electrochemically.

In addition to the adsorption-controlled pathway for disulfide reduction, direct reduction of solution-based cystine without any specific interaction with the electrode surface is observed at mercury, lead and silver electrodes (equation 3.9).

3.4 Conclusion

The electroreduction of cystine and 2-HED has been examined at a range of electrodes including mercury, gold, silver, platinum, lead, nickel, copper, stainless steel and glassy carbon. Transition metal phthalocyanines immobilised onto glassy carbon electrodes were also investigated as mediators for disulfide reduction. The importance of using electrodes with high hydrogen overpotentials was highlighted in this study as hydrogen evolution and disulfide reduction occur as competitive reactions. Hence, it is beneficial if the reduction potential for cleavage of the S–S bond is less negative than hydrogen evolution. Mercury and lead electrodes were confirmed to be the best electrodes for disulfide reduction, however, these metals are toxic and therefore, other surfaces need to be considered. Of the remaining surfaces, the most practical electrodes for the reduction of cystine and 2-HED were gold and silver respectively. Further research towards improving the reaction kinetics in the presence of silver and gold is described in Chapter 4. The use of FePc/GC electrodes for the reduction of cystine was promising, however, the use of molecular catalysts is not practical for industrial processes.

The electrochemical reduction of cystine and 2-HED at the various electrodes was performed in media with an alkaline pH of 8.0-9.0 and cleavage of the S–S bond was observed to be similar to that reported at low pH, therefore, the mechanism for reduction is expected to be the same. The electroreduction of cystine and 2-HED proceeds through adsorption of the disulfide onto the electrode surface to form the surface-bound thiolate which is reduced off the electrode to give the corresponding thiol in solution. A key observation concerning the electroreduction of disulfides is that the thiolate is desorbed off the electrode, if this step does not occur then the electrode is blocked and disulfide reduction cannot be observed electrochemically.

3.5 References for Chapter 3

1. Ralph, T. R.; Hitchman, M. L.; Millington, J. P.; Walsh, F. C. The electrochemistry of L-cystine and L-cysteine .2. Electrosynthesis of l-cysteine at solid electrodes. *Journal of Electroanalytical Chemistry* **1994**, *375*, 17-27.

2. Weinberg, N. L. Introduction to industrial electrosynthesis. In *Electrosynthesis: From laboratory, to pilot, to production*; Genders, J. D.; Derek, P., Eds; The Electrosynthesis Company Inc.: New York, NY, USA, 1990; p 11.

3. Kolthoff, I. M.; Barnum, C. The reduction of cystine at the dropping-mercury electrode. *Journal of the American Chemical Society* **1941**, *63*, 520-526.

4. Stankovich, M. T.; Bard, A. J. Electrochemistry of proteins and related substances .1. Cystine and cysteine at mercury-electrode. *Journal of Electroanalytical Chemistry* **1977**, *75*, 487-505.

5. Vavřička, S.; Heyrovský, M. Ac polarography and ac voltammetry of cystine. *Journal of Electroanalytical Chemistry* **1994**, *375*, 371-373.

6. Heyrovský, M.; Mader, P.; Veselá, V.; Fedurco, M. The reactions of cystine at mercury-electrodes. *Journal of Electroanalytical Chemistry* **1994**, *369*, 53-70.

7. Ralph, T. R.; Hitchman, M. L.; Millington, J. P.; Walsh, F. C. The reduction of L-cystine in hydrochloric acid at mercury drop electrodes. *Journal of Electroanalytical Chemistry* **2006**, *587*, 31-41.

8. Ralph, T. R.; Hitchman, M. L.; Millington, J. P.; Walsh, F. C. The reduction of L-cystine hydrochloride at stationary and rotating disc mercury electrodes. *Electrochimica Acta* **2005**, *51*, 133-145.

9. Hitchman, M. L.; Millington, J. P.; Ralph, T. R.; Walsh, F. C. Electrochemical reduction of L-cystine hydrochloride to L-cysteine hydrochloride. *Institution of Chemical Engineers Symposium Series* **1989**, *112*, 223-237.

10. Thirunavukkarasu, P. Effect of cathode materials on the electrochemical reduction of L-cystine to L-cysteine. *Bulletin of Electrochemistry* **1999**, *15*, 286-288.

11. Watanabe, T.; Maeda, H. Adsorption-controlled redox activity - surface-enhanced Raman investigation of cystine versus cysteine on silver electrodes. *Journal of Physical Chemistry* **1989**, *93*, 3258-3260.

12. Ralph, T. R.; Hitchman, M. L.; Millington, J. P.; Walsh, F. C. The electrochemistry of L-cystine and L-cysteine .1. Thermodynamic and kinetic-studies. *Journal of Electroanalytical Chemistry* **1994**, *375*, 1-15.

13. Pradáč, J.; Koryta, J. Electrode processes of the sulfhydryl-disulfide system. I. Cystine at a platinum electrode. *Journal of Electroanalytical Chemistry and Interfacial Electrochemistry* **1968**, *17*, 167-175.

14. Koryta, J.; Pradáč, J. Electrode processes of the sulfhydryl-disulfide system. II. Cystine at a gold electrode. *Journal of Electroanalytical Chemistry and Interfacial Electrochemistry* **1968**, *17*, 177-183.

15. Zagal, J. H.; Herrera, P. Electrochemistry of cysteine and cystine on metal phthalocyanines adsorbed on a graphite electrode. *Electrochimica Acta* **1985**, *30*, 449-454.

16. Zagal, J. H.; Henriquez, J. J. H. Potentiometric response of a graphite electrode modified with cobalt phthalocyanine for thiols and disulfides. *Boletin de la Sociedad Chilena de Quimica* **2000**, *45*, 237-242.

17. Zagal, J. H.; Gulppi, M. A.; Cárdenas-Jirón, G. Metal-centered redox chemistry of substituted cobalt phthalocyanines adsorbed on graphite and correlations with MO calculations and hammett parameters. Electrocatalytic reduction of a disulfide. *Polyhedron* **2000**, *19*, 2255-2260.

18. Zagal, J. H.; Gulppi, M. A.; Caro, C. A.; Cárdenas-Jirón, G. I. Paradoxical effect of the redox potential of adsorbed metallophthalocyanines on their activity for the oxidation of 2-mercaptoethanol. Inner versus outer sphere electrocatalysis. *Electrochemistry Communications* **1999**, *1*, 389-393.

19. Leung, P. S. K.; Betterton, E. A.; Hoffmann, M. R. Kinetics and mechanisms of the reduction of cobalt(II) 4,4',4",4"'-tetrasulfophthalocyanine by 2-mercaptoethanol under anoxic conditions. *Journal of Physical Chemistry* **1989**, *93*, 430-433.

20. Lezna, R. O.; Juanto, S.; Zagal, J. H. Spectroelectrochemical studies of tetrasulfonated metallophthalocyanines adsorbed on the basal plane of graphite in the presence of cysteine. *Journal of Electroanalytical Chemistry* **1998**, *452*, 221-228.

21. Nikolic, B. Ž.; Adzic, R. R.; Yeager, E. B. Reflectance spectra of monolayers of tetrasulfonated transition-metal phthalocyanines adsorbed on electrode surfaces. *Journal of Electroanalytical Chemistry* **1979**, *103*, 281-287.

22. Arai, G.; Sugaya, T.; Sakamoto, M.; Yasumori, I. Electrochemical studies of poly(mercaptohydroquinone) and poly(mercapto-para-benzoquinone) films prepared by electrochemical polymerization .6. Electroreduction of L-cystine on thiolates fixed in the polymer film. *Bulletin of the Chemical Society of Japan* **1992**, *65*, 594-596.

23. Wang, Z. L.; Pang, D. W. Electrocatalysis of metalloporphyrins .9. Catalytic electroreduction of cystine using water-soluble cobalt porphyrins. *Journal of Electroanalytical Chemistry* **1990**, *283*, 349-358.

24. Stricks, W.; Frischmann, J. K.; Mueller, R. G. Polarography of mercaptoalkyl compounds and their disulfides. *Journal of the Electrochemical Society* **1962**, *109*, 518-521.

25. Van Hove, M. A. Surface cystallography at the metal-gas interface. In *Structure of electrified interfaces*; Lipkowski, J.; Ross, P. N., Eds; VCH Publishers, Inc.: New York, NY, USA, 1993; p 11-14.

26. Kolb, D. M. Surface reconstruction at metal-electrolyte interfaces. In *Structure of electrified interfaces*; Lipkowski, J.; Ross, P. N., Eds; VCH Publishers, Inc.: New York, NY, USA, 1993; p 65-102.

27. Kolb, D. M. Reconstruction phenomena at metal-electrolyte interfaces. *Progess in Surface Science* **1996**, *51*, 109-173.

28. Ralph, T. R.; Hitchman, M. L.; Millington, J. P.; Walsh, F. C. The reduction of L-cystine hydrochloride at lead using static and rotating disc electrodes. *Journal of Electroanalytical Chemistry* **2005**, *583*, 260-272.

29. Leach, S. J.; Meschers, A.; Swanepoel, O. A. The electrolytic reduction of proteins. *Biochemistry* **1965**, *4*, 23-27.

30. Casassas, E.; Ariño, C.; Esteban, M.; Muller, C. Anodic behavior of 2-mercaptoethanol at a mercury-electrode. *Analytica Chimica Acta* **1988**, *206*, 65-74.

31. Lever, A. B. P.; Pickens, S. R.; Minor, P. C.; Licoccia, S.; Ramaswamy, B. S.; Magnell, K. Charge-transfer spectra of metallophthalocyanines - correlation with electrode-potentials. *Journal of the American Chemical Society* **1981**, *103*, 6800-6806.

32. Schlettwein, D.; Yoshida, T. Electrochemical reduction of substituted cobalt phthalocyanines adsorbed on graphite. *Journal of Electroanalytical Chemistry* **1998**, *441*, 139-146.

33. Zagal, J. H.; Gulppi, M.; Isaacs, M.; Cárdenas-Jirón, G.; Aguirre, M. J. Linear versus volcano correlations between electrocatalytic activity and redox and electronic properties of metallophthalocyanines. *Electrochimica Acta* **1998**, *44*, 1349-1357.

Chapter 4

Electrodeposition of Metals onto Carbon Electrodes for Disulfide Reduction

4.1 Introduction

A range of metal and carbon electrodes were examined in Chapter 3 to find electrode materials which promoted efficiemt reduction of the disulfide bonds in cystine and 2-HED. This research is focused towards using the corresponding thiols as mediators for the reduction of wool disulfide bonds in the process of wool setting (see Chapter 5). Solid gold and silver electrodes were found to be the most practical for reducing cystine and 2-HED, respectively; however, for an industrial process the use of large area solid metal electrodes is very expensive and hence, methods for reducing the amount of metal are of interest. This chapter describes the fabrication of high surface area metal nanoparticle electrodes for the electroreduction of cystine and 2-HED.

4.1.1 Electrode Materials used for Industrial Electrochemical Processes

Industrial electrochemical processes require large surface area electrodes to drive reactions to completion. Ideally, the selected material should be stable in the electrolysis medium (physically and chemically) and allow the desired reaction to occur at low overpotentials with high efficiency.[1] In reality, these characteristics are not always met as so-called “inert” electrodes are frequently affected by corrosion and physical wear which consequently limit the lifetime of the electrode and overpotentials of several hundred millivolts are often accepted.[2] The role of electrochemical technology in industry and the types of electrode materials employed in these processes have been extensively reviewed by Pletcher and co-workers.[1,2] Some common cathode and anode materials are given in Table 4.1. Electrode materials which promote efficient electrochemical reactions are usually expensive and therefore, it is more common for the active material to be coated onto a cheaper substrate such as titanium, stainless steel or carbon.[2] Coated electrodes can be prepared by a variety of deposition techniques including electroplating, spraying, physical vapour deposition or

impregnation of a porous support with an aqueous salt solution followed by drying and gas-phase reduction of the dispersed salt at high temperatures under an atmosphere of hydrogen gas.[2] In addition to being low cost, coated electrodes are advantageous because they are microrough and possess high electroactive surface areas and the crystallite size can be altered to improve activity.[2] Dispersion of the active material within carbon powder is another attractive method for fabricating high surface area electrodes.[2]

Table 4.1. Common electrode materials used in industrial electrochemical processes. Table adapted from references 1 and 2.

Cathode	Anode
Hg, Pb, Ni, Ag	Pt, Pt/Ti, Ir/Ti, Pt-Ir/Ti
Graphite and other forms of carbon[a]	Graphite and other forms of carbon[a]
Dispersed Pt on high surface area carbon	Pb or Fe in acid-sulphate media
Coatings of materials on steel with low hydrogen-overpotentials, *e.g.*, Ni, Ni/Al, Ni/Zn	PbO_2 on Ti, Nb or carbon
Precious metal coatings	Ni in alkaline media
Steels Stainless steel	Dimensionally stable anodes, *i.e.*, a mixed Ru-Ti oxide on Ti for Cl_2, IrO_2 on Ti
Ni-Mo-Fe or Ni-Mo-Cr alloys	Magnetite: $Fe_{3-x}O_4$
TiO_x	Conducting ceramics, *e.g.*, Ti_4O_7

[a] Sometimes treated thermally with organics or polymers to modify porosity, density, corrosion resistance and/or wettability.

Industrial electrode materials are used in a variety of forms and shapes depending on the needs of the particular process and the geometry of the reactor.[1,2] Electrodes fabricated from meshes, expanded metals and other related porous structures are commonly used to maximise surface area and reduce the cost and weight of the electrode.[2] A wide range of 3-D electrode structures are available including stacked meshes, beds of carbon granules or fibres, microporous carbon felt or cloth and reticulated metals (*e.g.*, nickel, stainless steel and copper) or carbon

(*e.g.*, reticulated vitreous carbon).[1,2] The use of 3-D electrodes in electrochemical processes is attractive because these structures allow the cell to be operated at high currents whilst maintaining low current densities at the electrode surface and mass transfer limitations within the cell are reduced.[1] In addition, these electrodes create good turbulence when used in a flow cell configuration and therefore, mass transfer is increased at the electrode surface.[1]

Industrial production of cysteine based on the electroreduction of cystine in acidic electrolytes is typically carried out using lead or silver cathodes. Both the advantages and disadvantages of using these metals have been discussed in Chapter 3, Section 3.1.1.2.

4.1.2 Electrodeposition of Metal Nanoparticles onto Solid Supports

The electrochemical deposition of metal nanoparticles onto conductive substrates is an attractive method for fabricating large surface area electrodes for use in industrial processes. Metal nanoparticles possess a high surface area to volume ratio and offer an efficient use of metal as less material is required to achieve sensitivities comparable to those obtained at large-scale solid metal electrodes. For example, hydrogen evolution with current densities comparable to bulk platinum is achieved at electrodeposited platinum nanoparticle-modified glassy carbon electrodes containing platinum loadings of 10 to 20 μg cm^{-2}.[3] The fabrication of metal nanoparticle electrodes by electrochemical techniques is advantageous because it is a single step process involving reduction of the metal salt at an applied potential and therefore, is a convenient, fast and low-cost method for the preparation of metal nanoparticles on large areas of conductive substrates. Furthermore, electrodeposited metal nanoparticle electrodes can be easily manufactured under ambient conditions on an industrial scale by simple modification of commercial electroplating operations. Industrial electrochemical processes are usually used for depositing thin metallic films of adequate thickness, structure and adhesion and are used for a wide range of applications including corrosion protection of metal parts in the automotive industry[4] and for fabricating metal (usually gold) contacts in the electronics industry.[5] Electrochemical deposition procedures are also advantageous because they allow the properties of the deposited materials to be easily controlled in order to optimise the electrode for the desired reaction. The nucleation and growth mechanism and hence, the size and density of metal particles can be controlled simply by varying the deposition conditions such as electrolyte composition, deposition time and/or overpotential as is discussed in Section 4.1.2.1.

4.1.2.1 Mechanism for Nucleation and Growth of Metal Nanoparticles Electrodeposited at Carbon Surfaces

The mechanism of electrochemically assisted deposition of metal nanoparticles includes the electrochemical reduction of the metal salt, primary formation of ad-atoms, and further growth of the nanocrystallites on the conducting surface. Investigations into the early stages of electrochemical deposition have been carried out by many researchers to elucidate the nucleation and growth mechanisms of the metal phase on the substrate.[6-15] These processes are determined by the nature of the substrate[15] and whilst metals can be deposited onto a variety of conducting substrates, the mechanisms associated with the nucleation and growth of metal nanoparticles at carbon substrates is of most interest for the work described in this thesis.

Two limiting cases can be distinguished for the nucleation of metal nanoparticles at carbon substrates: instantaneous and progressive nucleation. In the case of instantaneous nucleation, nuclei are immediately generated at high nucleation rate on specific active sites and the number of nuclei remains constant during the growth process. In contrast, progressive nucleation refers to a continuous increase in the number of nuclei with time. Studies regarding the electrodeposition of copper and gold nanoparticles onto pyrolytic graphite and glassy carbon substrates respectively have shown that the mechanism for nucleation is dependent on the potential applied to reduce the solution-based metal salt at the electrode.[6,7] At low applied potentials the nucleation process is progressive until the maximum number of nuclei are formed. As the potential shifts more negative, the nucleation of metal nanoparticles at carbon substrates occurs *via* the instantaneous process and the number of nuclei increases with overpotential.[6,7] Further growth of the nanoparticles takes place by the Volmer-Weber island growth mechanism (Figure 4.1).[8,9,16,17] Only small clusters of atoms are required to form the critical nucleus for which the probability of attaching a new atom is larger than one-half, stabilising the cluster and allowing further growth to occur spontaneously.[7] For silver and gold deposits, the critical nucleus is reported to consist of between one and four atoms depending on overpotential and the bulk concentration of the metal salt solution.[7,8] The 3-D particles grow by hemispherical diffusion until the diffusion layers from adjacent nanoparticles overlap and hemispherical mass-transfer gives way to linear mass-transfer to an effectively planar surface (Figure 4.2).[10,11] This diffusion-controlled growth process leads to the development of nucleation exclusion zones around already nucleated centers. Hence, metal deposition at the electrode surface is

hindered and further growth occurs by metal being deposited perpendicularly onto the already existing nanoparticles.[10]

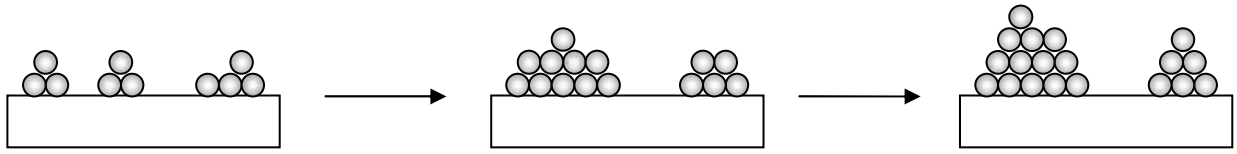

Figure 4.1. Schematic representation of the early growth stages for metal deposited onto carbon substrates *via* the Volmer-Weber island growth mechanism. This figure illustrates the initial nucleation of metal atoms at the surface and the subsequent growth and overlapping of nuclei to form hemispherical deposits on the substrate. Figure taken from reference 16.

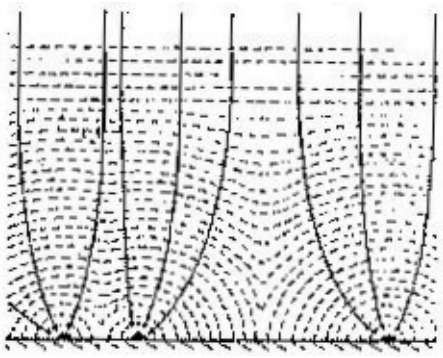

Figure 4.2. Schematic representation of the growth and overlapping of diffusion zones around stable nuclei. The vertical solid lines indicate the directions of the diffusional field during growth of the nuclei. Figure taken from reference 10.

It is well-established that the electrodeposition reaction occurs preferentially at step defect sites on the surface. Extensive studies of the electrochemical deposition of silver and platinum onto HOPG have been carried out by Zoval and co-workers who showed that the deposition process occurs by preferential decoration of step edges at low potentials, followed by the electrocrystallisation of metal at defect-free regions of the graphite surface at high potentials.[11-13] The edge plane (or steps) on the graphite surface typically show faster electron kinetics than the basal plane and hence, nucleation and growth occurs at these sites first.[14] Figure 4.3 shows an HOPG surface decorated with electrochemically deposited platinum nanoparticles using the

conditions employed by Zoval *et al.* whereby a potential of -600 mV (*vs*. mercurous sulfate reference electrode) was applied to the electrode for 50 milliseconds.[11] Under these conditions, small closely-packed nanoparticles are observed at the step edges whilst larger particles are deposited on the basal plane and are more separated. Similar images were obtained for electrochemically deposited silver nanoparticles on HOPG and the size disparity between particles located at the step edges and on the basal plane was attributed to the differing symmetry associated with the diffusional growth of the nuclei located at the two planes of the graphite surface.[13] At the highly populated edge plane graphite, diffusion of metal ions from the bulk solution has a cylindrical symmetry due to overlapping of the diffusion layers from adjacent nuclei. In comparison, nuclei at the less dense basal plane are subjected to efficient hemispherical diffusion leading to faster growth and larger particle diameters.[13]

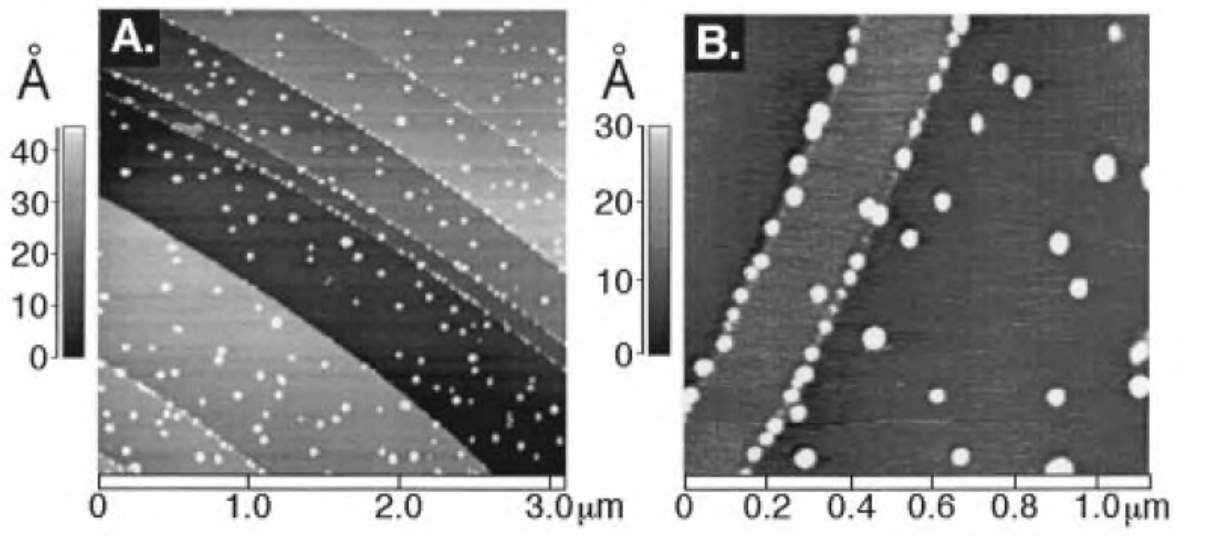

Figure 4.3. Non-contact AFM images of a graphite basal plane surface decorated with platinum nanoparticles after applying a potential of -600 mV (*vs*. mercurous sulfate reference electrode) for 50 milliseconds. Image areas are (a) 3 μm × 3 μm and (b) 1 μm × 1 μm. Figure taken from reference 11.

The overall surface area of the metal as well as nanoparticle size, density and shape can be controlled to some extent by varying the deposition conditions. The electrochemical deposition potential in particular has been shown to strongly affect the number of particles, their size and the surface coverage. Ghodbane and co-workers showed that the application of positive potentials

(0.20 V *vs*. Ag/AgCl) for the electrochemical deposition of copper particles on pyrolytic graphite resulted in the formation of small nanoparticles on the surface.[6] At this potential the distance between two neighbouring particles was large and the growth process was very slow enabling dimensionally uniform particles to be deposited on the electrode surface. As the deposition potential was shifted to more negative values the size and density of the particles increased. A broader size distribution was observed for larger nanoparticles. Further control over the size and density of electrodeposited metal nanoparticles can be obtained by varying the concentration of the bulk metal salt solution and the deposition time.[18] In addition, the shape of metal particles can also be controlled through the deposition conditions. Tian *et al.* electrodeposited gold nanoparticles onto a gold substrate with nanopyramidal, nanorod-like and spherical structures by manipulating the overpotential and concentration of the gold salt solution.[19] These workers characterised the crystallographic orientation of the gold nanostructures by X-ray diffraction and evaluated their activity towards the electroreduction of oxygen. Nanostructures that were tuned to contain mostly Au (100) faces were the most active towards the four electron reduction of oxygen. Spherical nanoparticles were more active than nanorods followed by nanopyramids for this reaction.

4.1.3 Applications of Electrodeposited Metal Nanoparticle Electrodes

Electrochemical deposition of metal nanoparticles onto carbon supports is attracting considerable research interest for applications in fuel cell design and the fabrication of chemical and biosensors. No examples of the use of electrodeposited metal nanoparticle electrodes in industrial electrochemical processes have been found; however, this is most likely due to the strategies adopted by commercial companies to protect intellectual property.

High surface area nanostructures prepared by electrochemically depositing platinum-based nanoparticles onto carbon based electrodes have been shown to efficiently catalyse the electro-oxidation of methanol and are attracting considerable attention in the development of direct methanol fuel cells (DMFC). Early work focused on the use of platinium nanoparticle electrodes but more recent research has revealed that PtRu and PtRuMo nanoparticles are more promising catalysts as they show improved activity for the electro-oxidation of methanol and tolerance for carbon monoxide poisoning.[20-22]Several high surface area nanostructures such as carbon-Nafion layers, carbon nanotubes (CNTs) and pressed graphite have been examined as potential electrodes in the

DMFC. Particles with small dimensions enhance the electrocatalytic efficiency for the electrooxidation of methanol and are advantageous as low particle loadings are required. Tsai *et al.* compared the catalytic activity of platinum and Pt-Ru nanoparticles electrodeposited onto CNT arrays and a commercial Pt-Ru electrode supported on carbon black for the direct oxidation of methanol.[21] Electrochemical testing revealed that Pt-Ru electrodes exhibited better electroactivity (current density of methanol oxidation per unit Pt loading mass) than solely platinum nanoparticle electrodes. Furthermore, the Pt-Ru/CNTs showed significantly improved catalytic activity when compared to the Pt-Ru electrode supported on carbon black. In more recent literature Pt-Ru and PtRuMo nanoparticles electrodeposited on pressed graphite were investigated as electrodes for DMFC.[22] The research revealed that the power density from the DMFC at 353K was higher for PtRuMo electrode (2200 W m^{-2}) than the PtRu electrode (1925 W m^{-2}). However, the degradation rate of the Mo containing electrode was higher. The research also revealed that the nanoparticle-based pressed graphite felt electrodes gave higher power densities compared to conventional gas diffusion electrodes, which rely on a thin catalyst layer containing Pt-Ru supported on carbon black, due to an increased reaction zone for methanol oxidation at the former electrodes.

The electrodeposition of platinum, palladium and gold nanoparticles onto carbon substrates has been widely investigated for the development of chemical and biosensors to detect molecules such as hydrogen, arsenic and dopamine.[23-27] These electrodes exhibit enhanced sensitivity towards the reaction of interest compared to the carbon substrate and the bulk metal material and have been shown to be capable of detecting low analyte concentrations. For example, the peak current associated with the oxidation of dopamine (100 μM in PB (pH 7.4)) at platinum nanoparticles (size range 50 to 500 nm) electrodeposited onto a glassy carbon support was 11.6 times greater and occurred at a lower overpotential than at the bare glassy carbon electrode.[26] A detection limit of 10 nM was calculated for the oxidation of dopamine at the platinum nanoparticle-modified glassy carbon electrode. In comparison, negligible currents for dopamine oxidation were observed at bulk platinum, even at larger overpotentials than those used for dopamine detection at unmodified and platinum nanoparticle-modified glassy carbon electrodes. Electrodeposition has also been highlighted as a straight forward and low-cost method of electrode preparation in sensor development as these electrodes exhibit similar if not superior sensitivity compared to electrodes fabricated by lithography techniques or other deposition methods such as vacuum evaporation or sputtering. Compton *et al.* used the significantly simpler method of electrodeposition to prepare gold

nanoparticle electrodes which showed similar sensitivity (detection limit = 0.014 ppb) towards the electrochemical detection of arsenic (As (III)) to that obtained using an array of 564 gold ultramicroelectrode disks which was fabricated by electron beam evaporation.[27] Each ultramicroelectrode disk in the array was 12 μm in diameter with center-to-center spacing of 58 μm. In comparison, the average size of the electrodeposited gold nanoparticles was 11 nm and the density of nanoparticles on the surface was ~ 75 particles μm^{-2}.[27] Palladium nanoparticles electrodeposited onto single walled carbon nanotubes have also been observed to exhibit superior sensitivity for the detection of hydrogen compared to electrodes fabricated using vacuum evaporation or sputtering techniques.[24] In this case the increased sensitivity was attributed to metal being deposited onto defect sites which serve as a conduction barrier. In addition to high sensitivities, electrodeposited metal nanoparticle electrodes exhibit fast response times and can be used in ambient conditions making them practical for real time/field analysis. Palladium nanoparticle-based sensors fabricated by electrodepositing palladium nanoparticles onto single walled carbon nanotubes can be operated at room temperature and show high sensitivity and selectivity towards hydrogen.[23,24] This is in contrast to most commercially available hydrogen sensors which are fabricated using metal oxide films and require heating to over 400 °C in order to maintain proper operation.[28]

This brief literature review highlights the considerable potential of electrodeposited metal nanoparticle electrodes for commercial application. Hence, this method was adopted in the research described in this chapter to fabricate high surface area metal nanoparticle electrodes for the reduction of cystine and 2-HED.

4.1.4 Research Directions for Chapter 4

The work presented in this chapter investigates the use of silver and gold nanoparticle electrodes for the electroreduction of cystine and 2-HED. These electrodes were fabricated by electrochemically depositing metal nanoparticles onto carbon supports such as glassy carbon and carbon fabric. In developmental work, the effect of metal loading at glassy carbon electrodes on disulfide reduction was studied by controlling the deposition time. The metal nanoparticle electrode which gave the best performance was then used in bulk electrolysis experiments to obtain a greater conversion of the disulfide to the thiol. Carbon fabric, made from woven carbon fibers, was used in

these experiments because bulk electrolysis techniques require a working electrode with a large surface area. A survey was conducted to optimise the electroreduction of cystine using bulk electrolysis conditions.

4.2 Experimental Methods

4.2.1 Electrodeposition of Metal Particles onto Carbon Supports

Silver and gold particles were electrodeposited onto glassy carbon disk electrodes or large surface area carbon fabric. The construction of these electrodes has been described previously in Chapter 2 (Sections 2.4.2.1 and 2.4.2.3). The geometric area of the glassy carbon disk electrodes was 0.07 cm^2 and the carbon fabric electrodes had a geometric surface area of 0.95 cm^2 per side. Metal deposition was performed by reducing metal salt solutions of $AgNO_3$ (1 mM, 10 mL) or $KAuCl_4$ (1 mM, 10 mL for deposition onto glassy carbon; 1mM or 2mM, 20 mL for deposition onto carbon fabric) using either a computer interfaced PAR Model 273A Potentiostat/Galvanostat or an EG & G PAR Model 173 Potentiostat coupled to a Powerlab 4SP (ADInstruments). The conditions used for metal deposition are given in Table 4.2. A standard three electrode cell was used for all electrochemical measurements. The auxiliary electrode was a platinum wire when depositing metal onto glassy carbon disk electrodes and high surface area platinum gauze when carbon fabric electrodes were employed as the working electrode. The reference electrode was either a saturated calomel electrode (SCE) (for depositing gold) or a silver wire pseudo-reference electrode (for depositing silver). The potential for the silver wire pseudo-reference electrode was 0.074 V *vs*. SCE. Prior to metal deposition, the glassy carbon electrodes were polished with alumina slurries (1.0 μm and 0.05 μm) on polishing microcloth (LECO Lecloth) whilst the carbon fabric electrodes were sonicated (10 seconds) in successive baths of acetone, methanol and isopropyl alcohol and dried with gaseous nitrogen. At the end of each experiment, the metal particles were electrochemically stripped off the glassy carbon electrodes using $AgNO_3$ (1 mM, 10 mL) or HCl (1 M, 10 mL) for silver and gold respectively. The stripping conditions are detailed in Table 4.3.

Table 4.2. Conditions for electrochemically depositing silver and gold particles onto carbon substrates.

Carbon Substrate	Metal	Metal Salt Solution	Conditions for depositing metal particles
Glassy carbon	Silver	1 mM $AgNO_3$ 0.1 M KNO_3	The potential was scanned from 0.20 to -1.20 V.
			The potential was held at -0.60 V for deposition times between 5 and 900 seconds.
Glassy carbon	Gold	1 mM $KAuCl_4$ 0.5 M H_2SO_4	A potential step was applied from 1.10 to 0 V for deposition times between 5 and 900 seconds
Carbon fabric	Gold	1 mM $KAuCl_4$ 0.5 M H_2SO_4	A potential step was applied from 1.10 to -0.4 V over 30 minutes.
		2 mM $KAuCl_4$ 0.5 M H_2SO_4	Initially a conditioning potential of 1.10 V was applied for 5 seconds. The potential was then held at -0.4 V until a total charge of -2.5 C had been passed.

Table 4.2. Conditions for electrochemically stripping silver and gold particles off glassy carbon electrodes.

Metal	Stripping solution	Conditions for stripping metal particles off glassy carbon substrates
Silver	1 mm $AgNO_3$ 0.1 M KNO_3	The potential was scanned from -1.00 to 0.60 V (υ = 10 mV s^{-1}).
		The potential was stepped from -0.10 to 0.20 V over 300 seconds.
Gold	1 M HCl	The potential was stepped from 0 to 1.00 V over the time period equal to the deposition time.

A new carbon fabric electrode was used each time gold was deposited. Electrodes fabricated by depositing silver and gold particles onto glassy carbon will be referred to as nanoAg/GC and nanoAu/GC respectively. Gold particles supported on carbon fabric will be described as nanoAu/CF.

4.2.1.1 Characterisation of Metal Particles Supported on Carbon Electrodes

Silver and gold particles were deposited onto glassy carbon plate electrodes (geometric surface area of modified area was 0.31 cm^2) for characterisation using SEM. Prior to deposition, the glassy carbon plates were polished with alumina slurries (1.0 and 0.05 μm) and sonicated (10 minutes) in Milli-Q water to remove excess alumina before drying with nitrogen. Carbon fabric electrodes were sonicated (10 seconds) in successive baths of acetone, methanol and isopropyl alcohol and dried with nitrogen prior to fabricating nanoAu/CF electrodes for characterisation. SEM images were obtained using a Raith 150 e-beam lithography system operating at an accelerating voltage of 10 keV. The average size for silver and gold particles deposited onto glassy carbon was determined from the SEM image using CorelDRAW 11 software. The vertical axis of the particles was measured using the dimension tool (195 particles were sampled for each surface).

4.2.2 Electrochemistry

For developmental work, the electroreduction of cystine and 2-HED at nanoAg/GC, nanoAu/GC and the respective solid metal electrodes was investigated using cyclic voltammetry. The bulk electrolysis of cystine at nanoAu/CF electrodes was carried out using controlled-potential coulometry. These experiments were performed using a computer interfaced PAR Model 273A Potentiostat/Galvanostat. The supporting electrolyte was KH_2PO_4 buffer (0.05 M, pH 8.0) containing 0.1 M $NaClO_4$ or 0.1 M KNO_3 for the nanoAg/GC and nanoAu/GC (CF) electrodes respectively.

4.2.2.1 Cyclic Voltammetry

The conditions used for the cyclic voltammetry of cystine and 2-HED (1 mM) at solid silver and gold electrodes were described in Chapter 3. NanoAg/GC and nanoAu/GC electrodes were electrochemically pretreated in the background electrolyte by potential cycling between -0.40 and -1.20 V or -1.30 V. After 7 cycles, no changes were observed in successive cyclic voltammograms indicating that the surface had reached a steady state. The electroreduction of cystine and 2-HED (1 mM) at these electrodes was investigated over the same potential range. A platinum wire was used as the auxiliary electrode and the reference electrode was a saturated calomel electrode (SCE). All voltammetric data were obtained using a scan rate (υ) of 50 mV s^{-1}.

4.2.2.2 Controlled-Potential Coulometry

The bulk electrolysis of cystine at a nanoAu/CF electrode was performed using controlled-potential coulometry. The bulk electrolysis cell (see Chapter 2, Section 2.4.3.4, Design 1) consisted of two compartments separated by a sintered glass frit (porosity 5). The nanoAu/CF electrode was suspended vertically in the inner compartment along with a saturated calomel electrode (SCE) as the reference. The auxiliary electrode was constructed from high surface area platinum gauze. This electrode was positioned symmetrically in the outer compartment of the cell to produce a uniform potential and current density across the nanoAu/CF electrode. For the electroreduction of cystine, the disulfide solution (1 mM, 20 mL) was placed in the inner compartment whilst the outer compartment contained blank electrolyte filled to the same level as the inner compartment. Cystine was reduced by applying a constant potential to the nanoAu/CF electrode until 2 coulombs (C) of charge had passed. To achieve effective mass transfer during the reaction, the cystine solution was stirred and bubbled with nitrogen. Bulk electrolysis experiments were performed at room temperature (20 °C) and at 85 °C. For the experiments carried out at 85 °C the bulk electrolysis cell was heated to the required temperature using a silicone oil bath.

4.2.3 Ellman's Assay for Quantifying Cysteine

Cysteine concentration was determined by reaction with 5,5'-dithio-*bis*-(2-nitrobenzoic acid) (DTNB) based on the method described by Ellman.[29,30] The advantages of using this reagent over other methods for quantifying cysteine concentration are that the reagent is water-soluble, reaction with free thiols is fast and it can be used at neutral pH with few side reactions. For this work, the reaction of cysteine with DTNB was carried out at pH 8.0. Under these conditions, DTNB is present as the corresponding benzoate anion ($DTNB^{2-}$). $DTNB^{2-}$ reacts with free thiol groups to yield a mixed disulfide and 2-nitro-5-thiobenzoate (TNB^{2-}) (Scheme 4.1). TNB^{2-} is an intensely yellow-coloured compound, the concentration of which can be quantified by measuring the absorbance at 412 nm.

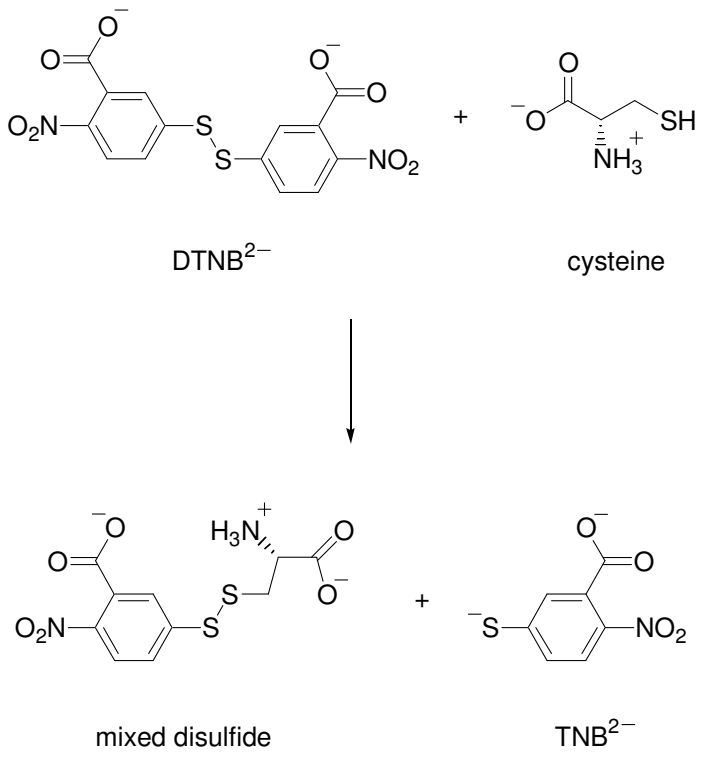

Scheme 4.1. The reaction of DTNB with cysteine at pH 8.0.

To carry out the determination of cysteine concentration at the end of the electrolysis, half the electrolysis solution (10 mL) was transferred from the cell to a vial containing EDTA, giving a final EDTA concentration of 2 mM. EDTA was added as a stabiliser to bind trace metal ions which are known to catalyse the oxidation of thiols to the corresponding disulfide in the presence of oxygen.[31-33] A sample of the 10 mL solution was diluted (10 to 50 times depending on final cysteine concentration) with reaction buffer (KH_2PO_4 buffer (0.05 M, pH 8.0) containing 2 mM EDTA) to give a total volume of 5 mL. DTNB dissolved in reaction buffer (1.67 mM, final concentration) was added to give a final volume of 6 mL. Following incubation at room temperature for 15 minutes the absorbance was measured at 412 nm using a Diode Array UV-Vis spectrophotometer (Hewlett Packard 8452AX). The amount of cysteine present was quantified by comparison to a standard curve composed of known cysteine concentrations (Figure 4.4). The molar extinction coefficient for TNB obtained from this standard curve was 12,853 M^{-1} cm^{-1}. This value is comparable to the reported literature value of 14,150 M^{-1} cm^{-1} measured in phosphate buffer (0.1 M, pH 7.27, containing 1 mM EDTA).[30]

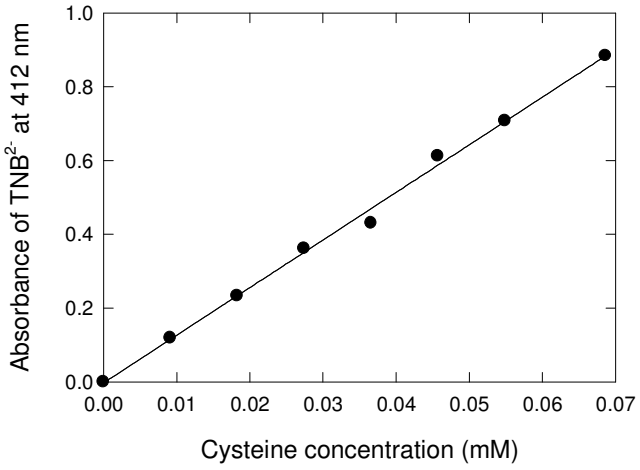

Figure 4.4. Standard curve for the reaction of DTNB with known concentrations of cysteine in KH_2PO_4 buffer (0.05 M, pH 8.0, containing 2 mM EDTA).

4.3 Results and Discussion

4.3.1 The Electroreduction of Disulfides at Metal Nanoparticle Electrodes

A survey was conducted to find the optimum conditions for preparing nanoAg/GC and nanoAu/GC electrodes for the electroreduction of cystine and 2-HED. This involved controlling the amount of metal deposited on the glassy carbon substrate through deposition time and examining the effect on disulfide reduction. Cyclic voltammograms for the reduction of cystine and 2-HED were evaluated by measuring the peak potentials and peak current densities (based on geometric area). A less negative peak potential indicates faster electrode kinetics and suggests that these potentials could be used for a large-scale reduction process. This is advantageous for industrial applications as it represents an energy saving. A high peak current density is also desirable but is less important than the peak potential. Current density issues can be addressed using large surface area carbon supports.

4.3.1.1 Electrodeposition of Silver Nanoparticles onto Glassy Carbon for the Electroreduction of Cystine

Silver was deposited onto the glassy carbon substrate initially using linear sweep voltammetry (LSV). The effect of scan rate (10, 20, 50, 80, 100 mV s^{-1}) on silver deposition was investigated along with the performance of these electrodes for the electroreduction of cystine (Table 4.3). The amount of silver deposited onto the glassy carbon substrate increased as the scan rate decreased. At slow scan rates the reaction time increases and therefore, silver deposition occurs over a longer period of time. The increasing amount of silver on the nanoAg/GC electrode was associated with a shift to less negative potentials for the cleavage of the disulfide bond in cystine (-1.20 to -1.15 V as scan rate decreased from 100 to 10 mV s^{-1}) and an increase in current density (22 to 62 μA cm^{-2} as scan rate decreased from 100 and 10 mV s^{-1}). The nanoAg/GC electrode prepared using a scan rate of 10 mV s^{-1} showed similar activity towards cystine reduction to that observed at solid silver (E_{pc} = -1.15 V, j_{pc} = 64 μA cm^{-2}). These results suggest that by increasing the amount of silver electrodeposited on the glassy carbon substrate further, the activity of nanoAg/GC

electrodes for cystine reduction may be enhanced relative to that obtainable using a solid silver electrode.

Table 4.3. The effect of scan rate on the fabrication of nanoAu/GC electrodes for the electroreduction of cystine. Silver was deposited onto glassy carbon substrates by reducing 1 mM $AgNO_3$ using linear sweep voltammetry to scan between 0.20 and -1.20 V. Cyclic voltammograms of 1 mM cystine in KH_2PO_4 buffer (pH 8.0) were obtained at the nanoAg/GC electrodes by recording one scan between -0.40 and -1.20 V or -1.30 V (υ = 50 mV s^{-1}).

Scan rate (mV s^{-1})[a]	**Geometric area of the electrode (cm^2)**	**Amount of Ag deposited onto GC (mol cm^{-2})**[b]	**Cyclic voltammetry data for the electroreduction of cystine**		
			E_{pc} **(V)**	i_{pc} **(μA)**	j_{pc} **(μA cm^{-2})**[c]
100	0.07	1.48×10^{-8}	-1.20	1.54	22
80	0.07	1.54×10^{-8}	-1.18	2.69	38
50	0.07	2.01×10^{-8}	-1.18	2.73	38
20	0.07	2.92×10^{-8}	-1.16	2.92	41
10	0.07	3.99×10^{-8}	-1.15	4.41	62
Solid Ag	0.025	-	-1.15	1.60	64

[a] Scan rate for the deposition of silver onto glassy carbon using LSV.

[b] Determined from the charge passed during silver deposition.

[c] Based on the geometric area of the electrode.

In order to improve the reaction kinetics for cystine reduction at nanoAg/GC electrodes, longer deposition times were investigated for the electrodeposition of silver particles onto glassy carbon. NanoAg/GC electrodes were prepared by applying a deposition potential of -0.60 V for between 60 and 900 seconds, after which time the response of the electrode towards cystine reduction was measured (Table 4.4).

Table 4.4. The effect of silver deposition time on the fabrication of nanoAg/GC electrodes for the electroreduction of cystine. Silver was deposited onto glassy carbon substrates from 1 mM $AgNO_3$ by applying a potential of -0.60 V for between 60 and 900 seconds. Cyclic voltammograms of 1 mM cystine in KH_2PO_4 buffer (pH 8.0) were obtained at the nanoAg/GC electrodes by recording one scan between -0.40 and -1.30 V (υ = 50 mV s^{-1}).

Deposition time (sec)[a]	**Geometric area of the electrode (cm^2)**	**Amount of Ag deposited onto GC (mol cm^{-2})**[b]	**Cyclic voltammetry data for the electroreduction of cystine**		
			E_{pc} (V)	i_{pc} (µA)	j_{pc} (µA cm^{-2})[c]
60	0.07	6.47×10^{-8}	-1.14	6.39	90
120	0.07	9.64×10^{-8}	-1.14	6.13	86
180	0.07	1.35×10^{-7}	-1.20	5.81	82
240	0.07	1.94×10^{-7}	-1.14	7.57	107
300	0.07	3.09×10^{-7}	-1.10	8.90	125
600	0.07	4.28×10^{-7}	-1.10	7.33	103
900	0.07	8.71×10^{-7}	-1.10	7.14	100
Solid Ag	0.025	-	-1.15	1.60	64

[a] E_{dep} = -0.60 V.

[b] Determined from the charge passed when the silver is stripped off the surface.

[c] Based on the geometric area of the electrode.

The amount of silver deposited onto the glassy carbon increased linearly with deposition time. The most favourable peak potential for cleavage of the disulfide bond in cystine occurred for deposition times greater than 300 seconds and was observed at -1.10 V. This potential was 50 mV less negative than the cystine reduction potential observed at the solid silver electrode (-1.15 V). At deposition times less than 300 seconds, the peak potential (-1.14 V) was comparable to that observed at solid silver. The longer deposition times improved the sensitivity of the nanoAg/GC electrodes towards cystine reduction compared to solid silver. This is reflected by the increase in current density observed for the nanoAg/GC electrodes. In general, the current density increases with increasing silver particle deposition time until it reaches a maximum at the deposition time of

300 seconds (125 μA cm^{-2}). At longer deposition times the current density decreased. In the early stages of silver deposition, hemispherical mass-transfer is present leading to the growth of hemispherical 3-D silver deposits on the glassy carbon substrate.[8,9] As the deposition time increases the diffusion fields overlap and the mass-transfer becomes linear.[10] It is proposed that the silver deposits grow upwards at long deposition times instead of continuing to form hemispherical clusters on the glassy carbon surface. The change in the morphology of the surface as a result of this process would lead to a decrease in active surface area because of diffusion limitations towards the base of the deposits. The growth mechanism for silver electrochemically deposited onto carbon substrates is described further in the following sections. Considering the current density data reported in Table 4.4, although the overall trend is clear, there is some scatter in the data at short deposition times. The variation observed for current density between experiments is most likely caused by differences in the initial glassy carbon surface after polishing with alumina prior to silver particle deposition. A similar observation has been made by other workers who found that the number of electrochemically deposited gold nanoparticles depended strongly on the preparation of the glassy carbon surface.[34]

Reproducibility of NanoAg/GC Electrode Preparation

The optimum deposition time for preparing nanoAg/GC electrodes for the electroreduction of cystine is 300 seconds (Table 4.4). This electrode showed the greatest current density and a favourable shift in the peak potential for formation of cysteine. The ability to reproducibly fabricate nanoAg/GC electrodes is an important factor if these electrodes are to be used in an industrial process such as the application proposed in this project, *i.e.*, electrochemical regeneration of the thiol setting agent during wool setting. Over time the electrode may become fouled and activity towards disulfide reduction may be decreased, requiring a new nanoAg/GC electrode to be implemented. Linear sweep voltammetry and controlled-potential electrolysis methods used for the electrodeposition of silver particles onto glassy carbon led to different amounts of silver being deposited under the same solution conditions. In initial controlled-potential electrolysis experiments, the charge was not recorded during deposition of silver at -0.60 V. Instead, the amount of silver deposited was determined by measuring the charge associated with the stripping of silver. This method could be unreliable if silver is lost from the surface during the electroreduction of cystine. Therefore, to accurately determine the amount of silver deposited onto glassy carbon the charge was

recorded during the deposition process. Silver was deposited from 1 mM $AgNO_3$ containing 0.1 M KNO_3 by stepping the potential from 0.20 to -0.60 V over 300 seconds during which time the charge was recorded. The experiment was carried out three times and the amount of silver deposited onto glassy carbon showed excellent reproducibility between experiments. The charge recorded during the deposition process (Q = 2.00 ± 0.07 mC) corresponded to (2.98 ± 0.01) × 10^{-7} mol cm^{-2} (n = 3) of silver on the glassy carbon surface. This value has been blank corrected by repeating the experiment using a bare glassy carbon electrode in 0.1 M KNO_3. It is noted that this value agrees well with that obtained by stripping silver (300 seconds value, Table 4.4), however, the later value was not blank corrected.

The cyclic voltammogram of 1 mM cystine in KH_2PO_4 buffer (pH 8.0) at a nanoAg/GC electrode prepared using the optimum deposition time of 300 seconds is shown in Figure 4.5 (a). For comparison, the response of a solid silver electrode towards the electroreduction of 1 mM cystine is shown in Figure 4.5 (b). The shapes of the cyclic voltammograms and the peak currents recorded at these electrodes are very similar. The small shift in peak potential for the direct reduction of cystine is observed for the nanoAg/GC electrode (-1.10 V) compared to the solid silver electrode (-1.15 V). An additional reduction peak is observed at -0.88 V at the solid silver electrode. This peak is attributed to the reduction of surface-bound silver (I) cysteine thiolate. It is presumed that cystine is also adsorbed at the silver particles to give silver (I) cysteine thiolate, however, due to the increased background capacitance recorded at the nanoAg/GC electrode the reduction of this species is not observed.

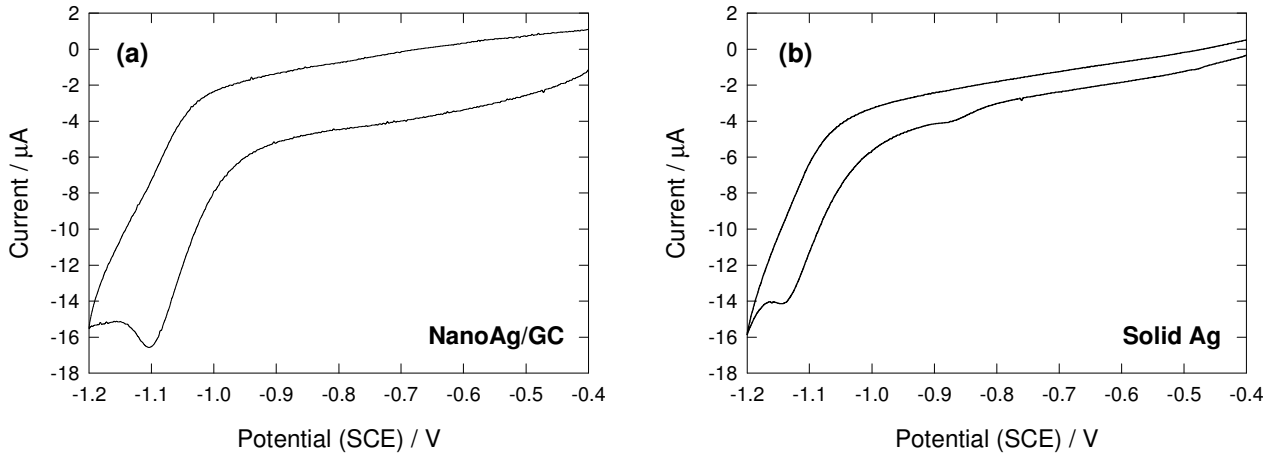

Figure 4.5. Cyclic voltammograms of 1 mM cystine in KH_2PO_4 buffer (8.0) at (a) nanoAg/GC and (b) solid silver electrodes (υ = 50 mV s^{-1}). Supporting electrolyte for cyclic voltammetry was 0.1 M $NaClO_4$. Silver was deposited onto the glassy carbon substrate from 1 mM $AgNO_3$ by stepping the potential from 0.20 to -0.60 V over 300 seconds.

Characterisation of Silver Nanoparticles Electrochemically Deposited onto Glassy Carbon

Scanning electron microscopy was used to examine the size and density of the silver particles deposited onto the glassy carbon surface using the optimum conditions found for fabricating nanoAg/GC electrodes with respect to the electroreduction of cystine. Figure 4.6 shows that the silver forms deposits on the glassy carbon surface that have an average diameter of 53 nm and are separated by areas of bare glassy carbon. This discrete particle island growth is consistent with reports in the literature regarding the deposition of silver onto HOPG (see Section 4.1.2.1).[8,9]

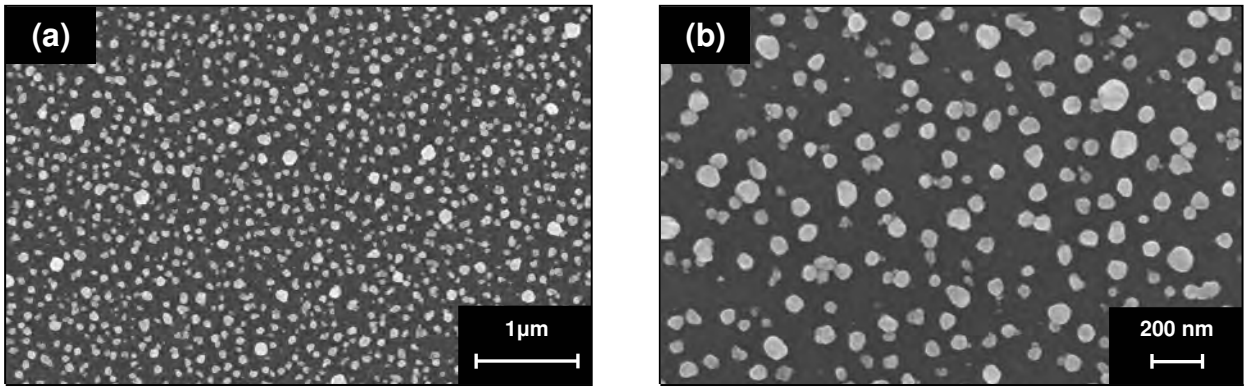

Figure 4.6. SEM images of silver particles deposited onto a glassy carbon substrate. Electrodeposition of silver particles was performed by reducing a 1 mM $AgNO_3$ solution using the optimised deposition conditions; potential was stepped from 0.20 to -0.60 V over 300 seconds.

Further insight into the morphology of the silver-decorated glassy carbon surface was gained by assuming that the total mass of silver deposited formed hemispherical particles. This allowed the fractional surface coverage of glassy carbon occupied by metal deposits to be estimated. An expression for calculating the fractional surface coverage (θ) was derived from equations 4.1 to 4.8, where Q_m is the cumulative charge passed during metal deposition, n is the number of electrons required to reduce the metal, F is the Faraday constant, M_m is the molar mass of metal, r is the average radius of a hemispherical metal particle and ρ_m is the density of the metal:

$$\text{Amount of metal deposited, } N_m = \frac{Q_m}{nF} \tag{4.1}$$

$$\text{Total mass of metal deposited, } m_T = N_m M_m \tag{4.2}$$

Assuming hemispherical diffusion during metal deposition:

$$\text{Average particle volume, } V_h = \frac{2\pi r^3}{3} \tag{4.3}$$

$$\text{Mass of a single particle, } m_p = V_h \rho_m \tag{4.4}$$

Number of particles, $X = \frac{m_T}{m_p}$ (4.5)

Surface area (of GC) occupied by a single particle, $A_p = \pi r^2$ (4.6)

Total area (of GC) occupied by particles, $A_T = XA_p$ (4.7)

Geometric area of glassy carbon, $A_{GC} = 0.31\,cm^2$

Fractional surface coverage (of GC) occupied by particles, $\theta = \frac{A_T}{A_{GC}}$ (4.8)

An overall expression for the fractional surface coverage of glassy carbon occupied by metal particles, as determined from the total mass of metal deposited, is given in equation 4.9:

Fractional surface coverage (of GC) occupied by particles, $\theta = \frac{3Q_m M_m}{2nFr\rho_m A_{GC}}$ (4.9)

From this expression, the fractional surface coverage of glassy carbon occupied by silver particles was calculated to be 0.55 using the following values; Q_{silver} = 2.89 × 10^{-3} C, M_{silver} = 108 g mol^{-1}, n = 1, F = 96485 C mol^{-1}, r = 26.5 nm, ρ_{silver} = 10.5 g cm^{-3} and A_{GC} = 0.31 cm^2. This surface coverage represents 55 % of the glassy carbon substrate covered by silver deposits. For comparison, the fractional surface coverage of glassy carbon occupied by hemispherical silver deposits was estimated from the SEM image itself (Figure 4.6 (b)) using equation 4.10 where X_{SEM} represents the total number of silver deposits observed in the image and $A_{GC/SEM}$ is the area of glassy carbon in the SEM image:

Fractional surface coverage (of GC) occupied by particles, $\theta = \frac{A_p X_{SEM}}{A_{GC/SEM}}$ (4.10)

The fractional surface coverage of glassy carbon occupied by silver deposits, determined from Figure 4.6 (b), was calculated to be 0.17 using the following values; r = 26.5 nm, X_{SEM} = 195 and $A_{GC/SEM}$ = 2.58 $\times 10^{-8}$ cm^2. This fractional surface coverage of silver particles is lower than that determined from the total mass of metal deposited (θ = 0.55), hence, the assumption of hemispherical particles is clearly incorrect and the deposits must elongate as they grow and adopt a pillar-like structure.

The growth of tall islands is consistent with the reported nucleation and growth mechanism of silver particles on HOPG. The early stages of the electrodeposition of silver onto HOPG occurs *via* the Volmer-Weber island growth mechanism as described in Section 4.1.2.1.[8,9,16,17] The nucleation sites of glassy carbon have been reported to have approximately the same activity as those on edge plane HOPG,[8,35] and therefore, the same nucleation and growth mechanism reported for HOPG is assumed for the electrodeposition of silver onto glassy carbon in this work. The areas of bare glassy carbon observed between the silver deposits are attributed to the development of zones of reduced nucleation around stable nuclei where hemispherical mass-transfer gives way to linear mass-transfer to an effectively planar surface (see Figure 4.2).[10] Once the reduced nucleation zones cover the whole surface the process of nucleation stops, hence, new silver deposits cannot be formed and already existing silver deposits are expected to grow upwards instead of retaining the shape of a hemisphere. The morphology observed here is consistent with the work of Sonnenfeld *et al.* who showed using scanning tunneling microscopy (STM) that after depositing 300 monolayers of silver onto HOPG the metal was still observed to form islands tens of microns in diameter on the substrate which were separated by bare graphite regions of a similar size.[9]

4.3.1.2 Electrodeposition of Gold Nanoparticles onto Glassy Carbon for the Electroreduction of Cystine

To fabricate nanoAu/GC electrodes for the electroreduction of cystine, gold nanoparticles were electrochemically deposited onto glassy carbon substrates using methods established in the literature.[18] The activity of these electrodes towards disulfide reduction was studied as a function of gold nanoparticle deposition time (Table 4.5). As the deposition time increased, the amount of gold deposited onto the glassy carbon substrate increased. This was associated with a shift to less negative potentials for the reduction of cystine (-0.93 to -0.80 V as the deposition time increased from 5 to 900 seconds) and a general trend of increasing current density. However, a decrease in current density for the electroreduction of cystine is observed between nanoAu/GC electrodes fabricated using deposition times of 240 and 300 seconds. SEM images shown in the next section for a nanoAu/GC electrode prepared using a deposition time of 600 seconds reveal that the gold particles are fused together and form clusters on the glassy carbon surface. A similar surface morphology has been reported by El-Deab and co-workers for gold nanoparticles electrochemically deposited onto glassy carbon substrates at deposition times greater than 300 seconds.[18] It is expected that in the present work fusing of the gold particles at deposition times greater than 240 seconds leads to a decrease in active electrode surface area. The presence of gold nanoparticles did not increase the sensitivity of the metal towards the electroreduction of cystine as the greatest current density was observed at the solid gold electrode (88 μA cm^{-2}). However, a favourable cyclic voltammetric peak potential was achieved at the nanoAu/GC electrode prepared using a deposition time of 600 seconds (-0.80 V). The electrodeposited gold nanoparticle electrode is advantageous for the fabrication of industrial electrodes as less gold is used compared to expensive large-scale solid gold electrodes and these electrodes can be easily manufactured on an industrial scale without requiring the expensive and complicated instrumentation needed for lithography techniques or other deposition methods such as vacuum evaporation or sputtering. There is no added advantage of depositing for longer times as no further shift in peak potential is observed and current density issues can be overcome by employing a large surface area carbon electrode material.

Table 4.5. The effect of gold deposition time on the fabrication of nanoAu/GC electrodes for the electroreduction of cystine. Gold was electrodeposited onto glassy carbon substrates from 1 mM $KAuCl_4$ by stepping the potential from 1.10 to 0 V for deposition times between 5 and 900 seconds. Cyclic voltammograms of 1 mM cystine in KH_2PO_4 buffer (pH 8.0) were obtained at the nanoAu/GC electrodes by recording one scan between -0.40 and -1.20 V (υ = 50 mV s^{-1}). Errors are reported for experiments that were replicated three times and correspond to one standard deviation. All other experiments were only carried out once.

Deposition time (sec)	**Geometric area of the electrode (cm^2)**	**Amount of Au deposited onto GC (mol cm^{-2})**[a]	**Cyclic voltammetry data for the electroreduction of cystine**		
			E_{pc} **(V)**	i_{pc} **(μA)**	j_{pc} **(μA cm^{-2})**[b]
5	0.07	$(1.02 \pm 0.09) \times 10^{-8}$	-0.93 ± 0.031	1.59 ± 0.3	22 ± 4
10	0.07	1.46×10^{-8}	-0.89	2.14	30
20	0.07	2.02×10^{-8}	-0.89	1.87	26
40	0.07	3.04×10^{-8}	-0.84	3.22	45
60	0.07	4.03×10^{-8}	-0.85	3.93	55
120	0.07	7.79×10^{-8}	-0.82	4.59	65
180	0.07	9.66×10^{-8}	-0.82	4.58	65
240	0.07	1.28×10^{-7}	-0.82	5.00	70
300	0.07	$(2.00 \pm 0.68) \times 10^{-7}$	-0.82 ± 0.015	2.40 ± 0.86	34 ± 12
600	0.07	$(3.60 \pm 0.86) \times 10^{-7}$	-0.80 ± 0.012	3.33 ± 1.69	47 ± 24
900	0.07	$(4.84 \pm 0.15) \times 10^{-7}$	-0.80 ± 0.006	3.96 ± 1.30	56 ± 18
Solid Au	0.008	-	-0.92	0.70	88

[a] Determined from the charge passed during gold deposition.

[b] Based on the geometric area of the electrode.

Characterisation of Gold Nanoparticles Electrochemically Deposited onto Glassy Carbon

SEM was used to examine the size and density of gold particles deposited onto glassy carbon using the optimum deposition time of 600 seconds (Figure 4.7). The SEM images obtained are consistent with those reported by El-Deab *et al.*[18] The gold deposits are not homogenously distributed on the glassy carbon surface, instead, fusing of individual gold particles to form clusters is observed. The clusters vary in shape and size with an average diameter of approximately 60 nm. Small gold deposits with diameters ranging from 30-40 nm are also present. Comparison of the SEM images for nanoAu/GC and nanoAg/GC electrodes prepared using the optimum conditions (Figures 4.6 and 4.7) shows that the density of the gold deposits is greater than that of the silver deposits.

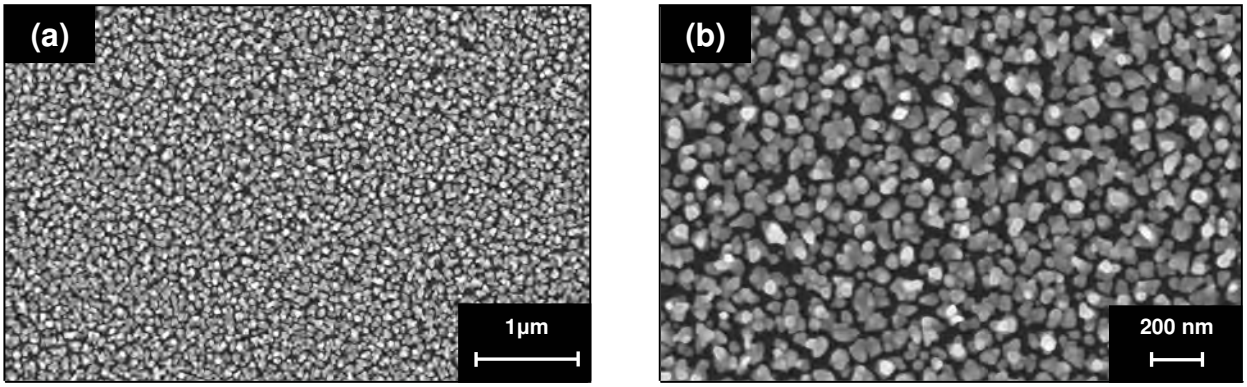

Figure 4.7. SEM images of gold particles deposited onto a glassy carbon substrate. Electrodeposition of gold particles was performed by reducing a 1 mM $KAuCl_4$ solution using the optimised deposition conditions; potential was stepped from 1.10 to 0 V over 600 seconds.

As for the nanoAg/GC electrode, a calculation was carried out to determine whether the gold deposits could be described as hemispherical. Using equation 4.9, the fractional surface coverage of the glassy carbon substrate occupied by the gold deposits was determined from the total mass of metal deposited. Due to the fusing of individual gold particles observed by SEM it was difficult to determine the particle size, however, an average radius (*r)* of 30 nm was assumed for the hemispherical gold clusters. The fractional surface coverage of glassy carbon occupied by the gold particles was calculated to be 0.85 using the following values; $Q_{gold} = 1.25 \times 10^{-2}$ C,

M_{gold} = 197 g mol^{-1}, n = 3, F = 96485 C mol^{-1}, r = 30 nm, ρ_{gold} = 19.3 g cm^{-3} and A_{GC} = 0.31 cm^2. This surface coverage represents 85 % of the glassy carbon substrate covered by gold deposits. Due to the large range of cluster sizes, it is difficult to estimate the fractional surface coverage of glassy carbon occupied by the gold deposits from the SEM images shown in Figure 4.7. However, it appears somewhat less than 85 % and therefore, some elongation of the gold deposits may occur during particle growth as described for the growth of silver deposits (see Section 4.3.1.1).

The cyclic voltammogram of 1 mM cystine in KH_2PO_4 buffer (pH 8.0) at a nanoAu/GC electrode prepared using the optimum deposition time of 600 seconds is shown in Figure 4.8 (a). A cyclic voltammogram for the electroreduction of 1 mM cystine at a solid gold electrode is shown for comparison (Figure 4.8 (b)). The shape of the cyclic voltammograms recorded at these electrodes is very similar, hence, the mechanism for reduction of cystine at the nanoAu/GC electrode was assumed to be analogous to that described for disulfide reduction at a solid gold electrode (see Chapter 3). The reduction of cystine *via* the formation of surface-bound gold (I) cysteine thiolate has shifted 12 mV less negative at the nanoAu/GC electrode (-0.80 V) compared to the solid gold electrode (-0.92 V). The shoulder observed at the solvent limit for both electrodes (~ -1.15 V) is likely to be due to the direct reduction of cystine.

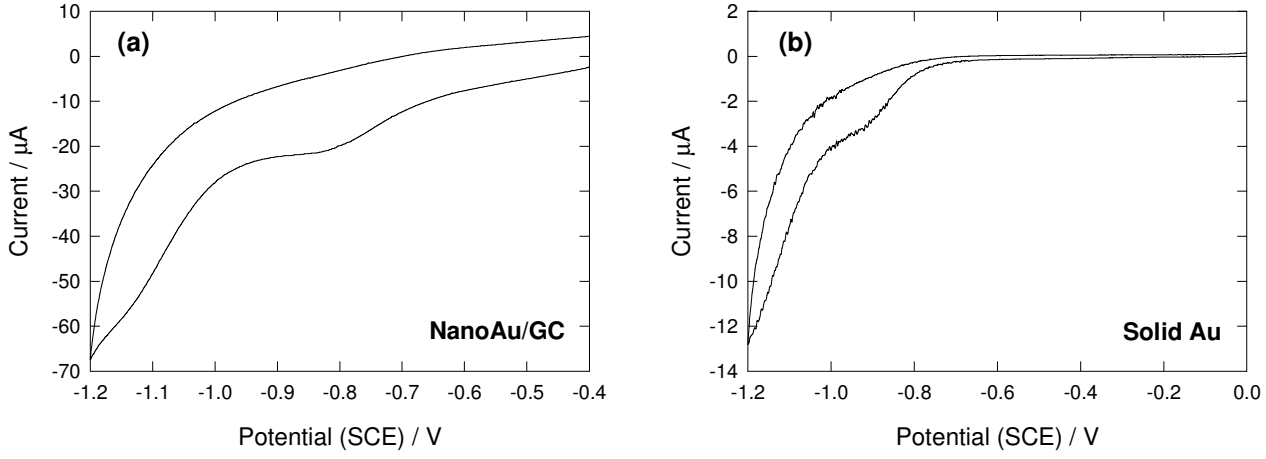

Figure 4.8. Cyclic voltammograms of 1 mM cystine in KH_2PO_4 buffer (pH 8.0) at (a) nanoAu/GC electrode and (b) solid gold electrodes (υ = 50 mV s^{-1}). Supporting electrolyte for cyclic voltammetry was 0.1 M KNO_3. Gold was deposited onto the glassy carbon substrate from 1 mM $KAuCl_4$ by stepping the potential from 1.10 to 0 V over 600 seconds.

Using the nanoAu/GC electrode, cyclic voltammograms were recorded at a range of scan rates (10 to 100 mV s^{-1}) to confirm the reaction mechanism for the electroreduction of cystine at the nanoAu/GC electrode. At the solid gold electrode reduction of cystine occurs *via* formation of surface-bound gold (I) cysteine thiolate and the thiolate is subsequently reduced off the electrode surface to yield the corresponding thiol in solution. At the nanoAu/GC electrode, a plot of peak current *versus* scan rate did not show the expected linear relationship for an adsorption-controlled mechanism. This is not surprising due to the structure of the nanoAu/GC electrode and the complex mechanism of cystine adsorption and reduction observed at a solid gold electrode. It was also noted that the plot of peak current versus $\upsilon^{1/2}$ was non-linear, therefore, the reduction of cystine at nanoAu/GC electrodes does not occur solely *via* a diffusion-controlled mechanism.

4.3.1.3 Electrodeposition of Metal Nanoparticles onto Glassy Carbon for the Electroreduction of 2-Hydroxyethyl Disulfide

The electrochemical reduction of 2-HED was also studied at nanoAg/GC and nanoAu/GC electrodes fabricated using the optimised deposition conditions described for the reduction of cystine. At the solid metal electrodes, the peak potential for 2-HED and cystine occur at similar potentials suggesting that the energy required to cleave the disulfide bond is similar for both compounds (see Chapter 3) Therefore, it was proposed that the deposition conditions for fabricating nanoAg/GC and nanoAu/GC electrodes which gave the most promising results for cystine reduction would also be optimised for the electrochemical reduction of 2-HED.

The electroreduction of 1 mM 2-HED at nanoAg/GC and nanoAu/GC electrodes is compared with the respective solid metal electrodes in Table 4.6. The shape of the cyclic voltammograms recorded at the metal nanoparticle electrodes were similar to those recorded at the solid metal electrodes (refer to Chapter 3, Section 3.3.2.2). A favourable shift towards less negative potentials was observed for disulfide reduction at the nanoAu/GC electrode (-0.90 V) compared to solid gold (-1.00 V), whereas at the nanoAg/GC electrode the peak potential shifted to more negative potentials (-0.99 V) compared to solid silver (-0.96 V). For both metals, the current density was greater at the solid electrodes. However, the shift in peak potential is the most important factor, therefore, the nanoAu/GC electrode is the most promising electrode for the electrochemical

reduction of 2-HED. At this electrode, the cleavage of the S–S bond occurs at the least negative potential of -0.90 V leading to a more energy efficient process.

Table 4.6. Comparison of the electroreduction of 1 mM 2-HED at nanoAg/GC, nanoAu/GC and solid silver and gold electrodes. Cyclic voltammograms of 1 mM 2-HED in KH_2PO_4 buffer (pH 8.0) were obtained at nanoAg/GC, solid silver and solid gold electrodes by recording one scan between -0.40 and -1.20 V and at the nanoAu/GC electrode by scanning between -0.40 and -1.30 V (υ = 50 mV s^{-1}).

Electrode	**Geometric area of the electrode (cm^2)**	**Amount of Au deposited onto GC (mol cm^{-2})**[c]	**Cyclic voltammetry data for the electroreduction of 2-HED**		
			E_{pc} **(V)**	i_{pc} **(μA)**	j_{pc} **(μA cm^{-2})**[d]
NanoAg/GC[a]	0.07	1.58×10^{-7}	-0.99	7.30	103
Solid Ag	0.025	-	-0.96	5.44	218
NanoAu/GC[b]	0.07	2.64×10^{-7}	-0.90	1.18	17
Solid Au	0.008	-	-1.00	0.30	38

[a] Silver was deposited onto glassy carbon from 1 mM $AgNO_3$ by stepping the potential from 0.20 to -0.60 V over 300s.

[b] Gold was deposited onto glassy carbon from 1 mM $KAuCl_4$ by stepping the potential from 1.10 to 0 V over 600s.

[c] Determined from the charge passed during metal deposition.

[d] Based on the geometric area of the electrode.

When the concentration of 2-HED was increased to 4 mM a second reduction peak appeared at -1.26 and -1.13 V for the nanoAg/GC and nanoAu/GC electrodes respectively. This observation was also made at the solid metal electrodes and is proposed to be due to the reduction of 2-hydroxyethanesulfinic acid (see Chapter 3, Section 3.3.2.2). The additional peaks occur at similar potentials for the metal nanoparticle and solid metal electrodes hence, the presence of metal nanoparticles does not significantly increase the rate of reduction of this species.

4.3.1.4 Comparison of Metal Nanoparticle Electrodes for the Electroreduction of Cystine and 2-Hydroxyethyl Disulfide

The results obtained for the electroreduction of cystine and 2-HED at nanoAg/GC and nanoAu/GC electrodes prepared using optimised conditions are summarised in Table 4.7. The cyclic voltammetry data obtained at the respective solid metal electrodes is included for comparison.

Table 4.7. Summary of cyclic voltammetry data for the electroreduction of cystine and 2-HED at metal nanoparticle electrodes compared to the corresponding solid metal electrodes. Cyclic voltammograms of cystine and 2-HED (1 mM) in KH_2PO_4 buffer (pH 8.0) were obtained by recording one scan between -0.40 and -1.20 V or -1.30 V (υ = 50 mV s^{-1}).

Electrode	**Cystine**		**2-HED**	
	E_{pc} **(V)**	j_{pc} **(μA cm^{-2})**[c]	E_{pc} **(V)**	j_{pc} **(μA cm^{-2})**[c]
NanoAg/GC[a]	-1.10	67	-0.99	103
Solid Ag	-1.15	64	-0.96	218
NanoAu/GC[b]	-0.80	47	-0.90	17
Solid Au	-0.92	88	-1.00	38

[a] Silver was deposited onto glassy carbon from 1 mM $AgNO_3$ by stepping the potential from 0.20 to -0.60 V over 300s.

[b] Gold was deposited onto glassy carbon from 1 mM $KAuCl_4$ by stepping the potential from 1.10 to 0 V over 600s.

[c] Based on the geometric area of the electrode.

In general, the presence of metal nanoparticles supported on glassy carbon substrates shifted the peak potential for disulfide reduction to less negative potentials compared to the respective solid metal. With the exception of cystine reduction at a nanoAg/GC electrode, the metal nanoparticle electrodes gave lower current densities than the solid metals for disulfide reduction. However, the shift in peak potential is most important and hence, the most promising electrode for the electroreduction of cystine and 2-HED is nanoAu/GC. Although this electrode exhibited the lowest current density overall, the greatest shift in the peak potential for the cleavage of the S–S bond was observed. The current density issues observed in this study will be addressed in Section 4.3.2

through the use of large surface area carbon fabric to support the electrochemical deposition of gold nanoparticles.

Of the disulfide compounds studied, the nanoAu/GC electrode performed best for the electroreduction of cystine. The peak potential for this reaction (-0.80 V) was 10 mV less negative than that for 2-HED (-0.90 V) demonstrating that the reduction of cystine is energetically more favourable.

4.3.2 Bulk Electrolysis of Cystine at Gold Deposited onto Carbon Fabric

A main focus of this research is to use electrochemical techniques to regenerate the thiol setting agent during the process of wool setting. In order to achieve this efficiently, the bulk solution needs to undergo complete electrochemical conversion. In developmental work, the electroreduction of cystine has been examined using cyclic voltammetry. This technique uses a small ratio of electrode area to solution volume allowing experiments to be carried out over long time periods without appreciable changes in the concentration of reactant and products in the bulk solution. In contrast, bulk electrolysis methods are characterised by large electrode area to solution volume ratios and lead to the electroactive species being completely electrolysed within a much shorter time period. In this work, bulk electrolysis methods have been used to convert cystine to cysteine by reduction at a nanoAu/CF electrode. For these experiments, the carbon fabric electrode described in the Experimental Methods Section was used to support immobilised gold deposits. The electrode was double-sided and had a geometric area of 0.95 cm^2 per side.

Controlled-potential electrolysis was used to maintain a constant potential at the nanoAu/CF electrode during the electroreduction of 1 mM cystine in KH_2PO_4 buffer (pH 8.0). For these experiments, the nanoAu/CF electrode was fabricated using chronoamperometry to reduce a gold salt solution at a carbon fabric working electrode (1 mM $KAuCl_4$ in 0.5 M H_2SO_4, 20 mL) by stepping the potential from 1.10 to -0.40 V for 30 minutes. At the nanoAu/GC electrode used in developmental work (Section 4.3.1.2) the peak potential for reduction of the S–S bond in cystine was observed at -0.80 V; however, large surface area electrodes require a greater overpotential. A potential of -1.00 V was applied to the nanoAu/CF electrode for initial bulk electrolysis studies. The cystine solution (1 mM, 20 mL) contained 2×10^{-5} mol of disulfide. The charge required to

quantitatively reduce cystine (4 C) was determined using equation 4.11. This expression is derived from Faraday's laws,

$$Q = nN_jF \qquad (4.11)$$

where Q is the charge, n is the number of electrons required to reduce cystine ($n = 2$), N_j is the total amount of cystine and F is the Faraday constant. To decrease the electrolysis time, a charge of 2 C was used. This charge is sufficient to reduce 50 % of the cystine. After stopping the electrolysis the concentration of cysteine was determined using Ellman's assay. The results for the bulk electrolysis of cystine at a nanoAu/GC electrode compared with a bare carbon fabric electrode using these conditions are given in Table 4.8. Each experiment was carried out three times. Although there is scatter in the data it is clear that the presence of gold particles on the carbon fabric increases the rate of electroreduction of cystine to cysteine. At the nanoAu/CF electrode the average time taken to pass the required charge of 2 C was 67 ± 33 minutes, after which time 11.60 ± 5.40 % of the initial cystine concentration was converted to cysteine. In contrast, after bulk electrolysis of cystine was performed at a bare carbon fabric electrode for an average time of 105 ± 5 minutes, the charge passed was only 0.38 ± 0.10 C and the amount of cystine converted to cysteine was 0.77 ± 0.49 %. Note that the applied potential was -1.00 V using the nanoAu/CF electrode and -0.90 V using the bare carbon fabric electrode. As explained below (refer to Section 4.3.2.1), the highest yield of cysteine was achieved at the nanoAu/CF electrode by applying a potential of -0.90 V for approximately 105 minutes and hence, these conditions were used for the control experiment.

Table 4.8. Bulk electrolysis of cystine at nanoAu/CF and bare carbon fabric electrodes. The concentration and volume of cystine used for bulk electrolysis were 1 mM and 20 mL respectively.

Electrode	Run	*Q* (C)	Time (min)	[Cysteine] (mM)[c]	Conversion of cystine to cysteine (%)[d]
NanoAu/CF[a]	1	2.00	100	0.170	17.00
	2	2.00	52	0.095	9.50
	3	2.00	50	0.083	8.30
Bare carbon fabric[b]	1	0.31	105	0.002	0.20
	2	0.35	110	0.011	1.10
	3	0.48	105	0.010	1.00

[a] The potential applied during the bulk electrolysis of cystine was -1.00 V.

[b] The potential applied during the bulk electrolysis of cystine was -0.90 V.

[c] The concentration of cystine determined at the end of bulk electrolysis using Ellman's assay.

[d] Percentage conversion based on the theoretical maximum conversion of 50 %.

4.3.2.1 Optimisation of Bulk Electrolysis Conditions for the Electroreduction of Cystine

To improve the conversion of cystine to cysteine, a survey to investigate the effects of varying the potential applied during bulk electrolysis and the conditions for preparing nanoAu/CF electrodes was carried out. The standard conditions chosen for the electrochemical deposition of gold onto carbon fabric involved reducing $KAuCl_4$ (2 mM, 20 mL) salt solution by applying an overpotential of -0.40 V until a total charge of -2.5 C was passed. The amount of gold deposited using these conditions was 9.09 x 10^{-6} mol cm^2 (based on a total geometric electrode area of 0.95 cm^2 per side).

The Effect of Varying the Potential Applied During the Bulk Electrolysis of Cystine

The potential applied (E_{app}) during the bulk electrolysis of cystine was varied between -0.80 V and -1.20 V (Table 4.9). The greatest conversion of cystine to cysteine was achieved using a potential of -0.90 V, where 56 % of the disulfide was converted to thiol after a stoichiometric amount of charge (2 C) was passed. At more negative potentials, the required charge was passed more quickly and the amount of cysteine produced decreased. This is most likely due to hydrogen evolution competing with the electroreduction of cystine.

Table 4.9. The effect of varying the potential applied during the bulk electrolysis of cystine at a nanoAu/CF electrode. The reduction of cystine (1 mM, 20 mL) was carried out by applying the required potential until 2 C of charge was passed.

E_{app} (V)	[Cysteine] (mM)[a]	Conversion of cystine to cysteine (%)[b]	Time (min)[c]
-0.80	0.34	34	250
-0.90	0.56	56	112
-1.00	0.28	28	40
-1.10	0.17	17	30
-1.20	0.08	8	18

[a] The concentration of cysteine determined at the end of the bulk electrolysis using Ellman's assay.

[b] Percentage conversion based on the theoretical maximum conversion of 50 %.

[c] The time taken to pass 2 C of charge.

The lifetime of the nanoAu/CF electrode is an important consideration for use in an industrial process as it is beneficial if the electrode can be used repeatedly. Hence, once the optimum potential (-0.90 V) was determined for the bulk electrolysis of cystine, the ability of the electrode to be used for repeat reactions was studied (Table 4.10). The conversion of cystine to cysteine decreased upon the second use of the electrode (compare runs 1 and 2). Continued use of the electrode maintained the conversion of disulfide to thiol at approximately 50 % (runs 2-4). Upon

prolonged use, this level of disulfide conversion was maintained; however, the time taken to pass the required charge increased (runs 5-6). This is most likely due to fouling of the nanoAu/CF electrode.

Table 4.10. The response of a nanoAu/CF electrode used repeatedly for the electroreduction of cystine. For each electrolysis, cystine (1 mM, 20 mL) was reduced by applying a potential of -0.90 V until 2 C of charge was passed.

Run	[Cysteine] (mM)[a]	Conversion of cystine to cysteine (%)[b]	Time (min)[c]
1	0.71	71	85
2	0.51	51	100
3	0.52	52	93
4	0.51	51	95
5	0.47	47	145
6	0.61	61	135

[a] The concentration of cysteine determined at the end of the bulk electrolysis using Ellman's assay.

[b] Percentage conversion based on the theoretical maximum conversion of 50 %.

[c] The time taken to pass 2 C of charge.

The reproducibility of cystine reduction at nanoAu/CF electrodes was also investigated using newly prepared electrodes for each electrolysis. The conversion of disulfide to thiol was found to be 58 ± 3 % (n = 3) and the time taken for a stoichiometric amount of charge to be passed was 107 ± 4 min. Hence, due to the excellent reproducibility observed, nanoAu/CF electrodes are promising for the development of an industrial wool setting process whereby the thiol setting agent is regenerated by electrochemically reducing the cystine side-product formed (see Chapter 5).

The Effect of Varying the Conditions for Fabricating NanoAu/CF Electrodes on the Bulk Electrolysis of Cystine

The size and morphology of the gold deposits immobilised onto carbon fabric can be varied by altering the gold deposition conditions. Based on findings where nanoAu/GC electrodes were used for the reduction of oxygen,[18] it was expected that a specific particle size and morphology may be more reactive towards the electroreduction of cystine. In this study, the following parameters were altered in an effort to increase the conversion of cystine to cysteine during bulk electrolysis: (1) deposition potential, (2) the concentration of the gold salt solution and (3) the charge passed during deposition (Table 4.11).

A decrease in the amount of cysteine produced was observed when the gold deposition potential was moved away from the standard potential of -0.40 V and when the total charge passed for cystine reduction was increased to -5 C. All other modifications to the standard gold deposition conditions did not have any significant effect on the amount of cysteine produced.

Table 4.11. The effect of changing the conditions for fabricating nanoAu/CF electrodes used for the bulk electrolysis of cystine. Cystine (1 mM, 20 mL) was reduced by applying a potential of -0.90 V until 2 C of charge were passed.

Deposition of gold onto carbon fabric			Run	[Cysteine]	Conversion of cystine to cysteine	Time
E_{dep} (V)	Q (C)	[$KAuCl_4$] (mM)		(mM)[b]	(%)[c]	(min)[d]
-0.4[a]	-2.5[a]	2[a]	1	0.56	56	112
			2	0.62	62	104
-0.3	-2.5	2	1	0.44	44	110
			2	0.61	61	72
-0.5	-2.5	2	1	0.50	50	80
			2	0.33	33	95
-0.4	-0.5	2	1	0.63	63	160
			2	0.58	58	200
-0.4	-5	2	1	0.40	40	85
			2	0.54	54	60
-0.4	-2.5	0.5	1	0.60	60	100
			2	0.66	66	102

[a] Standard conditions used for the electrochemical deposition of gold onto carbon fabric.

[b] The concentration of cysteine determined at the end of the bulk electrolysis using Ellman's assay.

[c] Percentage conversion based on the theoretical maximum conversion of 50 %.

[d] The time to pass 2 C of charge.

The size and morphology of the gold deposits formed using the various gold deposition conditions described in Table 4.10 were characterised using SEM (Figure 4.9).

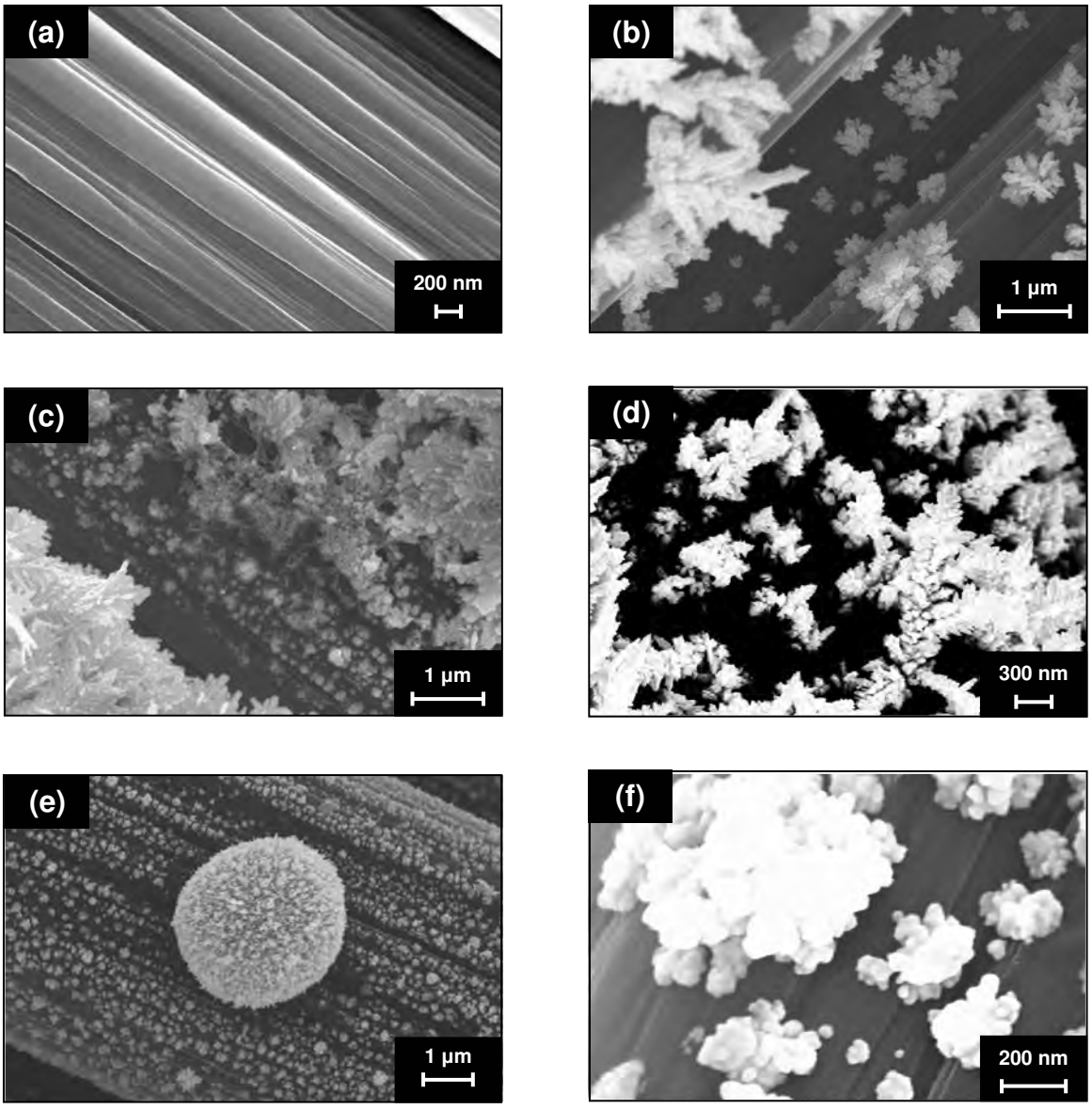

Figure 4.9. SEM images of nanoAu/CF electrodes prepared under different deposition conditions: bare carbon fabric (a), nanoAu/CF electrodes with gold particles deposited under (b) standard deposition conditions, (c) deposition potential = -0.3 V, (d) [$KAuCl_4$] = 0.5 mM, (e) deposition charge = -0.5 C and (f) deposition charge = -5 C.

The first image (Figure 4.9 (a)) shows the structure of bare carbon fabric. This material is woven from carbon fibers which have a width of approximately 6 μm. When gold was deposited onto the carbon fiber material using standard deposition conditions a mixture of particle sizes and morphologies was observed (b). Areas of dense gold deposition had large feathery deposits, whilst smaller spherical clusters (150 nm – 1 μm diameter) were observed in areas where less gold was deposited. In general, the gold deposition was observed to be denser around carbon fibers which were situated higher on the main bundle of the fiber material or those fibers which strayed from the bulk of the material. These carbon fibers act like microelectrodes and have a higher rate of mass transport which leads to more gold being deposited in these areas. Upon varying the gold deposition conditions used to prepare the nanoAu/CF electrodes, the same morphologies were observed for the gold deposits, however, the density of the gold particles on the carbon fabric surface changed. Gold deposited using conditions where either a less negative deposition potential was applied (c) or a greater deposition charge was employed (d) led to a greater density of gold on the carbon fabric substrate. Under these conditions the gold deposits had mostly a feathery morphology and a few large gold clusters were also observed varying in size from 1-2 μm in diameter. When either the concentration of the $KAuCl_4$ salt solution (e) or the deposition charge (f) was decreased the density of the gold deposited onto the carbon fabric surface decreased giving rise to the majority of the deposits consisting of small spherical clusters with a diameter of 20 nm – 1 μm. Larger clusters that were about 2.5 μm in diameter and had a perfect spherical shape were also randomly observed under these conditions (e).

The results of this study confirm that by changing the gold deposition conditions the morphology and size of the gold deposits on the nanoAu/CF electrodes can be varied. However, for our work it is difficult to comment on whether small gold clusters or large feathery deposits are best for facilitating the electroreduction of cystine. All the electrodes prepared had a mixture of particle sizes and morphologies and did not significantly influence the efficiency of the reduction of cystine during electrolysis to give the corresponding thiol.

4.3.2.2 Investigation of Side Reactions Occurring During the Bulk Electrolysis of Cystine

A problem encountered with this work relates to incomplete conversion of cystine to cysteine during bulk electrolysis at a nanoAu/CF electrode. The efficiency of this reaction can be defined by equation 4.12,

$$\text{Conversion Efficiency} = \frac{\text{Final [cysteine]}}{\text{Maximum theoretical [cysteine]}} \times \frac{100}{1} \qquad (4.12)$$

where the terms 'final [cysteine]' respresents the cysteine concentration in the final electrolysis solution as determined by Ellman's assay and 'maximum theoretical [cysteine]' is the maximum concentration of cysteine that can be produced from the electroreduction of cystine. The maximum theoretical efficiency is 100 %; however, in our work the greatest efficiency achieved for the electroreduction of cystine to cysteine is 58 ± 3 %.

Reduction of water to give hydrogen is a possible side reaction that decreases the efficiency of the electrolysis. The reduction of cystine at the nanoAu/CF electrode occurs at a potential near where hydrogen evolution occurs. To determine if hydrogen evolution was having an impact on the electroreduction of cystine, the electrolysis was carried out at pH 8.0 in the absence of disulfide. The average charge passed during this experiment was 1.6 ± 0.2 C after an electrolysis time of 105 minutes and was comparable to the 2 C passed for cystine reduction. This result confirms that hydrogen evolution can occur under these conditions. However, hydrogen evolution must occur at a much slower rate during the electroreduction of cystine as 58 ± 3 % of cysteine is produced after passing 2 C of charge (based on the theoretical maximum conversion of 50 % for the electroreduction of cystine to give cysteine after passing 2 C of charge). Therefore, in the presence of cystine, 1.6 C of charge cannot be attributed solely to hydrogen evolution. It seems likely that hydrogen evolution is a competing reaction but its importance was not investigated further.

Another possible reaction accounting for the incomplete conversion of cystine to cysteine is re-oxidation of cysteine as it forms. Under basic conditions in the presence of oxygen, thiols readily oxidise to the corresponding sulfonic acid or disulfide (Scheme 4.2).[31,36,37]

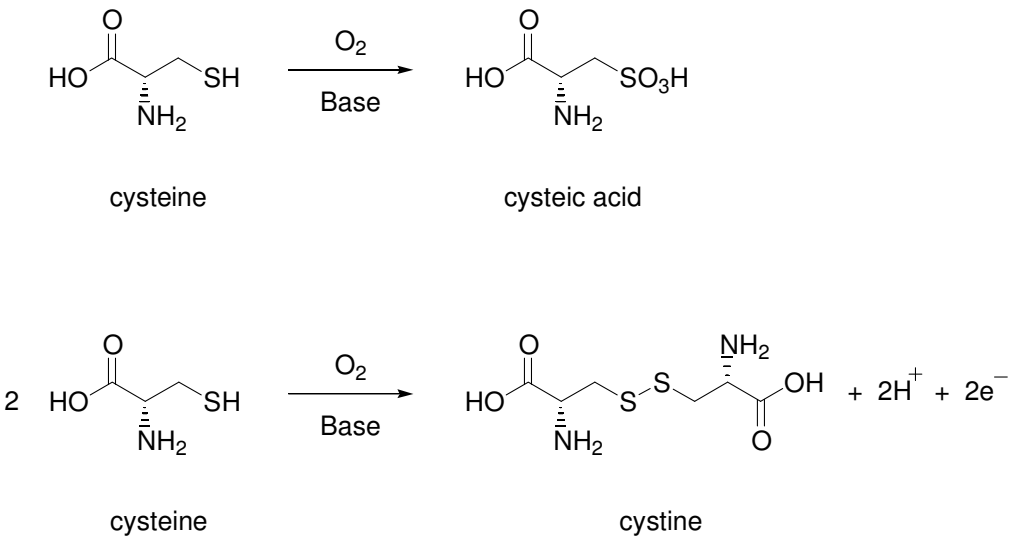

Scheme 4.2. Oxidation of cysteine to cysteic acid or cystine.

To investigate the role of these reactions in the electrolysis of cystine, the effect of electrolysis time on the yield of cysteine was examined. The electrolysis was carried out until charges of 1, 2 and 4 C were passed, after which time the maximum conversion of cystine to cysteine was 25, 50 and 100 % respectively. The cysteine concentration was determined using Ellman's assay at the end of each electrolysis (Table 4.12). A linear relationship was observed between electrolysis time and the charge passed. The conversion of cystine to cysteine was maintained at a constant level (~ 55 %) after passing a charge of 1 or 2 C even though the electrolysis time increased. The efficiency of the reaction decreased after passing more charge (42 %, 4 C). This is most likely due to greater cysteine re-oxidation occurring during the increased electrolysis time.

Table 4.12. The effect of charge passed on the efficiency of the electroreduction of cystine at a nanoAu/CF electrode. Bulk electrolysis of cystine (1 mM, 20 mL) was performed by applying a potential of -0.90 V until a charge of 1, 2 or 4 C was passed.

Q **(C)**	**Run**	**Time (min)**[a]	**[Cysteine] (mM)**[b]	**Conversion of Cystine to Cysteine (%)**[c]
1	1	30	0.25	50
	2	50	0.28	56
2	1	112	0.56	56
	2	104	0.62	62
4	1	212	0.78	38
	2	218	0.91	46

[a] The time taken to pass the required charge.

[b] The concentration of cysteine determined at the end of the bulk electrolysis using Ellman's assay.

[c] Percentage conversion based on the theoretical maximum conversion of 25, 50 and 100 % after passing charges of 1 , 2 and 4 C respectively.

^{1}H NMR analysis was used to directly observe the oxidised species present in solution after the bulk electrolysis of cystine. Firstly, reference ^{1}H NMR spectra were recorded from commercially available samples of cysteine, cystine and cysteic acid (Figure 4.10, (a), (b) and (c)). Characteristic chemical shifts for the α-protons were observed at 3.84 ppm, 3.93-3.94 ppm and 4.32 ppm for cysteine, cystine and cysteic acid respectively (Table 4.13). The β-protons also have characteristic shifts (see Appendix A for ^{1}H NMR assignments). To determine if cysteine is oxidised upon standing, a solution of cysteine (1 mM, 20 mL) at pH 8.0 was purged with nitrogen for 105 mins. An aliquot (2 mL) was lyophilised and an NMR sample was prepared using deuterated water (D_2O). Examination of the ^{1}H NMR spectrum (Figure 4.10, (d)) revealed the presence of cysteine and the corresponding disulfide, cystine. Due to the presence of phosphate buffer salts in the lyophilised sample, the pH of the NMR samples was slightly altered compared to the reference samples. This resulted in a small change in chemical shift for all the protons and coalescence of the β-protons of cysteine. However, cysteine and cystine are clearly identified by characteristic chemical shifts for the α-protons which correspond to the reference spectra and are observed at 3.79 ppm and 3.96 ppm

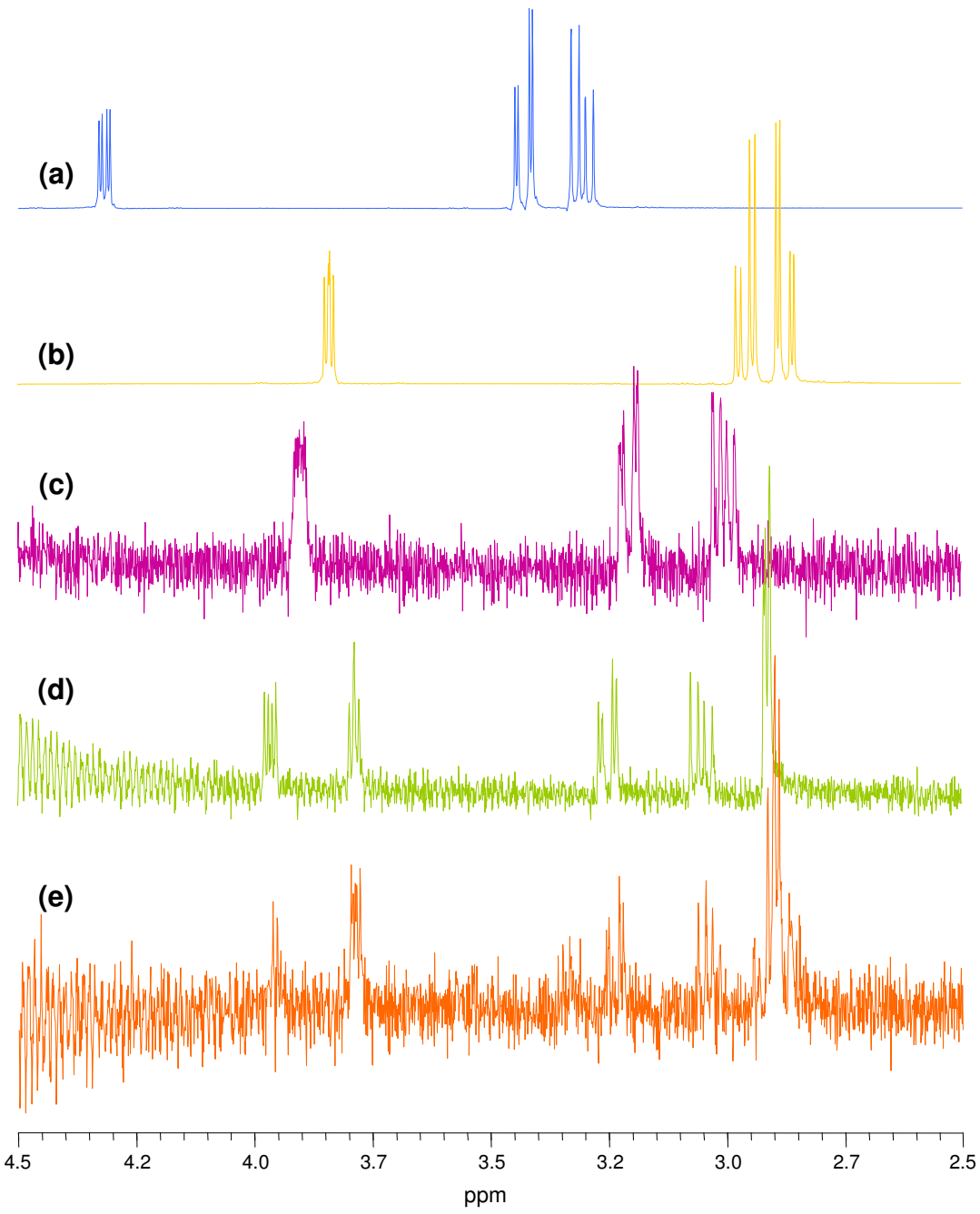

Figure 4.10. ^{1}H NMR (500 MHz, D_2O) of (a) cysteic acid, (b) cysteine, (c) cystine, (d) product of the auto-oxidation of cysteine, and (e) product of the bulk electrolysis of cystine.

for cysteine and cystine respectively. No peak is observed at 4.32 ppm indicating that cysteic acid is not a product of cysteine oxidation under these conditions. Using Ellman's assay the ratio of thiol to disulfide was 1:1.5. However, from the integration of the ^{1}H NMR spectrum the ratio of thiol to disulfide was 2.4:1 (Table 4.13). The inconsistency observed between these results reflects the low solubility of cystine (0.11 g L^{-1}) in D_2O as can be clearly seen from the weak NMR spectrum obtained from the commercially available sample. Bulk electrolysis of cystine (1 mM, 20 mL) was carried out at a nanoAu/CF electrode by applying a potential of -0.90 V until a charge of 4 C was passed. The theoretical maximum conversion of cystine to cysteine for the reaction was 100 %. Analysis of the bulk electrolysis product at the end of the reaction showed the presence of cysteine and cystine in the ^{1}H NMR spectrum (Figure 4.10, (e)). Again there was no evidence of cysteic acid (Table 4.13). Using Ellman's assay the ratio of thiol to disulfide was 1:2.3 whereas from integration of the ^{1}H NMR the ratio was 4.5:1, again due to the low solubility of cystine.

Table 4.13. Summary of the ^{1}H NMR data to determine the species present following bulk electrolysis of cystine.

	Chemical shift of the α-proton (ppm)	**Integration per α-proton**	**Ratio of cysteine: cystine from ^{1}H NMR data**	**Ratio of cysteine: cystine from Ellman's assay**
Cysteine	3.84	21.93		
Cystine	3.93-3.94	14.48		
Cysteic acid	4.32	22.44		
Product of the auto-oxidation of cysteine[a]	3.79 (cysteine) 3.96 (cystine)	15.93 6.75	2.4:1	1:1.5
Product of the bulk electrolysis of cystine[b]	3.78-3.79 (cysteine) 3.95 (cystine)	20.80 4.58	4.5:1	1:2.3

[a] Cysteine solution (1 mM, 20 mL) degassed with nitrogen for 105 minutes.

[b] Bulk electrolysis of cystine (1 mM, 20 mL) was performed by applying a potential of -0.90 V until a charge of 4 C was passed, after which time the maximum theoretical conversion was 100 %.

The results from the ^{1}H NMR analysis confirm that the thiol generated during the bulk electrolysis of cystine at a nanoAu/CF electrode is being re-oxidised by adventitious oxygen. Further evidence of this was indirectly obtained by purging a solution of cysteine (1 mM, 20 mL) at pH 8.0 with argon for 105 minutes. The thiol concentration did not decrease during this experiment. In comparison, the cysteine concentration was observed to decrease when the experiment was repeated using nitrogen. This result indicates that oxygen is present in the nitrogen supply which subsequently allows oxidation of cysteine. For the future application of this process (see Chapter 5), the re-oxidation of cysteine back to the disulfide is preferred compared to oxidation of the thiol to give cysteic acid. Any cystine present will continue to be reduced back to the thiol during the wool setting process, whereas formation of cysteic acid represents a loss of reactant from the solution.

4.3.2.3 Effect of Temperature on the Bulk Electrolysis of Cystine

Conventional wool setting processes are carried out at elevated temperatures. In particular, the industrial setting process which uses the chemical reducing agent sodium metabisulfite (referred to as CHEMSET, see Chapter 5) is carried out at 85 °C. For this work, the effect of temperature on the bulk electrolysis of cystine at a nanoAu/CF electrode was investigated by performing the reaction at room temperature and at 85 °C (Table 4.14). The rate of reaction was faster at the elevated temperature of 85 °C as the time taken to pass the required charge of 2 C (45 minutes) was shorter than the time taken for the reaction carried out at room temperature (107 minutes), however, the conversion of cystine to cysteine was lower for the reaction performed at 85 °C (41 %) compared the reaction carried out at room temperature (58 %). This is most likely due to the elevated temperature increasing the rate of re-oxidation of cysteine by adventitious oxygen.

Table 4.14. The effect of temperature on the bulk electrolysis of cystine at a nanoAu/CF electrode. Cystine was reduced by applying a potential of -0.90 V until 2 C of charge was passed. For the experiment carried out at room temperature (20 °C) the concentration and volume of cystine was 1 mM and 20 mL respectively. This experiment was replicated three times and the errors correspond to one standard deviation. The electroreduction of cystine (1.25 mM, 20 mL) was performed once at 85 °C.

Temperature (°C)	[Cysteine] (mM)[a]	Conversion of cystine to cysteine (%)[b]	Time (min)[c]
20	0.58 ± 0.03	58 ± 3	107 ± 4
85	0.51	41	45

[a] The concentration of cysteine determined at the end of the bulk electrolysis using Ellman's assay.

[b] Percentage conversion based on the theoretical maximum conversion of 50 %.

[c] The time taken to pass 2 C of charge.

4.4 Conclusions

Metal nanoparticle electrodes fabricated by electrochemically depositing silver or gold onto glassy carbon substrates exhibited a small increase in activity towards the reduction of cystine and 2-HED. In general, a small shift in to more positive peak potentials was observed for the reduction peak corresponding to cleavage of the S–S bond compared to the response obtained at the solid metal electrodes. The advantages of employing metal nanoparticle electrodes in industrial processes are that high surface area metal electrodes can be easily fabricated using less metal compared to bulk metal electrodes, hence, metal nanoparticle electrodes are potentially less expensive and more economically viable. The optimum conditions for fabricating nanoAg/GC and nanoAu/GC electrodes was determined by controlling the amount of metal deposited onto the surface through deposition time. An increase in deposition time led to an increase in metal loading which subsequently shifted the cystine reduction peak to less negative potentials. The best performance of these electrodes with respect to disulfide reduction was observed at nanoAg/GC and nanoAu/GC electrodes prepared using deposition times of 300 seconds and 600 seconds respectively. The reduction of cystine at the nanoAu/GC electrode was observed to be the most energetically

favourable as the peak potential was observed at the least negative potential of -0.80 V, representing a small energy saving compared to the response at solid gold (-0.92 V) and the reduction of 2-HED at nanoAu/GC (-0.90 V).

Bulk electrolysis methods were used in an effort to completely reduce cystine to cysteine during electrolysis. The optimum potential for the reduction of cystine at a nanoAu/CF electrode was -0.90 V. At more negative potentials, hydrogen evolution is presumed to occur as a competing reaction. The greatest conversion of cystine to cysteine achieved was 58 ± 3 %. Variation of the gold deposition conditions to change the size and morphology of the gold deposits on the nanoAu/CF electrode did not have any significant effect on the efficiency of the reduction of cystine. Analysis of the bulk electrolysis product solution using ^{1}H NMR showed that the thiol was being converted back to the disulfide during the reaction.

4.5 References for Chapter 4

1. Genders, J. D. Electrodes, membranes and cell design for electrosynthesis. In *Electrosynthesis: From laboratory, to pilot, to production*; Pletcher, D.; Genders, J. D., Eds; The Electrosynthesis Company Inc.: East Amherst, NY, USA, 1990; p 65-92.

2. Pletcher, D.; Walsh, F. C., *Industrial electrochemistry;* Chapman and Hall Ltd: London, UK, 1990; p 91-94.

3. Shimazu, K.; Weisshaar, D.; Kuwana, T. Electrochemical dispersion of Pt microparticles on glassy-carbon electrodes. *Journal of Electroanalytical Chemistry* **1987**, *223*, 223-234.

4. Crotty, D. Zinc alloy plating for the automotive industry. *Metal Finishing* **1996**, *94*, 54-58.

5. Okinaka, Y.; Hoshino, M. Some recent topics in gold plating for electronics applications. *Gold Bulletin* **1998**, *31*, 3-13.

6. Ghodbane, O.; Roué, L.; Bélanger, D. Copper electrodeposition on pyrolytic graphite electrodes: Effect of the copper salt on the electrodeposition process. *Electrochimica Acta* **2007**, *52*, 5843-5855.

7. Schmidt, U.; Donten, M.; Osteryoung, J. G. Gold electrocrystallisation on carbon and highly oriented pyrolytic graphite from concentrated solutions of LiCl. *Journal of the Electrochemical Society* **1997**, *144*, 2013-2021.

8. Pötzschke, R. T.; Gervasi, C. A.; Vinzelberg, S.; Staikov, G.; Lorenz, W. J. Nanoscale studies of Ag electrodeposition on HOPG (0001). *Electrochimica Acta* **1995**, *40*, 1469-1474.

9. Sonnenfeld, R.; Schardt, B. C. Tunneling microscopy in an electrochemical-cell - images of Ag-plating. *Applied Physics Letters* **1986**, *49*, 1172-1174.

10. Scharifker, B.; Hills, G. Theoretical and experimental studies of multiple nucleation. *Electrochimica Acta* **1983**, *28*, 879-889.

11. Zoval, J. V.; Lee, J.; Gorer, S.; Penner, R. M. Electrochemical preparation of platinum nanocrystallites with size selectivity on basal plane oriented graphite surfaces. *Journal of Physical Chemistry B* **1998**, *102*, 1166-1175.

12. Zoval, J. V.; Biernacki, P. R.; Penner, R. M. Implementation of electrochemically synthesised silver nanocrystallites for the preferential SERs enhancement of defect modes on thermally etched graphite surfaces. *Analytical chemistry* **1996**, *68*, 1585-1592.

13. Zoval, J. V.; Stiger, R. M.; Biernacki, P. R.; Penner, R. M. Electrochemical deposition of silver nanocrystallites on the atomically smooth graphite basal plane. *Journal of Physical Chemistry* **1996**, *100*, 837-844.

14. Ji, X. B.; Banks, C. E.; Xi, W.; Wilkins, S. J.; Compton, R. G. Edge plane sites on highly ordered pyrolytic graphite as templates for making palladium nanowires *via* electrochemical decoration. *Journal of Physical Chemistry B* **2006**, *110*, 22306-22309.

15. Li, Y. G.; Lasia, A. Electrodeposition of hard gold from acidic solution - the influence of substrates. *Journal of the Electrochemical Society* **1997**, *144*, 1979-1988.

16. Cao, G., *Nanostructure and nanomaterials: Synthesis, properties and applications;* Imperial College Press: London, UK, 2004; p 174.

17. Zangwill, A., *Physics at surfaces;* Cambridge University Press: Cambridge, UK, 1988; p 428-432.

18. El-Deab, M. S.; Okajima, T.; Ohsaka, T. Electrochemical reduction of oxygen on gold nanoparticle-electrodeposited glassy carbon electrodes. *Journal of the Electrochemical Society* **2003**, *150*, A851-A857.

19. Tian, Y.; Liu, H. Q.; Zhao, G. H.; Tatsuma, T. Shape-controlled electrodeposition of gold nanostructures. *Journal of Physical Chemistry B* **2006**, *110*, 23478-23481.

20. Löffler, M. S.; Groß, B.; Natter, H.; Hempelmann, R.; Krajewski, T.; Divisek, J. Synthesis and characterisation of catalyst layers for direct methanol fuel cell applications. *Physical Chemistry Chemical Physics* **2001**, *3*, 333-336.

21. Tsai, M. C.; Yeh, T. K.; Tsai, C. H. An improved electrodeposition technique for preparing platinum and platinum-ruthenium nanoparticles on carbon nanotubes directly grown on carbon cloth for methanol oxidation. *Electrochemistry Communications* **2006**, *8*, 1445-1452.

22. Bauer, A.; Gyenge, E. L.; Oloman, C. W. Direct methanol fuel cell with extended reaction zone anode: PtRu and PtRuMo supported on graphite felt. *Journal of Power Sources* **2007**, *167*, 281-287.

23. Sun, Y.; Wang, H. H. Electrodeposition of Pd nanoparticles on single-walled carbon nanotubes for flexible hydrogen sensors. *Applied Physics Letters* **2007**, *90*, 213107.

24. Mubeen, S.; Zhang, T.; Yoo, B.; Deshusses, M. A.; Myung, N. V. Palladium nanoparticles decorated single-walled carbon nanotube hydrogen sensor. *Journal of Physical Chemistry C* **2007**, *111*, 6321-6327.

25. Kong, J.; Chapline, M. G.; Dai, H. Functionalised carbon nanotubes for molecular hydrogen sensors. *Advanced Materials* **2001**, *13*, 1384-1386.

26. Selvaraju, T.; Ramaraj, R. Electrochemically deposited nanostructured platinum on Nafion coated electrode for sensor applications. *Journal of Electroanalytical Chemistry* **2005**, *585*, 290-300.

27. Dai, X.; Nekrassova, O.; Hyde, M. E.; Compton, R. G. Anodic stripping voltammetry of arsenic(III) using gold nanoparticle-modified electrodes. *Analytical Chemistry* **2004**, *76*, 5924-5929.

28. Katsuki, A.; Fukui, K. H_2 selective gas sensor based on SnO_2. *Sensors and Actuators B-Chemical* **1998**, *52*, 30-37.

29. Ellman, G. L. Tissue sulfhydryl groups. *Archives of Biochemistry and Biophysics* **1959**, *82*, 70-77.

30. Riddles, P. W.; Blakeley, R. L.; Zerner, B. Reassessment of Ellman's reagent. *Methods in Enzymology* **1983**, *91*, 49-60.

31. Capozzi, G.; Medina, G. Oxidation of thiols. In *The chemistry of the thiol group* Patai, S., Eds., John Wiley & Sons Ltd.: Bristol, UK, 1974; Vol. 2, p 785-840.

32. Bridgart, G. J.; Fuller, M. W.; Wilson, I. R. Metal-ion catalysis in reactions of hexacyanoferrate(III)ions. I. Copper catalysis in the oxidation of cysteine and related thiols. *Journal of the Chemical Society, Dalton Transactions: Inorganic Chemistry (1972-1999)* **1973**, 1274-1280.

33. Bridgart, G. J.; Wilson, I. R. Metal-ion catalysis in reactions of hexacyanoferrate(III) ions. II. Oxidation of cysteine and related thiols in the presence of ethylenediaminetetraacetic acid. *Journal of the Chemical Society, Dalton Transactions: Inorganic Chemistry (1972-1999)* **1973**, 1281-1284.

34. Finot, M. O.; Braybrook, G. D.; McDermott, M. T. Characterisation of electrochemically deposited gold nanocrystals on glassy carbon electrodes. *Journal of Electroanalytical Chemistry* **1999**, *466*, 234-241.

35. Milchev, A.; Vassileva, E. Electrolytic nucleation of silver on a glassy-carbon electrode .2. Steady-state nucleation rate. *Journal of Electroanalytical Chemistry* **1980**, *107*, 337-352.

36. Louden, G. M., *Organic chemistry;* (3rd ed.); The Benjamin/Cummings Publishing Company, Inc.: California, USA, 1995; p 482.

37. March, J., *Advanced organic chemistry;* (4th ed.); John Wiley & Sons Ltd.: New York, USA, 1992; p 1199, 1204.

Chapter 5

Application of Electrochemical Techniques to Wool Setting

5.1 Introduction

The reduction of wool disulfide bonds with thiol reducing agents during wool setting has been discussed in Chapter 1 (Section 1.1.3). In brief, the thiol reducing agents are converted to disulfides during reduction of wool disulfide bonds (equation 1, Scheme 5.1) and after the wool is removed from the reducing conditions, the adjacent wool thiol groups can be re-oxidised in air to form disulfide bonds giving the wool a more stable conformation without being strained (equation 2). Efficient conversion of the disulfide back to the thiol reducing agent would allow catalytic amounts of thiols to be used in wool setting (equation 3). Hence, this chapter describes the electrochemical regeneration of the thiol reducing agent during wool setting.

(1) Disulfide reduction: $\underset{\text{Strained}}{\text{W-S-S-W}} + 2\text{RS-H} \longrightarrow 2\text{WS-H} + \text{R-S-S-R}$

(2) Disulfide oxidation: $2\text{WS-H} + {}^{1}/_{2}\text{O}_2 \longrightarrow \underset{\text{Unstrained}}{\text{W-S-S-W}} + \text{H}_2\text{O}$

(3) Regeneration of thiol: $\text{R-S-S-R} + 2e^- + 2H^+ \xrightarrow{\text{Electrode}} 2\text{RS-H}$

Scheme 5.1. Electrochemical regeneration of the thiol reducing agent used to cleave the disulfide bonds in wool (W) during wool setting. W-S-S-W and WS-H represent the disulfide bonds and thiol groups of the wool respectively. RS-H and R-S-S-R represent the thiol setting agent and the corresponding disulfide respectively.

5.1.1 Electroreduction of Wool Disulfide Bonds using Thiol Mediators

The use of thiols as mediators in the electroreduction of wool disulfide bonds is very attractive. It is not feasible to directly reduce the cystine in wool electrochemically because it is in the solid form and cannot undergo efficient electron transfer at a solid electrode. At present, Leach *et al.* are the only workers to report on the electrolytic reduction of wool disulfide bonds in the presence of low concentrations of a thiol reducing agent, namely 2-mercaptoethanol.[1] The optimum conditions for complete electroreduction of wool disulfide bonds were to treat wool (200 mg) with 2-mercaptoethanol (7130 μmol) in Tris buffer (0.2 M, 100 mL containing 0.2 M HCl and 0.1 M KCl, pH 7.0) for 24 hours in the presence of electrolysis. The disulfide form of the catalyst (2-HED) was reduced at a mercury electrode during treatment. A constant potential of -1.50 or -1.60 V (*vs*. SCE) was applied for the first 1-2 hours of treatment after which time the potential was held at -1.20 V for the remainder of the experiment. A control experiment was performed in the absence of electrolysis by treating wool (100 mg) with 2-mercaptoethanol (3565 μmol) in Tris buffer overnight. The reduction of wool proteins in the absence and presence of electrolysis was carried out at 20 °C under an atmosphere of nitrogen. Reduced wools were washed with a mixture of acetone and hydrochloric acid (1 M) (39:1), followed by acetone again to prevent the cysteine residues on the wool from oxidising and reforming disulfide crosslinks. The amount of cysteine and cystine present in untreated and treated wool samples was estimated by amperometric titration with methylmercuric iodide at a dropping mercury electrode (Table 5.1). Compared to the cystine and cysteine content detected in untreated wool (440 μmol g^{-1} of cystine and 30 μmol g^{-1} of cysteine), the number of disulfide bonds present in wool treated with 2-mercaptoethanol in the absence of electrolysis decreased by 40 % (to 265 μmol g^{-1}) and the cysteine content increased (375 μmol g^{-1}) demonstrating that 2-mercaptoethanol reduces wool disulfide bonds to yield the corresponding thiol residues. Electrolysis was observed to drive the reaction further towards completion. Very few disulfide bonds remained in the wool sample after reduction with 2-mercaptoethanol in the presence of electrolysis (10-40 μmol g^{-1}). Leach *et al.* proposed that the electrolytic reduction of wool proceeded in two steps: (1) the reduction of wool disulfide bonds by 2-mercaptoethanol (equation 1, Scheme 5.1) followed by (2) the electroreduction of the 2-HED by-product at the mercury electrode to regenerate the thiol reducing agent (equation 3).

Table 5.1. The effect of electrolysis on the reduction of wool in the presence of 2-mercaptoethanol. Wool was treated with 2-mercaptoethanol[a] in Tris buffer (0.2 M, 100 mL containing 0.2 M HCl and 0.1 M KCl, pH 7.0) for 24 hours. Table adapted from reference 1.

Reduction of wool disulfide bonds with 2-mercaptoethanol	Concentration of cysteine (RSH) residues in wool (μmol g^{-1})[b]	Concentration of cystine (RSSR) residues in wool (μmol g^{-1})[b]
Prior to treatment	30	440
Without electrolysis	375	265
After electrolysis[c]	700	10-40

[a] In the absence of electrolysis, 100 mg of wool was treated with 3565 μmol of 2-mercaptoethanol. In the presence of electrolysis, 200 mg of wool was treated with 7130 μmol of 2-mercaptoethanol.

[b] The amount of cysteine and cystine residues in wool was determined by amperometric titration with methylmercuric iodide at a dropping mercury electrode. The values are the averages obtained from at least four experiments and were rounded to the nearest 5 μmol g^{-1}.

[c] Electrolysis was performed at a mercury electrode by applying a constant potential of -1.50 or -1.60 V (*vs*. SCE) for the first 1-2 hours of treatment after which time the potential was held at -1.20 V (*vs*. SCE) for the remainder of the experiment.

The extent of wool disulfide bond reduction was found to be dependent on the potential applied during electrolysis. At potentials less negative than -1.20 V the extent of disulfide reduction to yield cysteine was observed to decrease. For example, after electrolysis at -0.70 V the concentration of cysteine residues detected in the reduced wool was only 140 μmol per gram of wool compared with 700 μmol per gram of wool detected for wool reduced at -1.20 V. This result suggests that it may be possible to control the final level of wool disulfide bond reduction by selecting the appropriate electrolysis potential. This would be advantageous for wool processes such as setting where the reduction of a limited number of wool disulfide bonds is required to produce useful changes in fibre properties whilst maintaining fibre strength.

5.1.2 Research Directions for Chapter 5

The work presented in this chapter investigates the use of low concentrations of cysteine for reducing wool disulfide bonds during the process of wool setting. The cysteine reducing agent was regenerated by electrochemically reducing solution-based cystine, formed during reaction with the wool, at a nanoAu/CF electrode. The electroreduction of cystine and 2-HED, the corresponding disulfides of cysteine and 2-mercaptoethanol respectively, was assessed at a range of metal and carbon electrodes in work previously described in Chapters 3 and 4. The reduction of cystine at gold nanoparticles electrodeposited onto carbon supports was observed to be the most favourable process, hence, cysteine was chosen as the thiol reducing agent in this work. In order to demonstrate that cysteine could be efficiently regenerated during wool processing, limiting conditions were investigated under which setting was observed to be maintained in the presence of electrolysis and decreased in the absence of electrolysis.

5.2 Experimental Methods

5.2.1 Specifications of the Yarn used for Wool Setting

For this work a balanced 2-fold yarn was used consisting of coarse wool fibres (average diameter 38.00 ± 9.82 μm). In the textile industry the construction of the yarn is represented by R600/2 tex. This term describes the linear density (unit tex, mass of yarn per 1000 meters) and the construction of the yarn. Hence, the final material consisted of two single strands of yarn (each 300 tex) twisted together (as represented by '/2') to give a resultant (R) yarn linear density of 600 tex. Twist was imparted into the single strands to give the yarn strength and to stop individual fibres from sliding apart (Figure 5.1 (a)). The single yarn (300 tex) contained a twist of 165 turns per meter. To prepare the 2-fold yarn used in this work, two single strands were twisted together with 109 turns per meter. Twisting of two single strands together is referred to as 'folding' and occurs in the opposite direction to the twisting of a single strand (Figure 5.1 (b)).

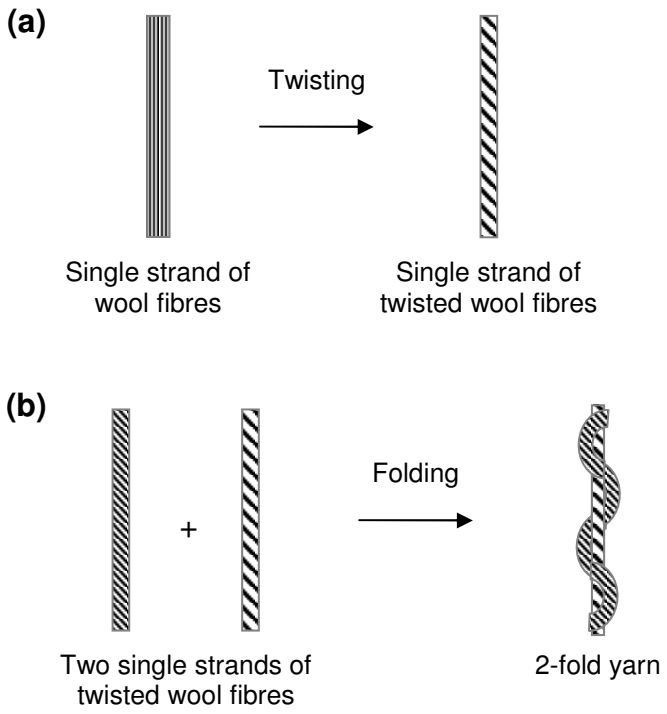

Figure 5.1. Illustration of (a) twist imparted into wool fibres to strengthen the yarn and (b) the folding of two single strands of yarn together to give a 2-fold yarn.

5.2.2 Wool Setting in the Presence of Cysteine

Wool setting in the presence of cysteine was performed at 85 °C or room temperature (20 °C). The mass of wool, concentration of cysteine solution and treatment time varied and are given in the Results and Discussion Section for each experiment. The supporting electrolyte was KH_2PO_4 buffer (0.05 M, pH 8.0) containing 0.1 M KNO_3. Unless otherwise stated, all experiments were performed under an atmosphere of nitrogen except for those described in the Results and Discussion Sections 5.3.2.1 and 5.3.2.2. Following treatment, the wool was rinsed with Milli-Q water (1 L) for 1 to 4 minutes at 85 °C. The wool was allowed to dry for 24 hours before analysing the degree of setting using the methods described in Section 5.2.4. For the experiments described in the Results and Discussion Sections 5.3.2.3, 5.3.2.4 and 5.3.3 the wool was pre-wet prior to treatment with cysteine by immersion in blank electrolyte (150 mL) for 10 minutes at room temperature. By doing this, loss of the treatment solution due to absorption by the wool was less and the thiol setting agent should enter the fibres more easily.

5.2.2.1 Electrochemical Regeneration of Cysteine during Wool Setting

The cysteine setting agent was regenerated during wool setting by electrochemically reducing the cystine produced as a result of the reaction between cysteine and the wool (equations 1 and 3, Scheme 5.1). Cystine was reduced at a nanoAu/CF electrode by applying a constant potential of -0.90 V. Electrolysis of the cysteine treatment solution was performed whilst the wool was treated and for a further 5 minutes after the wool was removed to regenerate more of the thiol reducing agent before treating the next batch of wool. All electrochemical measurements were performed using a computer interfaced PAR Model 273A Potentiostat/Galvanostat.

5.2.2.2 Electrochemical Cell for the Treatment of Wool

For this work, the bulk electrolysis cell used in Chapter 4 for the electroreduction of cystine at a nanoAu/CF electrode was scaled up to allow wool to be placed in the cell. These electrochemical cells have been previously described in Chapter 2 (Section 2.4.3.4) and for wool setting experiments Designs 2 and 3 were used (Results and Discussion Sections 5.3.2.2, and 5.3.2.3 to 5.3.3 respectively). For the experiments carried out at 85 °C, a silicone oil bath was used with cell Design 2 to heat the treatment solution to the required temperature. For cell Design 3 the outer compartment was fitted with a water jacket and water was continuously pumped from a water bath (85 °C) through the water jacket throughout the experiment to maintain the cysteine treatment solution at a constant temperature. Thermal wool (Kaowool) was wrapped around the water jacket to prevent heat loss. The cells consisted of two compartments separated by a sintered glass frit (porosity 5). The inner compartment contained a nanoAu/CF electrode positioned around the inside of the compartment and the wool was placed inside the nanoAu/CF electrode to allow efficient reduction of the cystine produced during wool setting. A saturated calomel electrode (SCE) was used as the reference electrode and was placed at the top of the cell within the inner compartment. A platinum gauze auxiliary electrode was positioned symmetrically in the outer compartment of the cell to produce a uniform potential and current density across the nanoAu/CF electrode. For wool treatment, blank electrolyte at 85 °C was placed into both compartments of the electrochemical cell under an atmosphere of nitrogen. The inner compartment contained 80 mL (Design 2) or 150 mL (Design 3) of solution whilst the outer compartment contained blank electrolyte to the same level as the inner compartment. Cysteine was added to the inner compartment immediately before treating

wool to reduce oxidation of cysteine by adventitious oxygen. The cysteine solution was stirred and bubbled with nitrogen to achieve effective mass transfer.

5.2.2.3 Fabrication of NanoAu/CF Electrodes

Electrodepositon of gold onto carbon fabric supports has been previously described in Chapter 4 for fabricating nanoAu/CF electrodes for the bulk electrolysis of cystine. A larger working electrode area was required for experiments involving wool setting, therefore, in these experiments the carbon fabric support took the form of a cylinder (see Chapter 2, Section 2.4.2.3). For developmental work, the geometric area of the carbon fabric electrode was 44 cm^2 per side. For the experiments described in the Results and Discussion Sections 5.3.2.3 to 5.3.3, the geometric area of the carbon fabric electrode was increased to 99 cm^2 per side to allow all the wool to be placed within the area of the nanoAu/CF electrode. Electrodeposition of gold onto carbon fabric electrodes was performed by reducing a solution of $KAuCl_4$ in 0.5 M H_2SO_4 using a computer interfaced PAR Model 273A Potentiostat/Galvanostat. The electrochemical cells designed for bulk electrolysis (Designs 2 and 3) were used for this process (see Chapter 2, Section 2.4.3.4). The solution of $KAuCl_4$ in 0.5 M H_2SO_4 was placed in the inner compartment of the electrochemical cell and the outer compartment contained blank electrolyte (0.5 M H_2SO_4) to the same level as the inner compartment. A standard three electrode configuration was used where the carbon fabric electrode and a saturated calomel reference electrode (SCE) were placed in the inner compartment and a platinum gauze auxiliary electrode was positioned in the outer compartment of the cell. Prior to metal deposition, the carbon fabric electrodes were ultrasonicated (10 seconds) in successive baths of acetone, methanol and isopropyl alcohol and dried with nitrogen. Controlled potential electrolysis was used to electrochemically deposit gold onto the carbon fabric support by applying a conditioning potential of 1.10 V for 5 seconds and then holding the potential at -0.4 V. The reaction was carried out until the charge passed was equivalent to a gold surface coverage of 3.80×10^{-6} mol cm^{-2} (based on a geometric area of 44 cm^2 or 99 cm^2). The concentrations and volumes of $KAuCl_4$ and the charges passed for the fabrication of nanoAu/CF electrodes are given in Table 5.2.

Table 5.2. Conditions for the electrochemical deposition of gold onto carbon fabric electrodes. Gold was deposited onto the carbon fabric by applying a potential of -0.40 V until the required charge was passed.

Geometric Area of Carbon Fabric Electrode (cm^2)	$[KAuCl_4]$ (mM)	Volume of gold salt solution (mL)[a]	Q (C)[b]
44	2	60	48
44	4	60	48
99	5	125	109

[a] The gold salt solution consists of $KAuCl_4$ in 0.5 M H_2SO_4.

[b] The charge passed to give a gold surface coverage of 3.80×10^{-6} mol cm^{-2}.

5.2.3 Wool Setting in the Presence of Sodium Metabisulfite

Wool was treated with sodium metabisulfite simulating the treatment conditions used in the CHEMSET process. The wool was treated consecutively in three solution baths with a 90 second immersion time in each bath. The first step in the process involved immersing the wool in Leophen M (0.05 %, 400 mL) at 60 °C. Leophen M is a detergent which acts as a wetting agent and allows complete immersion of the wool in solution. The wool was then treated with sodium metabisulfite (7.5 g L^{-1}, 400 mL), adjusted to pH 7.0 with anhydrous sodium carbonate, at 85 °C. Finally, the wool was rinsed with Milli-Q water (1 L) at 85 °C and left to dry for 24 hours before the degree of set imparted into the wool was analysed using methods described in Section 5.2.4.

5.2.4 Methods for Determining the Degree of Setting for Treated Yarn

The degree of setting for treated wool samples was assessed using two methods. The first test was carried out in the laboratory at the University of Canterbury and is referred to as the Crink Angle Test whilst the second test employed the WRONZ Set Tester developed on site at Canesis Network Ltd.* To allow these tests to be carried out, the wool was mounted for treatment by winding the yarn around a flat wooden stick (dimensions 9 mm × 112 mm) or a glass rod (dimensions 10 mm diameter × 245 mm length). The various ways of mounting the wool for treatment are shown in Figure 5.2. Method 1 was used to prepare samples for the Crink Angle Test and Methods 2 and 3 were used to prepare samples for the WRONZ Set Tester.

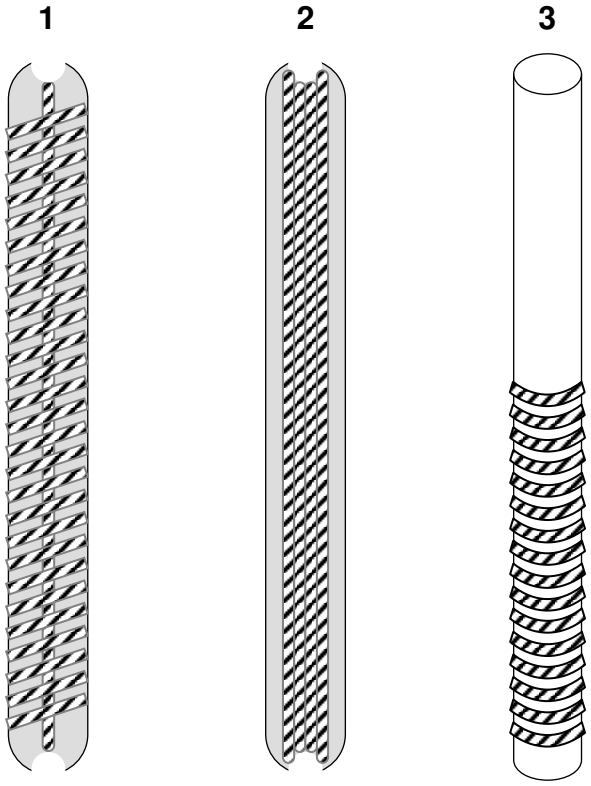

Figure 5.2. Methods for mounting wool for setting. Wool was wound around a flat wooden stick (Method 1 and 2) or a glass rod (Method 3). The degree of setting was analysed using the Crink Angle Test for wool treated using Method 1 and the WRONZ Set Tester was used for Methods 2 and 3.

* Canesis Network Ltd is now AgResearch Ltd.

5.2.4.1 Crink Angle Test

The Crink Angle Test was based on a method reported by Wood for analysing the effectiveness of various treatments for the setting of woollen yarn.[2] The treated wool was cut from the wooden stick by running a razor blade along one edge of the stick, cutting the yarn into a series of V-shaped segments (Figure 5.3). For qualitative analysis of the degree of setting, segments of the treated wool sample (n = 10 or 15) were immersed into Milli-Q water (50 mL) overnight at room temperature (20 °C) to observe whether the original shape and twist of the segments was retained. A greater degree of setting is represented by the ability of the wool segments to retain their shape and twist. Development of the Crink Angle Test as a quantitative measure of the degree of setting in treated yarns is described in the Results and Discussion Section 5.3.1. The quantitative test involved immersing V-shaped wool segments (n = 30 or 60) into Milli-Q water (200 mL) at 50 °C for 30 minutes and measuring the angle of the V-shaped segments of wool after drying.

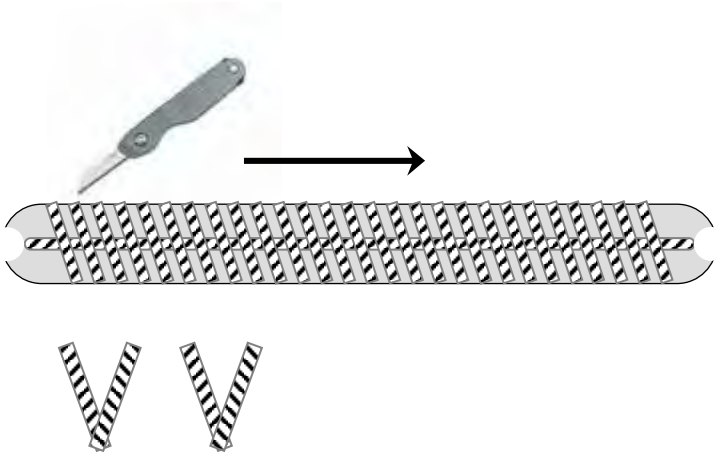

Figure 5.3. Preparation of samples for the Crink Angle Test. Treated wool was cut from the wooden support into a series of V-shaped wool segments. Figure adapted from reference 2.

5.2.4.2 WRONZ Set Tester

The WRONZ Set Tester (Figure 5.4) consisted of a hollow cylinder, containing a small aperture (21 mm), attached to a motor driven piston that cycles the cylinder in and out of the piston casing. The piston casing was fitted with a water jacket through which water at 50 °C was continuously pumped.

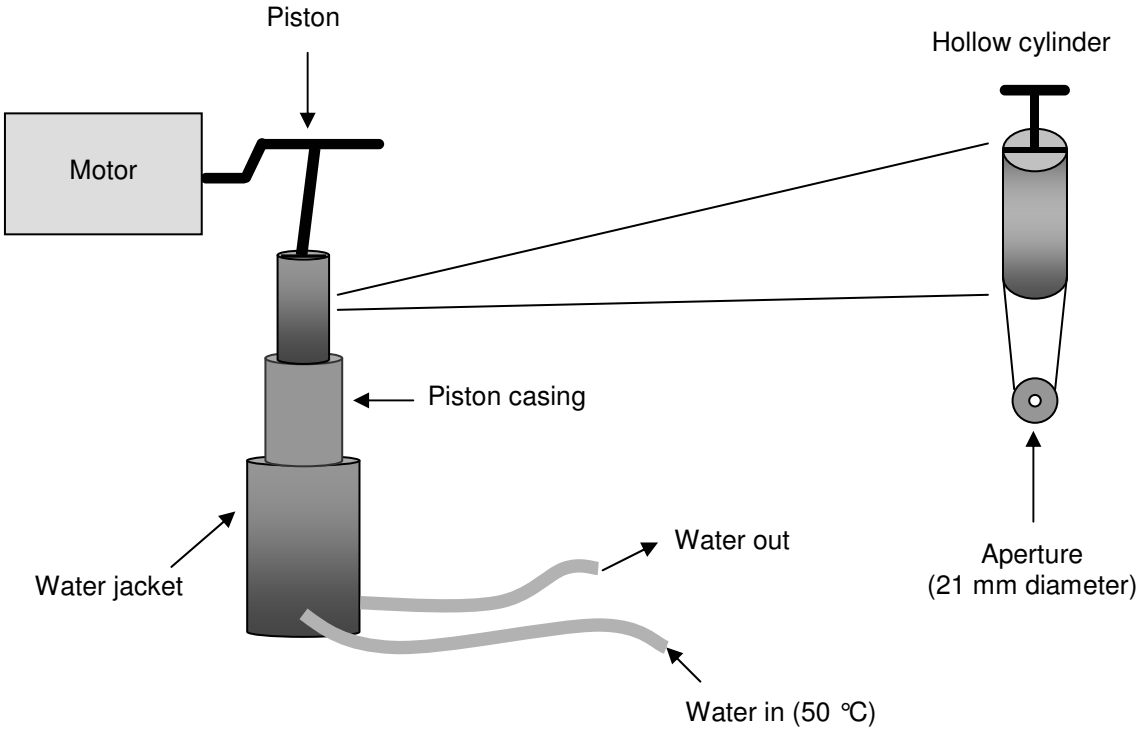

Figure 5.4. The WRONZ Set Tester apparatus used to quantify the degree of setting imparted into treated yarn during the wool setting process.

To determine the degree of setting in treated wool samples using the WRONZ Set Tester, snippets of the wool sample (17 mm each, n = 30 or 50) were placed into water (950 mL) containing Teric (0.002 %) at 50 °C. Teric is a detergent and was used as a wetting agent so that the snippets could be immersed in the water. The water and the snippets of wool were placed into the piston casing and pumped through the small aperture (21 mm) in the hollow cylinder for a set number of cycles. For each sample this process was carried out for 200 and 300 cycles. This is a destructive test for determining the degree of setting in the wool and is based on the principle that the better the wool is set, the better the two strands of wool comprising the 2-fold yarn will stay twisted together.

Therefore, the degree of set imparted into a treated wool sample was quantified as a percentage (% set) by counting the number of snippets of wool that remained twisted together at the end of the test. For some experiments, as indicated, the degree of setting was determined by analysing subsets of the treated wool sample (n = 50 snippets) at 100, 200, 300 and 400 cycles. Analysis of the degree of setting performed using the WRONZ Set Tester was carried out by Jenny Gamble, a senior technician at Canesis Network Ltd.

5.3 Results and Discussion

The application of electrochemical techniques to regenerate the cysteine setting agent during wool setting was the major focus of this work as this would allow the use of small amounts of setting agent and make the process more environmentally friendly. Preliminary experiments were carried out to find conditions under which the effects of electrochemical regeneration of the cysteine setting agent could be observed. The results of these experiments were analysed using the WRONZ Set Tester to quantify the degree of setting in treated wool samples; however, after a large number of experiments it became clear that this method does not give sufficiently reliable data for small sample sizes such as those used in this work. Hence, the Crink Angle Test was developed as a reliable quantitative measure of the degree of setting. The methods used with the WRONZ Set Tester and the results obtained are discussed in Section 5.3.5.

5.3.1 Development of the Crink Angle Test for Quantifying the Degree of Wool Setting

The effectiveness of industrial setting processes can be assessed by imparting folds into fabrics, such as pleats or creases, and measuring the stability of the resultant creases.[3] Yarns are removed from the creased area and released into water at 50 °C for 30 minutes. Measurement of the yarn crease angles allows comparison of different setting conditions. Well-set creased fabrics give crease angles of less than 60° and poorly-set fabrics have crease angles of 170-180° (Figure 5.5). This concept was used as the foundation for developing the Crink Angle Test to quantify the degree of setting in woollen yarn treated with cysteine. The angles of the V-shaped segments of wool obtained from the test were measured to determine the effectiveness of industrial setting processes.

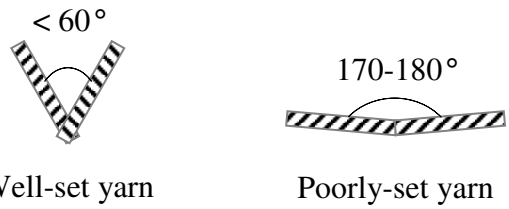

Figure 5.5. Measurement of yarn crease angles to compare the degree of setting imparted into wool using different treatment conditions.

As described in Section 5.2.4.1, qualitative analysis of the degree of wool setting imparted into wool during treatment using the Crink Angle Test involved immersing segments of the treated wool sample (n = 10 or 15) into Milli-Q water (50 mL) overnight at room temperature (20 °C) to observe if the original shape and twist of the wool segments were retained. For the quantitative Crink Angle Test treated wool segments (n = 30 or 60) were immersed in Milli-Q water (200 mL) at 50 °C for 30 minutes. After the V-shaped wool segments had dried, they were photographed and the inside angle (referred to as the crink angle) of each segment was measured manually from the image obtained using a protractor (Figure 5.6). The degree of setting for a wool sample was represented by the average crink angle measured for the V-shaped segments of wool tested (n = 30 or 60). The sample size required to obtain an accurate representation of the degree of wool setting in a treated wool sample was determined using the Students t-Test and outliers were identified by the Dixon Q Test using a 95 % confidence interval (see Appendix B for application of the Students t-Test and the Dixon Q Test).

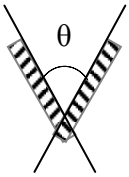

Figure 5.6. Measurement of the inside angle of a V-shaped wool segment for determining the degree of setting using the Crink Angle Test.

The feasibility of the Crink Angle Test as a method for quantifying the degree of wool setting was examined by treating wool with sodium metabisulfite. This setting agent is the conventional chemical reducing agent used in industrial setting processes. Wool was subjected to CHEMSET conditions for treatment (see Section 5.2.3) and the experiment was carried out five times to assess the reproducibility of setting determined by the Crink Angle Test. For each experiment the degree of setting was examined using a sample size of 60 V-shaped wool segments. The average crink angle for the five sets of experiments ranged from 77 ± 24 to 99 ± 20° indicating that a good level of set is achieved by treating wool with sodium metabisulfite under the CHEMSET conditions (Table 5.3). Excellent reproducibility was observed between experiments considering that wool is a natural fibre and has natural variation which cannot be controlled. The relative standard deviation (RSD) for these experiments was 9.3 %. These results prove that the Crink Angle Test is a valid method for determining the degree of wool setting.

Table 5.3. Reproducibility of the degree of setting for wool treated in the presence of sodium metabisulfite using the conditions employed in the CHEMSET process. The Crink Angle Test was carried out by immersing V-shaped wool segments (n = 60) into Milli-Q water (200 mL) for 30 minutes at 50 °C and measuring the inside crink angle. The quoted errors correspond to two standard deviations and these values cover the range of values observed in the raw data.

Run	Mass of wool (g)	Mass of sodium metabisulfite (g)	pH of sodium metabisulifite	Temperature (°C)			Average crink angle (°)
				Bath 1[a]	Bath 2[b]	Bath 3[c]	
1	2.1692	3.0050	7.07	62	83	85	87 ± 24
2	2.1555	3.0020	7.01	63	84	81	99 ± 20
3	2.1684	3.0049	7.00	61	84	83	94 ± 24
4	2.1667	3.0041	7.08	62	84	84	77 ± 24
5	2.1660	3.0008	7.08	62	84	82	88 ± 24

[a] Leophen M (0.05 %, 400 mL).

[b] Sodium metabisulfite (7.5 g L^{-1}, 400 mL, pH 7.0).

[c] Milli-Q water (1 L)

5.3.2 Use of Cysteine as a Reducing Agent for Wool Setting in the Absence of Electrolysis

5.3.2.1 Comparison of Sodium Metabisulfite and Cysteine as Chemical Reducing Agents for Wool Setting

Initial studies involved comparing the effectiveness of sodium metabisulfite and cysteine as reducing agents for the process of wool setting. Previous studies performed at Canesis Network Ltd regarding the use of cysteine as a setting agent showed that the best setting conditions were obtained by treating wool with cysteine (5 g L^{-1}) at 85 °C for 90 seconds.[4] Hence, the treatment conditions used in this experiment were based on these results and those used in the CHEMSET process where sodium metabisulfite is employed as the setting agent.[5]

Wool samples were firstly prepared for treatment by winding the yarn (~ 0.80 g) around a flat wooden stick. The samples were immersed into a solution of either sodium metabisulfite (10 g L^{-1}, 500 mL) or cysteine (5 g L^{-1}, 500 mL) for 2 minutes at 85 °C and then rinsed with Milli-Q water (500 mL) at 85 °C for 1 minute. Rinsing removes excess thiol setting agent and promotes the air oxidation of cysteine residues on the wool to re-form disulfide crosslinks. A control wool sample was also prepared by immersing wool into Milli-Q water (500 mL) at 85 °C for 3 minutes. After the treated wool samples had been left to dry for 24 hours, the degree of setting in the yarn was analysed qualitatively using the Crink Angle Test by immersing V-shaped wool segments (n = 15) into Milli-Q water (50 mL) overnight at room temperature. The wool treated with sodium metabisulfite and cysteine was observed to retain the V-shape and twist of the yarn better than the control wool sample demonstrating that a greater degree of setting had occurred in the presence of the two setting agents (Figure 5.7). In comparing the wool treated with sodium metabisulfite and cysteine, the twist of the yarn was retained better in the presence of sodium metabisulfite as was the shape of the tufts of wool. This result indicates that sodium metabisulfite is the better setting agent; however, cysteine is a promising candidate in the quest to find an alternative setting agent to replace sodium metabisulfite.

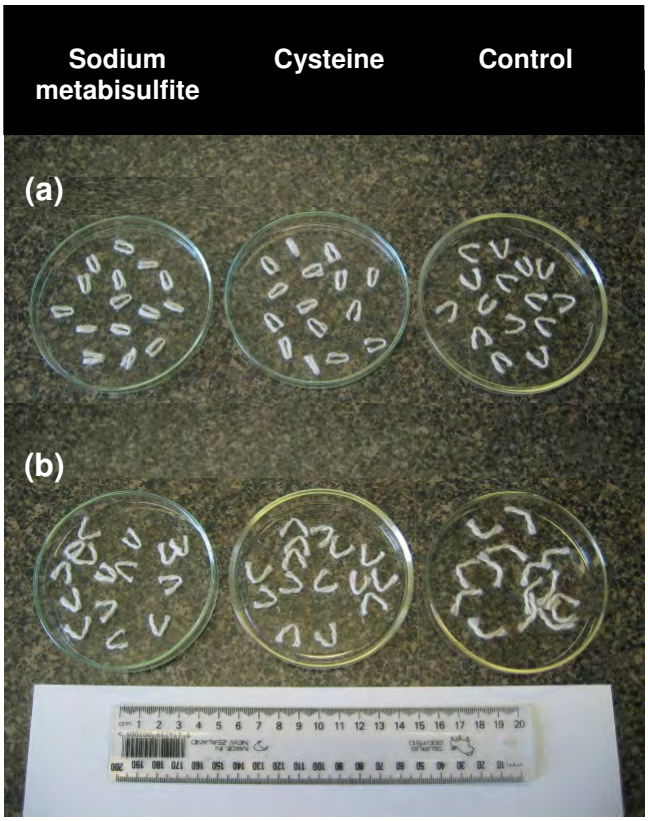

Figure 5.7. Comparison of the twist and shape of wool segments treated with sodium metabisulfite and cysteine reducing agents (a) before and (b) after immersion in Milli-Q water (50 mL) overnight at room temperature (20 °C) to examine the degree of set imparted into the wool. Wool setting was performed by immersing wool into solutions of sodium metabisulfite (10 g L^{-1}, 500 mL) and cysteine (5 g L^{-1}, 500 mL) for 2 minutes at 85 °C followed by rinsing in Milli-Q water (500 mL) at 85 °C for 1 minute. The control wool sample was prepared by immersing wool into Milli-Q water at 85 °C for 3 minutes.

5.3.2.2 Effect of Temperature and Treatment Time on Wool Setting in the Presence of Cysteine

Conventional wool setting processes are commonly carried out at elevated temperatures, *e.g.*, the CHEMSET process is performed at 85 °C whilst steam setting and boil setting are carried out at temperatures greater than 100 °C. However, if setting could be achieved at room temperature the process would be more energy efficient and economically more viable. Further studies were performed to investigate the effect of temperature on wool setting in the presence of cysteine. In this work, wool samples (~ 0.80 g wool per sample) were treated with cysteine (5 g L^{-1}, 500 mL) at room

temperature for between 2 minutes and 24 hours. After treatment, the wool was rinsed with Milli-Q water (500 mL) at room temperature for 1 minute. The setting of the yarn was analysed qualitatively using the Crink Angle Test which showed that the shape of the wool segments and the twist imparted into the yarn was retained better as the treatment time increased; however, even after 24 hours, the degree of setting was not as great as that achieved after 2 minutes when the process was carried out at 85 °C. These results suggest that elevated temperatures are necessary for wool setting.

A series of control experiments were performed in order to establish the parameters required to demonstrate the effect of cysteine on wool setting. Wool (~ 0.80 g) was treated in blank electrolyte (80 mL KH_2PO_4 buffer (0.05 M, pH 8.0) containing 0.1 M KNO_3) for 10, 20, 30 and 60 minutes at room temperature and at 85 °C. These and subsequent experiments were performed under an atmosphere of nitrogen. For setting using cysteine, a nitrogen atmosphere prevents oxidation of cysteine by oxygen which yields the corresponding disulfide, cystine. The degree of setting was analysed qualitatively using the Crink Angle Test. No setting was observed for the wool samples treated at room temperature. The wool segments did not retain any V-shape after immersion in Milli-Q water (50 mL) at room temperature overnight, instead a crink angle of 180° was observed. The cut-ends of the wool segments had also untwisted resulting in an ill-defined, fuzzy appearance indicating that the yarn was poorly-set. Setting was observed for all wool samples treated at 85 °C and retention of the shape and twist of the wool segments increased as the treatment time increased representing a greater degree of set in the yarn. These results confirm that heat is required to set wool and that a significant amount of set is achieved at long times. Therefore, in order to observe the effect of the cysteine reducing agent on wool setting, the treatment time must be short. Unless stated otherwise, all subsequent experiments were carried out at 85 °C and wool was treated for 5 minutes.

5.3.2.3 Effect of Cysteine Concentration on Wool Setting

The effect of cysteine concentration on wool setting was studied using a range of cysteine concentrations (1, 4 and 6 mM). A control experiment was also carried out by treating wool in blank electrolyte (150 mL KH_2PO_4 buffer (0.05 M, pH 8.0) containing 0.1 M KNO_3). Wool (2 g) was treated for 5 minutes followed by rinsing in Milli-Q water (1 L) for 4 minutes and left to dry for 24 hours. The experiments were performed at 85 °C and carried out twice to assess the reproducibility of the reactions. Quantitative analysis of the degree of setting was performed by immersing V-shaped wool segments (n = 30) into Milli-Q water (200 mL) overnight at room temperature or for 30 minutes at 50 °C. The inside crink angle of the wool segments was measured after they had been allowed to dry over 24 hours. In addition to studying the effect of cysteine concentration on wool setting, the effect of temperature on the Crink Angle Test was also examined during these experiments. A linear relationship was observed for crink angle with respect to cysteine concentration (Table 5.4, Figure 5.8). The degree of setting was observed to increase (represented by a decrease in crink angle) as the cysteine concentration increased. The greatest degree of setting was achieved using 6 mM cysteine (89 ± 23° (n = 2)). Excellent reproducibility is observed between experiments when the natural variability of wool is taken into consideration. The measured crink angles were greater when V-shaped wool segments were immersed in water for 30 minutes at 50 °C compared to immersion overnight at room temperature. Temporary setting, involving the cleavage and reformation of hydrogen bond networks within wool proteins, is rapidly and completely relaxed by immersion in warm water, therefore, testing the degree of setting at 50 °C allows for differentiation between semi-permanent and temporary setting. All subsequent wool setting experiments were performed using 6 mM cysteine and the Crink Angle Tests were carried out at 50 °C to achieve a more accurate representation of the set imparted into the wool during treatment.

Table 5.4. The effect of cysteine concentration on wool setting. Wool (2 g) was treated with cysteine at 85 °C for 5 minutes followed by rinsing in Milli-Q water (1 L) at 85 °C for 4 minutes. The quoted errors correspond to two standard deviations and these values cover the range of values observed in the raw data.

[Cysteine] (mM)	Average crink angle (°)[a]			
	Room temperature		50 °C	
	Run 1	Run 2	Run 1	Run 2
KH_2PO_4 buffer (0.05 M, pH 8.0)	103 ± 19	109 ± 25	118 ± 19	128 ± 19
1	96 ± 24	99 ± 30	118 ± 27	116 ± 21
4	83 ± 22	92 ± 21	94 ± 26	114 ± 20
6	60 ± 26	58 ± 17	89 ± 23	89 ± 22

[a] The inside crink angle was measured after immersing V-shaped wool segments (n = 30) into Milli-Q water (200 mL) for 30 minutes at 50 °C and dried over 24 hours.

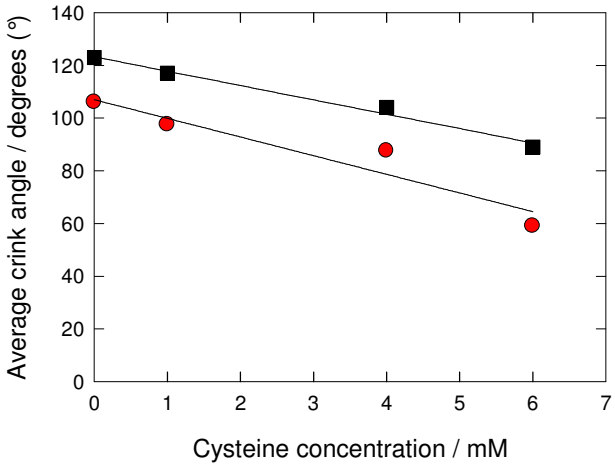

Figure 5.8. Plot of average crink angle measured *versus* cysteine concentration. Wool (2 g) was treated with cysteine at 85 °C for 5 minutes followed by rinsing in Milli-Q water (1 L) at 85 °C for 4 minutes. The Crink Angle Test was carried out by immersing V-shaped wool segments (n = 30) into Milli-Q water (200 mL) overnight at room temperature (●) or for 30 minutes at 50 °C (■) and measuring the inside crink angle.

5.3.2.4 Effect of Depletion of the Cysteine Reducing Agent on Wool Setting During the Batch Treatment of Wool

Further experiments were performed using limiting conditions to demonstrate the effect that depletion of the cysteine reducing agent has on wool setting. To determine the appropriate ratio of cysteine to wool for these experiments, the chemistry of the wool setting reaction was considered. During conventional wool setting processes approximately 20 % of the wool disulfide bonds (cystine residues) are cleaved.[3,6] The total amount of cystine in wool is 400-500 μmol g^{-1},[3] therefore, the estimated range of wool disulfide bonds cleaved per gram of wool is 80-100 μmol. For the experiments carried out in this study, each batch of wool consisted of 1.6 g of wool, hence it is expected that 128-160 μmol of wool disulfide bonds are cleaved during treatment. From the stoichiometry of equation 1 (Scheme 5.1), 256-320 μmol of cysteine is required to cleave the wool disulfide bonds during the setting process. The setting solution (150 mL) was prepared containing 900 μmol of cysteine (6 mM) so that the setting agent would rapidly become limiting as 20 batches of wool (~ 1.6 g wool per batch) were treated consecutively in the solution. Each batch was immersed in the setting solution at 85 °C for 5 minutes followed by rinsing in Milli-Q water (1 L) at 85 °C for 4 minutes. The experiment was replicated three times. The degree of setting was examined by immersing V-shaped wool segments (n = 30) into Milli-Q water (200 mL) for 30 minutes at 50 °C. Examination of batches one, two and every second batch thereafter was found to be sufficient to show the trends in wool setting. It should also be noted that for this and subsequent experiments the outside angle of the V-shaped segments of wool were measured to also account for loss of yarn twist (Figure 5.9).

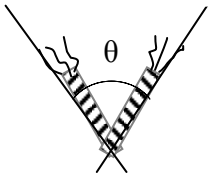

Figure 5.9. Measurement of the outside angle of a V-shaped wool segment for determining the degree of setting using the Crink Angle Test.

A linear relationship was observed between the number of batches of wool treated and the measured crink angle (Figure 5.10, Table 5.5). The average crink angle measured for each batch of wool increased as the number of batches of wool treated consecutively in the cysteine treatment solution increased (100 ± 31 to 158 ± 24° for wool batches 1 to 20 (n = 3)) indicating that the degree of wool setting decreases as more batches of wool are treated due to depletion of the cysteine reducing agent. Retention of the twist imparted into the yarn was also observed to decrease as the number of wool batches treated increased. The cut ends of the V-shaped wool segments were observed to untwist resulting in an increasingly ill-defined, fuzzy appearance. Excellent reproducibility was observed between experiments considering the natural variation of the wool sample. The scatter observed in the data was attributed to natural variation within the wool fibre.

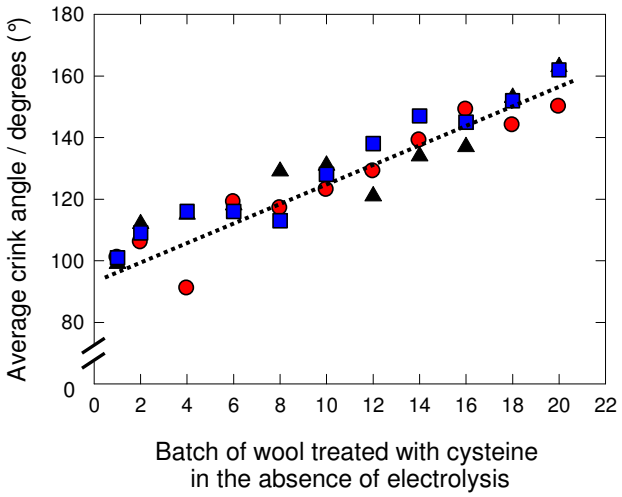

Figure 5.10. Plot of average crink angle measured *versus* the batch of wool treated with cysteine in the absence of electrolysis. Twenty batches of wool (~ 1.6 g wool per batch) were treated consecutively with cysteine (initial concentration 6 mM, 150 mL) at 85 °C for 5 minutes followed by rinsing in Milli-Q water (1 L) at 85 °C for 4 minutes. The Crink Angle Test was carried out by immersing V-shaped wool segments (n = 30) into Milli-Q water (200 mL) for 30 minutes at 50 °C and measuring the outside crink angle. The experiment was replicated three times (run 1 (▲), run 2 (●) and run 3 (■)). The dotted line is a visual guide only.

Table 5.5. The effect of depletion of the cysteine reducing agent on wool setting. Twenty batches of wool (~ 1.6 g wool per batch) were treated consecutively with cysteine (initial concentration 6 mM, 150 mL) at 85 °C for 5 minutes followed by rinsing in Milli-Q water (1 L) at 85 °C for 4 minutes. Examination of the degree of setting was carried out by performing the Crink Angle Test on batches one, two and every second batch there after. The quoted errors correspond to two standard deviations and these values cover the range of values observed in the raw data.

Batch	Average Crink Angle (°)[a]		
	Run 1	Run 2	Run 3
1	99 ± 24	101 ± 36	101 ± 34
2	112 ± 36	106 ± 28	109 ± 28
4	115 ± 30	91 ± 26	116 ± 30
6	118 ± 30	119 ± 24	116 ± 28
8	129 ± 36	117 ± 26	113 ± 28
10	131 ± 34	123 ± 28	128 ± 28
12	121 ± 30	129 ± 30	138 ± 26
14	134 ± 20	139 ± 24	147 ± 24
16	137 ± 32	149 ± 16	145 ± 28
18	153 ± 22	144 ± 28	152 ± 30
20	162 ± 18	150 ± 26	162 ± 26

[a] The outside crink angle was measured after immersing V-shaped wool segments (n = 30) into Milli-Q water (200 mL) for 30 minutes at 50 °C and dried over 24 hours.

5.3.3 Electrochemical Regeneration of Cysteine during Wool Setting

The batch treatment of wool described in Section 5.3.2.4 was repeated in the presence of electrolysis to regenerate the cysteine setting agent. Twenty batches of wool (~ 1.6 g wool per batch) were treated consecutively with cysteine (initial concentration 6 mM, 150 mL) at 85 °C for 5 minutes followed by rinsing in Milli-Q water (1 L) at 85 °C for 4 minutes. The cysteine setting agent was regenerated by applying a constant potential of -0.90 V at a nanoAu/CF electrode (geometric area of 99 cm^2 per side). For each batch of wool, electrolysis was performed during wool

treatment and for a further 5 minutes whilst the wool was subjected to the rinsing procedure. The experiment was replicated three times and excellent reproducibility was observed between experiments. Quantitative analysis of the degree of setting showed that setting was maintained for the first 6 batches of wool treated as the average crink angle remained constant (99 ± 30° (n = 3)) (Figure 5.11, Table 5.6). Treatment of subsequent batches of wool (batches 8-20) showed a general increase in the average crink angle as the number of batches of wool treated increased indicating a gradual decline in the degree of set (107 ± 25 to 136 ± 25° for batches 8 to 20 (n = 3)). These results suggest that regeneration of the cysteine setting agent is having the greatest effect on the first 6 batches of wool treated. Scatter observed in the data is attributed to natural variation in the wool which cannot be controlled.

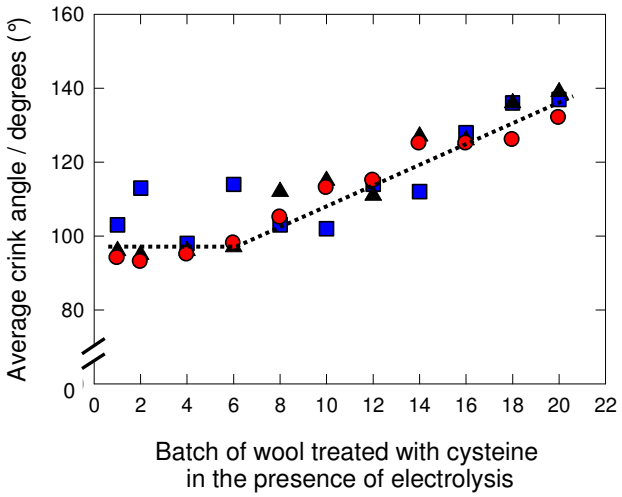

Figure 5.11. Plot of average crink angle measured *versus* the batch of wool treated with cysteine in the presence of electrolysis. Twenty batches of wool (~ 1.6 g wool per batch) were treated consecutively with cysteine (initial concentration 6 mM, 150 mL) at 85 °C for 5 minutes followed by rinsing in Milli-Q water (1 L) at 85 °C for 4 minutes. Cysteine was electrochemically regenerated at a nanoAu/CF electrode by applying a constant potential of -0.90 V. The Crink Angle Test was carried out by immersing V-shaped wool segments (n = 30) into Milli-Q water (200 mL) for 30 minutes at 50 °C and measuring the outside crink angle. The experiment was replicated three times (run 1 (▲), run 2 (●) and run 3 (■)). The dotted line is a visual guide only.

Table 5.6. The effect of electrochemical regeneration of cysteine on wool setting. Twenty batches of wool (~ 1.6 g wool per batch) were treated consecutively with cysteine (initial concentration 6 mM, 150 mL) at 85 °C for 5 minutes in the presence and absence of electrolysis. Cysteine was electrochemically regenerated at a nanoAu/CF electrode by applying a constant potential of -0.90 V. Examination of the degree of setting was carried out by performing the Crink Angle Test on batches one, two and every second batch there after. The quoted errors correspond to two standard deviations and these values cover the range of values observed in the raw data.

Batch	**Average Crink Angle (°)**[a]		
	Run 1	**Run 2**	**Run 3**
1	96 ± 40	94 ± 26	103 ± 28
2	95 ± 26	93 ± 32	113 ± 26
4	96 ± 24	95 ± 26	98 ± 26
6	97 ± 36	98 ± 42	114 ± 26
8	112 ± 28	105 ± 26	103 ± 28
10	115 ± 32	113 ± 24	102 ± 48
12	111 ± 32	115 ± 22	114 ± 11
14	127 ± 38	125 ± 26	112 ± 48
16	126 ± 36	125 ± 26	128 ± 34
18	136 ± 36	126 ± 46	136 ± 30
20	139 ± 20	132 ± 26	137 ± 28

[a] The outside crink angle was measured after immersing V-shaped wool segments (n = 30) into Milli-Q water (200 mL) for 30 minutes at 50 °C and dried over 24 hours.

The cysteine setting agent was regenerated by electrochemically reducing cystine produced as a result of the wool setting reaction (Scheme 5.1). For each batch of wool treated, the total charge passed during electrolysis represents the amount of cystine reduced. In general, the charge passed (per batch) was observed to decrease from batches 1 to 5 and then remain almost constant for batches 5 to 20 (Figure 5.12). The charge passed for the first batch of wool treated was much greater than that for subsequent batches. No corrections were made for the background current in these experiments, hence the charge passed for the first batch of wool most likely includes a contribution from the background.

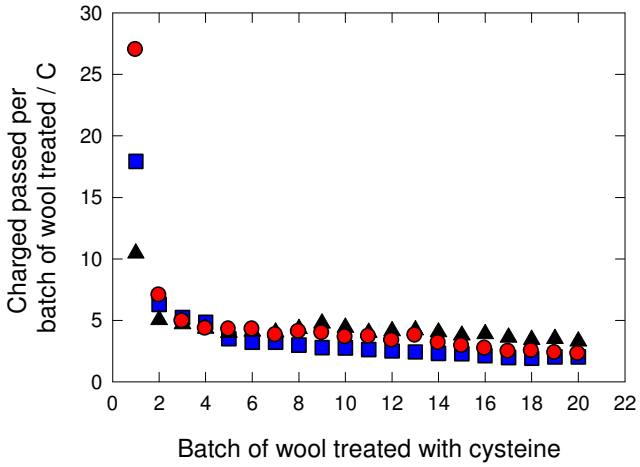

Figure 5.12. Plot of the number of batches of wool treated with cysteine *versus* the charge passed during electrolysis for each batch of wool. Twenty batches of wool (~ 1.6 g wool per batch) were treated consecutively with cysteine (initial concentration 6 mM, 150 mL) at 85 °C for 5 minutes followed by rinsing in Milli-Q water (1 L) at 85 °C for 4 minutes. Cysteine was electrochemically regenerated at a nanoAu/CF electrode by applying a constant potential of -0.90 V. The experiment was replicated three times (run 1 (▲), run 2 (●) and run 3 (■)).

The amount of cystine reduced during each electrolysis for batches 5 to 20 (17.00 ± 3.80 μmol (n = 3)) was determined from the average charge passed (3.27 ± 0.70 C (n = 3)) using equation 5.1. This expression is derived from Faraday's laws,

$$N_j = \frac{Q}{nF} \tag{5.1}$$

where N_j is the total number of mols of cystine, Q represents the average charge passed during electrolysis, n is the number of electrons required to reduce cystine (n = 2) and F is the Faraday constant. From the stoichiometry of equation 3 (Scheme 5.1), 34 μmol of the cysteine setting agent is regenerated during the treatment of each batch of wool in the presence of electrolysis.

For the experiments carried out in this study, each batch consisted of 1.6 g of wool and hence, as explained in Section 5.3.2.4, the amount of cystine produced should be 128-160 μmol per batch for 'complete' setting. Subsequently, from the stoichiometry of equation 3 (Scheme 5.1), if all the cystine produced was electrochemically reduced at the nanoAu/CF electrode then a yield of 256-320 μmol of cysteine would be expected; however, the amount of cysteine produced during electrolysis for each batch of wool (34.00 μmol) is much lower. The turnover of cysteine obtained during electrolysis can be determined using equation 5.2,

$$\text{Turnover of cysteine during electrolysis} = \frac{(\text{mols cysteine})_{\text{electrolysis}}}{(\text{mols cysteine})_{\text{maximum}}} \times \frac{100}{1} \tag{5.2}$$

where '$(\text{mols cysteine})_{\text{electrolysis}}$' represents the amount of cysteine determined from the charge passed during electrolysis (34.00 μmol) and '$(\text{mols cysteine})_{\text{maximum}}$' is the maximum theoretical amount of cysteine that can be obtained from the electroreduction of the cystine produced during wool setting (256-320 μmol). Using these values and equation 5.2, the turnover of cysteine obtained during electrolysis for each batch of wool was 10-13 %. The low turnover associated with the steady charge passed for batches 5 to 20 in Figure 5.12 suggests fouling of the nanoAu/CF electrode. This would cause the electrode to become blocked and hence, the efficiency of the electroreduction of cystine would decrease. As a result the degree of setting would also decrease as the cysteine setting agent is effectively being depleted due to low turnover of cysteine. This was observed in Figure 5.12

where the degree of setting decreased from batches 6 to 20 treated in the presence of electrolysis. A progressive colour change from colourless to yellow is observed for the cysteine treatment solution over the course of the experiment in the presence and absence of electrolysis. This colour change may be due to contaminants such as small amounts of residual processing lubricant or wool grease leaching out of the wool during treatment and hence, surface fouling could result from these contaminants absorbing to the electrode surface. Alternatively, the wool itself could block the electrode surface as it is positioned inside the nanoAu/CF electrode in the cell set-up. Degradation of the cysteine setting agent at the elevated temperatures used in this research may also be a contributing factor to the colour change observed during the experiment.

5.3.4 Comparison of Wool Setting with Cysteine in the Absence and Presence of Electrolysis

The degree of setting, represented by crink angle, determined for 20 batches of wool treated with cysteine (initial concentration 6mM, 150 mL) at 85 °C for 5 minutes in the absence and presence of electrolysis is shown in Figure 5.13. Electrolysis is observed to have the greatest effect on the first 6 batches of wool treated as the degree of setting is maintained at 99 ± 30° (n = 3). In comparison, the average crink angle gradually increased over the same number of wool batches treated in the absence of electrolysis (100 ± 31 to 118 ± 27° for wool batches 1 to 6 (n = 3)) representing a decline in the degree of setting due to depletion of the cysteine reducing agent. Treatment of subsequent batches of wool in the presence and absence of electrolysis (batches 8 to 20) shows a general increase for the average crink angle measured as the number of batches of wool treated increases; however, after treatment of 20 batches of wool, the degree of setting is still greater in the presence of electrolysis (136 ± 25° (n = 3)) compared to in the absence of electrolysis (158 ± 23° (n = 3)). The decrease in wool setting observed in the presence of electrolysis is attributed to low turnover of the cysteine reducing agent at the nanoAu/CF electrode as discussed in Section 5.3.3.

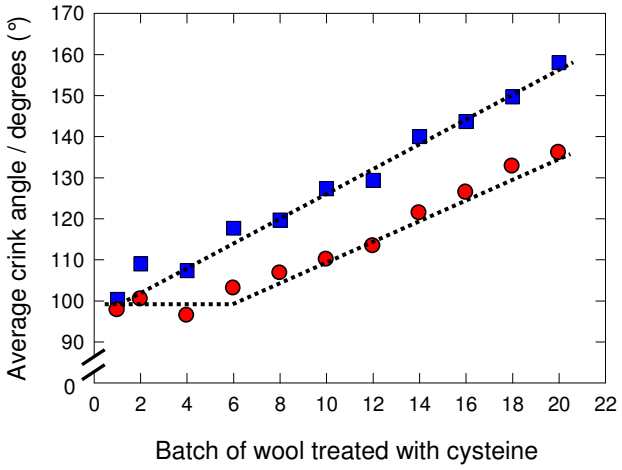

Figure 5.13. Plot of average crink angle measured *versus* the batch of wool treated with cysteine in the absence (■) and presence (●) of electrolysis. Twenty batches of wool (~ 1.6 g wool per batch) were treated consecutively with cysteine (initial concentration 6 mM, 150 mL) at 85 °C for 5 minutes followed by rinsing in Milli-Q water (1 L) at 85 °C for 4 minutes. Cysteine was electrochemically regenerated at a nanoAu/CF electrode by applying a constant potential of -0.90 V. The Crink Angle Test was carried out by immersing V-shaped wool segments (n = 30) into Milli-Q water (200 mL) for 30 minutes at 50 °C and measuring the outside crink angle. The crink angles plotted are the average values measured for three replicate experiments. The dotted lines are a visual guide only.

Analysis of the twist imparted into the woollen yarn for batches 1, 6 and 20 after performing the Crink Angle Test also revealed that twist was retained to a greater extent when wool setting was carried out in the presence of electrolysis (Figure 5.14). The degree of twisting was retained from batch 1 to 6 treated in the presence of electrolysis and a small amount of untwisting was observed for batch 20. For wool treated in the absence of electrolysis, the cut ends of the V-shaped wool segments were observed to untwist resulting in an increasingly ill-defined, fuzzy appearance indicating that the wool was poorly-set.

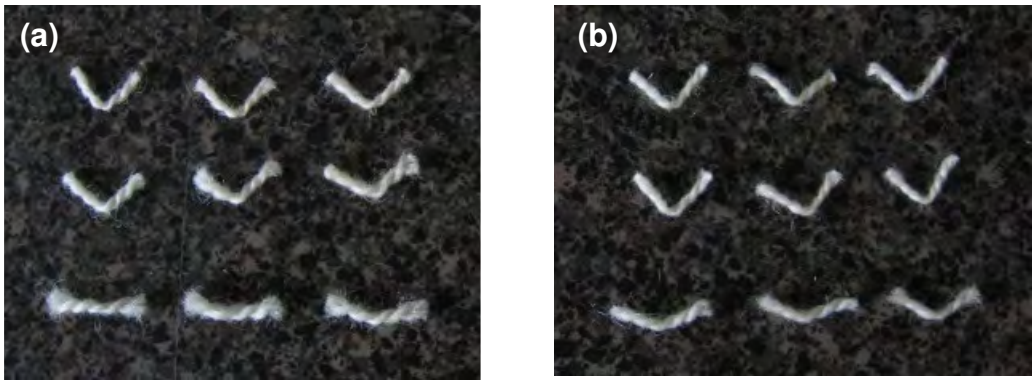

Figure 5.14. Retention of twist imparted into woollen yarn (batches 1, 6 and 20 from top to bottom respectively) after consecutive treatment with cysteine (initial concentration 6 mM, 150 mL) at 85 °C for 5 minutes in (a) the absence and (b) the presence of electrolysis. Cysteine was electrochemically regenerated at a nanoAu/CF electrode by applying a constant potential of -0.90 V. The retention of twist was analysed after immersing V-shaped wool segments (n = 30) into Milli-Q water (200 mL) for 30 minutes at 50 °C. The V-shaped wool segments shown in this figure are representative of the sample analysed (n = 30).

5.3.5 Method Development for the Electrochemical Regeneration of Cysteine during Wool Setting using the WRONZ Set Tester

As previously mentioned, the WRONZ Set Tester was used in preliminary experiments to examine wool setting. The results obtained using this method were internally inconsistent and showed poor reproducibility for identical experiments. Initially, these observations were assumed to be due to the chemistry and experimental method of the setting process rather than the method used to quantify the degree of setting. Later experiments confirmed that the WRONZ Set Tester was not a reliable method for measuring the amount of setting in this work. The poor reproducibility observed between identical experiments is illustrated in Figure 5.15 which shows the degree of setting determined for 4 batches of wool treated consecutively with cysteine (initial concentration 6 mM, 150 mL) at 85 °C for 5 minutes in the presence of electrolysis. In addition to poor reproducibility between experiments, setting was not maintained for all batches of wool treated as expected.

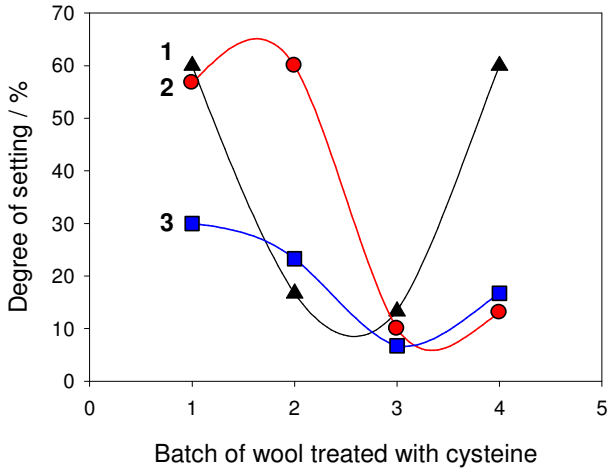

Figure 5.15. Reproducibility of the degree of setting, determined using the WRONZ Set Tester at 200 cycles, for the batch treatment of wool with cysteine (initial concentration 6 mM, 150 mL) at 85 °C for 5 minutes in the presence of electrolysis. The experiment was replicated three times (run 1 (▲), run 2 (●) and run 3 (■)) and 4 batches of wool were used for each experiment.

Further analysis of the results obtained provided convincing evidence that the source of the inconsistencies observed was due to the WRONZ Set Tester and not the experimental method used for the setting process. Set testing was performed at 200 and 300 cycles for each wool sample analysed (30 snippets of wool were used for each test). Due to the destructive nature of the test, it is expected that the number of wool snippets that remain intact will be greater after 200 cycles compared to 300 cycles; however, no clear relationship was observed when all wool samples analysed were considered (Figure 5.16) and different conclusions could be reached depending on whether the data for 200 or 300 cycles was used to determine the degree of setting for an experiment. A lack of reproducibility was also observed between the number of snippets intact after 300 cycles for the same number of snippets intact after 200 cycles and vice versa.

(a)

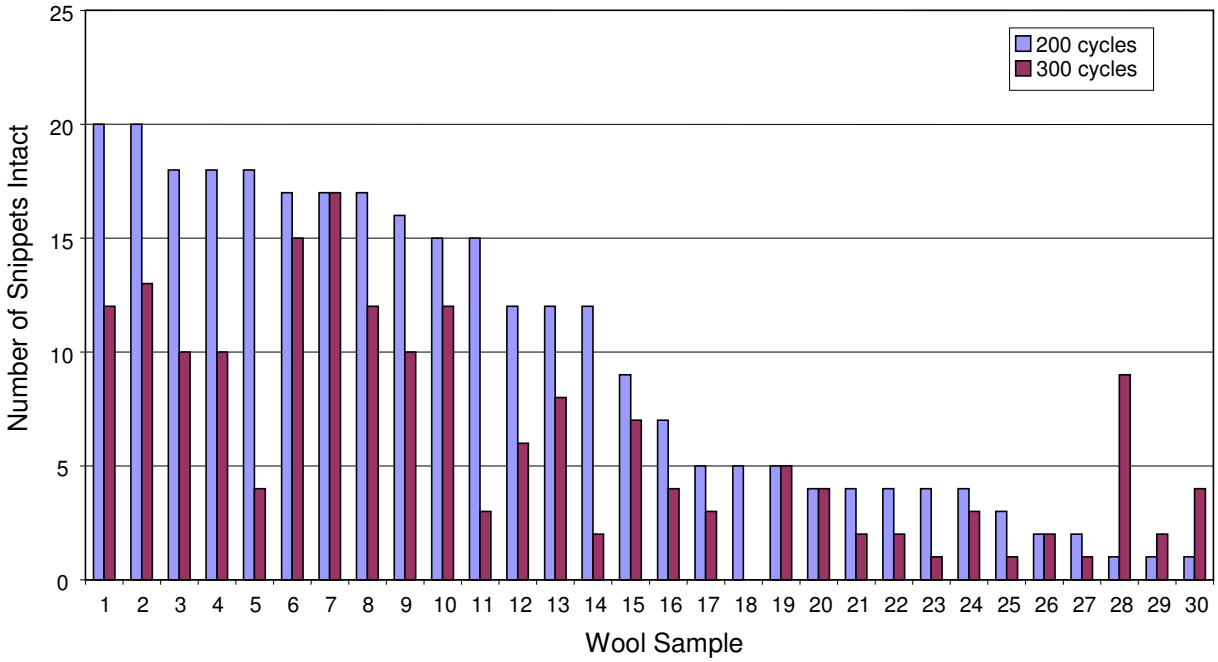

(b)

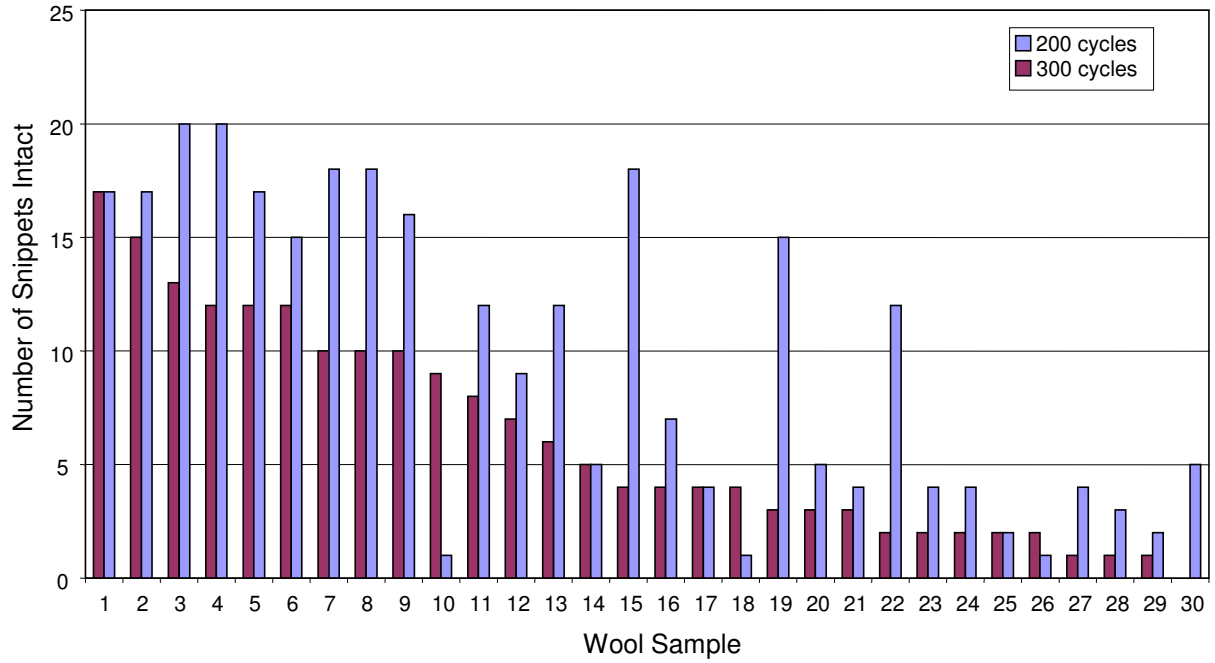

Figure 5.16. Relationship between the number of snippets intact after 200 cycles and 300 cycles when analysing wool setting using the WRONZ Set Tester; (a) decreasing order of 200 cycle data, (b) decreasing order of 300 cycle data.

Additional evidence for the WRONZ Set Tester being the source of inconsistency was obtained by treating two batches of wool simultaneously with cysteine (initial concentration 6 mM, 150 mL) at 85 °C for 5 minutes. The degree of setting for each batch of wool was analysed separately. For this experiment, the sample size for each batch of wool was increased to give 200 snippets for analysis. The increased sample size allowed the test to be carried out using standard Set Tester methods where subsets of the wool sample (50 snippets) were analysed after 100, 200, 300 and 400 cycles. The number of snippets which did not remain intact (% breakdown) was plotted against the number of cycles and a logarithmic trendline was fitted to the data. From the trendline, the number of cycles to 50 % breakdown (representing 50 % set in the wool sample) was determined as a comparative test for set. Poor reproducibility was once again exhibited as the number of cycles required to achieve 50 % set was 414 and 157 cycles for batch one and two respectively.

The WRONZ Set Tester was developed using large sample sizes (50 g of wool) and therefore, the internal inconsistencies and lack of reproducibility experienced using this method to examine the degree of setting in this study is most likely due to small sample size (0.8-2 g of wool) and natural variation in the wool.

5.4 Conclusions

Electrochemical setting using low concentrations of cysteine to mediate the reduction of wool disulfide bonds has been successfully demonstrated with excellent reproducibility. Electrolysis of solution-based cystine at a nanoAu/CF electrode to regenerate the cysteine reducing agent allowed the degree of setting for the first 6 batches of wool treated to be maintained. In the absence of electrolysis, a gradual decline in the degree of setting over the same number of wool batches was observed due to depletion of the cysteine reducing agent. Treatment of subsequent batches of wool in the presence and absence of electrolysis showed a decrease in setting as the number of batches treated increased. In the presence of electrolysis, this was attributed to fouling of the nanoAu/CF electrode at the monolayer level causing the electrode to become blocked and hence, the efficiency of the electrochemical regeneration of the cysteine reducing agent was decreased.

The application of electrochemical methods to regenerate the cysteine setting agent by reduction of the disulfide product formed during reaction with the wool shows great promise. A major advantage of using electrochemical methods is that they require lower levels of reagents. In this work, the initial concentration of cysteine (6 mM = 0.73 g L^{-1}) used was 10 times less than the amount of sodium metabisulfite used in industrial processes (7.5 g L^{-1}). However, to make the use of cysteine economically viable, further research needs to be carried out to increase the turnover of the thiol reducing agent regenerated at the nanoAu/CF electrode so that the degree of setting can be maintained for more than 6 batches of wool. It is envisaged that design of a two compartment cell where the electrochemical system is separated from the wool by a porous membrane allowing diffusion of cysteine and cystine would reduce fouling of the nanoAu/CF electrode due to the wool blocking the electrode and increase the efficiency of the reaction to regenerate the cysteine reducing agent. Alternatively, the electrochemical cell for regenerating the cysteine could be remote from the wool itself and the treatment solution could be pumped to and from the wool being set. In addition, the use of anti-fouling coatings could also be investigated to reduce fouling of the nanoAu/CF electrode by residual contaminants leaching into solution from the wool. It is noted that the design of a new electrochemical cell for wool setting requires consideration of the technical parameters involved in wool setting processes and needs to be suitable to scale up the reaction for industrial purposes.

As a result of this research, the concept of electrochemical regeneration of the setting agent during wool processing has been achieved and the organisation sponsoring this work has adopted a strategy for protecting the intellectual property in the interim whilst the economic and environmental drivers for this technology become increasingly important.

5.5 References for Chapter 5

1. Leach, S. J.; Meschers, A.; Swanepoel, O. A. The electrolytic reduction of proteins. *Biochemistry* **1965**, *4*, 23-27.

2. Wood, E. J., Get set, stay, in book, *Tangling with wool*. Wool Research Organisation of New Zealand (Inc.), Chaucer Press Ltd: Christchurch, New Zealand, 2000; p 10.1-10.7.

3. Maclaren, J. A.; Milligan, B., *Wool science: The chemical reactivity of the wool fibre.* Science Press: Marrickville, NSW, Australia, 1981; p 6, 19-20.

4. Gamble, J., *Effectiveness of various wool setting agents*, Wool Research Organisation of New Zealand (Inc.), **1998**, *unpublished report*.

5. McKinnon, A. J. Package-to-package carpet yarn wet processing: The CHEMSET technology. *Wool Science Review* **1990**, *66*, 3-43.

6. Watson, A. A.; Page, C. T. In *Chemical aspects of setting and set release in wool carpet yarns*, 8th International Wool Textile Research Conference, Christchurch, New Zealand, **1990**, p 502-511.

Chapter 6

Characterisation of Ethylenediamine Films Grafted to Carbon Electrodes

6.1 Introduction

Electrochemically assisted covalent modification of carbon surfaces is an increasingly active research area. Methods for binding specific organic groups to the surface of the carbon electrodes have been reviewed by Downard.[1] Electroreduction of aryl diazonium salts is the most common approach leading to grafting of the aryl group to the surface through a C–C bond and results in very stable layers.[2-5] Electro-oxidation of primary and secondary amines is also well established and attachment of the modifier to the surface occurs by a C–N bond.[6-8] Other methods have also been reported for functionalising carbon electrodes *via* the oxidation of alcohols,[9,10] carboxylates[11-13] and hydrazides[14,15] leading to strong covalent attachment of –OR, $–CH_2R$, –NHR groups respectively on the surface. Except for the oxidation of alcohols, all these modification methods proceed *via* the formation of solution radicals. For modification of carbon surfaces in the presence of anhydrous alcohol solutions, Ohmori and co-workers proposed that oxidation of the carbon surface generates an aromatic radical on the electrode surface, which subsequently undergoes nucleophilic attack by the alcohol leading to the covalent attachment of a layer of alkyl groups to the electrode, most likely by an ether link.[9]

Modification of carbon surfaces *via* the oxidation of amines is of most interest for the work described in this thesis. Hence, the following sections review the modification methods and mechanisms for grafting amine layers to carbon surfaces. Film stability and the redox activity of solution-based probes at amine-modified carbon electrodes are also discussed.

6.1.1 Covalent Modification of Carbon Electrodes *via* Oxidation of Amines

The grafting of primary and secondary amines to carbon surfaces by electro-oxidation in anhydrous ethanol or acetonitrile electrolyte solutions is well-established.[6-8] Cyclic voltammetric scans to potentials past the irreversible amine oxidation peaks or controlled potential electrolysis at sufficiently positive potentials lead to surface modification. Barbier and Pinson *et al.* were the first to describe this surface modification process by electrochemically oxidising primary amines onto glassy carbon and carbon fibre electrodes.[6] The proposed overall reaction resulted in the formation of a surface C–N covalent bond (Scheme 6.1).

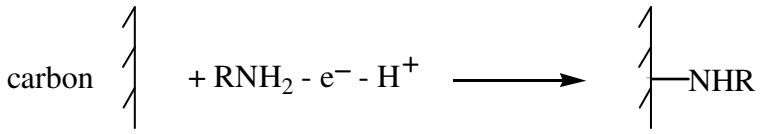

Scheme 6.1. Electrochemically assisted covalent modification of a carbon electrode *via* oxidation of a primary amine.

The attachment of the amino group to the carbon surface was initially assigned to the radical-cation formed upon oxidation of the amine (Scheme 6.2, Path A);[6] however, more comprehensive studies investigating the grafting mechanism of amines onto gold, platinum and carbon surfaces performed by Adenier *et al.* showed that the radical obtained after deprotonation of the radical-cation is responsible for the attachment reaction.[7] Amine modified surfaces were characterised using cyclic voltammetry, infrared reflection-absorption spectroscopy (IRRAS) and X-ray photoelectron spectroscopy (XPS). Although XPS analysis could not distinguish between the carbon-nitrogen bonds of the amine molecule grafted to the carbon surface and that responsible for surface attachment, analysis of modified gold and platinum surfaces provided direct evidence of the presence of a nitride (peaks at 398.1 and 397.9 eV for gold and platinum respectively) which was assigned to the metal-nitrogen bond. Further evidence for the radical mechanism was supported by IRRAS examination of platinum surfaces modified with deuterated 4-nitrobenzylamine which allowed the aromatic and nitro-groups to be observed and established that it was the amine radical obtained by deprotonation of the initial radical cation that binds directly to the surface. The combined results of these studies demonstrate that grafting of amines takes place through the nitrogen on gold and platinum and the same reaction was assumed to take place on carbon.[7] The

overall mechanism for modifying conducting substrates *via* the oxidation of amines is shown in Scheme 6.2 (Path B) and involves deprotonation of the radical-cation initially formed to yield a carbon-centered radical, followed by isomerisation to an amino radical which covalently couples to the surface.[7] Hence, the key reagent in the attachment reaction is the intermediate carbon-centered radical in equilibrium with its tautomeric amino radical.

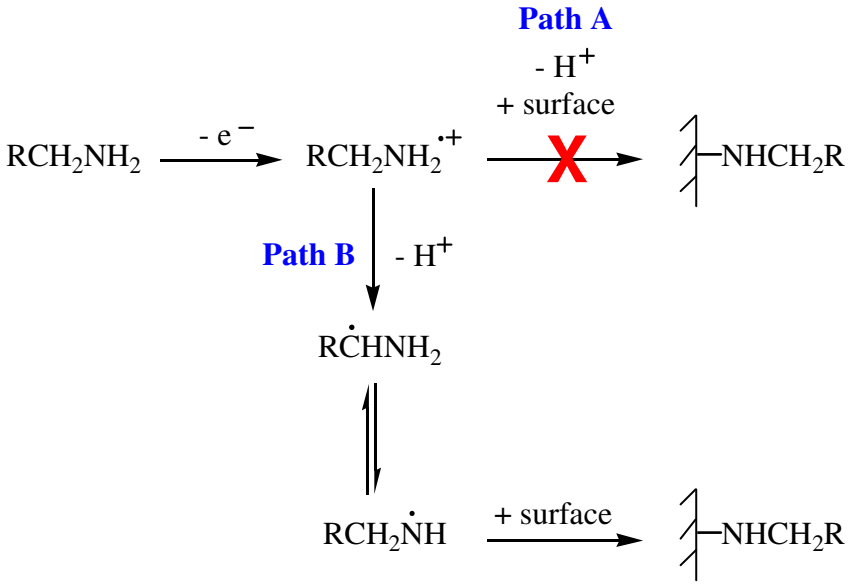

Scheme 6.2. Proposed mechanisms for the electrochemical grafting of amines to carbon surfaces *via* the formation of solution radicals. Path A: the radical forms directly on the nitrogen of the amine radical-cation *via* loss of a proton. Path B: a proton is lost from the methyl group directly attached to the amine radical-cation to yield a carbon-centered radical which subsequently isomerises to give the nitrogen-centered radical. Scheme taken from reference 7.

Immobilisation of primary, secondary and tertiary amines onto glassy carbon electrodes has been studied to examine the scope of the attachment reaction.[7,8] Cyclic voltammetric scans for primary, secondary and tertiary amines in anhydrous conditions exhibited well defined oxidation processes for all amine derivatives. The oxidation peak current for three repeat scans remained approximately the same for tertiary and secondary amines; however, for primary amines the peak current decreased upon repeat scanning and after three scans the electrode was completely blocked indicating that the grafting reaction is much more efficient with primary amines than secondary or tertiary amines. Sharpening of the oxidation peak coupled with a shift to less negative potentials was

also observed as alkyl substituents were added to the amine group. This was attributed to the alkyl substituents stabilising the amine radical-cation formed during the oxidation process.[8] The efficiency of the grafting reaction was determined by estimating the surface coverage of the grafted modifiers. Surface modification on carbon was detected using XPS[8] (surface coverage was estimated through N/C ratios) and by measuring the surface concentration of electroactive groups on the modifier using cyclic voltammetry, *e.g.*, the presence of nitrobenzylamine derivatives grafted to carbon surfaces was confirmed by observing the reversible one-electron redox reaction of the nitrophenyl group in anhydrous acetonitrile electrolyte.[6,7] Using these methods, primary amines gave the greatest surface coverages, low surface coverages were obtained for secondary amines and there was no evidence of immobilisation of tertiary amines. These results indicate that steric effects are important due to the substituents on the amine functionality hindering access to active sites at the carbon surface. It has also been noted that the proposed mechanisms for grafting amines to carbon surfaces require loss of a proton from the amine radical-cation and these pathways would not be available to tertiary amines (Scheme 6.2).[1] A wide variety of primary amines have been grafted to carbon surfaces, some examples of which are given in Table 6.1.

For primary alkylamines, the length of the alkyl chain has been reported to influence the yield and efficiency of the coupling reaction.[1,16] Hoekstra and Bein compared the surface coverages of glassy carbon electrodes modified with butylamine, 6-aminohexanol, decylamine and octadecylamine which possess different carbon chain lengths.[16] Based on N1s/C1s XPS peak ratios and assuming that the carbon signal originates from the glassy carbon surface, the surface coverages of 6-aminohexanol, decylamine and octadecylamine were similar but only 40-60 % of that observed for the butylamine modified electrode. It was noted by the authors that the C1s content includes a contribution from the carbons of the alkyl chain which may lower the N/C ratio for longer amines and hence, this needs to be considered when viewing these results. The efficiency of the grafting reaction was also shown to decrease as the length of the alkyl chain increased by the high amine concentrations or the greater number of cycles required to achieve maximum surface coverage. It was suggested that conformational disorder within the grafted alkyl chains may hinder access of further amine groups to the surface.

Table 6.1. Examples of primary amines which have been used for the electrochemically assisted covalent modification of carbon electrodes.

Amine	**Carbon Surface**	**References**
Ethylenediamine	GC, carbon fibre	6,17,18
Triethylenetetramine	Carbon fibre	6,18
Isobutylamine	Carbon fibre	6
2-Amino-4-methyl thiazole	Carbon fibre	6
Aminomethyl-9-anthracene	GC	6
4-Nitrobenzylamine	GC	6,7,19
N-(2-aminoethyl)-4-fluorobenzamide	Carbon fibre	6
n-Butylamine	GC	7,8,16
n-Hexylamine	GC	7,20
Cyclohexylamine	GC	7
tert-Butylamine	GC	7
3-Nitrobenzylamine	GC	7,19
N-Acetylethylenediamine	GC	8
N-Propylacetamide	GC	8
N-(5-Aminopentyl)biotinamide	GC	8
Dopamine	GC	8
6-Amino-1-hexanol	GC	16
Octadecylamine	GC	16
Decylamine	GC	16
1,7-Diaminoheptane	GC	21
1,10-Diaminodecane	GC	21
1,12-Diaminododecane	GC	21
Tetraethylene glycol diamine	GC	20
4-aminobenzoic acid	GC	22,23
Cysteine	GC	24

The carbon surface has also been shown to influence the efficiency of the grafting reaction for immobilisation of amines. Deinhammer *et al.* attempted to graft butylamine to the basal plane of HOPG and although amine oxidation was observed in cyclic voltammograms, there was no evidence of coupling from XPS analysis. Therefore, due to the basal plane of HOPG being unreactive, it was suggested that immobilisation of amines onto glassy carbon occurs only at edge plane sites.[8]

In addition to the electrografting of monoamines and aromatic amines, diamines have also received considerable attention. The orientation of diamines on the electrode surface and the mechanism of multilayer film growth has been of particular interest. Diamines with long alkyl chains, *e.g.*, 1,7-diaminoheptane, 1,10-diaminodecane and 1,12-diaminododecane, are assumed to bind to surfaces through one amine group and are expected to be aligned upright on the surface leaving the other amine group free in solution.[21] In contrast, several workers have examined the grafting of ethylenediamine (ED) to carbon surfaces and have reported that this species can bind through one amine group, leaving the other amine group free in solution, or through both amine groups in a bridged conformation (Scheme 6.3 (a, b)).[1,6,17] Barbier, Pinson *et al.* determined the relative amounts of each conformation by treating ED modified carbon fibres with 4-fluoro-benzoyl chloride, a protecting group for amines. This species would only react with ED bonded to the surface in the straight chain conformation with free amine groups. In the bridged conformation, the secondary amine groups formed through attachment of ED *via* both amine groups at the surface are sterically hindered. XPS was used to quantify the fluorine atoms in 4-fluoro-benzoyl chloride coupled to the ED-modified carbon fibres. The results were interpreted as showing that approximately 75 % of the diamines were bonded to the surface in the bridged conformation and 25 % were bound to the surface through a single amine. However, this conclusion should be viewed with caution because the formation of a polymeric structure when ED is grafted to carbon fibres leading to a multilayer film would also account for the lack of terminal primary amines. Other researchers have observed multilayer amine films after electro-grafting ED to conductive surfaces suggesting that the formation of polymeric chains is more predominant than binding of the amine molecule to the surface *via* both amino groups in the bridged conformation. Antoniadou *et al.* determined the total amount of ED bonded to the surface of carbon fibres by measuring the charge passed during the grafting reaction and assuming 100 % efficiency.[17] Based on the electrochemically active surface area of the carbon fibres (1 g of unmodified carbon fibres corresponded to 0.17 m^2 of electrochemically active surface area), it was estimated that

2.1 milli equivalents of ED was bonded per gram of carbon fibres. This result demonstrated that greater than a monolayer of ED molecules was attached to the surface during modification and suggested that polymeric chains were formed on the fibre surface (Scheme 6.3 (c)). It is noted that assuming 100 % grafting efficiency when determining the total amount of ED bonded to the surface of carbon fibres is likely to significantly overestimate the amount of attached ED as electrografting is generally accepted to be less than 100 % efficient.[2]

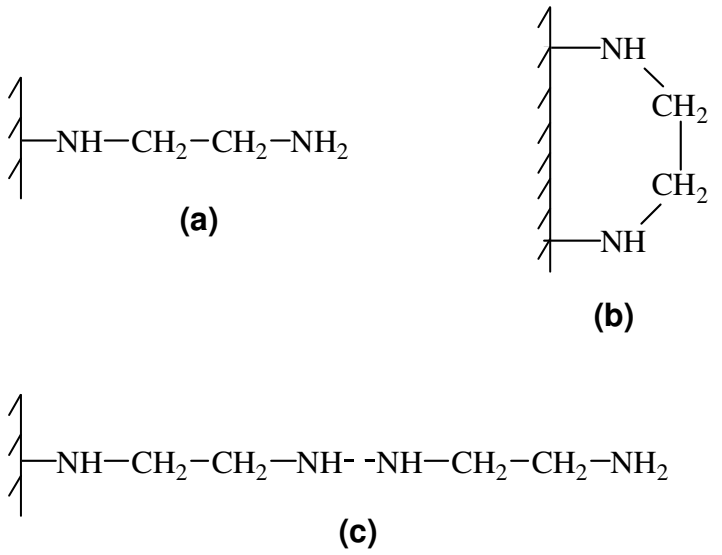

Scheme 6.3. Grafting of ED to carbon surfaces through (a) one amine group, (b) both amine groups and (c) the formation of polymeric chains. Scheme adapted from reference 1.

The formation of polymeric chains was investigated further by coupling the electroactive dinitrobenzoyl chloride to primary amine groups on ED-modified surfaces.[17] The amount of dinitrobenzoyl chloride attached to the ED film was determined by measuring the charge passed during the reaction. It was estimated that ~ 1.8×10^{-2} milli equivalents of the electroactive species were attached to the amine groups indicating that only a small number (> 1 %) of the total amino groups were terminal, *i.e.*, not bound to carbon in the bridged conformation or involved in polymer formation.

Whilst the mechanism for the multilayer grafting process of diamines at carbon electrodes has not been investigated, Herlem *et al.* have examined the electrochemical polymerisation of ED, diethylenetriamine and 1,3-diaminopropane (all primary amines) at platinum and gold electrodes

using pure liquid amines with inert supporting electrolyte (no added solvent).[25,26] From spectroscopic examination of ED films only linear polymers could be detected, the presence of alkyl and amino groups was observed but N–N, N=N, C=N or C=C bonds were not detected suggesting that the polymer coating network contained the pattern $–CH_2–CH_2–N$ with terminal $–NH_2$ groups. The tentative mechanism proposed to explain the growth of multilayer films on metallic electrodes was based on scission of the radical cation formed during the oxidation of primary amines to yield a primary carbocation at the surface followed by elimination of an amine radical from the modifier.[26] It was suggested that the resulting carbocation could subsequently attack the amino group of another diamine molecule in solution to yield a linear multilayer coating (Scheme 6.4).[26] However, the formation of a primary carbocation and an amine radical from the proposed scission of the radical cation seems unlikely given the mechanism shown in Scheme 6.2, Path B. Reaction of solution-based carbon or nitrogen-centered radicals with modifier attached to the surface would lead to multilayer film growth and incorporation of terminal primary amines in the film.

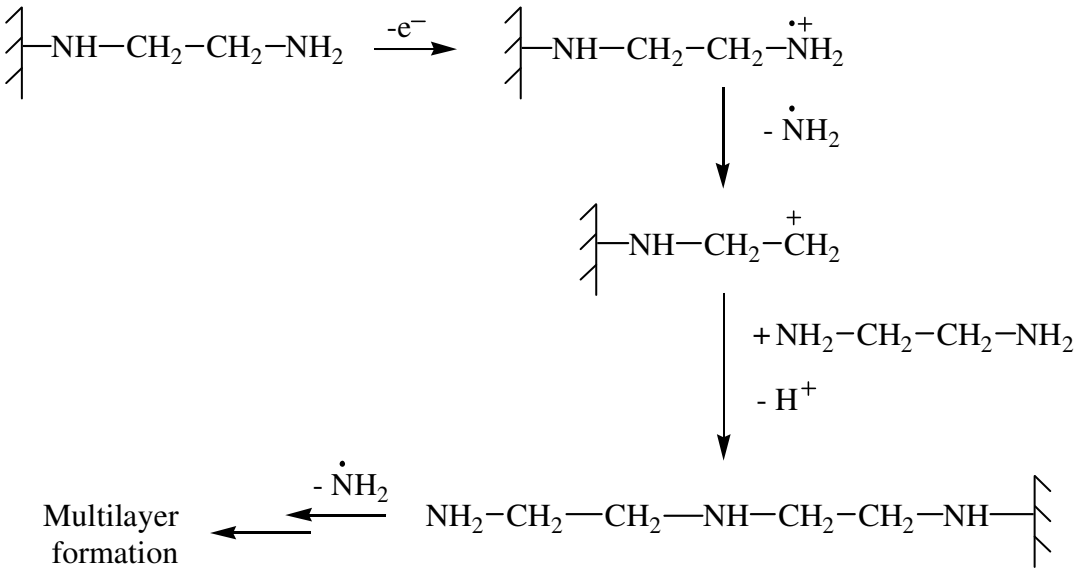

Scheme 6.4. Proposed mechanism for the multilayer formation of ethylenediamine at platinum and gold electrodes based on the formation of a primary carbocation generated during the oxidation of primary amines already attached to the surface by cleaving the carbon-nitrogen bond and eliminating the amine group from the modifier. Scheme adapted from reference 26.

For the electropolymerisation of primary amines, Herlem *et al.* also proposed that in the presence of moisture a side reaction could lead to the formation of aldehyde and ammonia.[25] XPS analysis of surface films showed the presence of a few oxygen atoms which were attributed to the formation of C=O bonds *via* the reaction shown in Scheme 6.5.[25,26]

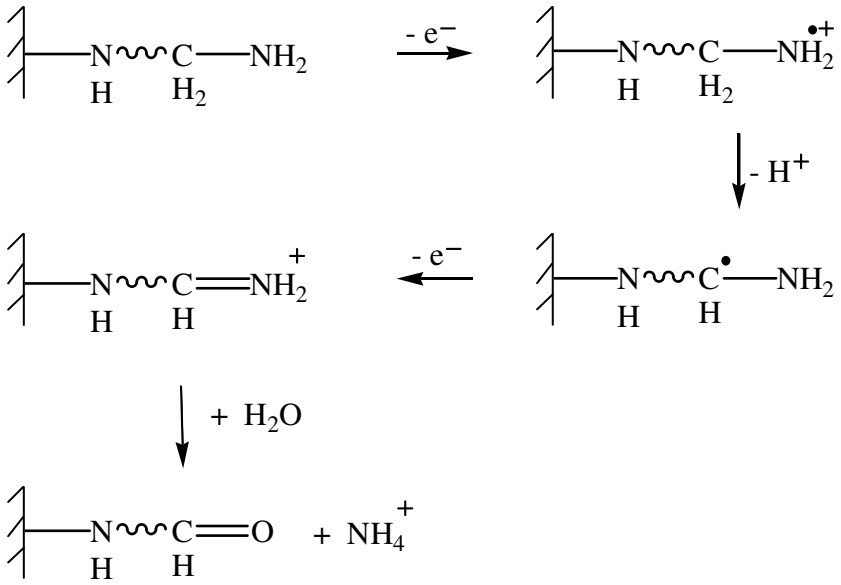

Scheme 6.5. The formation of aldehyde groups within the surface-attached amine film during the electropolymerisation of primary amines in the presence of moisture.

6.1.2 Stability of Amine Films Grafted to Carbon Electrodes

A variety of physical techniques and chemical treatments have been applied to amine-grafted electrodes to test the stability of the film. Covalent attachment of the modifier film to the surface has been supported by a number of observations. XPS analysis of unmodified carbon fibres soaked in ED solution at open circuit potential did not show any increase in surface nitrogen, however, modification of the carbon fibre surface was observed after the electrochemical oxidation of ED (the amount of nitrogen measured by XPS at the surface increased from 2.2 % for unmodified carbon fibres to ~ 20 % after treatment). It is noted that the spontaneous reaction of amines with glassy carbon has recently been reported[19] and hence, this earlier work may demonstrate that spontaneous attachment of amines does not occur at carbon fibres or, alternatively, that the amount of modifier attached was very small. For electrochemically grafted ED-modified carbon fibres, the

atomic percentage of nitrogen on the surface did not alter after the modified carbon fibres were subjected to thermal desorption under high vacuum (10^{-9} torr) for 1 hour at 110 °C demonstrating strong attachment of the modifier to the surface.[6] The stability of amine films towards sonication and soaking in a variety of media has also been investigated. No changes in the XPS spectra were observed after sonicating *N*-acetylethylenediamine modified glassy carbon electrodes in water, ethanol and phosphate buffer (pH 7.0) or after soaking butylamine modified glassy carbon electrodes in 0.1 M H_2SO_4 for 24 hours.[8] Spontaneously grafted films (without any electrochemical induction) of 4-nitrobenzylamine and 3-nitrobenzylamine at glassy carbon surfaces have been reported to be resistant to sonication in ethanol followed by acetone for 10 minutes as evidenced by the redox peaks associated with the nitro group of the modifier observed in cyclic voltammograms recorded in blank electrolyte.[19] Potential cycling of butylamine modified electrodes in 0.1 M $HClO_4$ between 0.20 and 0.80 V (*vs*. Ag/AgCl) for 100 cycles gave only a 10 % decrease in the N/C ratio determined by XPS.[8] These observations confirm that the modifier is not physisorbed on the surface but that a hydrolytically stable bond is formed during the attachment reaction.

6.1.3 Redox Probe Voltammetry at Amine Films Grafted to Carbon Electrodes

The redox probe response at amine modified electrodes depends on the length of the modifier, the modification conditions and the probe. Modifiers with long alkyl chains lead to slower electron transfer kinetics and therefore, are more blocking. Hoekstra and Bein studied the redox activity of potassium ferricyanide (0.1 M $K_3Fe(CN)_6$ in 0.1 M KCl) at glassy carbon surfaces modified with butylamine, 6-aminohexanol, decylamine and octadecylamine.[16] For butylamine and 6-aminohexanol modified surfaces, the response towards the probe species was similar to that obtained at polished glassy carbon, whereas the rate of electron transfer across decylamine and octadecylamine modified surfaces was greatly reduced. The authors noted that the inability of the short chain modifiers to block electron transfer was consistent with results obtained for short-chain alkanethiol monolayers deposited on gold where at least 10 methylene units were found to be necessary for formation of a highly ordered and insulating layer. Similar observations were made by Liu and Dong regarding the cyclic voltammetry of ruthenium (III) hexaamine (2 mM $Ru(NH_3)_6^{3+}$ in 0.1 M KCl, pH 5.0) at 1,7-diaminoheptane, 1,10-diaminodecane and 1,12 diaminododecane modified glassy carbon surfaces.[21] All the modifiers exhibited blocking behaviour and as the alkyl chain length increased the capacitance decreased indicating a more compact layer which would slow

the rate of electron transfer. Electrochemical impedance spectroscopy (EIS) of the modified surfaces performed in 2 mM $Ru(NH_3)_6^{3+}$ at -0.14 V (*vs*. Ag/AgCl) agreed with the results obtained using cyclic voltammetry and indicated that electrode kinetics became slower as the length of the alkylamine modifier increased. The influence of the probe species on the blocking properties of amine films was demonstrated by investigating the response of glassy carbon electrodes modified with 4-aminobenzoic acid towards two oppositely charged redox probes, $Fe(CN)_6^{3-}$ and $Ru(NH_3)_6^{2+}$ (5 mM and 2 mM respectively in 0.1 M phosphate buffer, pH 7.0).[22] No redox peaks were observed at the modified electrode in the cyclic voltammogram for $Fe(CN)_6^{3-}$ due to electron transfer being completely blocked; however, a well-defined redox response similar to that observed at bare glassy carbon was observed in the presence of $Ru(NH_3)_6^{2+}$ indicating no blocking effects of the grafted layer towards the redox reaction. The different effects of the 4-aminobenzoic acid modified glassy carbon electrode on the electrochemical behaviour of the two oppositely charged redox probes was attributed to electrostatic interactions between the modified surface and the probe. At pH 7.0, the carboxyl group of the modifier was expected to be deprotonated, therefore, on the negatively charged amine film, $Ru(NH_3)_6^{2+}$ was attracted to the surface and could get access to the underlying glassy carbon surface giving rise to the response observed. In comparison, no response was observed for $Fe(CN)_6^{3-}$ due to electrostatic repulsions between the modified surface and the probe. Electrostatic interactions between glassy carbon electrodes modified with 1,7-diaminoheptane and $Fe(CN)_6^{3-}$ and $Ru(NH_3)_6^{2+}$ probes at pH 5.0 were also observed to influence the probe responses.[21] At pH 5.0 the amine-containing film is protonated. No response was observed for $Ru(NH_3)_6^{2+}$ under these conditions as the redox probe species is electrostatically repelled from the surface. In comparison, a response was obtained for the negatively charged $Fe(CN)_6^{3-}$ species which is attracted to the surface and can gain access to the underlying electrode for faster electron transfer.

6.1.4 Research Directions for Chapter 6

The work described in this chapter concerns thin films of ED grafted to glassy carbon and pyrolysed photoresist film (PPF) by the electro-oxidation of the primary amine. Redox probe studies, AFM depth profiling and surface roughness analysis, and XPS measurements were used to characterise film structure and examine film stability in solution.

6.2 Experimental Methods

6.2.1 Electrochemistry

Electrochemical measurements were performed using computer-controlled EG & G PAR Model 362 and Model 273A Potentiostats. The experimental details concerning electrochemical measurements are described in Chapter 2, Section 2.4. Aqueous electrochemical experiments were carried out in phosphate buffer (PB, 0.04 M, pH 7.4) or Tris·HCl buffer (0.05 M, pH 9.0) with added 0.1 M $NaClO_4$ electrolyte and non-aqueous electrochemical experiments were performed in acetonitrile containing 0.1 M $[Bu_4N]BF_4$. Cyclic voltammograms were obtained using a scan rate of 100 mV s^{-1}.

6.2.1.1 Modification of Carbon Surfaces

Electrochemical grafting of ED films to carbon substrates was carried out in 0.1 M $[Bu_4N]BF_4$-acetronitrile solution containing approximately 5 mM ED. Before modification, glassy carbon electrodes were polished with alumina slurries (1.0 and 0.05 μm) and rinsed with Milli-Q water. When grafting to PPF, a fresh sample was used for each modification. The standard modification procedure involved cycling from 0 to 1.20 V for 6 cycles at 100 mV s^{-1}. After modification, the surfaces were rinsed with acetonitrile followed by Milli-Q water and dried with nitrogen prior to further use or storage under vacuum.

6.2.1.2 Adsorption of Benzoquinone at Unmodified and Ethylenediamine-Modified Electrodes

Two methods were used for adsorbing benzoquinone (BQ) from a BQ-PB solution (1 mM, 10 mL) onto polished glassy carbon and ED grafted electrodes: (1) a cyclic voltammogram was recorded in the BQ-PB solution from 0.80 to -0.50 V or (2) the electrode was soaked in the BQ-PB solution for a required amount of time as specified in the Results and Discussion Section 6.3.2.3. Cyclic voltammetry of the adsorbed species was carried out in blank PB by scanning between 0.80 and -0.50 V.

6.2.2 Surface Characterisation

6.2.2.1 Contact Angle

To obtain static water contact angle measurements for ED films, the modified PPF sample was placed on a horizontal stage and 1 μL of Milli-Q water was dispensed onto the surface from a microsyringe. The drop was imaged 5-10 seconds after the water droplet was applied using an Edmund Scientific video camera and Video for Windows NT software. Three measurements of the angle the drops makes with the surface were taken from each side of the drop (rotated 90° with respect to each other) and two drops were applied to each surface consecutively. The average water contact angle of two separate samples (*i.e.*, of 24 measurements) was calculated and the stated errors indicate the range of values obtained.

6.2.2.2 Film Thickness and Surface Roughness Measurements using Atomic Force Microscopy

Unless otherwise stated, AFM topographical measurements were carried out in non-contact tapping mode with a silicon cantilever (NSC 15 Model, Ultrasharp) operating at moderate resonant frequencies (265-400 kHz). High resolution images were collected (512 samples per line) using a scan rate of 1 Hz. All AFM measurements were made with dry films in ambient air conditions and three separate film samples were prepared and analysed to ensure all measurements were reproducible. Film thickness and surface roughness (R_a) values were measured using Nanoscope (III) software.

AFM film thickness measurements were made by scratching a section of film from the modified PPF surface following the procedures of Brooksby and Downard.[27] The technique of 'scratching' the modified PPF surface uses a chip consisting of three silicon cantilever tips (CSC 12 Model, Ultrasharp, Figure 6.1). The tips have lengths given as (D) 300, (E) 350 and (F) 250 ± 5 μm with corresponding typical resonant frequencies of 14, 10 and 20 kHz. Note that only two tips were used for the film thickness measurements. One of the two shorter tips (D or F) located on either side of the central longest tip was aligned for operation in non-contact tapping mode. As the shorter AFM tip (D or F) approached the surface to begin a tapping mode scan, the longest tip (E) (not in resonance) imbedded into the surface film with a constant force of 0.4 or

0.7 μN when using tips D and F respectively (Figure 6.2).[27] The AFM optical system was focused on the longest tip to allow visual inspection of the surface whilst the scratching procedure was performed. During scanning (2.5 cycles, scan angle 0°), the longest tip removed material from an area of 10 μm × 2.5 μm by effectively scratching the modifier from the PPF surface. For each sample, three scratches were made at different locations. The resulting scratches was imaged in tapping mode (scan angle 90°) at two different locations along each scratch using a chip containing only one silicon cantilever tip (NSC 15 Model, Ultrasharp). The single tip has a length of 125 ± 5 μm and a typical resonant frequency of 325 kHz. Loose debris from the scratch was removed by gentle air convection prior to imaging. The depth of the ED film was determined from the average cross-sectional profile of the resulting trench made in the film during 'scratching'. From the cross-sectional profile, at least 8 paired data points were collected where each pair contained one point from within the scratch and one outside. The height difference of the films was recorded and two new random locations were selected for scratch measurements. The estimated error in the paired data points is ± 0.2 nm.[27] Bare PPF surface, to an average depth of 0.3 nm, was also removed by scratching and film thickness data have been adjusted accordingly. The depth of PPF removed was determined by scratching and depth profiling bare PPF samples and the measurement was repeated three times. After correction for the scratch depth at bare PPF, quoted thickness measurements have an associated uncertainty of ± 0.4 nm.

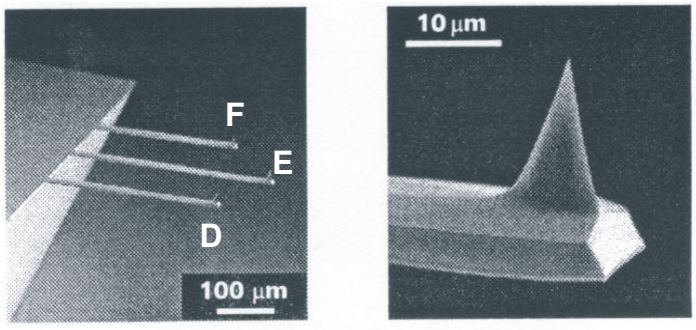

Figure 6.1. SEM images of the AFM cantilever consisting of three silicon tips (CSC 12 Model, Ultrasharp) used for making film thickness measurements by AFM depth profiling across scratches in the film. The images were taken from the cantilever specification sheet supplied by Ultrasharp.

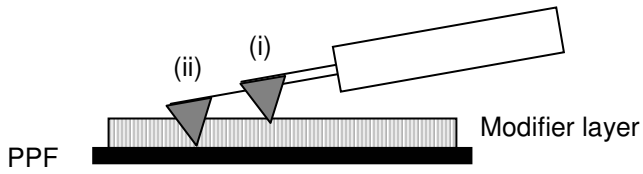

Figure 6.2. Schematic of the 'scratching' technique used in AFM depth profiling experiments to determine film thickness. As the shorter AFM tip (i) engages the surface to perform a tapping mode scan, the longest tip (ii) is imbedded into the surface film. During scanning, tip (ii) removes material from an area of 10 μm × 2.5 μm by effectively scratching the modifier from the PPF surface.

The average surface roughness of bare PPF or ED modified PPF surfaces was determined from topography images obtained by scanning an area of 1 μm × 1 μm. The stated average surface roughness values (R_a) are an arithmetic average of measured mean roughness values obtained from 10 randomly selected areas (200 × 200 nm^2) of the surface. Stated errors indicate the range of values observed.

6.2.2.3 X-ray Photoelectron Spectroscopy

XPS data were obtained on glassy carbon plates. Wide scans were recorded from 1100 to 0 eV, with a step size of 1 eV and a pass energy of 160 eV. Most narrow scans were conducted using a step size of 0.1 eV and a pass energy of 20 eV. All scans were obtained at a take-off angle of 0° and all peak positions were referenced to aromatic carbon at 284.7 eV.

6.3 Results and Discussion

6.3.1 Preparation and Characterisation of Ethylenediamine Films

Cyclic voltammetric scans of ED at a glassy carbon electrode were consistent with grafting a blocking film to the electrode (Figure 6.3 (a)). An irreversible redox process was observed at E_{pa} = 0.82 V in the initial scan. This process is assigned to amine oxidation. On repeat scans the peak current decreased and was totally absent by the 6th cycle implying passivation of the electrode due to attachment of ED to the glassy carbon surface. The presence of a surface film was confirmed by comparing the voltammetry of the probe redox species, hydroxymethyl ferrocene (FcOH, 1 mM in PB), before and after the grafting procedure (Figure 6.3 (b)). At a polished glassy carbon surface, the voltammogram of FcOH was chemically reversible with $E_{1/2}$ = 0.19 V and ΔE_p = 80 mV. At the ED-modified surface, the FcOH anodic peak potential shifted more positive, the peak current was lower and there was a very small associated reduction peak. These changes are consistent with the presence of a surface film which changes the apparent electron transfer kinetics to the solution species. Surface films act as a physical barrier which hinders electron transfer between the electrode and the solution-based probe species. A detailed discussion of these results is given in Section 6.3.2.4. The observation of a smaller peak current for the reduction peak of FcOH compared to the oxidation peak is consistent with the formation of a surface film containing amines which can be protonated, to some extent, at pH 7.4. At this pH, the ferrocenium ion ($FcOH^+$) formed upon oxidation of FcOH is electrostatically repelled from the cationic film, therefore, there is less of this species at the surface to be reduced giving rise to the lower currents observed for reduction compared to oxidation.

Essentially the same behaviour was observed using PPF and hence the grafting process was assumed to be the same at both PPF and glassy carbon surfaces.

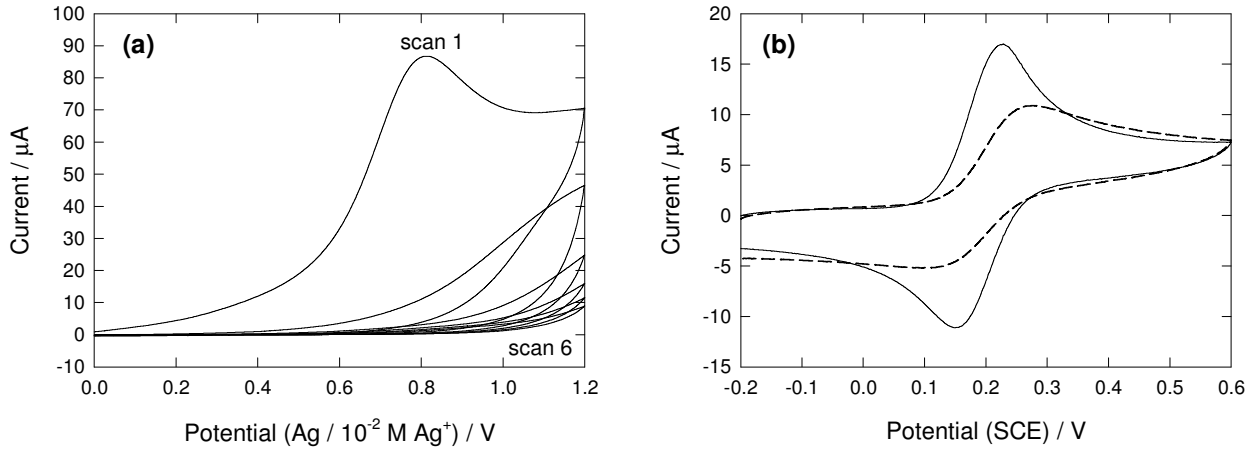

Figure 6.3. Cyclic voltammograms at glassy carbon of: (a) 5 mM ED in $[BuN_4]BF_4$-acetronitrile, showing the first 6 scans, and (b) FcOH (1 mM in PB) before (—) and after (---) grafting ED (υ = 100 mV s^{-1}).

Freshly-prepared films of ED were characterised by contact angle measurements. Prior to modification, the static water contact angle on unmodified PPF was 61 ± 2^{o} and after grafting of ED a value of 58 ± 2^{o} was obtained. Amine-terminated alkyl layers assembled on silicon surfaces by covalent attachment of 11-aminoundecyldimethylsilane[28] and electrostatic attachment of 1,12-diaminododecane[29] have reported water contact angles of 58 and 59^{o} respectively, and hence the unchanged wettability of the PPF surface after grafting of ED is not inconsistent with formation of an amine-terminated layer.

AFM topography images and film thickness measurements confirmed the presence of a grafted layer. The topography of PPF before and after grafting an ED film using standard modification procedures is shown in Figure 6.4. The average surface roughness (R_a) values of the PPF increased from 0.35 ± 0.09 nm to 0.63 ± 0.02 nm (n = 3) when ED was grafted to the surface. It is noted that the R_a value for the ED-modified surface represents the surface roughness of the film excluding the high protrusions observed in the topography image (Figure 6.4 (b)).

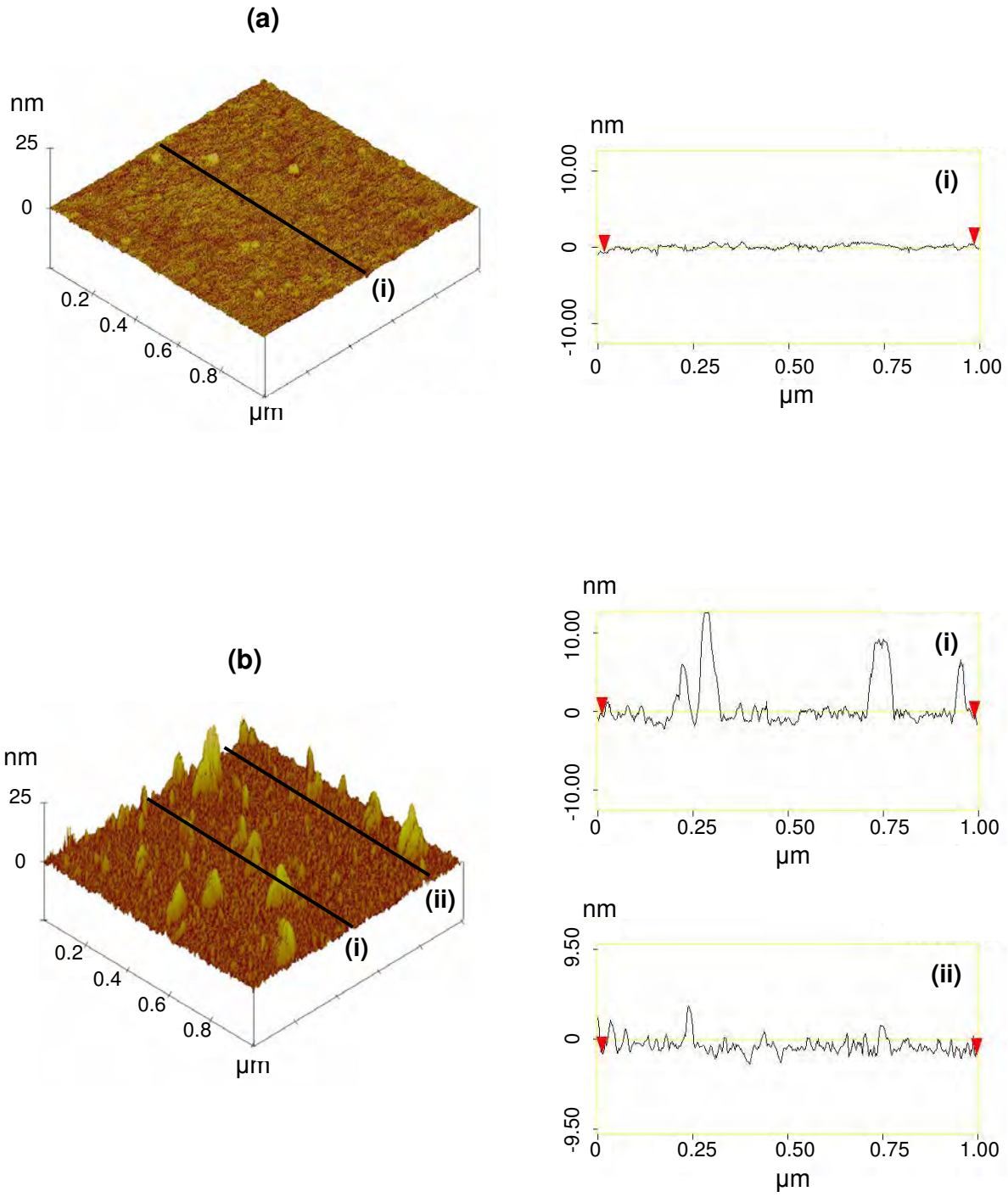

Figure 6.4. AFM topographical images (left) and line profiles (right) of PPF (a) before and (b) after grafting ED using standard modification procedures. Scan size 1 µm × 1 µm. Lines (i) and (ii) on the topographical images represent the areas where the corresponding line profiles were recorded.

The average film thickness of ED films grafted using standard procedures was measured by scratching through the layer with an AFM tip and profiling across the scratch to measure its depth (Figure 6.5). The average thickness of the ED film, excluding the high features observed in the topography image, was 2.70 ± 0.40 nm (n = 3). The length of the ED modifier from the carbon surface to the outermost atomic radii was calculated to be 0.49 nm using Spartan software.[30] Assuming the molecular orientation of the film is perpendicular to the PPF surface, the grafted film contains an average minimum of 5.5 molecular layers. Only the minimum number of layers can be determined from AFM thickness measurements; it is possible that a greater number of layers are incorporated in a tilted or collapsed structure. Formation of multilayer films is consistent with the findings of Downard *et al.*[20] for electrografted tetraethylene glycol diamine and *n*-hexylamine films, and provides direct evidence supporting Antoniadou's suggestion that oxidation of ED at carbon fibre bundles leads to amine multilayers.[17]

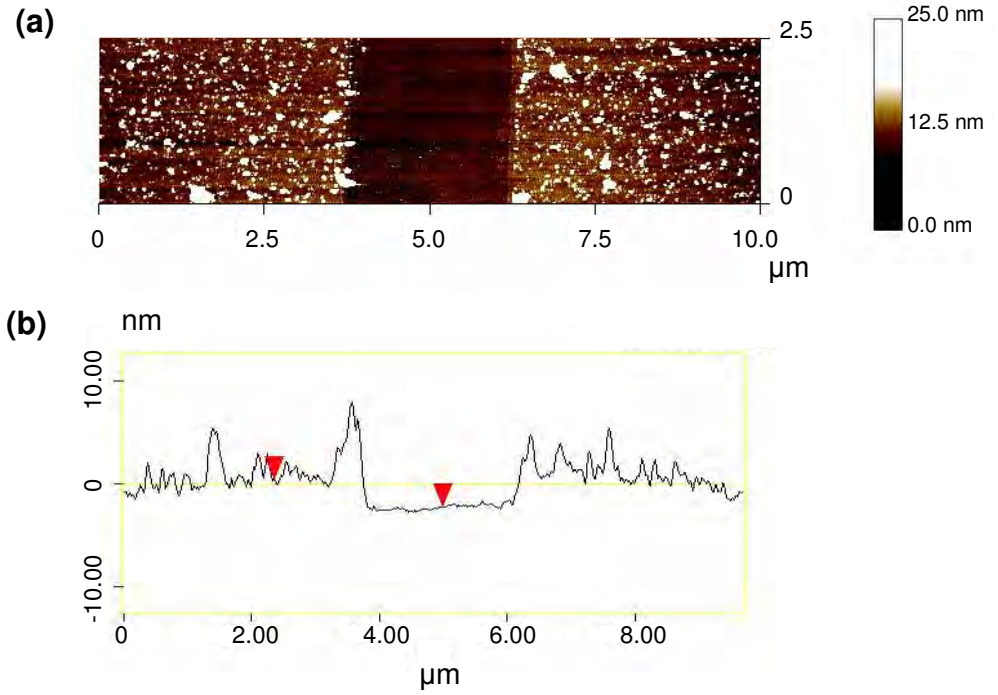

Figure 6.5. (a) Tapping mode AFM image of a scratched ED film grafted on PPF; (b) cross-sectional profile of the scratch generated in (a).

The identity of the large island features observed in the topography image for the ED-modified surface (Figure 6.4 (b)) and the reason for their growth is unclear. Control experiments involving soaking bare PPF surfaces in PB for 60 minutes followed by rinsing in Milli-Q water (see Section 6.3.2.2) suggested that these features were not due to electrolyte residues as similar features were not observed on the PPF surface after soaking in PB and the average film thickness (0.75 nm) corresponding to buffer salt residues does not account for the large, island features observed for the ED film. An alternative explanation is that the features correspond to areas of the film where the amine has formed particularly long polymeric chains on the PPF surface.[17] The island-like growth may indicate that the PPF surface is not uniformly active for the grafting process. Kairuki and McDermott studied the nucleation and growth mechanism for the electrografting of diazonium cations at HOPG and found that film growth was initiated at the steps of highly reactive edge plane graphite first followed by nucleation at atomic scale defects on the less reactive basal plane graphite.[31] Whilst there are no reports of PPF exhibiting variable activity towards the grafting of organic molecules, a similar mechanism could be operating in this work. It is proposed that the large island features occur at the more active areas of the PPF surface due to early nucleation whilst growth at the less active areas of the surface is initiated later in the grafting process and therefore, less ED is grafted.

XPS analysis was also used to confirm the presence of a grafted layer. XPS measurements were made of three surfaces: two as-prepared ED films grafted to glassy carbon and a polished glassy carbon surface which had been treated using the grafting conditions (*i.e.*, potential cycling) but in the absence of ED. Survey spectra were obtained for each surface, giving the data shown in Table 6.2. Excellent reproducibility is observed for the ED-modified surfaces, confirming reproducible preparation of the samples. As expected, an increase in percentage nitrogen coupled with a decrease in percentage carbon is observed for ED-grafted surfaces compared to the polished glassy carbon blank. However, the N:C ratio at an ED-grafted electrode (0.25) is less than that expected for a compact ED film (1:1) indicating that a large amount of surface carbon is being detected. An increase in percentage oxygen at the grafted surfaces is also observed. This result is opposite to that which would be expected. In the presence of the ED film, the contribution from surface carbon and oxygen atoms of the glassy carbon substrate should be less than in the absence of the film, therefore, the oxygen content is expected to decrease. This result could indicate the

incorporation of oxygen-containing groups into the film during grafting (see Scheme 6.5, Section 6.1.1).

Table 6.2. XPS data for ED films grafted to glassy carbon.[a]

Sample	Atomic %[c]		
	N	C	O
Blank GC[b]	1.8	86.4	9.0
ED, as-prepared	17.3	69.0	11.1
ED, as-prepared	17.3	67.1	11.9

[a] All samples were ultrasonicated in Milli-Q water for 30 seconds and dried with nitrogen prior to analysis.

[b] Glassy carbon cycled six times from 0 to 1.20 V at 100 mV s^{-1} in blank 0.1 M $[BuN_4]BF_4$-acetonitrile solution.

[c] Estimated relative error on atomic percentage is 10 %.

Figure 6.6 shows the typical wide scan spectrum and narrow scan spectra for the C1s, N1s and O1s regions for an as-prepared ED film. The binding energies and atomic percentages for peaks fitted to the C, N and O signals obtained at the bare and ED-modified glassy carbon electrodes are listed in Table 6.3.

For the C1s region of the ED-grafted electrode, the signal is fitted with five peaks at 284.7, 285.1, 286.3, 287.1 and 288.5 eV (Figure 6.6 (b)). In comparison, the signal observed for a bare glassy carbon electrode (not shown) is fitted with three peaks at 284.6, 285.3 and 286.5 eV. For bare glassy carbon, the peak at 284.6 eV is assigned to aromatic carbons and the peaks at 285.3 and 286.5 eV are attributed to oxygen-containing carbon groups (*e.g.*, alcohol, phenol and ether groups) at the surface.[32] At the ED-grafted electrode, the peak at 284.7 eV due to aromatic carbons on the glassy carbon surface is relatively less important as the atomic percentage of carbon measured at this binding energy decreases from 64.7 % for bare glassy carbon to 28.0 ± 1.6 % (n = 2) for the ED-grafted electrode. This result confirms the presence of a grafted film. The atomic percentage for the carbon peak fitted with a binding energy of 285.1 eV for the ED-grafted electrode is the same (within experimental uncertainty) as that measured for bare glassy carbon. Gallardo *et al.* reported a peak at 285 eV in the XPS spectra for 11-aminoundecanoic acid films grafted to copper and iron

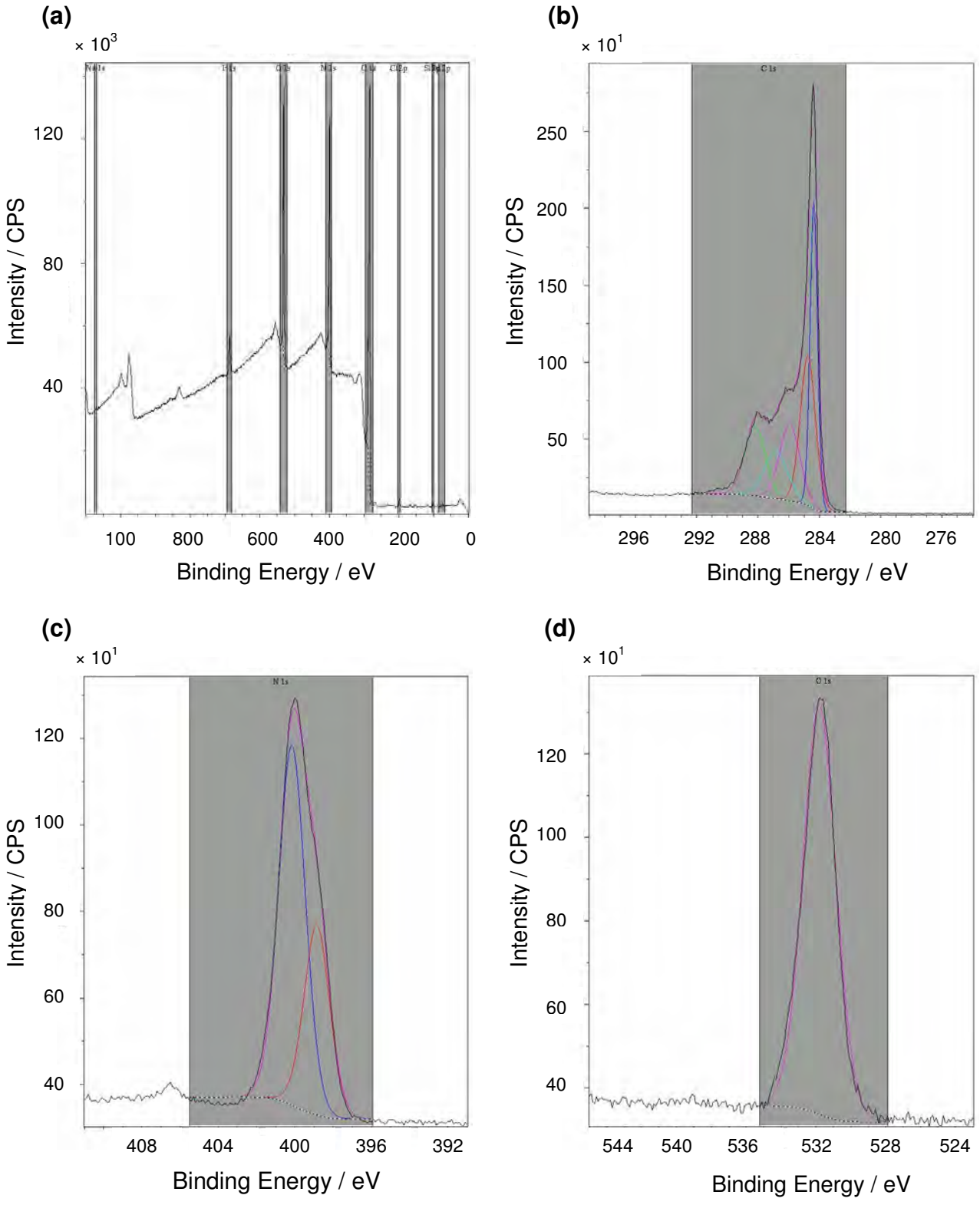

Figure 6.6. XPS spectra of an ED film grafted to glassy carbon: wide scan (a) and narrow scan spectra for C1s (b), N1s (c) and O1s (d) regions. The black line is the spectra recorded whilst the coloured lines represent those used for peak fitting.

Table 6.3. Atomic % of C, N and O at the binding energies observed for XPS narrow scan spectra for bare glassy carbon and as-prepared ED films grafted to glassy carbon.[a]

Sample	C			N			O		
	Binding Energy (eV)[b]	**Peak Assignment**	**Atomic %**	**Binding Energy (eV)[b]**	**Peak Assignment**	**Atomic %**	**Binding Energy (eV)[b]**	**Peak Assignment**	**Atomic %**
Bare GC[c]	284.6	aromatic C	64.7	399.9	surface N	61.2	532.3	surface O	53.6
	285.3	C-OH,	26.3	402.1	surface N	20.3	533.0	surface O	46.4
	286.5	Ar-OH,C-O-	9.0	406.0	surface N	18.5			
ED film as-prepared[d]	284.7 ± 0.1	aromatic C[e]	28.0 ± 1.6	399.1 ± 0.1	[e,f] covalent C-N, $C\text{-}NH_2$	30.4 ± 2.8	532.1 ± 0.1	[e,f] surface O, C=O,C-O-, CO_3^{2-}, HCO_3^-	100 ± 0.0
	285.1 ± 0.4	alkyl chain[f]	23.1 ± 3.3	400.5 ± 0.1	[e,f] covalent C-N, $C\text{-}NH_2$, $C\text{-}NH_3^+$	68.7 ± 3.7 1.7 ± 0.0			
	286.3 ± 0.5	[e] C-OH, Ar-OH,C-O-	22.9 ± 5.0	406.8 ± 0.0	surface N				
	287.1 ± 0.0	C=O, C-O-[f]	12.8 ± 0.0						
	288.5 ± 0.1	[f] C=O, CO_3^{2-}, HCO_3^-	19.7 ± 3.2						

[a] All samples were ultrasonicated in Milli-Q water for 30 seconds and dried with nitrogen prior to analysis.

[b] All peak positions were referenced to aromatic carbon at 284.7 eV.

[c] Glassy carbon cycled six times from 0 to 1.20 V at 100 mV s^{-1} in blank 0.1 M $[Bu_4N]BF_4$-acetonitrile solution.

[d] Errors are stated for experiments performed twice and indicate the range of values obtained.

[e] Contribution from glassy carbon surface.

[f] Contribution from ED film.

surfaces.[19] The authors attributed this peak to the 10 carbon chain of the amine modifier and hence, in our work the peak observed at ~ 285.1 eV is considered to contain both a contribution from the alkyl chain of the ED modifier and from the glassy carbon surface. The atomic percentage of carbon detected at a binding energy of 286.5 eV at bare glassy carbon corresponding to surface alcohol, phenol or ether groups increases markedly in the presence of an ED film. ED is hygroscopic and water added to the modification solution with the ED sample may lead to surface oxidation concurrent with grafting. The O/C ratios for a polished glassy carbon blank (0.10) and an ED-modified surface (0.20 ± 0.04 (n = 2)) are consistent with studies reported in the literature examining the effect of oxidative electrochemical pretreatment on glassy carbon electrodes.[33] In these studies the O/C ratio was observed to increase from 0.084 for a freshly polished glassy carbon electrode to 0.22 after the electrode was oxidised. For the ED-grafted electrode, additional peaks were fitted at 287.1 and 288.5 eV which most likely indicates the incorporation of oxygen-containing groups within the film. Peaks at similar binding energies were observed by Herlem *et al.* for platinum surfaces modified by oxidation of pure ethylenediamine and were attributed to the presence of carbonyl or ether groups in the film.[25] Water present in the modification solution during the electro-grafting of ED could promote the side reaction shown in Scheme 6.5 (Section 6.1.1) and lead to the formation of terminal aldehyde groups within the film. Further evidence of the peak at 288.5 eV corresponding to the presence of a carbonyl group is provided by Gallardo *et al.* who observed a peak at the same binding energy for the carboxylic acid group of 11-aminoundecanoic acid electrografted to an iron surface.[19] An alternative explanation for the increase in oxygen content observed upon grafting of an ED film may be due to the incorporation of carbonate anions (CO_3^{2-} and/or HCO_3^-) into the film upon interaction with atmospheric carbon dioxide and water. Aminophenol groups formed on gold surfaces by the reduction of a 4-nitrothiophenol monolayer[34] and by electroreduction of the aminobenzene diazonium cation[35] have been suggested to interact with atmospheric carbon dioxide and water to form carbonate anions giving rise to C1s peaks at ~ 288 eV.

For the N1s region of the ED-grafted electrode, the signal was fitted with three peaks at 399.1, 400.5 and 406.8 eV (Figure 6.6 (c)). In comparison, the corresponding signal recorded at a bare glassy carbon electrode (not shown) was fitted with three peaks at 399.9, 402.1 and 406.0 eV corresponding to surface nitrogen-containing species. At the ED-grafted electrode, the peak at 406.8 eV was relatively less important as the atomic percentage of nitrogen at this binding energy

decreased markedly from 18.5 % at the bare glassy carbon electrode to 1.7 % after grafting an ED film. The other two nitrogen peaks observed at 399.1 and 400.5 eV in the presence of the ED film are attributed to nitrogen from the amine modifier. In this work, it is difficult to distinguish between nitrogen covalently attached to the glassy carbon surface and that present due to amino groups within the multilayer film or in a terminal position. The peak at 399.1 eV may tentatively be assigned to surface-bound nitrogen and that at 400.5 eV to other amines in the film. For butylamine films electrografted to gold and platinum electrodes and 11-aminoundecanoic acid electrografted to iron, peaks at similar binding energies (398.1 eV for gold, 397.9 eV for platinum and 398.5 eV for iron) were assigned to nitrogen bound at the metal surface.[7,19] Alternatively, the peaks at 399.1 eV and 400.5 eV could represent amino groups within the multilayer film and/or in a terminal position. In comparison, Adenier *et al.* suggested that the peak at ~ 400 eV observed for butylamine grafted to gold and platinum electrodes corresponds to an amine group not bound to the electrode surface on the basis that the XPS spectra for solution-based butylamine presents a peak at 398.9 eV.[7] Other possible assignments of the nitrogen peaks at 399.1 eV and 400.5 eV is that they could correspond to unprotonated and protonated amines respectively. Herlem *et al.* attributed the peaks observed at 398.5 and 399.5 eV in the N1s region for pure ED grafted to platinum electrodes to unprotonated ($R\text{-}NH_2$) and protonated ($R\text{-}NH_3^+$) amine groups respectively[25] and Adenier *et al.* suggested that the nitrogen peak observed at 402 eV for butylamine grafted to platinum may correspond to protonated amines.[7]

At the bare glassy carbon electrode, two peaks were fitted for the O1s signal at 532.3 and 533.0 eV corresponding to surface oxygen-containing functional groups.[33] Only one peak was fitted at 532.1 eV for the signal in the O1s region for the ED-modified electrode. This peak is attributed to surface oxide and reaction of the amine film yielding oxygen-containing functional groups within the amine film as discussed above.

6.3.2 Stability of Ethylenediamine Films in Solution

6.3.2.1 Redox Probe Voltammetry at Ethylenediamine-Grafted Electrodes

The voltammogram of FcOH obtained at an ED-grafted electrode immediately after preparation and rinsing in acetonitrile followed by Milli-Q water is shown in Figure 6.1 (b). On

repeat scanning in the FcOH-PB solution, the FcOH response changed. The peak currents were observed to increase and ΔE_p decreased. These changes are consistent with the film becoming less blocking. After further investigation it became apparent that these changes were independent of potential scanning (between -1.50 and 0.80 V in blank PB) and occurred at the same rate and to the same extent when the modified electrode was simply soaked in PB at open circuit potential. The experiments performed to study the effects of applied potential and soaking on ED films were conducted over the same time period. Cyclic voltammograms recorded at a polished glassy carbon electrode and at an ED-grafted electrode in the FcOH-PB solution immediately after film grafting, and after soaking for 15 and 60 minutes in PB are shown in Figure 6.7 (a). A progressive change in the voltammograms is observed as soaking time increases. The peak currents are observed to increase (from 10 to 14.75 μA for the oxidation peak current) and the ΔE_p decreases (from 166 to 86 mV) upon soaking an as-prepared ED film in PB for 60 minutes, after which time the response is very similar to that at polished glassy carbon (Table 6.4). These changes were reproducible with repeat electrode modifications.

Table 6.4. Effect of soaking ED-grafted films in PB, Tris·HCl and acetonitrile on the anodic peak current (i_{pa}) and peak separation (ΔE_p) for the redox probe FcOH.[a]

Sample	**PB (0.04 M, pH 7.4)**		**Tris·HCl (0.05 M, pH 9.0)**		**Acetonitrile**
	ΔE_p **(mV)**	i_{pa} **(μA)**	ΔE_p **(mV)**	i_{pa} **(μA)**	i_{pa}[b] **(μA)**
Blank GC	82	16.00	72	15.00	32.00
ED, as-prepared	166	10.00	76	13.45	6.35
ED, soaked for 15 min	110	12.65	74	13.45	4.70
ED, soaked for 60 min	86	14.75	74	14.00	4.70

[a] Cyclic voltammograms recorded for 1 mM FcOH between -0.2 and 0.6 V (υ = 100 mV s^{-1}).

[b] Anodic peak current measured at 0.08 V (*vs.* SCE).

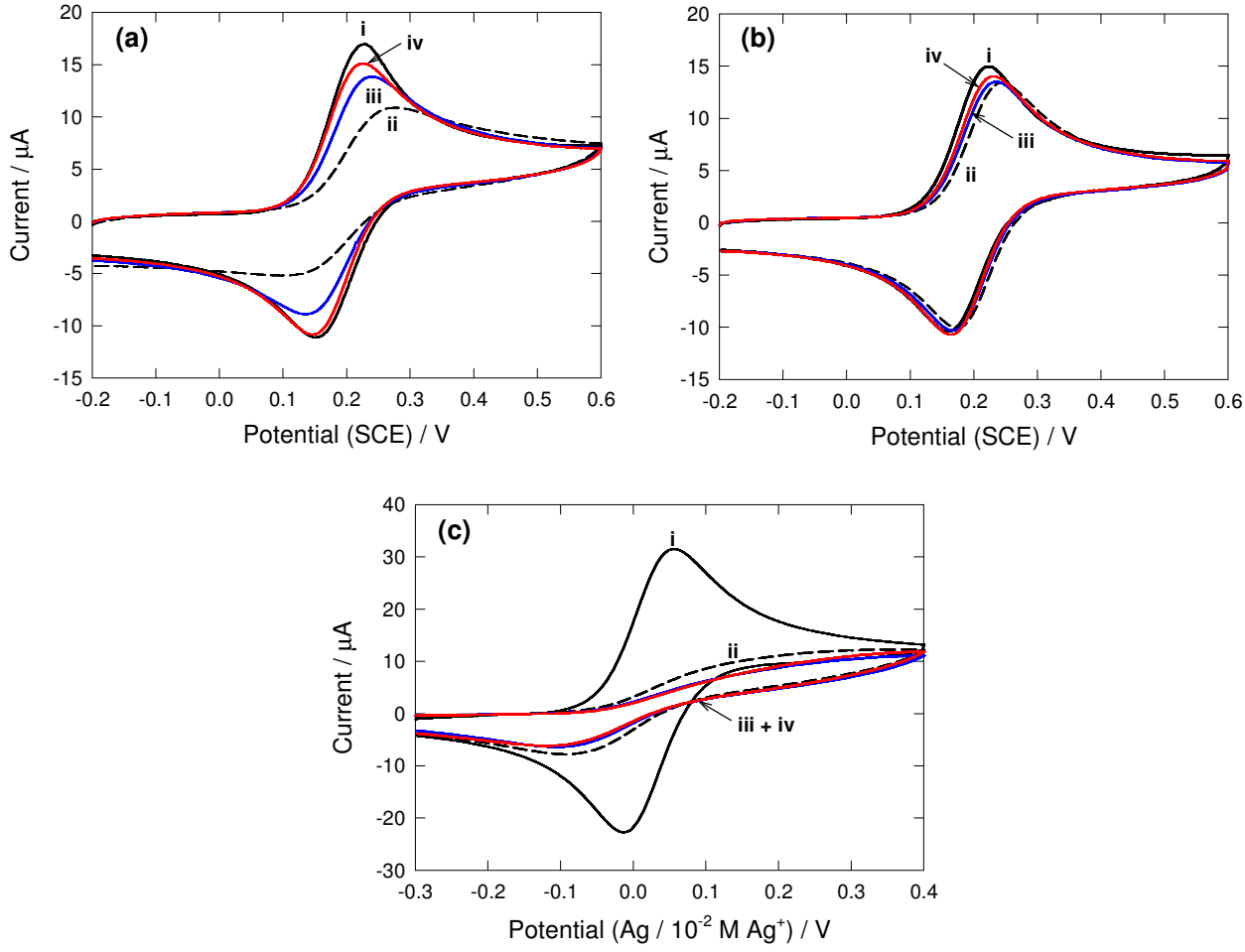

Figure 6.7. Cyclic voltammograms at glassy carbon of (a) FcOH in PB (0.04 M, pH 7.4), before (i) and after (ii-iv) grafting ED: (ii) freshly grafted film, (iii) after soaking in PB for 15 minutes and (iv) after soaking in PB for 60 minutes; (b) FcOH in Tris·HCl (0.05 M, pH 9.0), before (i) and after (ii-iv) grafting ED: (ii) freshly grafted film, (iii) after soaking in Tris·HCl buffer for 15 minutes and (iv) after soaking in Tris·HCl buffer for 60 minutes; (c) FcOH in acetonitrile, before (i) and after (ii-iv) grafting ED: (ii) freshly grafted film, (iii) after soaking in acetonitrile for 15 minutes and (iv) after soaking in acetonitrile for 60 minutes (υ = 100 mV s^{-1}).

The effect of pH on the return of the probe response was investigated by soaking an ED-grafted surface in Tris·HCl buffer (0.05 M, pH 9.0) (Figure 6.7 (b)). The cyclic voltammogram recorded at the ED-grafted electrode in FcOH-Tris·HCl solution immediately after preparation is not as blocking compared to the response recorded in FcOH-PB solution (compare Figures 6.7 (a) and (b), scan ii). For the ED-grafted surface at pH 9.0, the response was similar to that observed at a polished glassy carbon electrode. The FcOH anodic peak potential shifted only slightly more positive after grafting an ED film and a small decrease in the anodic peak current was observed whilst the reduction peak current remained the same. The greater currents observed for the reduction peak at pH 9.0 compared to at pH 7.4 is attributed to the amine groups within the surface film being protonated to a lesser extent at pH 9.0. Under these conditions, the ferrocenium ion formed upon oxidation of FcOH is electrostatically repelled from the cationic film to a lesser extent; therefore, there is more of this species at the surface to be reduced. After soaking the ED-modified electrode in Tris·HCl for 15 and 60 minutes, a small decrease in ΔE_p associated with a slight increase in peak current is observed (Table 6.4).

A similar series of experiments was performed with soaking in acetonitrile in place of PB or Tris·HCl. After grafting, the electrodes were rinsed with acetonitrile and transferred to a solution of 1 mM FcOH in 0.1 M $[BuN_4]BF_4$-acetronitrile. After obtaining an initial cyclic voltammogram, the electrode was soaked in acetonitrile and voltammograms were recorded after 15 and 60 minutes (Figure 6.7 (c)). The grafted electrode was initially significantly more blocking to FcOH electrochemistry in acetonitrile compared to in PB. For FcOH in acetonitrile, the anodic peak current at 0.08 V was observed to decrease from 32 μA at a polished glassy carbon electrode to 6.33 μA after grafting an ED film (Table 6.4). A small increase in the blocking effect of the film was observed after soaking in acetonitrile as the FcOH anodic peak current at 0.08 V decreased further to 4.70 μA.

The reversibility of the changes in the FcOH response was examined by returning an ED-grafted electrode, previously soaked in PB for 60 minutes, to 0.1 M $[BuN_4]BF_4$-acetonitrile solution and soaking the electrode for a further 60 minutes or subjecting the electrode to film-preparation conditions in the blank electrolyte solution. Under these conditions, the FcOH response did not return to that prior to soaking in PB indicating that PB causes an irreversible change to the film.

6.3.2.2 Characterisation of Film Changes After Soaking Using Thickness, Surface Roughness and XPS Measurements

ED films were grafted to PPF surfaces using standard modification procedures and the resulting film thicknesses were measured by AFM depth profiling across scratches in the film. After immersing the films in PB for 60 minutes, followed by rinsing in Milli-Q water and drying with nitrogen, the film thicknesses were measured again by depth profiling across the same scratches. The average film thickness measured, excluding the high features observed in the topography image, remained the same (within experimental uncertainty) after soaking in PB (Table 6.5). This result was reproducible for three repeat experiments. The average surface roughness, also excluding the high features, was also examined before and after soaking (Table 6.5). Again no changes in the films were observed after soaking. It was noted that the average surface roughness values were not as reproducible between identical experiments compared to the film thickness measurements. On further investigation, the surface roughness of the bare PPF surfaces used to graft the ED-films was found to vary, and hence PPF samples with rough surfaces led to greater surface roughness for the ED-grafted film and vice versa. However, despite the variation in surface roughness, all the ED-films exhibited the same behaviour. These results are consistent with those reported for *n*-tridecylamine (TDA) films grafted to PPF surfaces and immersed twice in 0.1 M $[Bu_4N]BF_4$-acetonitrile for 10 minutes. No changes in film thickness or surface roughness were observed after soaking for these films.[36] The unchanged film thickness and surface roughness values observed for ED-grafted films before and after soaking indicate that a large-scale loss of film is not occurring during the soaking protocol. On the other hand, the formation of nanometer-sized pinholes in the film cannot be discounted due to the lateral resolution limits of the AFM instrument (in the order of ~10 nm).

Table 6.5. The effect of soaking ED-grafted PPF surfaces in PB (pH 7.4) on film thickness and surface roughness as measured using AFM. ED-grafted electrodes were prepared in 0.1 M $[Bu_4N]BF_4$-acetronitrile solution containing 5 mM ED by cycling from 0 to 1.20 V for 6 cycles at 100 mV s^{-1}. The experiment was performed three times. Each film thickness measurement is the average value determined for three scratches made during AFM depth profiling.

Sample [a]	Film thickness (nm) [bd]		Surface roughness (R_a) (nm) [cd]	
	As-prepared	After soaking in PB for 60 minutes	As-prepared	After soaking in PB for 60 minutes
1	2.63 ± 0.17	2.90 ± 0.16	0.77 ± 0.09	0.76 ± 0.07
2	2.68 ± 0.82	2.85 ± 0.48	0.67 ± 0.09	0.59 ± 0.12
3	2.90 ± 1.47	2.68 ± 1.20	0.45 ± 0.06	0.48 ± 0.06

[a] Measurements were made on three identical samples.

[b] Film thickness measurements are the average of three scratches made in different locations on the same sample. The scratches used to determine film thickness for the as-prepared film were re-measured after soaking the film in PB for 60 minutes.

[c] Average surface roughness values (R_a) are an arithmetic average of measured mean roughness values obtained from 10 randomly selected areas (200×200 nm^2) of the surface.

[d] Stated errors indicate the range of values observed.

Control experiments involving soaking bare PPF surfaces in PB for 60 minutes were carried out to assess whether buffer salt residues had any effect on AFM thickness and surface roughness measurements. No changes were revealed in the average surface roughness (0.35 ± 0.09 nm) and the average depth of the scratches made at the bare PPF surface remained the same (within experimental uncertainty) (0.26 ± 0.02 nm). However, when new scratches were made at different locations on the surface, the average depth increased by 0.45 ± 0.04 nm. The results can be explained by assuming that after soaking in buffer a uniform layer of buffer salt residue coats the entire surface (*i.e.*, both the PPF surface beside the scratch and the base of the scratch). This would result in no change of measured scratch depth when profiling a scratch before and after buffer soaking. However, when a new scratch is made on a buffer soaked PPF surface the measured scratch depth increases because it is the sum of the depth of the salt layer and the scratch into the PPF layer. Film thickness measurements for ED films after soaking in PB were made by re-measuring the scratches made prior

to soaking and hence, buffer salt residues are expected to have an insignificant effect on measured film thickness.

To further investigate ED film changes on soaking in PB, XPS measurements were made of two films after soaking in PB. The results were compared with those obtained for two as-prepared ED films grafted to glassy carbon, described in Section 6.3.1. There were no significant differences in the nitrogen, carbon and oxygen atomic percentages for ED films before and after soaking in PB (Table 6.6); most importantly, the amount of nitrogen remained constant within experimental variability, indicating that any loss of film from the surface is relatively small.

Table 6.6. XPS data analysing the effect of soaking ED films grafted to glassy carbon in PB (0.04 M, pH 7.4) for 60 minutes.[a]

Sample	**Atomic %**[c]		
	N	**C**	**O**
ED, as-prepared	17.3	69.0	11.1
ED, as-prepared	17.3	67.1	11.9
ED, soaked in PB 1 hr	18.7	68.0	11.6
ED, soaked in PB 1 hr	18.5	68.1	11.3

[a] All samples were ultrasonicated in Milli-Q water for 30 seconds and dried with nitrogen prior to analysis.

[b] Glassy carbon cycled six times from 0 to 1.20 V at 100 mV s^{-1} in blank 0.1 M $[BuN_4]BF_4$-acetonitrile solution.

[c] Estimated relative error on atomic percentage is 10 %.

A typical wide scan spectrum and narrow scan spectra for the C1s, N1s and O1s regions for an ED film after soaking in PB for 60 minutes are shown in Figure 6.8 and the atomic percentage at each binding energy for C, N and O are listed in Table 6.7. The peaks observed in the narrow scan spectra regions occur at the same binding energies for ED films before and after soaking in PB and the atomic percentage observed at each binding energy remains relatively unchanged within experimental error. Thus, it appears that the composition of the film is not altered significantly upon soaking.

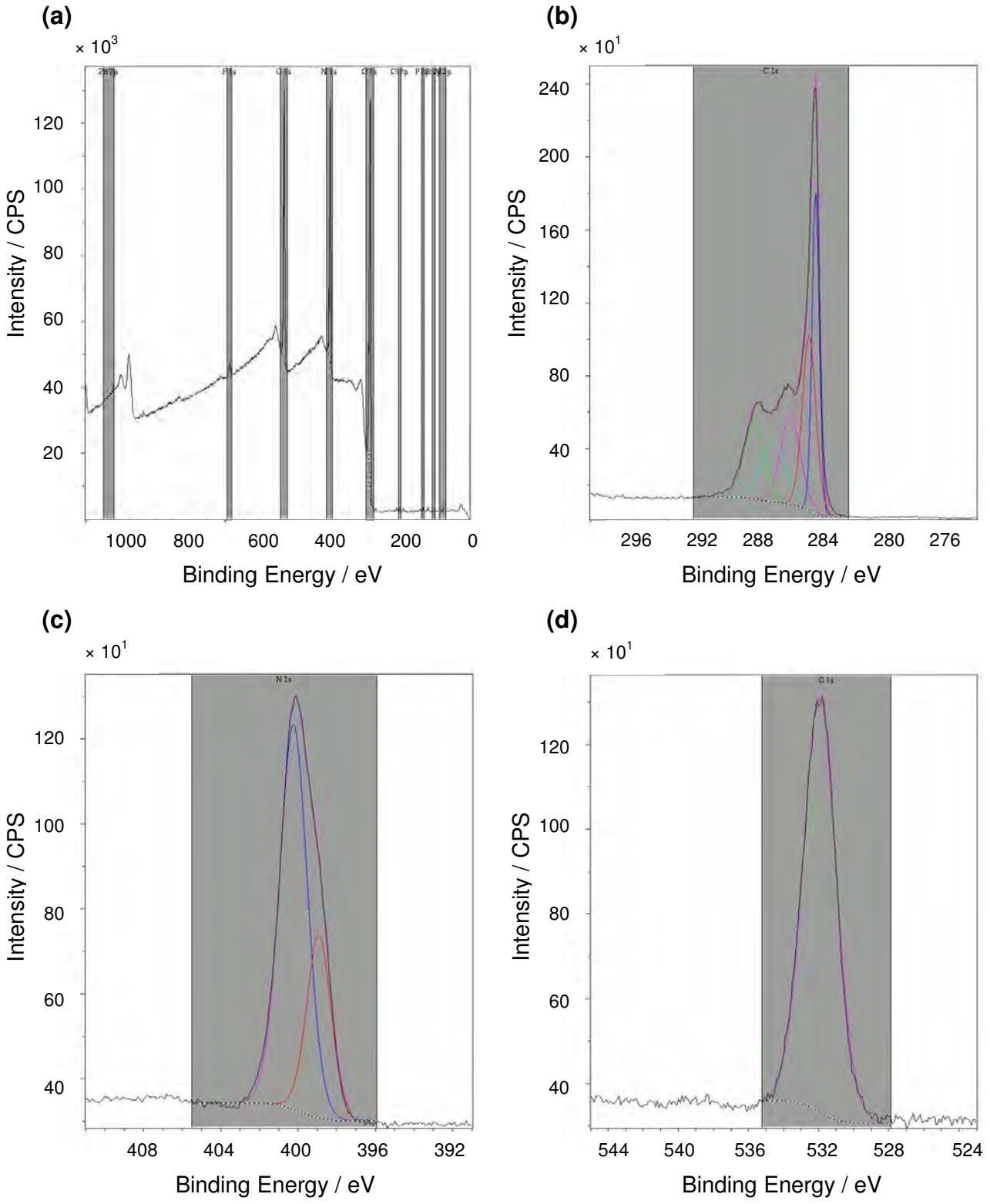

Figure 6.8. XPS spectra of an ED film grafted to glassy carbon after soaking in PB (0.04 M, pH 7.4) for 60 minutes: wide scan (a) and narrow scan spectra for C1s (b), N1s (c) and O1s (d) regions. The black line is the spectra recorded whilst the coloured lines represent those used for peak fitting.

Table 6.7. Atomic % of C, N and O at the binding energies observed for XPS narrow scan spectra for ED films grafted to glassy carbon before and after soaking in PB (pH 7.4).[a] Errors indicate the range of values obtained.

Sample	C			N			O		
	Binding Energy (eV)[b]	**Peak Assignment**	**Atomic %**	**Binding Energy (eV)[b]**	**Peak Assignment**	**Atomic %**	**Binding Energy (eV)[b]**	**Peak Assignment**	**Atomic %**
ED film as-prepared	284.7 ± 0.1	aromatic C[c]	28.0 ± 1.6	399.1 ± 0.1 [c,d]	covalent C-N	30.4 ± 2.8	532.1 ± 0.1	surface O	100 ± 0.0
					$C\text{-}NH_2$		[c,d]	C=O,C-O-	
	285.1 ± 0.4	alkyl chain[d]	23.1 ± 3.3	400.5 ± 0.1 [c,d]	covalent C-N	68.7 ± 3.7		CO_3^{2-}	
	[c]	C-OH,			$C\text{-}NH_2$, $C\text{-}NH_3^+$	1.7 ± 0.0		HCO_3^-	
	286.3 ± 0.5	Ar-OH,C-O-	22.9 ± 5.0	406.8 ± 0.0	surface N				
	287.1 ± 0.0	C=O, C-O- [d]	12.8 ± 0.0						
	288.5 ± 0.1	[d] C=O, CO_3^{2-}	19.7 ± 3.2						
		HCO_3^-							
ED film soaked in PB for 60 mins	284.7 ± 0.0	aromatic C[c]	25.2 ± 0.5	399.2 ± 0.1 [c,d]	covalent C-N	27.8 ± 1.8	532.3 ± 0.0	surface O	100 ± 0.0
					$C\text{-}NH_2$		[c,d]	C=O,C-O-	
	285.3 ± 0.2	alkyl chain[d]	24.4 ± 1.1	400.6 ± 0.1 [c,d]	covalent C-N	72.2 ± 1.8		CO_3^{2-}	
	[c]	C-OH,			$C\text{-}NH_2$, $C\text{-}NH_3^+$			HCO_3^-	
	286.3 ± 0.0	Ar-OH,C-O-	17.8 ± 0.7						
	287.3 ± 0.1	C=O, C-O- [d]	15.6 ± 0.1						
	288.7 ± 0.0	[d] C=O, CO_3^{2-}	17.1 ± 1.2						
		HCO_3^-							

[a] All samples were ultrasonicated in Milli-Q water for 30 seconds and dried with nitrogen prior to analysis.

[b] All peak positions were referenced to aromatic carbon at 284.7 eV.

[c] Contribution from glassy carbon surface. [d] Contribution from ED film.

6.3.2.3 Investigation of the Formation of Pinholes in Ethylenediamine Films during Soaking

As there was no evidence for large scale loss of the ED film during soaking from AFM film thickness and surface roughness measurements and XPS, it was proposed that the return of the FcOH probe response observed upon soaking an ED-grafted electrode in PB may be due to the formation of pinholes in the ED film. Possible scenarios which would lead to the formation of pinholes include: (1) desorption of non-covalently attached ED molecules, (2) cleavage of covalently-bound surface modifiers or (3) re-organisation of covalently attached molecules (Figure 6.9). Based on the high bond dissociation energy for a C–N bond (770 kJ mol^{-1})[37] and the work of Porter *et al.* who showed that the covalent C–N bond formed upon grafting amines to carbon surfaces is hydrolytically stable towards sonication and soaking in aqueous solutions[8] (see Section 6.1.2), it seems unlikely that pinholes would form in the ED grafted film as a result of cleavage of the covalently-bound surface modifiers under the conditions used in this work.

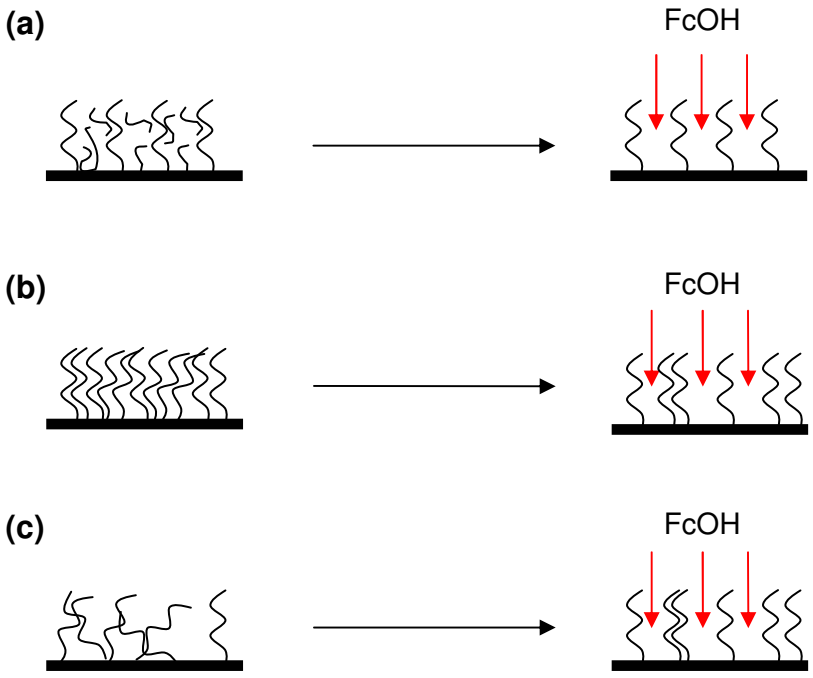

Figure 6.9. Formation of pinholes in ED films after soaking in PB by (a) desorption of non-covalently attached modifier, (b) cleavage of covalently-bound surface modifiers and (c) re-organisation of covalently attached modifier, leading to the return of the FcOH response at ED-grafted electrodes.

In an attempt to determine whether pinholes form in the ED-grafted films after soaking, quinones were used as redox probes. Duvall, McCreery and co-workers have investigated the self-catalysis of catechols and quinones during electron-transfer at glassy carbon electrodes in the presence and absence of modifying films.[38-40] Several species were investigated including dopamine, 4-methylcatechol, 3,4-dihydroxyphenylacetic acid (DOPAC) and benzoquinone. These species appear to require an adsorption site for rapid electron transfer and they have been shown to be electroinactive on glassy carbon surfaces completely covered by a modifying layer. Hence, the redox chemistry of these catechols and quinones may provide a useful test for pinholes. In the presence of a modifying layer, a response from the catechol or quinone species should be an indication of the presence of bare glassy carbon, as might occur from pinhole formation. For the present study, the benzoquinone/hydroquinone redox system (Scheme 6.6) in PB (pH 7.4) was chosen to investigate the formation of pinholes. At pH 7.4, the amine groups of the ED film are protonated whilst benzoquinone remains neutral. A neutral quinone and hydroquinone species was required for these experiments to avoid complications arising from electrostatic attraction or repulsion between the ED film and the solution redox system.

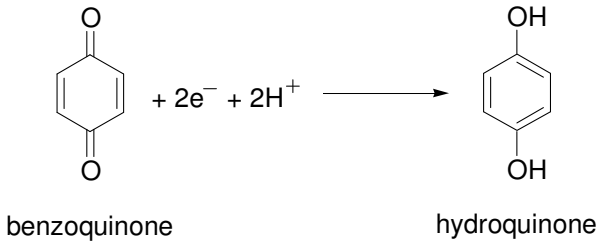

Scheme 6.6. The benzoquinone/hydroquinone redox system.

Benzoquinone (BQ) was initially adsorbed onto polished glassy carbon and ED-grafted electrodes by recording a cyclic voltammogram in BQ-PB solution (1 mM, 10 mL) from 0.80 to -0.50 V at 100 mV s^{-1} (scans not shown). The amount of BQ adsorbed at the surface was subsequently monitored by transferring the electrode to a blank PB solution and recording another cyclic voltammogram over the same potential range. Figure 6.10, scans (i) and (ii), show the response of polished glassy carbon and an as-prepared ED-modified electrode in blank PB after the adsorption of BQ. At polished glassy carbon, the redox peaks of the adsorbed BQ are clearly observed and the voltammogram is chemically reversible with $E_{1/2} = 0$ V. A large peak separation is

observed indicating slow electron transfer (ΔE_p = 268 mV). In comparison, no BQ redox chemistry is observed at the ED-modified surface examined immediately after film grafting. This result suggests that the initial surface film is impermeable and/or contains no bare areas of glassy carbon that allow BQ to pre-adsorb for reaction. The ED-modified electrode was subjected to the adsorption of BQ again after soaking the ED-film in PB for 15 and 60 minutes. A progressive change in the amount of BQ adsorbed at the electrode was observed as soaking time in PB increased (Figure 6.10, scans (iii) and (iv)). The peak currents increased and ΔE_p decreased, tending towards those observed at polished glassy carbon. These results are analogous to those recorded using FcOH (see Section 6.3.2.1) and suggest that small amounts of the ED film are being desorbed from the surface during soaking leading to pinholes in the film and/or the film is opening up and exposing pinholes that were present immediately after grafting.

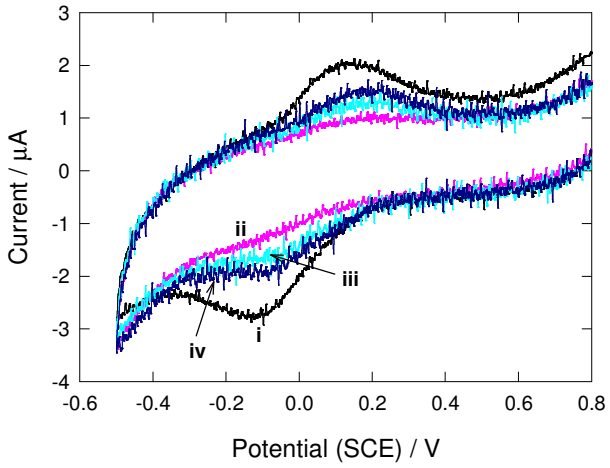

Figure 6.10. Cyclic voltammograms obtained in PB of BQ adsorbed at glassy carbon before (i) and after (ii-iv) grafting ED: (ii) freshly grafted ED film, (iii) ED film soaked in PB for 15 minutes prior to adsorption of BQ and (iv) ED film soaked in PB for 60 minutes prior to adsorption of BQ. BQ was adsorbed at the surfaces by recording one cyclic voltammogram between 0.80 and -0.50 V in 1 mM BQ-PB solution (υ = 100 mV s^{-1}) (not shown).

To adsorb BQ onto the surface, soaking of the electrode in 1 mM BQ-PB solution was investigated as an alternative to potential cycling. At a polished glassy carbon surface, the maximum response towards adsorbed BQ was reached after soaking in 1 mM BQ-PB solution for 4 minutes. The peak currents did not increase upon further soaking and hence, the adsorption equilibrium was

reached under these conditions. The surface concentration of BQ adsorbed at the polished glassy carbon surface by potential cycling or soaking in 1 mM BQ-PB solution was determined from the charge associated with the reduction peak (see Chapter 2, Section 2.7). The maximum response for the adsorption of BQ obtained upon soaking for 4 minutes (3.42×10^{-10} mol cm^{-2}) was similar (within experimental uncertainty) to that obtained after recording one cyclic voltammogram between 0.80 and -0.50 V at 100 mV s^{-1} ((3.85 ± 0.53) $\times 10^{-10}$ mol cm^{-2} (n = 3)). The associated uncertainty indicates the range of values observed. Potential scanning increased the rate of adsorption as the time taken to record one cyclic voltammogram in the presence of BQ was less than the soaking time of 4 minutes.

The effect of soaking an ED-modified surface in 1 mM BQ-PB solution was examined to determine whether pinholes were formed in the film during soaking in PB. An ED-grafted electrode, previously soaked in PB for 60 minutes, was soaked in the BQ-PB solution for 5, 30 and 60 minutes after which time cyclic voltammograms were recorded in blank PB to monitor the amount of BQ adsorbed on the surface. As the soaking time in the BQ-PB solution increased the amount of BQ detected at the surface increased. Data from a typical experiment are shown in Table 6.8. After soaking in BQ-PB solution for 60 minutes, the surface concentration of BQ measured in blank PB (4.33×10^{-10} mol cm^{-2}) was greater than that adsorbed at bare glassy carbon (3.81×10^{-10} mol cm^{-2}) indicating that the BQ must be accumulating in the film over time. These results demonstrate that pinholes must exist in the ED film after soaking in PB because BQ must adsorb onto bare areas of the glassy carbon surface in order to observe its electrochemistry.[38-40] However, it is not possible to establish whether loss of non-covalently bound material off the surface to produce pinholes (Figure 6.9 (a)) or reorganisation of the film to expose already existing pinholes (Figure 6.9 (c)) is the dominant mechanism.

Table 6.8. The effect of soaking time on the surface concentration of BQ at an ED-grafted electrode previously treated with PB for 60 minutes. BQ was pre-adsorbed onto the surface by soaking the electrode in 1 mM BQ. The amount of BQ at the surface was monitored in blank electrolyte (PB, 0.04 M, pH 7.4) using cyclic voltammetry to scan between 0.80 and -0.50 V (υ = 100 mV s^{-1}).

Surface	Soaking time in BQ (min)	Surface concentration of BQ (mol cm^{-2})[a]
Bare GC	[b]	3.81×10^{-10}
ED-GC, soaked in PB 1 hr	[b]	2.44×10^{-10}
ED-GC, soaked in PB 1 hr	5	3.67×10^{-10}
ED-GC, soaked in PB 1 hr	30	3.72×10^{-10}
ED-GC, soaked in PB 1 hr	60	4.33×10^{-10}

[a] Determined from the charge associated with the reduction peak.

[b] BQ was pre-adsorbed onto the surface from a 1 mM solution by scanning between 0.80 and -0.50 V (υ = 100 mV s^{-1}).

6.3.2.4 Theory for Electron Transfer at Film-Coated Electrodes

In order to interpret the observed changes in the FcOH redox response at ED-modified electrodes upon soaking, the relevant theory for electron transfer at film-coated electrodes must first be considered. Films form a barrier between the electrode and solution species. This property allows film structure to be monitored using cyclic voltammetry by comparing the response of a redox probe at bare and modified electrodes. The electrochemical response of solution-based redox probe species at film-coated electrodes can be explained by two limiting models: (1) electron transfer by tunneling through blocking films and (2) permeation through pores and pinholes.[41]

Electron Transfer by Tunneling Through Blocking Films

The presence of a compact modifying film increases the distance of closest approach between the solution-based redox probe species and the electrode. For very thin films, electrons can tunnel through the film and cause faradaic reactions (Figure 6.11).

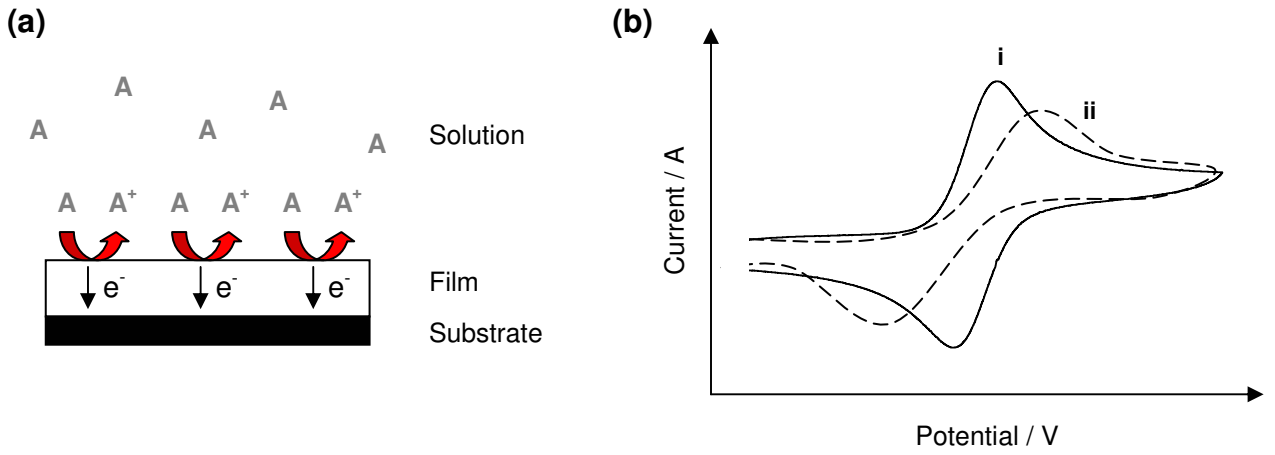

Figure 6.11. Electron tunneling through a modifying film for the electro-oxidation of species A: (a) illustration of electron transfer *via* tunneling across a thin film and (b) cyclic voltammogram for a solution-based probe species where the rate of electron transfer at an unmodified electrode (i) is slowed in the presence of a modifying film (ii).

The effect of a blocking film on the electron transfer rate constant is given by equation 6.1 where k^0_{obs} is the observed rate constant at the modified electrode, k^0 is the standard heterogeneous rate constant at the polished electrode (cm s^{-1}), d is the distance of closest approach between the solution-based redox probe species and the electrode (*i.e.*, the thickness of the modifying layer) (Å) and β is the tunneling parameter which depends on the chemical nature of the monolayer (Å $^{-1}$). For equation 6.1, β is assumed to be independent of potential.[41]

$$k^0_{obs} = k^0 \exp(-\beta d) \qquad (6.1)$$

Equation 6.1 shows that the rate of electron transfer due to tunneling across the modifying film, decreases exponentially with distance and magnitude of β (usually on the order of 1 $Å^{-1}$) and implies that electron tunneling is only important with blocking films that are thinner than ~ 15 Å.[41] A typical cyclic voltammogram illustrating the probe response when electron transfer is slowed across the film is shown in Figure 6.11. An increase in peak separation (ΔE_p) after grafting, usually associated with a decrease in peak current, indicates the presence of a blocking film that decreases the rate of electron transfer between the redox probe and the electrode. As the thickness of the modifying layer is increased the electron transfer rate due to tunneling decreases, as evidenced

by further increases in ΔE_p and decreasing peak currents, until eventually the thickness of the layer is sufficiently large that electron transfer by tunneling is completely inhibited.

Although the average film thickness for the ED-grafted glassy carbon electrodes are significantly greater than 1.5 nm, it is possible that tunneling is the dominant electron transfer mechanism for probe species that can permeate into the film.

Permeation Through Pores and Pinholes

Electron transfer at partially blocked surfaces containing small-sized active sites has been studied extensively by Amatore and co-workers.[42] For electrodes covered by an insulating film containing pores or channels from the solution to the electrode (Figure 6.12), the degree to which the electrolysis of a solution-based redox probe species differs from that observed at the bare (unmodified) electrode depends on the fractional coverage of the electrode by the film (θ), the size and distribution of the pinholes, the standard heterogeneous rate constant at the unmodified electrode (k^0) and the time scale of the experiment (υ).[41,42] It is noted that theoretical treatments of films containing pores and/or pinholes often use idealised models relating to those for ultramicroelectrode arrays as they usually possess a uniform distribution of active sites with a well-defined geometry.[41] However, for film-coated electrodes the size and distribution of pinholes within the film are not necessarily uniform.

For the ED-modified electrodes, Figure 6.12 (a) is not considered an accurate representation of the surface as this structure would give large areas of bare electrode surface that could be detected by AFM imaging. The structure shown in Figure 6.12 (b) is also not appropriate because sigmoidal voltammograms are not observed. Hence, the behaviour of the ED films should be examined by consideration of the film structure shown in Figure 6.12 (c).

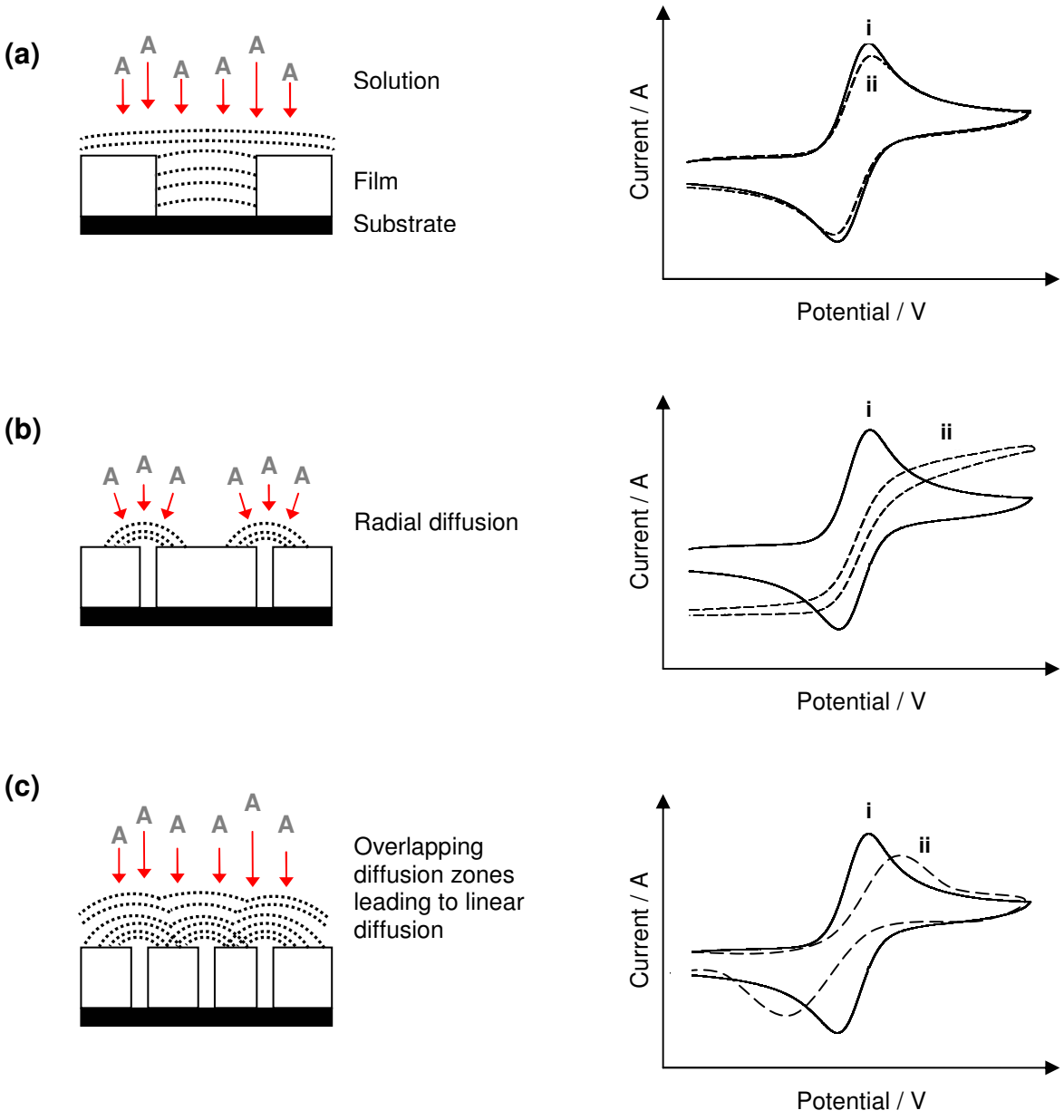

Figure 6.12. The effect of pinhole size and spacing on the electrochemical response towards a solution-based redox probe (species A): (a) when θ is small giving rise to large pinholes and (b-c) represent the two limiting cases when θ is large and the small pinholes are widely-spaced (b) or closely-spaced (c). For the voltammograms, (i) is the response at an unmodified electrode and (ii) is the response at a film-coated electrode.

The rate constant for electron transfer observed at a modified electrode containing pinholes of the size and distribution in Figure 6.12 (c) is given by equation 6.2, where k^0_{obs} is the observed rate constant at the modified electrode, k^0 is the standard heterogeneous rate constant at the polished electrode (cm s^{-1}) and the term (1- θ) represents the fraction of the surface not covered by the modifying film.[41,42]

$$k^0_{obs} = k^0(1-\theta) \qquad (6.2)$$

Equation 6.2 shows that as the surface coverage of the film decreases (*i.e.*, the number of pinholes increases) the rate constant for electron transfer of a probe molecule across a film appears to increase.

6.3.2.5 Interpretation of Changes in Redox Probe Response at Ethylenediamine-Grafted Electrodes

The electrochemical response of FcOH in PB (pH 7.4) obtained at a freshly prepared ED-grafted electrode exhibited a peak shaped-voltammogram where the ΔE_p had increased and the peak currents were lower compared to the response recorded at an unmodified electrode (Figure 6.7 (a), scans (i) and (ii)). Considering the relevant theory for electron transfer at film-coated electrodes discussed in Section 6.3.2.4, the shape of the voltammogram observed at an ED-grafted electrode immediately after preparation suggests that electron transfer is occurring by electron tunneling after permeation of the probe into the film (Figure 6.11) and/or as a result of electron transfer at closely-spaced pinholes where the probe molecules approach the surface by linear diffusion (Figure 6.12 (c)). After soaking the ED-grafted electrode in PB for 60 minutes, the FcOH response was very similar to that at an unmodified electrode (Figure 6.7 (a), scans (i) and (iv)). A decrease in ΔE_p, associated with an increase in peak current, is observed indicating that the ED film is less blocking after soaking and that the rate of electron transfer between the redox probe molecule and the electrode is increased. The increased response towards FcOH at an ED-grafted electrode after soaking in PB is most likely due to a decrease in the distance of closest approach between the solution-based redox probe and the electrode as a result of increased permeability of the probe into the film and/or reorganisation of the film leading to a more open structure increasing access to

pre-existing pinholes. Alternatively, new pinholes could be formed by loss of material from the surface.

In an attempt to determine whether pinholes are present in the ED film before and after soaking in PB, BQ was used as a redox probe (Figure 6.10). No response was observed for BQ at a freshly prepared ED-grafted electrode prior to soaking. This indicates that BQ is not adsorbing to areas of bare glassy carbon and hence, there are no readily accessible pinholes in the film. This result suggests that the mechanism of electron-transfer at an ED-grafted electrode immediately after preparation must be due to electron tunneling across the film. After soaking in PB for 60 minutes, the redox peaks associated with BQ were observed at the ED-grafted electrode. Therefore, assuming McCreery's findings are relevant to this work,[38-40] pinholes (bare glassy carbon surface) must be present after soaking because the BQ electrochemistry is observed. During soaking the film may undergo reorganisation to adopt a more open structure, thereby increasing access to pre-existing pinholes and/or new pinholes could be formed by loss of material from the surface. Hence, these results show that after soaking, electron transfer at the ED-grafted electrode occurs at pinholes in the film. Electron tunneling across the film will also occur to some extent.

The effect of solvent on the FcOH response before and after soaking an ED-grafted electrode was examined using Tris·HCl buffer (pH 9.0) and acetonitrile (Figure 6.7 (b) and (c)). The ED film was slightly less blocking upon short exposure times to Tris·HCl compared to PB. This result was unexpected and cannot be explained at present. In comparison, the ED film was significantly more blocking in acetonitrile indicating a compact film structure which is not permeable to probe molecules and hence, electron transfer *via* electron tunneling across the film is slowed considerably. After extended soaking in acetonitrile, the ED film was observed to be more blocking suggesting that the film has become more compact and therefore, electron-tunneling across the film must be the dominant mechanism for electron transfer under these conditions.

In summary, the redox probe voltammetry data recorded at ED-grafted electrodes before soaking in buffer or acetonitrile is consistent with electron tunneling across the surface film being the dominant mechanism for electron transfer. The results demonstrate that before soaking the ED film permeability with respect to FcOH is dependent on the solvent. The film was significantly blocking in acetonitrile indicating a compact film, whilst in buffer peak-shaped voltammograms

were observed suggesting a more open structure. After soaking in buffer, the increased response towards FcOH and BQ is caused by changes in film structure exposing pinholes and it is assumed that a more open film structure also allows redox probe molecules to permeate further into the film for faster electron transfer by the tunneling mechanism. The increase in the blocking effect of the ED film after soaking in acetonitrile indicates that desorption of material from the surface is not a major factor and it seems unlikely that desorption of the ED film would be markedly enhanced in PB or Tris·HCl compared with acetonitrile. Instead, this observation points to the importance of solvent and/or electrolyte in determining permeability. This conclusion is supported by the measurements obtained using XPS and AFM which showed no evidence for large scale loss of the ED film during soaking. However, considering the uncertainties associated with AFM measurements combined with the sample-to-sample variation observed with XPS measurements, it is estimated that small amounts of the film (up to 15 %) could be lost from the surface without changing the AFM and XPS data. Nevertheless, in agreement with other authors, it is concluded that the electrografted ED layers are strongly attached to the glassy carbon surface and are stable under the conditions employed in this study (refer to Section 6.1.2).

The model proposed above for the mechanism of electron-transfer at the ED-grafted film based on changing film permeability in response to its environment indicates that the layer must be loosely-packed. Solvent-, ion- and potential-induced volume and permeability changes have been observed in phenyl films electrografted from diazonium salts[43-45] and it has also been demonstrated that these films, as prepared, are loosely packed.[27,43,45] A loosely packed structure would seem to be a necessary prerequisite for permeability changes that do not involve loss of material from the film, and a similar structure can be inferred for electrografted amine films.[36]

6.4 Conclusions

An important finding of this research is that reliable information about film stability cannot be derived from electrochemical, AFM or XPS studies individually. It cannot be assumed that reappearance of the probe response after soaking an ED-film in buffer indicates loss of film from the surface as no measurable loss is detected using AFM and XPS. It is also noted that due to the sensitivity limitations of AFM and XPS, it is difficult to distinguish between small losses of material and solvent- or ion-induced changes in film permeability using these techniques alone and hence, the importance of combining the results for electrochemical, AFM and XPS studies when investigating film stability is emphasised.

Consideration of all the results obtained in this study showed that electrografted ED films are stable in solution and examination of the FcOH probe response at ED-modified carbon electrodes in different media demonstrated that these films are responsive to their environment. In buffer solution, the ED films adopt an open film structure allowing probe molecules to access pinholes and to permeate into the film for faster electron-transfer by tunneling. After prolonged exposure to acetonitrile the film remains compact and electron transfer across the film is slowed. These results show that the films have dynamic behaviour and must have a loosely-packed structure.

6.5 References for Chapter 6

1. Downard, A. J. Electrochemically assisted covalent modification of carbon electrodes. *Electroanalysis* **2000**, *12*, 1085-1096.

2. Allongue, P.; Delamar, M.; Desbat, B.; Fagebaume, O.; Hitmi, R.; Pinson, J.; Savéant, J. M. Covalent modification of carbon surfaces by aryl radicals generated from the electrochemical reduction of diazonium salts. *Journal of the American Chemical Society* **1997**, *119*, 201-207.

3. D'Amours, M.; Bélanger, D. Stability of substituted phenyl groups electrochemically grafted at carbon electrode surface. *Journal of Physical Chemistry B* **2003**, *107*, 4811-4817.

4. Delamar, M.; Hitmi, R.; Pinson, J.; Saveant, J. M. Covalent modification of carbon surfaces by grafting of functionalised aryl radicals produced from electrochemical reduction of diazonium salts. *Journal of the American Chemical Society* **1992**, *114*, 5883-5884.

5. Pinson, J.; Podvorica, F. Attachment of organic layers to conductive or semiconductive surfaces by reduction of diazonium salts. *Chemical Society Reviews* **2005**, *34*, 429-439.

6. Barbier, B.; Pinson, J.; Desarmot, G.; Sanchez, M. Electrochemical bonding of amines to carbon-fibre surfaces toward improved carbon-epoxy composites. *Journal of the Electrochemical Society* **1990**, *137*, 1757-1764.

7. Adenier, A.; Chehimi, M. M.; Gallardo, I.; Pinson, J.; Vila, N. Electrochemical oxidation of aliphatic amines and their attachment to carbon and metal surfaces. *Langmuir* **2004**, *20*, 8243-8253.

8. Deinhammer, R. S.; Ho, M.; Anderegg, J. W.; Porter, M. D. Electrochemical oxidation of amine-containing compounds - a route to the surface modification of glassy-carbon electrodes. *Langmuir* **1994**, *10*, 1306-1313.

9. Maeda, H.; Yamauchi, Y.; Hosoe, M.; Li, T. X.; Yamaguchi, E.; Kasamatsu, M.; Ohmori, H. Direct covalent modification of glassy-carbon surfaces with 1-alkanols by electrochemical oxidation. *Chemical & Pharmaceutical Bulletin* **1994**, *42*, 1870-1873.

10. Maeda, H.; Hosoe, M.; Li, T. X.; Itami, M.; Yamauchi, Y.; Ohmori, H. Indirect detection of alkaline earth ions by the voltammetric response of ferricyanide anion at a glassy carbon electrode anodised in 1-octanol. *Chemical & Pharmaceutical Bulletin* **1996**, *44*, 559-564.

11. Andrieux, C. P.; Gonzalez, F.; Saveant, J. M. Derivatisation of carbon surfaces by anodic oxidation of arylacetates. Electrochemical manipulation of the grafted films. *Journal of the American Chemical Society* **1997**, *119*, 4292-4300.

12. Coulon, E.; Pinson, J.; Bourzat, J. D.; Commerçon, A.; Pulicani, J. P. Electrochemical attachment of organic groups to carbon felt surfaces. *Langmuir* **2001**, *17*, 7102-7106.

13. Vaik, K.; Maeorg, U.; Maschion, F. C.; Maia, G.; Schiffrin, D. J.; Tammeveski, K. Electrocatalytic oxygen reduction on glassy carbon grafted with anthraquinone by anodic oxidation of a carboxylate substituent. *Electrochimica Acta* **2005**, *50*, 5126-5131.

14. Nowall, W. B.; Wipf, D. O.; Kuhr, W. G. Localised avidin/biotin derivatisation of glassy carbon electrodes using SECM. *Analytical Chemistry* **1998**, *70*, 2601-2606.

15. Hayes, M. A.; Kuhr, W. G. Preservation of NaDH voltammetry for enzyme-modified electrodes based on dehydrogenase. *Analytical Chemistry* **1999**, *71*, 1720-1727.

16. Hoekstra, K. J.; Bein, T. Adsorption of zirconium-phosphonate multilayers onto phosphate-derivatised glassy carbon substrates. *Chemistry of Materials* **1996**, *8*, 1865-1870.

17. Antoniadou, S.; Jannakoudakis, A. D.; Jannakoudakis, P. D.; Theodoridou, E. Anion-exchange activity of electrochemically bonded ethylene diamine on carbon-fibres. *Journal of Applied Electrochemistry* **1992**, *22*, 1060-1064.

18. Park, S. J.; Donnet, J. B. Anodic surface treatment on carbon fibres: Determination of acid-base interaction parameter between two unidentical solid surfaces in a composite system. *Journal of Colloid and Interface Science* **1998**, *206*, 29-32.

19. Gallardo, I.; Pinson, J.; Vila, N. Spontaneous attachment of amines to carbon and metallic surfaces. *Journal of Physical Chemistry B* **2006**, *110*, 19521-19529.

20. Downard, A. J.; Jackson, S. L.; Tan, E. S. Q. Fluorescence microscopy study of protein adsorption at modified glassy carbon surfaces. *Australian Journal of Chemistry* **2005**, *58*, 275-279.

21. Liu, J. Y.; Dong, S. J. Grafting of diaminoalkane on glassy carbon surface and its functionalisation. *Electrochemistry Communications* **2000**, *2*, 707-712.

22. Liu, J. Y.; Cheng, L.; Li, B. F.; Dong, S. J. Covalent modification of a glassy carbon surface by 4-aminobenzoic acid and its application in fabrication of a polyoxometalates-consisting monolayer and multilayer films. *Langmuir* **2000**, *16*, 7471-7476.

23. Liu, Y. Q.; Yang, M. L.; Zheng, Z. K.; Zhang, B. L. Tailoring the electrochemical property of self-assembled monolayer of 16-mercaptohexadecanoic acid on gold(111) electrode with covalently coupling ethylene diamine. *Electrochemistry Communications* **2005**, *7*, 344-348.

24. Yan, Z.; Zhang, J. R.; Fang, H. Q. Electrocatalytic oxidation of uric acid at cysteine modified glassy carbon electrode. *Analytical Letters* **1999**, *32*, 223-234.

25. Herlem, G.; Goux, C.; Fahys, B.; Dominati, F.; Goncalves, A. M.; Mathieu, C.; Sutter, E.; Trokourey, A.; Penneau, J. F. Surface modification of platinum and gold electrodes by anodic oxidation of pure ethylenediamine. *Journal of Electroanalytical Chemistry* **1997**, *435*, 259-265.

26. Herlem, G.; Reybier, K.; Trokourey, A.; Fahys, B. Electrochemical oxidation of ethylenediamine: New way to make polyethyleneimine-like coatings on metallic or semiconducting materials. *Journal of the Electrochemical Society* **2000**, *147*, 597-601.

27. Brooksby, P. A.; Downard, A. J. Electrochemical and atomic force microscopy study of carbon surface modification *via* diazonium reduction in aqueous and acetonitrile solutions. *Langmuir* **2004**, *20*, 5038-5045.

28. Faucheux, N.; Schweiss, R.; Lützow, K.; Werner, C.; Groth, T. Self-assembled monolayers with different terminating groups as model substrates for cell adhesion studies. *Biomaterials* **2004**, *25*, 2721-2730.

29. Lee, W.; Lee, H.; Chun, M. S. Surface functional group effect on atomic force microscope anodisation lithography. *Langmuir* **2005**, *21*, 8839-8843.

30. *Spartan'02*, Wavefunction, Inc., Irvine, CA.

31. Kariuki, J. K.; McDermott, M. T. Nucleation and growth of functionalised aryl films on graphite electrodes. *Langmuir* **1999**, *15*, 6534-6540.

32. Ilangovan, G.; Pillai, K. C. Electrochemical and XPS characterisation of glassy carbon electrode surface effects on the preparation of a monomeric molybdate(VI)-modified electrode. *Langmuir* **1997**, *13*, 566-575.

33. Engstrom, R. C.; Strasser, V. A. Characterisation of electrochemically pretreated glassy-carbon electrodes. *Analytical Chemistry* **1984**, *56*, 136-141.

34. Tsutsumi, H.; Furumoto, S.; Morita, M.; Matsuda, Y. Electrochemical-behavior of a 4-nitrothiophenol modified electrode prepared by the self-assembly method. *Journal of Colloid and Interface Science* **1995**, *171*, 505-511.

35. Lyskawa, J.; Bélanger, D. Direct modification of a gold electrode with aminophenyl groups by electrochemical reduction of in situ generated aminophenyl monodiazonium cations. *Chemistry of Materials* **2006**, *18*, 4755-4763.

36. Cruickshank, A. C.; Tan, E. S. Q.; Brooksby, P. A.; Downard, A. J. Are redox probes a useful indicator of film stability? An electrochemical, AFM and XPS study of electrografted amine films on carbon. *Electrochemistry Communications* **2007**, *9*, 1456-1462.

37. Dean, J. A., *Lange's handbook of chemistry;* (14th ed.); McGraw-Hill, Inc.: New York, NY, USA, 1992; p 4.25.

38. DuVall, S. H.; McCreery, R. L. Control of catechol and hydroquinone electron-transfer kinetics on native and modified glassy carbon electrodes. *Analytical Chemistry* **1999**, *71*, 4594-4602.

39. DuVall, S. H.; McCreery, R. L. Self-catalysis by catechols and quinones during heterogeneous electron transfer at carbon electrodes. *Journal of the American Chemical Society* **2000**, *122*, 6759-6764.

40. Solak, A. O.; Eichorst, L. R.; Clark, W. J.; McCreery, R. L. Modified carbon surfaces as "organic electrodes" That exhibit conductance switching. *Analytical Chemistry* **2003**, *75*, 296-305.

41. Bard, A. J.; Faulkner, L. R., *Electrochemical methods: Fundamentals and applications;* (2nd ed.); John Wiley & Sons Inc.: New York, NY, USA, 2001; p 619-627.

42. Amatore, C.; Saveant, J. M.; Tessier, D. Charge-transfer at partially blocked surfaces - a model for the case of microscopic active and inactive sites. *Journal of Electroanalytical Chemistry* **1983**, *147*, 39-51.

43. Brooksby, P. A.; Downard, A. J. Multilayer nitroazobenzene films covalently attached to carbon. An afm and electrochemical study. *Journal of Physical Chemistry B* **2005**, *109*, 8791-8798.

44. Yu, S. S. C.; Downard, A. J. Dynamic behaviour of organic thin films attached to carbon surfaces. *e-Journal of Surface Science and Nanotechnology* **2005**, *3*, 294-298.

45. Paulik, M. G.; Brooksby, P. A.; Abell, A. D.; Downard, A. J. Grafting aryl diazonium cations to polycrystalline gold: Insights into film structure using gold oxide reduction, redox probe electrochemistry, and contact angle behaviour. *Journal of physical Chemistry C* **2007**, *111*, 7808-7815.

Chapter 7

Metal Nanoparticle Electrodes for the Detection of Hydrogen Peroxide

7.1 Introduction

The detection and quantitative determination of hydrogen peroxide (H_2O_2) is of great importance due to its use in a wide range of applications. The largest single market for H_2O_2 is in the textile and pulp and paper industries where it is used as a bleach.[1,2] Another common use of H_2O_2 is for the disinfection of water and treatment of industrial waste waters to remove environmental pollutants such as chlorine, sulfides and cyanide.[3-6] The food and pharmaceutical industries employ H_2O_2 as a sanitiser to kill bacteria, pathogens, fungi and other microbial organisms making it important to measure its residual concentration.[7,8] In addition, H_2O_2 is liberated as a side product of enzymatic reactions involving oxidases and therefore its concentration can be used to monitor the progress of a reaction. This concept is the foundation of many biomedical enzyme-based sensors where the detection of H_2O_2 is important for applications such as the monitoring of blood glucose for the treatment and control of diabetes and the determination of cholesterol which is directly related to the diagnosis of a variety of conditions such as heart disease.[9,10]

The determination of H_2O_2 has been performed using titrimetry,[11] spectrometry[12-15] and chemiluminescence.[16-18] Alternatively, electrochemistry has been recognised as an inexpensive and effective way to detect H_2O_2 and has led to a considerable research effort investigating the electro-oxidation (equation 7.1) and reduction of H_2O_2 (equation 7.2) at a variety of electrode materials.

$$H_2O_2 \rightleftharpoons O_2 + 2H^+ + 2e^- \quad (7.1)$$

$$H_2O_2 + 2H^+ + 2e^- \longrightarrow 2H_2O \quad (7.2)$$

7.1.1 Electrochemical Detection of Hydrogen Peroxide at Metal Electrodes

Direct electrochemical detection of H_2O_2 *via* its oxidation and reduction has been studied at platinum,[19-23] gold[21,24-26] and silver[27] electrodes. The majority of this research has been directed towards biological applications and therefore, has been carried out under neutral and alkaline conditions. Slow electron transfer kinetics at these metal electrodes means that large overpotentials are required increasing the opportunities for interference from electro-oxidisable and electro-reducible species present in biological samples, such as ascorbic acid, uric acid and oxygen. For analytical applications using metal electrodes, detection *via* the electro-oxidation of H_2O_2 is the most widely studied reaction because the mechanism for the reduction of H_2O_2 involves a complex series of reactions closely related to the reduction of oxygen and is not well understood.[19,28,29]

Platinum is the most commonly used electrode material for detecting H_2O_2 because of its relatively high reactivity towards the oxidation of H_2O_2. A typical detection potential is 0.60 V *vs*. Ag/AgCl in PB (pH 7.4).[22,23] H_2O_2 sensors employ platinum as the working electrode and in these devices a permselective coating is used to reduce interference from other oxidisable species.[30] The oxidation of H_2O_2 is extremely sensitive to surface conditioning and whilst platinum exhibits better reproducibility for this reaction than other metal electrodes,[21] the catalytic mechanism for the oxidation of H_2O_2 at a platinum electrode requires a layer of surface oxide (formed at potentials positive of 0.60 V *vs*. SCE) which is difficult to establish reproducibly.[20,22,23] Another major disadvantage of employing platinum electrodes is that platinum is an expensive material which is susceptible to poisoning and requires extensive pre-treatment.[22] Furthermore, the catalytic decomposition of H_2O_2 on a platinum electrode (equation 7.3) is a potential problem for the electrochemical detection of H_2O_2 because the concentration is decreased by this reaction.[22] Small amounts of oxygen formed by reaction 7.3 also hinders the quantitative analysis of H_2O_2 by reduction at platinum. When oxygen and H_2O_2 co-exist in solution their reduction occurs simultaneously and discrimination between the two species is not possible.[20]

$$H_2O_2 \longrightarrow {}^1/_2O_2 + 2H_2O \qquad (7.3)$$

Gold electrodes have been investigated as an alternative to platinum for the quantitative analysis of H_2O_2. The oxidation of H_2O_2 at gold surfaces has been reported to occur at two different potentials depending on the electrode preparation conditions. Brett and co-workers carried out the amperometric determination of H_2O_2 at a thin-film gold electrode produced by magnetron sputtering using a potential of 0.475 V (*vs*. Ag/AgCl/ 3 M KCl), however, Johnston *et al.* reported that it was impossible to oxidise H_2O_2 at potentials negative of 0.80 V (*vs*. SCE) using an evaporated gold electrode.[25,31] Similarly, Zhang and Wilson did not observe any response towards H_2O_2 at a gold wire electrode in the potential range 0.40 to 0.80 V (*vs*. Ag/AgCl/sat KCl).[22] A comprehensive study of the electrochemical behaviour of H_2O_2 at a polycrystalline gold electrode carried out by Gerlache *et al.* revealed that the potential at which H_2O_2 is oxidised depends on the composition and purity of the analyte solution and the oxidation state of the gold electrode.[21] At a clean polycrystalline gold surface prepared by polishing with alumina followed by electrochemical cycling between -0.40 and 1.20 V (*vs*. Ag/AgCl: 3 M NaCl) in PB (pH 7.4), two oxidation peaks were observed at 0.49 and 0.82 V in the presence of H_2O_2. These peaks correspond to oxidation of H_2O_2 and the gold surface respectively. In comparison, the presence of adsorbed impurities on gold, gold oxide species or acidic pH values inhibited the oxidation of H_2O_2 at low potentials in favour of the single oxidation peak observed at more positive potentials (0.87 V in PB). As a result of these findings, the authors suggest that oxidation of H_2O_2 at 0.49 V was favoured by the presence of an adsorbed layer of hydroxide ions on the gold surface.[21] With respect to sensor development, quantitative analysis of H_2O_2 at the more positive potential is favoured as this signal is less sensitive to the composition of the analyte solution and poisoning of the gold surface. However, application of an electrochemical cleaning procedure involving a sequence of amperometric pulses has been shown to produce a 'catalytic' and reproducible gold surface allowing the oxidative detection of H_2O_2 to be made at lower potentials in PB (pH 7.4).[24,25] Pulsing the potential to effect partial oxidation and then reduction of the gold surface prior to applying the actual detection potential ensures that the electrode characteristics remain constant for repeat measurements.

As illustrated above for gold and platinum electrodes, the direct electrochemical detection of H_2O_2 at conventional metal electrodes is often not suitable for analytical applications because of the large overpotentials required. In addition, the sensitivity of the response to surface conditioning and the composition of the analyte solution, leading to irreproducible behaviour (as discussed above), is a major disadvantage and has led to an increasingly active research area focused on developing

alternative electrocatalytic surfaces where the detection of H_2O_2 occurs at reduced overpotentials and greater electrode stability is achieved. Thin-film gold/palladium composite electrodes prepared by thermal evaporation[31] or sputtering[32] techniques have been reported to exhibit a significant increase in activity for H_2O_2 oxidation compared to the response obtained at gold electrodes constructed under the same preparative conditions. A potential more positive than 0.80 V (*vs*. SCE) was required to oxidise H_2O_2 in PB solution (pH 7.0-8.0) at gold film electrodes, however, in the presence of palladium (less than 40 % by weight) the overpotential was reduced to 0.40 V. Furthermore, the thin-film gold/palladium composite electrodes showed excellent long term stability and good reproducibility was obtained between electrodes. The activity of platinum/iridium alloy electrodes (consisting of 10 % iridium) have also been examined, however, these electrodes were less active towards the electro-oxidation of H_2O_2 than pure platinum.[22]

7.1.2 The Electrochemical Detection of Hydrogen Peroxide in the Presence of a Mediator

Modification of electrode surfaces with electroactive films and/or the incorporation of mediator molecules within permselective polymer coatings has been widely investigated to enhance the slow electron transfer reactions observed for the electrochemical detection of H_2O_2 at solid metal electrodes. Mediators have been shown to exhibit the greatest catalytic efficiency for the electro-reduction of H_2O_2 by considerably reducing the overpotentials so that it is possible to eliminate electroactive interferents. Several examples of mediated electrode designs that have been used for determining H_2O_2 *via* its reduction are given in Table 7.1.

The most extensively examined mediator for H_2O_2 detection is ferric hexacyanoferrate ($Fe_4[Fe(CN)_6]_3 \cdot xH_2O$), commonly known as Prussian Blue.[33-36] Chemically modified electrodes based on Prussian Blue have attracted widespread attention because well-defined electroactive films are formed after electrochemical or chemical deposition on a variety of conductive surfaces including platinum,[37,38] gold,[37] graphite[39] and glassy carbon.[34-36] The latter is the most commonly used substrate. Mixing of Prussian Blue with glassy carbon or graphite powder to prepare carbon paste electrodes has also been reported.[40,41] The reduced form of Prussian Blue electrocatalytically

Table 7.1. Illustrative examples of mediators used for the electro-reduction of H_2O_2.

Mediator	Method of immobilisation	Conditions for measuring H_2O_2 signal[a]	Limit of Detection (μM)	Ref.
Prussian Blue	Electrodeposited onto a glassy carbon electrode	FI, -0.05 V *vs*. Ag/AgCl, pH 5.5	0.50	35
Prussian Blue	Mixed with glassy carbon paste and mineral oil	Amp, 0 V *vs*. Ag/AgCl, pH 6.0	0.25	40
Prussian Blue	Electrodeposited onto a glassy carbon electrode and coated with a permeselective poly(sulfonate aniline) film	Amp, 0.05 V *vs*. Ag/AgCl, pH 3.8	80	42
CuHCF	Electrodeposited onto a glassy carbon electrode	FI, -0.20 V *vs*. Ag/AgCl, pH 5.5	500	36
MnHCF	Chemical deposition onto a aluminium electrode	Amp, 0 V *vs*. SCE, pH 6.5	0.20	43
Hemoglobin	Incorporated into hydroxyethylcellouse polymer film coated onto pyrolytic graphite	CV, -0.28 V *vs*. SCE, pH 6.0	0.80	44
Myoglobin	Incorporated into hydroxyethylcellouse polymer film coated onto pyrolytic graphite	CV, -0.30 V *vs*. SCE, pH 6.0	8.00	44
Myoglobin	Immobilised on a hexagonal mesoporous silica modified glassy carbon	Amp, -0.40 V *vs*. SCE, pH 7.0	0.062	45

[a] Amp = amperometry, FI = flow injection amperometry, CV = cyclic voltammetry.

reduces H_2O_2 in aqueous electrolytes acting as a mediator between the electrode and peroxide present in solution or formed as a side product of an enzyme-catalysed reaction.[38,41,42] This process proceeds at low applied potentials (~ 0 V *vs*. Ag/AgCl) and therefore allows for the selective detection of H_2O_2 in the presence of oxygen.[35,38,40,42] The high activity and selectivity of Prussian Blue towards the electro-reduction of H_2O_2 is comparable to biocatalysis with a natural peroxidase enzyme (see Section 7.1.3) and hence, Prussian Blue has been referred to as an 'artifical peroxidase'.[34] Using Prussian Blue-modified glassy carbon electrodes, initial sensitivities ranging from 0.3-0.6 A M^{-1} cm^{-2} and a detection limit of 0.50 μM have been achieved in flow-injection mode.[34,35] A disadvantage of employing Prussian Blue-modified electrodes is that they suffer from a lack of long-term stability due to gradual dissolution of the film during potential cycling.[37,42] However, the operational stability of these electrodes can be improved by adding stabilising agents[37] or coating the modified electrode with a permselective conducting polymer film.[42] An added advantage of employing a permselective coating is that penetration of electroactive interferents, such as ascorbic acid or uric acid, commonly present in biological samples can be avoided, thus improving the selectivity of the electrode.

Copper and manganese hexacyanoferrate complexes (CuHCF and MnHCF respectively) have also been shown to electrocatalytically reduce H_2O_2.[36,43] As illustrated in Table 7.1, CuHCF required a larger cathodic overpotential to achieve H_2O_2 reduction and the resulting limit of detection was three orders of magnitude higher than that of a similar electrode based on Prussian Blue.[36] In comparison, MnHCF films deposited on aluminium electrodes exhibited similar sensitivity to that observed for a Prussian Blue-modified glassy carbon electrode but were more stable. The increased stability was attributed to a passive surface state of the aluminum substrate rendering the surface more suitable for film deposition.[43]

As an alternative to transition metal hexacyanoferrate complexes, heme-containing proteins such as hemoglobin and myoglobin have also been utilised as mediators for the electro-reduction of H_2O_2. Immobilisation of heme proteins at the electrode surface has been shown to increase the rate of direct electron transfer between the electrode and the protein.[44] Natural polymers are extremely favourable for immobilising proteins at the electrode surface because they are both environmentally friendly and biocompatible. For example, pyrolytic graphite electrodes modified with hemoglobin and myoglobin embedded in a hydroxymethylcellulose film show catalytic activity towards the

electro-reduction of H_2O_2 (Table 7.1).[44] Compared to Prussian Blue-modified electrodes, large cathodic overpotentials are required which limits the selectivity of the electrode. Lower detection limits were achieved using hemoglobin (0.80 μM) compared to myoglobin (8.00 μM) under otherwise identical conditions. However, when myoglobin was immobilised onto a hexagonal mesoporous silica-modified glassy carbon electrode an excellent electrocatalytic response was obtained for the electro-reduction of H_2O_2 with a low detection limit (0.062 μM).[45] The increased activity was attributed to the high surface area of the hexagonal mesoporous silica film which allowed myoglobin to intercalate within the pores as well as on the electrode surface.

For the development of amperometric H_2O_2 sensors, the use of mediators immobilised at the electrode surface is attractive because of the simple modification processes involved and the high activity and selectivity obtained. Furthermore, these electrodes show good repeatability and reproducibility. Mediators are also commonly used with enzyme-based electrodes for the detection of H_2O_2 and further examples are given in Section 7.1.3.

7.1.3 Enzymatic Detection of Hydrogen Peroxide using Horseradish Peroxidase

Hydrogen peroxide can be detected enzymatically by employing peroxidase-modified electrodes as bioelectrocatalysts. The most widely studied enzyme is horseradish peroxidase (HRP) which has been shown to catalyse the reduction of H_2O_2 as a result of electron transfer between the electrode and the heme site of the immobilised HRP enzyme.[46,47]

A variety of approaches have been investigated for constructing HRP-based H_2O_2 sensors to provide high enzyme activity and sensitivity. Examples of the methods used are given in Table 7.2 and include: (1) physical adsorption of HRP molecules on the electrode surface (entries 1-3); (2) distribution of HRP within a mixture of conducting and insulating materials to prepare bulk modified composite electrodes (entries 4-6); (3) covalent attachment of HRP to modifying films grafted at the electrode surface (entries 7-8) and (4) coverage of the electrode surface with a conducting polymer, into which HRP molecules are physically or chemically attached (entries 9-11).

Table 7.2. Illustrative examples of the strategies employed to immobilise HRP at an electrode surface for the electro-reduction of H_2O_2.

Entry	Method for immobilising HRP	Conditions for measuring H_2O_2 signal[a]	Limit of Detection	Ref.
1	Physical adsorption at an oxidised gold macroelectrode	Amp., -0.05 V *vs*. Ag/AgCl, pH 6.0	0.10 μM	48
2	Physical adsorption onto a glassy carbon electrode	FI, -0.30 V *vs*. Ag/AgCl, pH 7.0 mediator: hydroquinone	0.01 μM	49
3	Physical adsorption onto a pyrolytic graphite electrode	Amp, -0.10 V *vs*. SCE, pH 7.0	-	50
4	Mixed with active carbon powder, followed by Nafion and coated onto a glassy carbon electrode	Amp, -0.50 V *vs*. SCE, pH 6.8	1.00 mM[f]	51
5	Mixed with graphite-epoxy composite	Amp, -0.025 V *vs*. Ag/AgCl, pH 7.4	50 μM[f]	52
6	Mixed with graphite-silicon grease composite	Amp, -0.025 V *vs*. Ag/AgCl, pH 7.4	10 μM[f]	52
7	Covalent immobilisation at cyclopentadienylnickel(II) -thiolato Schiff base[b]-modified gold electrode	CV, 0.20 V *vs*. Ag/AgCl, pH 7.4 mediator: Schiff base modifying SAM	6.25 mM[f]	53
8	Covalent immobilisation onto a DSTP[c]-modified gold electrode	CV, -0.30 V *vs*. SCE, pH 7.0 mediator: $[Os(phen\text{-}diaone)\text{-}(phen)_2](PF_6)_2$	0.25 mM	54
9	Entrapment in a sol-gel matrix prepared from chitosan and THEOS[d] coated onto a glassy carbon electrode	Amp, -0.20 V, pH 7.0	0.40 μM	55
10	Entrapment in an electropolymerised pyrrole film coated onto a platinum electrode	Amp, 0.15 V *vs*. Ag/AgCl, pH 6.2	0.10 μM	56
11	Entrapment in PEG[e] film coated on pyrolytic graphite	CV, -0.38 V *vs*. SCE, pH 7.2	0.67 μM	57

[a] Amp = amperometry, FI = flow injection amperometry, CV = cyclic voltammetry; [b] $[Ni(SC_6H_4NC(H)C_6H_4OCH_2CH_2SMe(\eta^5\text{-}C_5H_5)]_2$; [c] DTSP = dithiobis *N*-succinimidyl propionate, [d] THEOS = tetrakakis(2-hydroxyethyl)orthosilicates, [e] PEG = polyethylene glycol, [f] Limit of detection not reported, this value reflects the smallest addition in linear range.

Physical adsorption of HRP directly onto the electrode surface is an attractive strategy for constructing HRP-based electrodes for the electrochemical detection of H_2O_2. These electrodes are simple to construct and allow direct electron transfer between the electrode and the active heme site of the enzyme. Direct biocatalysis of H_2O_2 reduction has been observed with HRP adsorbed onto gold,[48] silver[48] and carbon electrode materials.[50,49,52] However, these electrodes suffer from some drawbacks. The surface coverage of HRP varies for different types of electrodes and is dependent on the condition of the electrode surface. In addition, it has been shown that only a small portion of adsorbed HRP molecules are suitably orientated at the electrode surface to be active in the direct electron transfer reaction.[46,51] It is also possible that some enzymes may undergo denaturation upon immobilisation leading to loss of bioactivity.[58] The adsorption and biocatalytic activity of HRP immobilised on bare surfaces can be controlled by oxidative pre-treatment of the electrodes.[46-48] For example, pre-oxidation of gold electrodes has been shown to significantly affect the adsorption/orientation of HRP at the gold surfaces resulting in the maximum surface coverage and a higher percentage of enzyme molecules orientated at the surface to give a higher efficiency for direct electron transfer.[46,48] Carbon based materials are the most common electrodes used for the preparation of surface modified HRP electrodes and the presence of surface oxygen-containing functional groups has also been shown to improve the bioelectrocatalytic activity of these surfaces.[47] The electroreduction of H_2O_2 at HRP-modified bare electrodes in the absence of a mediator occurs at ~ 0 V (*vs*. Ag/AgCl) with high sensitivity allowing the selective detection of H_2O_2 in the presence of common electrochemical interferents (Table 7.2, entries 1-3). The use of solution-based mediators to shuttle electrons between the active site of the protein buried deep within the molecule and the electrode improves the sensitivity of the electrode further and detection limits as low as 10 nM of H_2O_2 have been reported.[49] The electrode potential is usually shifted closer to the formal potential of the mediator in this situation. In comparison, electrodes prepared by distributing HRP within a carbon powder to prepare bulk modified carbon paste electrodes exhibit lower sensitivities for the electroreduction of H_2O_2 (Table 7.2, entries 4-6).[51,52] This may be due to the binder molecules insulating the adsorbed HRP.

Immobilisation of HRP onto electrodes modified with organic films has been studied as an alternative method for constructing HRP-based H_2O_2 sensors. In particular, the formation of thiol-terminating self-assembled monolayers (SAM) on gold electrodes has attracted considerable attention as they are known to form well-ordered assemblies and the terminal thiol groups allow

covalent immobilisation of HRP *via* the amino-groups of the enzyme.[53,54] Two illustrative examples of electrodes developed for the electrochemical detection of H_2O_2 using this method are given in Table 7.2 (entries 7-8). A mediator is employed to increase the rate of electron transfer between the active site of the HRP enzyme and the electrode. For entry 7 of Table 7.2, the cyclopentadienylnickel(II)thiolato Schiff base compound was used as an active redox center for the SAM layer and the nickel (II) centers provided effective electrochemical communication between the HRP enzymes and the electrode surface.[53] Compared to the bioelectrocatalytic activity of HRP directly adsorbed at the electrode surface, when HRP is covalently attached to the electrode surface *via* a modifying layer the detection limits are relatively high. This is possible due to loss of enzymatic activity upon cross-linking.[59] Preparation of HRP-based electrodes by covalently attaching the enzyme to a modifying layer at the solid electrode surface is attractive because the surface coverage of HRP can be controlled to a greater extent. However, relatively high detection limits are a major disadvantage for the development of electrochemical H_2O_2 sensors.

Sensitive determination of H_2O_2 can be realised by immobilising HRP at the electrode surface within a conducting polymer film (Table 7.2, entries 9-11).[55-57] Considering the examples given in Table 7.2, the electroreduction of H_2O_2 at HRP-based electrodes fabricated by immobilising the enzyme within a polymer film occurs at similar potentials to those observed at the electrodes prepared by covalently attaching the enzyme at a thiol-modified gold electrode (compare entries 7-8 with 9-11). However, the resulting detection limits are more than three orders of magnitude lower when HRP is entrapped within a polymer film. The increase in sensitivity is attributed to the polymer film providing a special microenvironment that can facilitate the direct electron transfer between the incorporated enzyme and the electrode.[57] Polymer films containing chitosan and polyethyleneglycol are especially attractive because they are biocompatible and therefore, the biological activity of the enzyme directly adsorbed at the electrode surface is retained.[55,57] Alternatively, Razola *et al.* found that coating a platinum electrode with a polypyrrole layer before immobilising HRP led to better adhesion of the biocatalyst film and avoided the enzyme folding onto the platinum electrode.[56] In addition to greater sensitivity, electrodes fabricated by immobilising HRP into a polymer film offer many attractive features for the development of a H_2O_2 sensor as the polymer films increase electrode stability and can be chosen to enhance the selectivity of the electrode by blocking electroactive interferents. Furthermore, the growth process and film thickness is easily controlled and can be performed at a variety of electrode surfaces.

Although HRP-modified electrodes prepared by the methods described above generally exhibit good sensitivity and selectivity towards the electroreduction of H_2O_2, several challenges concerning the retention of enzyme activity, stability and the lifetime of the immobilised enzymes still remain.

7.1.4 Incorporation of Metal Nanoparticles into Electrodes for Detecting Hydrogen Peroxide

The use of metal nanoparticles is attracting significant attention in the development of electrodes for the electrochemical detection of H_2O_2. Nanoparticle-based electrodes may overcome some of the drawbacks encountered with the use of unmodified and modified electrodes containing immobilised mediators or enzymes as described in Sections 7.1.1 to 7.1.3. The majority of this research has been directed towards fabricating composite electrodes by immobilising HRP or peroxidase-like proteins such as hemoglobin onto the nanoparticle surface (Table 7.3).[60-63] The modified metal nanoparticles are then typically assembled onto solid electrode supports by entrapment within a polymer film[60,62] or immobilisation at modifying films containing amine or thiol-terminating groups *via* electrostatic or covalent interactions.[61,63] Gold nanoparticles are commonly used because they are stable and exhibit good biocompatibility with proteins. Illustrative examples of the techniques used to incorporate gold nanoparticles into HRP-based and hemoglobin mediated electrodes for the detection of H_2O_2 are given in Table 7.3. These electrodes offer several advantages compared to those fabricated by immobilising the proteins directly at the electrode surface (see Sections 7.1.2 and 7.1.3). Attachment of HRP and hemoglobin to the nanoparticle surface gives the proteins more spatial freedom in their orientation due to the large surface area-to-volume ratio of the nanoparticles and allows the proteins to unfold and retain their biological activity, improving the stability of the HRP and hemoglobin sensing components.[61,63] In addition, the gold nanoparticles also enhance the analytical sensitivity of the electrode by facilitating electron transfer between the heme site of the immobilised proteins and the electrode surface.[61,62]

Table 7.3. Illustrative examples of methods used to incorporate metal nanoparticles into electrodes for the electro-reduction of H_2O_2.

Metal	Methodology	Conditions for measuring H_2O_2 signal[a]	Limit of Detection (μM)	Ref.
A. Sensing component: enzyme or mediator				
Gold	HRP immobilised onto collidal gold nanoparticles and incorporated into an electropolymerised m-phenylenediamine film coated onto a ferrocene-containing carbon paste electrode	Amp, 0.02 V *vs*. Ag/AgCl, pH 7.0 mediator: ferrocene	0.14	60
Gold	HRP immobilised at colloidal gold nanoparticles assembled onto a chitosan film coating a glassy carbon electrode	Amp, -0.15 V *vs*. SCE, pH 6.98 mediator: hydroquinone	6.10	62
Gold	Hemoglobin immobilised onto colloidal gold nanoparticles attached to glassy carbon through a sulfhydryl-teminated monolayer[b]	Amp, -0.15 V *vs*. Ag/AgCl, pH 6.8	0.91	61
Gold	Hemoglobin immobilised onto colliodial gold nanoparticles assembled at a cysteamine-modified gold electrode	Amp, -0.20 V *vs*. SCE, pH 7.0	0.13	63
B. Sensing component: metal nanoparticle				
Silver	Electrodeposited onto a glassy carbon electrode	CV, -0.68 V *vs*. SCE, pH 7.4	2.00	64
Silver	Electrodeposition of silver nanoparticles functionalised with DNA onto a glassy carbon electrode	CV, -0.45 V *vs.* SCE, pH 7.0	0.60	65
Gold	Colloidal gold nanoparticles functionalised with butanethiol and assembled onto a polystyrene substrate	CV, -0.36 V *vs.* Ag/AgCl, pH 6.9	[c]	66
Palladium	Dispersed within carbon paste	LSV, -0.30 *vs*. SCE, pH 7.4	1.47	67
Platinum	Mixed with graphite powder and mineral oil	Amp, 0.10 V *vs*. Ag/AgCl, pH 7.4	5.00	68

[a] Amp = amperometry, CV = cyclic voltammetry, LSV = linear sweep voltammetry; [b] 4-aminothiolphenol was covalently attached to a 4-aminobenzoic acid-modified glassy carbon surface; [c] Not reported.

The use of metal nanoparticles as the sensing component for the electrochemical detection of H_2O_2 has received little attention in comparison. However, the operation of metal nanoparticle electrodes at low overpotentials for the electro-oxidation and/or reduction of H_2O_2 is an attractive goal as interference should not be problematic and there would be no need for interferent-eliminating enzyme layers, permselective barriers or artificial electron mediators. The most common methods used to prepare metal nanoparticle electrodes for the direct determination of H_2O_2 have involved electrochemical deposition, assembly of functionalised colloidal metal particles onto a solid substrate or dispersion of pre-formed particles within a carbon paste mixture (Table 7.3). Metal nanoparticles exhibit efficient and preferential catalytic activity towards H_2O_2 and detection has been made *via* H_2O_2 oxidation or reduction at reduced overpotentials. [51,64-66,68,69] For example, silver nanoparticles electrodeposited onto a glassy carbon electrode enabled the detection of H_2O_2 by reduction at -0.68 V (*vs*. SCE) as no response was observed at the glassy carbon substrate.[64] Furthermore, a ~ 5-fold increase in sensitivity (based on geometric area) was also observed compared to the response obtained at a solid silver electrode.[64] It was noted by the authors that the increase in sensitivity could actually be several orders of magnitude larger, however, the true geometric area of the silver nanoparticle assembly was unknown. Functionalisation of electrodeposited silver nanoparticles with DNA was observed to enhance the catalytic activity of the metal nanoparticles further.[65] Aggregation of silver particles is avoided in the presence of the DNA-capping group giving a more uniform nanoparticle size and distribution. This causes the H_2O_2 overpotential to decrease further (-0.45 V *vs*. SCE) and leads to an increase in sensitivity (compared with an aggregated electrode) as the nanoparticles act as an array of small silver nano-electrodes which are diffusionally independent.[65] Metal-dispersed carbon paste electrodes containing platinum, palladium or rhodium particles can be operated at even lower potentials to detect H_2O_2 *via* its oxidation (0.10 to -0.10 V *vs*. Ag/AgCl).[68,69] Platinum-dispersed carbon paste electrodes exhibit the most efficient electrocatalytic activity as the H_2O_2 oxidation potential is decreased by 0.50 V compared to that required at a solid platinum electrode (> 0.60 V *vs*. Ag/AgCl).[68] These electrodes are very stable due to strong adherence of the metal particles to graphite and homogeneous distribution, together with the efficient catalytic activity of the metallised sites eliminating the need for redox mediators and hence, possible stability problems due to leaching of the mediator.[68,69] Co-immobilisation of glucose oxidase and platinum or rhodium particles within the carbon paste has been investigated for the development of biosensors to monitor glucose. These electrodes showed great promise for the proposed application as they exhibited excellent sensitivity and selectivity for

the determination of H_2O_2 liberated by the enyzmatic reaction with glucose in the presence of common interferents such as ascorbic acid and uric acid.[68,69]

7.1.5 Research Directions for Chapter 7

The work presented in this chapter examines the activity of gold and palladium nanoparticle assemblies for the electro-oxidation and reduction of H_2O_2 in the absence of mediators and additional reagents. For comparison, the electrochemical detection of H_2O_2 at solid gold and palladium electrodes was also investigated. Gold nanoparticles were selected because they are very stable and exhibit good biocompatibility. Palladium nanoparticles were included in this study because they are available on site (Nano Cluster Devices Limited) with a diverse range of (nominal) particle sizes and surface coverages. Palladium has similar properties to platinum, which is the most commonly used metal for the electrochemical detection of H_2O_2, and palladium nanoparticles have been previously investigated for H_2O_2 detection.[10,31,32,67] Therefore, it was of interest to examine the activity of locally-produced palladium nanoparticles. Gold and palladium nanoparticles were directly immobilised onto carbon supports using electrodeposition and vapour deposition techniques respectively. In addition, citrate-capped gold nanoparticles were electrostatically assembled onto amine tether layers attached to carbon surfaces (as described in Chapter 6). By pre-synthesising the gold colloids and exploiting the electrostatic interaction between the citrate-capping groups on the gold nanoparticles and the amine tether layer, it was envisaged that the architecture of the nanoparticle assemblies could be easily controlled and optimised for the detection of H_2O_2. The electrochemical detection of H_2O_2 was studied in phosphate buffer at pH 7.4 to simulate the physiological conditions of possible analytical applications.

7.2 Experimental Methods

7.2.1 Electrochemistry

Unless otherwise stated, aqueous electrochemical experiments were carried out in phosphate buffer (PB, 0.04 M, pH 7.4) with added 0.1 M $NaClO_4$. Non-aqueous electrochemical experiments were performed in acetonitrile containing 0.1 M $[Bu_4N]BF_4$.

7.2.1.1 Cyclic Voltammetry

Cyclic voltammetry experiments were performed using computer-controlled EG & G PAR Model 362 and Model 273A Potentiostats. The experimental details concerning electrochemical measurements are described in Chapter 2, Section 2.4. For most experiments, a standard three electrode cell was used containing a platinum wire auxiliary electrode and a SCE reference electrode. For the experiments performed at a gold plug electrode (see Section 7.2.2), a large area gold wire auxiliary electrode was employed. All voltammetric data were obtained using scan rates of 50 or 100 mV s^{-1}.

7.2.1.2 Hydrodynamic Voltammetry

Hydrodynamic voltammetry was performed at a stationary working electrode in a stirred solution. A glassy carbon rotating disc electrode (RDE, EG & G PAR Model 616) was used to stir the solution. Measurements were obtained using an EG & G PAR Model 362 Potentiostat coupled to a Powerlab 4SP (ADInstruments). The electrochemical cell set-up is described in Chapter 2, Section 2.4.3.3. For these experiments, the working electrode consisted of solid palladium or palladium nanoparticles immobilised on PPF (see Sections 7.2.2 and 7.2.4). A platinum wire was used as the auxiliary electrode and a Ag/AgCl electrode was employed as the reference electrode. The latter electrode was constructed by placing a silver wire, coated with a layer of AgCl, into a glass tube with a Vycor tip containing a saturated aqueous solution of KCl. It is noted that all potentials are reported with reference to SCE. The solution was stirred at 3000 rpm using a glassy carbon RDE that was placed low in the cell and centered above the working electrode.

7.2.2 Preparation of Solid Gold and Palladium Electrodes

Solid gold and palladium circular disk working electrodes were assembled using short plugs of metal (gold: 0.60 cm diameter, 0.40 cm in length; palladium: 0.45 cm diameter, 0.90 cm in length) connected to gold and copper wire on the backside respectively. These electrodes were suspended in the electrochemical cell by the hanging meniscus method (see Chapter 2, Section 2.4.3.1) allowing the front of the electrode surface to contact the solution without requiring the sides to be insulated. The geometric surface area for the gold and palladium electrodes was 0.28

and 0.16 cm^2 respectively. A second gold disk electrode was constructed by sealing gold wire into Teflon and contact to the metal was made *via* a brass rod (geometric surface area 0.008 cm^2). For hydrodynamic voltammetry at a solid palladium electrode, a planar electrode was constructed from palladium sheet (1 cm × 1 cm). The geometric area of the palladium sheet electrode exposed to the solution in the electrochemical cell set-up was 0.31 cm^2 (see Chapter 2, Sections 2.4.3.2 to 2.4.3.3).

7.2.2.1 Electrode Cleaning Procedures

Newly prepared electrodes were polished to achieve a mirror finish using graded sanding papers followed by 3 μm diamond paste followed by alumina slurries (1.0 and 0.05 μm) on polishing microcloth (LECO Lecloth). The electrodes were then sonicated in Milli-Q water to remove excess alumina from the surface. Between experiments, the gold disk electrode sealed in Teflon and the palladium electrodes were polished with 1.0 and 0.05 μm alumina and either rinsed or sonicated in Milli-Q water. The gold plug electrode was flame-annealed in between experiments using a hydrogen flame and cooled to room temperature. Mechanical polishing of this electrode was carried out periodically. The metal disk and palladium sheet electrodes were subjected to potential cycling in order to reconstruct the surface to achieve the same surface starting-state at the beginning of each experiment. Unless otherwise stated, the gold electrodes were cycled between -0.20 and 1.45 V in 0.01 M $HClO_4$ and the palladium electrodes were cycled between 0.15 and 1.35 V in 1 M H_2SO_4. Potential cycling was carried out using a scan rate of 50 mV s^{-1} until no changes were observed in successive voltammograms. Cycling was stopped at -0.20 V for the gold electrode and 0.15 V for the palladium electrodes to give an oxide free surface.

7.2.3 Fabrication of Gold Nanoparticle Electrodes

7.2.3.1 Preparation of Gold Colloid Solutions

Citrate-capped gold nanoparticles were prepared according to the methods of Natan and coworkers.[70,71] All glassware used in the preparation of gold nanoparticles was thoroughly cleaned in aqua regia (3 parts HCl, 1 part HNO_3), rinsed in Milli-Q water and oven-dried at 45 °C prior to use. Stock solutions of $HAuCl_4$ (1 % or 1 mM) and tri-sodium citrate (38.8 mM) were prepared from Milli-Q water that had been filtered through a 0.22 μm GV membrane filter (Durapore®, Millipore)

and $NaBH_4$ solution (0.075 %) was prepared using the filtered tri-sodium citrate stock solution (38.8 mM). Two typical gold colloid preparations are described below. The as-prepared solutions of colloidal particles were characterised by an absorption maximum determined from UV-Vis spectra (range 300-800 nm) and transmission electron microscopy (TEM). Samples for TEM were prepared by depositing one drop of the nanoparticle solution onto standard Formvar-coated copper grids. Excess solution was removed after 30 seconds by touching filter paper to the side of the grid. Average particle sizes were determined from the TEM image using CorelDRAW 11 software. The vertical axis of the particles was measured using the dimension tool.

Preparation I

In a round-bottom flask (1 L) equipped with a condenser, $HAuCl_4$ (1 mM, 500 mL) was brought to a rolling boil with vigorous stirring. Tri-sodium citrate (38.8 mM, 50 mL) was added rapidly to the vortex of the solution and a colour change from yellow to burgundy was observed. Boiling was continued for 1 hour, after which time the heating mantle was removed and stirring was continued for a further 30 minutes. After the solution had reached room temperature, it was stored in a dark bottle. The resulting solution of gold colloidal particles was characterised by an absorption maximum at 516 nm (Figure 7.1 (a)). TEM showed a range of particle diameters from 8.5-17.0 nm, with an average particle diameter of 12 nm (Figure 7.1 (b)).

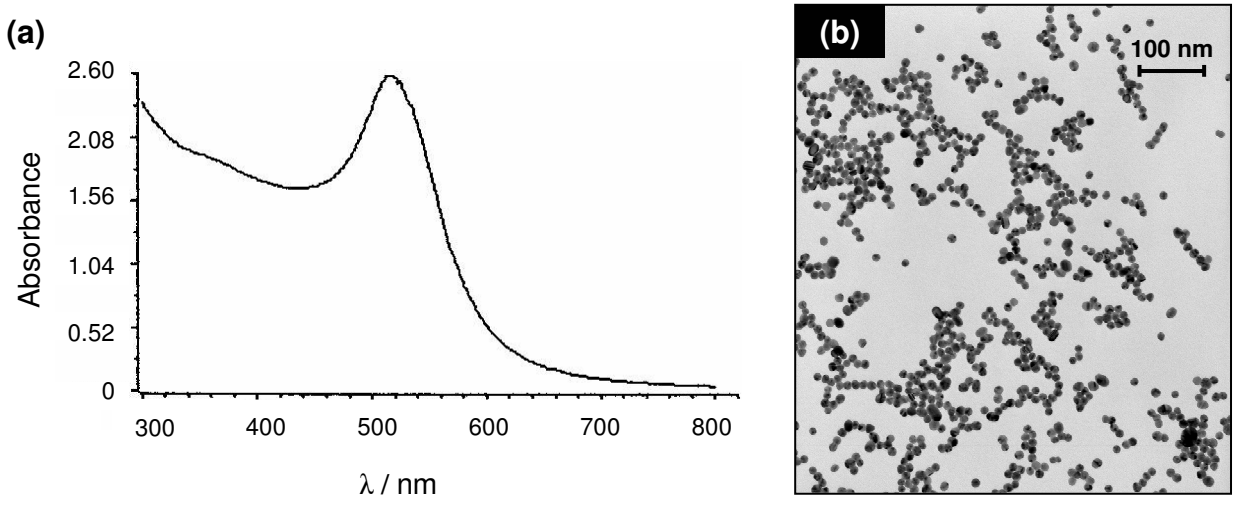

Figure 7.1. A representative UV-Vis spectrum (a) and TEM image (b) for a gold colloid solution prepared using the method described in Preparation I. Average particle diameter is 12 nm.

Preparation II

$HAuCl_4$ (1 %, 1 mL) was added to Milli-Q water (90 mL) at room temperature with constant stirring. Tri-sodium citrate (38.8 mM, 2 mL) was added after 1 minute followed by freshly prepared $NaBH_4$ (0.075 %, 1 mL) after a further 1 minute. The solution was stirred for an additional 5 minutes and then stored in a dark bottle at 4 °C. Four gold colloid solutions were made using this method. UV-Vis spectra recorded for these solutions exhibited a peak maximum at 514-516 nm (Figure 7.2 (a)). TEM showed a range of particle diameters from 1.0 to 7.0 nm, with the average particle size ranging from 2.8 to 3.6 nm between solutions (Figure 7.2 (b)).

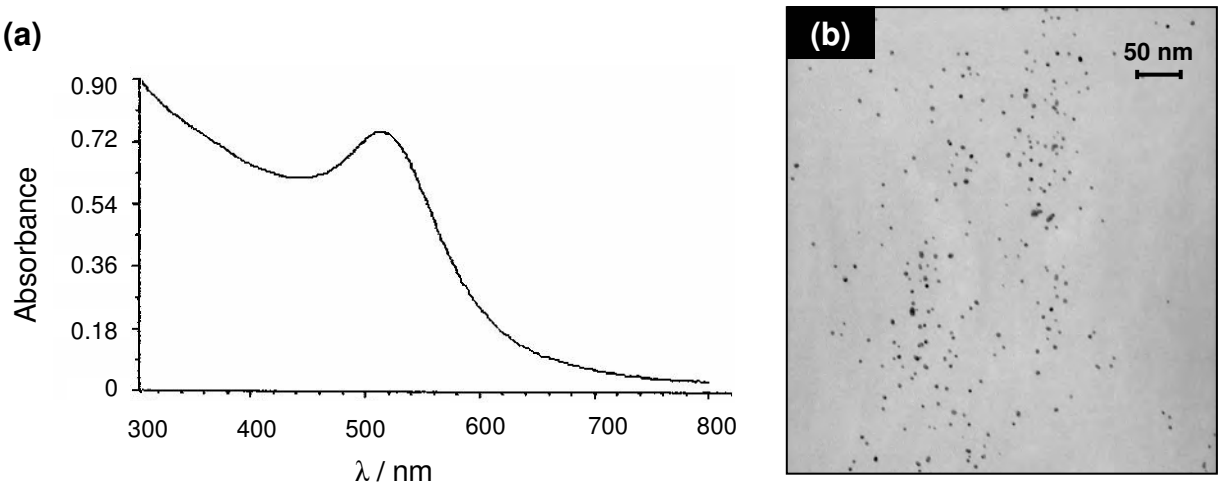

Figure 7.2. A representative UV-Vis spectrum (a) and TEM image (b) for a gold colloid solution prepared using the method described in Preparation II. Average particle diameter is 3.6 nm.

7.2.3.2 Modification of Glassy Carbon and Assembly of Gold Nanoparticles

Electrochemical grafting of amine films to glassy carbon electrodes was carried out in 0.1 M $[Bu_4N]BF_4$-acetronitrile solution containing ethylenediamine (ED, approximately 1 or 5 mM) or hexamethylenediamine (HD, approximately 5 mM). Before modification, glassy carbon electrodes were polished with alumina slurries (1.0 and 0.05 μm) and rinsed with Milli-Q water. In addition, the glassy carbon plate electrodes employed to prepare gold nanoparticle assemblies for characterisation using SEM were sonicated in Milli-Q water for 10 minutes to remove the polishing

debris. The standard modification procedure involved cycling from 0 to 1.20 V for a set number of cycles at 100 mV s^{-1} as specified in the Results and Discussion Section. After modification, the surfaces were rinsed with acetonitrile followed by Milli-Q water and dried with nitrogen prior to further use or storage under vacuum.

For assembly of gold nanoparticles, the nanoparticle solutions were used as-prepared. Amine-modified glassy carbon samples were immersed in the solution for a selected time at room temperature in the dark. All experiments were carried out using freshly grafted surfaces. After treatment, the samples were rinsed with Milli-Q water, dried with a gentle stream of nitrogen and used immediately or stored under vacuum.

7.2.3.3 Electrodeposition of Gold Nanoparticles onto Glassy Carbon Electrodes

Gold nanoparticles were electrodeposited onto glassy carbon electrodes using a computer-interfaced PAR Model 273A Potentiostat/Galvanostat. A solution of $KAuCl_4$ (0.01 M, 10 mL) in 0.5 M H_2SO_4 was reduced by stepping the potential from 1.10 to 0 V over 5 seconds. Prior to metal deposition, the glassy carbon electrodes were polished with alumina slurries (1.0 and 0.05 μm) on polishing microcloth (LECO Lecloth). In addition, the glassy carbon plate electrodes employed to allow characterisation of electrochemically deposited gold nanoparticles using SEM were sonicated in Milli-Q water for 10 minutes to remove the polishing debris.

7.2.4 Vapour Deposition of Palladium Nanoparticles onto Pyrolysed Photoresist Film

Deposition of nano-sized palladium clusters onto PPF substrates was performed by Andreas Lassesson of Nano Cluster Devices Limited using a ultra high vacuum (UHV)-compatible atomic cluster deposition system.[72] The design of the cluster deposition system consists of a cluster source and a series of differentially pumped chambers that allow ionisation, size selection, acceleration and focusing of clusters before they are finally deposited on a substrate. A magnetron sputtering source is used to produce ionised palladium clusters which can be readily mass selected. In brief, palladium atoms are sputtered in an argon gas discharge using a high pressure magnetron cathode. The argon gas atoms bombard the palladium substrate sputtering away palladium atoms which are subsequently de-accelerated by collisions with the argon gas in the liquid nitrogen cooled aggregation tube

causing the palladium atoms to aggregate and form clusters. The clusters are then carried through a nozzle by the argon gas stream (flow rate = 100 standard cubic centimeters per minute (sccm)) and directed as a molecular beam from the source through a mass filter and into the deposition chamber where the clusters are deposited onto the PPF substrate. The mass filter[73] is used to characterise the size distribution of the clusters and select the mass of clusters to be deposited. The aperture of the nozzle is variable and allows for adjustment of the pressure in the aggregation tube which influences cluster growth and formation. For this work, palladium clusters ranging in size from 2.4 to 7.8 nm were deposited onto PPF substrates to give nominal fractional surface coverages ranging from 0.20 to 2.00, as estimated from the total mass of metal deposited (measured using a quartz crystal film thickness monitor) and the cluster size. It is noted that the term 'cluster' usually refers to an entity smaller than a 'nanoparticle'. However, there is no agreed size range differentiating clusters from nanoparticles and after considering the size ranges of gold and palladium nanomaterials used in this work, all will be referred to as nanoparticles for simplicity.

7.3 Results and Discussion

In initial experiments, the electrochemical detection of H_2O_2 at solid gold, palladium and glassy carbon electrodes was examined using cyclic voltammetry. No response was observed at the glassy carbon electrode, however, the electro-oxidation and reduction of H_2O_2 was observed at gold and palladium electrodes. In addition to the solid electrodes, gold and palladium nanoparticle assemblies were investigated as alternative electrodes for H_2O_2 detection. The activity of each electrode towards H_2O_2 was evaluated by measuring the peak potentials and peak current densities. A low overpotential and high peak current density is advantageous for chemical and biosensing applications to reduce the effect of common electroactive interferents in real samples such as ascorbic acid, uric acid and oxygen.

7.3.1 Electrochemical Detection of Hydrogen Peroxide at Solid Gold Electrodes

7.3.1.1 Characterisation of a Polycrystalline Solid Gold Electrode

The physical state of the surface of a gold electrode at the metal/solution interface can be examined using cyclic voltammetry. Comprehensive studies carried out by Hamelin *et al.* regarding the cyclic voltammetric behaviour of gold single-crystal surfaces have shown that the properties of solid gold electrodes depends on the index plane presented to solution.[74-76] Voltammograms recorded over a range of potentials including those where it is possible to observe the electrochemical double layer region, the formation of a monolayer of oxide and its subsequent reduction, and the beginning of the reduction of protons provide a 'fingerprint' of the gold surface. The voltammograms of various crystallographic orientations of gold can differ significantly in these potential regions.[74-76] The electrochemistry of gold oxide formation and reduction and hence, the shape of the cyclic voltammogram is also influenced by the solution pH, concentration, and identity of the electrolyte anions, anodic polarisation time and temperature.[75,77] In this work, characterisation of the gold electrode was performed using 0.01 M $HClO_4$ to avoid significant pH changes at the electrode surface during gold oxide formation. Futhermore, perchlorate anions adsorb onto the gold surface to a lesser extent than other electrolyte species such as sulfate anions.[75]

The cyclic voltammogram recorded in 0.01 M $HClO_4$ at the polycrystalline solid gold electrode (assembled using a short gold plug, see Section 7.2.2) after reconstruction is shown in Figure 7.3. Polycrystalline gold surfaces are considered to be a mix of single crystal planes and defects at the surface.[78] Each region exhibits different electrochemical properties and hence, the behaviour observed at a polycrystalline electrode represents the combination of low and high index faces at the surface. The current observed in region (A) of Figure 7.3 is associated with charging of the double layer capacitance and the oxidation and reduction peaks observed in regions (B) and (C) correspond to the formation and reduction of gold surface oxide respectively.

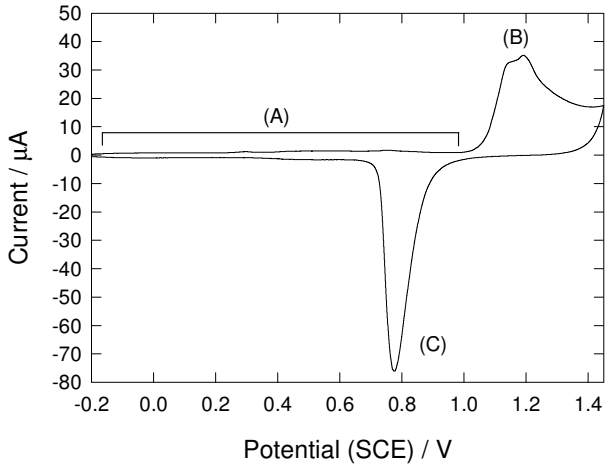

Figure 7.3. Cyclic voltammogram of a polycrystalline gold plug electrode in 0.01 M $HClO_4$ at 50 mV s^{-1} following reconstruction by potential cycling between -0.20 and 1.45 V for 3 hours.

The chemical nature of the gold oxide species formed at a gold surface during anodic polarisation is not yet clear and two pathways have been proposed for the electro-oxidation of gold. In the first pathway, oxide formation is considered to proceed in two steps to yield the gold (II) surface oxide species, AuO (equations 7.4 and 7.5).[74,79] The overall reaction representing the formation of AuO by this mechanism is given in equation 7.6 where subscript 's' represents the groups of atoms forming part of the surface. The subsequent electrochemical reduction of the oxide layer occurs *via* the reverse of equations 7.5 and 7.4.

$$Au_s + 2H_2O \rightleftharpoons AuOH_s + H^+ + e^- \quad (7.4)$$

$$AuOH_s \rightleftharpoons AuO_s + H^+ + e^- \quad (7.5)$$

$$Au_s + 2H_2O \rightleftharpoons AuO_s + 2H^+ + 2e^- \quad (7.6)$$

In other reports, the gold electrode is considered to be covered with a surface gold (III) oxide species.[75,76,80-82] A recent study has shown that the charge required to reduce a surface layer of gold oxide formed anodically in 0.5 M $NaHSO_4$ solution is directly proportional to the amount of Au(III) determined photometrically after the dissolution of the oxide layer.[82] The proposed mechanism for

the second pathway for gold oxidation involves one adsorbed and two nearby water molecules to yield gold (III) hydroxide as shown in equation 7.7,[75,76,81] and the subsequent electrochemical reduction of this species is given in equation 7.8. However, it seems unlikely that the hydroxide form of the gold oxide would be present in acidic media. For the current research, the chemical nature of the gold oxide species is not important and will simply be referred to as 'gold oxide'.

$$Au{\cdot}H_2O_s + 2H_2O \rightleftharpoons Au(OH)_{3,s} + 3H^+ + 3e^- \quad (7.7)$$

$$Au(OH)_{3,s} + 3e^- \longrightarrow Au_s + 3OH^- \quad (7.8)$$

Further characterisation of the polycrystalline gold electrode surface was carried out using lead underpotential deposition. Studies have shown that a monolayer of lead atoms will adsorb onto gold surfaces at potentials more positive than that required for bulk deposition.[83-90] Cyclic voltammograms for the adsorption and desorption of a monolayer of lead underpotentially deposited onto gold electrodes have been studied extensively and the shape of the voltammogram is sensitive to the crystallographic orientation of the gold surface.[83,84,86,87] For the current study, lead was underpotentially deposited onto the polycrystalline gold plug electrode by stepping the potential from 0.20 to -0.40 V for 5 seconds in a solution prepared by dissolving 1 mM PbO in 0.01 M $HClO_4$. The voltammogram corresponding to the stripping of the underpotentially deposited monolayer of lead from the gold surface is shown in Figure 7.4. Comparison with voltammograms reported for the stripping of underpotentially deposited lead recorded at a Au(111) single crystal electrode indicates that the polycrystalline gold electrode contains a large component of Au(111) domains.[83,86,87] The sharp peak observed at -0.24 V is indicative of the stripping of lead from the Au(111) crystal plane and the presence of the shoulder peak observed at -0.22 V is representative of lead stripping from Au(111) terraces.[83,86,87] The other main peak at -0.02 V corresponds to stripping from the Au(110)/Au(100) crystal planes and the small peak at -0.31 V is indicative of steps and Au(110) terraces.[83,86] Similar voltammograms have been reported in the literature by other workers for the oxidative desorption of lead underpotentially deposited onto polycrystalline gold electrodes.[84,90,91]

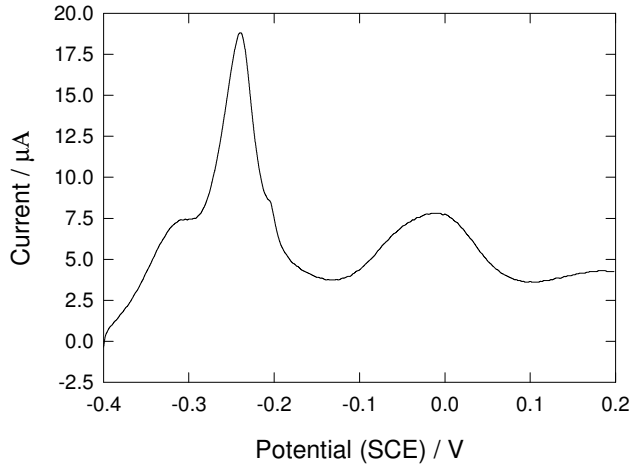

Figure 7.4. Stripping voltammogram recorded in a solution prepared by dissolving 1 mM PbO in 0.01 M $HClO_4$ for the oxidative desorption of a layer of lead underpotentially deposited onto a polycrystalline gold plug electrode (υ = 50 mV s^{-1}). Lead was underpotentially deposited onto the electrode surface from the solution of 1 mM PbO dissolved in 0.01 M $HClO_4$ by stepping the potential from 0.20 to -0.40 V for 5 seconds. The stripping voltammogram was initiated at -0.40 V.

7.3.1.2 Determination of the Electrochemically Active Surface Area for the Solid Gold Electrode

In this research, the activity of the electrodes examined for the electrochemical detection of H_2O_2 is expressed as a peak current density by normalising the peak currents to the surface area of the electrode according to equation 7.9,

$$j_p = \frac{i_p}{A} \qquad (7.9)$$

where j_p is the peak current density, i_p is the peak current and A is the surface area of the electrode.

The area of an electrode can be defined by two different measurements as depicted in Figure 7.5. The 'real' or microscopic surface area refers to the electrochemically active surface area under working conditions and takes into account the surface roughness of the electrode down to the atomic level.[92] In practice, the geometric area is much easier to evaluate as it is calculated on the

basis of known geometric dimensions of the electrode. The geometric area is defined as the cross-sectional area of the enclosure formed by projecting the boundary of the electrode outward in a plane parallel to the macroscopic boundary of the electrode surface.[78,92] For smooth surfaces with low roughness factors, the 'real' surface area is close to the geometric area and at these electrodes the peak current can be normalised with respect to the geometric surface area.[93] However, when the condition of a smooth surface with a low roughness factor is not satisfied, current density expressed with respect to geometric area is not an ideal measure of activity, especially when comparing two electrodes. In this situation, a higher peak current may simply be due to a larger surface area and not a genuine representation of greater activity.[93] Hence, peak current densities should be expressed with respect to the 'real' (active) surface area in order to evaluate the activities of different electrodes.

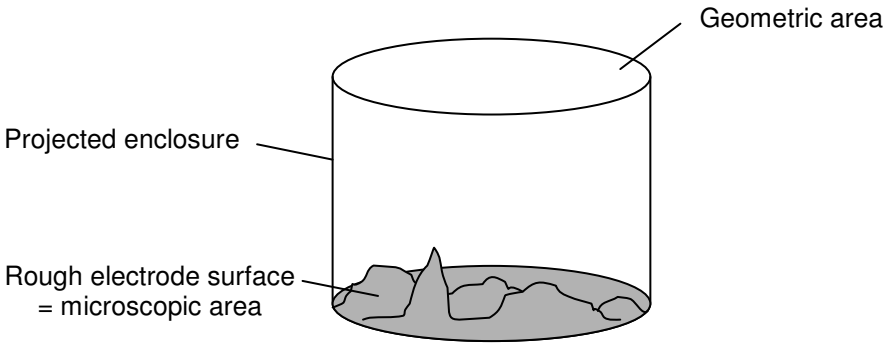

Figure 7.5. Illustration of the two different measures of surface area for a given electrode: (1) the 'real' or microscopic area takes into consideration the surface roughness and (2) the cross-section of the enclosure formed by projecting the boundary outward in a plane parallel to the macroscopic boundary represents the geometric area of the electrode. Figure adapted from reference 92.

For the polycrystalline gold electrode assembled using a short plug of metal, characterisation by the stripping of a layer of underpotentially deposited lead from the surface revealed that the surface is not simply a smooth plane but contains steps and terraces (refer to Section 7.3.1.1). A common method used to estimate the electrochemically active surface area of gold electrodes involves measuring the charge required to strip a monolayer of gold oxide from the surface.[78,92] For this research, the formation of a monolayer of gold oxide at the polycrystalline gold plug surface was investigated in 0.01 M $HClO_4$ solution as a function of potential. Potentials ranging from 0.90

to 1.70 V (E_{app}) were applied to the surface for 90 seconds, after which time the surface oxide species was subsequently reduced by scanning from E_{app} to 0 V at 50 mV s^{-1}. The charge passed during reduction of the surface oxide formed at each potential was determined from the area of the gold oxide reduction peak using equation 7.10,

$$Q = \frac{(i \times E)}{\upsilon} \qquad (7.10)$$

where Q is the charge passed during reduction of the surface oxide, the term ($i \times E$) represents the area of the gold oxide reduction peak as determined by curve-fitting the data (see Chapter 2, Section 2.7)) and υ is the scan rate (50 mV s^{-1}). The potential applied to the polycrystalline gold plug electrode to form a layer of surface oxide was plotted against the charge passed during the subsequent reduction of the gold oxide species as shown in Figure 7.6. It might be expected that as the applied potential is increased above 0.90 V the charge for gold oxide reduction increases to a maximum after which there is no further change. This maximum charge would correspond to the formation of a complete monolayer of gold oxide. However, this behaviour is not observed for the plot shown in Figure 7.6. A well defined plateau region is not observed and the charge associated with the reduction of gold oxide continues to increase as the applied potential is increased. This is most likely due to the dissolution of gold increasing the surface roughness and hence, the greater surface areas give rise to increased currents for the formation and subsequent reduction of gold oxide, coupled with gold dissolution, at higher potentials. The inflection point at approximately 1.45 V is taken as the best estimate of the potential at which a complete monolayer of gold oxide is formed. Additional investigations of the time required to form a complete monolayer of gold oxide at the electrode surface confirmed that a deposition time of 90 seconds was sufficient. It is noted that the shape of the curve shown in Figure 7.6 is consistent with that reported by Piela and Wrona who evaluated the effect of potential on the charge associated with the formation of a gold oxide layer at a polycrystalline gold electrode in 0.5 M H_2SO_4.[79] These workers selected 1.40 V (*vs.* SCE) as the potential representing the formation of a complete monolayer of gold oxide.

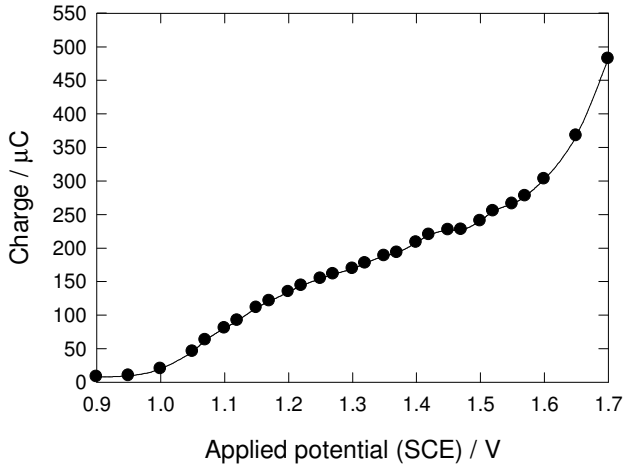

Figure 7.6. Plot of applied potential for gold oxide formation *versus* charge passed during the subsequent reduction of the gold surface oxide species at a polycrystalline gold plug electrode. The electrode was held at each potential (E_{app}) for 90 seconds in 0.01 M $HClO_4$ before the surface oxide species was subsequently reduced off the surface by scanning from E_{app} to 0 V at 50 mV s^{-1}.

The 'real' or electrochemically active surface area of the gold electrode is determined using equation 7.11,

$$A = \frac{Q}{Q_c} \qquad (7.11)$$

where A represents the electrochemically active surface area of the gold electrode under working conditions, Q is the experimentally determined charge associated with the reduction of a monolayer of gold oxide formed at 1.45 V and Q_c is the value generally accepted in the literature for the charge required to reduce a monolayer of gold oxide at a polycrystalline surface. Using the values of Q = 227 μC and Q_c = 400 μC cm^{-2}, the electrochemically active surface area of the polycrystalline gold electrode is calculated to be 0.568 cm^2. It is noted that the Q_c value of 400 μC cm^{-2} was chosen as an average value from several different values obtained from the literature.[74,77,80] From the ratio of the electrochemically active surface area to the geometric area, the roughness factor of the polycrystalline gold electrode employed in this study corresponds to 2.029. This is typical of roughness factors reported by other workers for polycrystalline gold electrodes.[54,79,92]

Further experiments were carried out using lead underpotential deposition to determine the electrochemically active surface area of the polycrystalline gold electrode in an attempt to confirm that derived from the reduction of a monolayer of gold surface oxide. In initial experiments, the formation of a monolayer of lead adsorbed at the gold surface was checked experimentally. Figure 7.7 (a) shows the stripping voltammograms for lead underpotentially deposited onto the polycrystalline gold plug electrode at various potentials between 0.05 and -0.45 V for 5 seconds in a solution prepared by dissolving 1 mM PbO in 0.01 M $HClO_4$. The current for the stripping voltammograms was integrated (the current under the full oxidation manifold was included) and the charge was plotted as a function of the underpotential deposition potential (Figure 7.7 (b)). The maximum value for a monolayer of lead deposited on the gold surface was obtained at -0.45 V. A lower potential limit of between -0.40 and -0.45 V has been reported by other workers for the underpotential deposition of a monolayer of lead at gold electrodes as the application of more negative potentials leads to bulk deposition.[83,86,87,91]

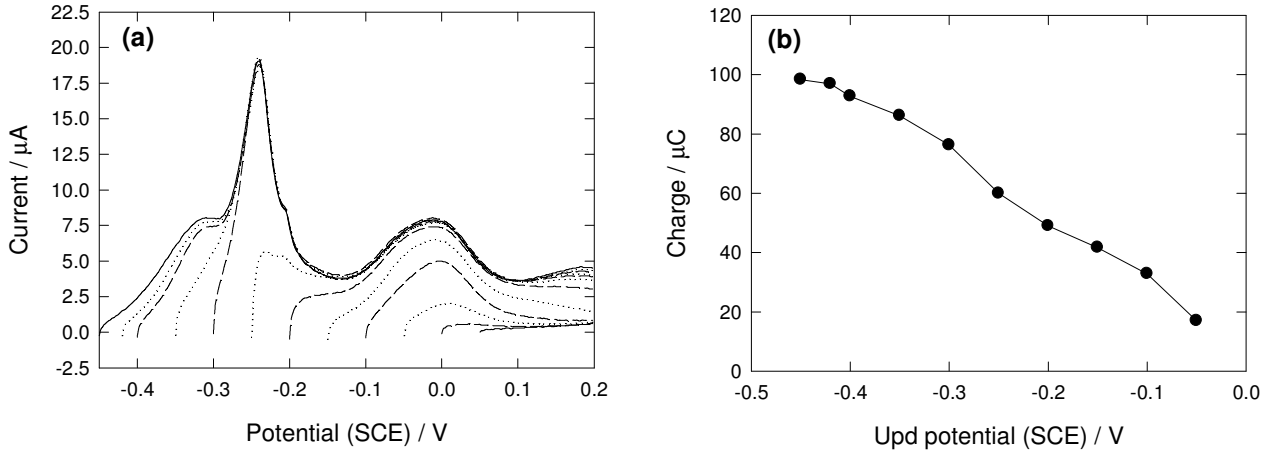

Figure 7.7. (a) Stripping voltammograms (υ = 50 mV s^{-1}) recorded in a solution prepared by dissolving 1 mM PbO in 0.01 M $HClO_4$ for the oxidative desorption of lead underpotentially deposited onto a polycrystalline gold plug electrode at various potentials for 5 seconds and (b) plot of the underpotential deposition potential *versus* the charge passed during stripping of the lead from the polycrystalline gold electrode surface. The stripping voltammogram was initiated at the underpotential deposition potential and scanned in the positive direction.

Using equation 7.11, the 'real' or electrochemically active surface area of the polycrystalline gold electrode was calculated to be 0.27 cm^2 using the values: Q = 98.28 μC (the charge associated with stripping a monolayer of lead underpotentially deposited onto the surface by applying a potential of -0.45 V for 5 seconds) and Q_c = 362 μC cm^{-2} (the generally accepted value for the charge required to strip a monolayer of lead from a polycrystalline gold surface).[84] This surface area is similar to the geometric area (0.28 cm^2) and is significantly lower than that determined from the reduction of a monolayer of gold oxide (0.57 cm^2). Additional experiments were carried out in which lead was underpotentially deposited onto the gold surface for 20 seconds to ensure that the deposition time was sufficient for formation of a monolayer of lead. The electrochemically active surface area calculated from the charge for stripping a monolayer of underpotentially deposited lead was the same for deposition times of 5 and 20 seconds, demonstrating that a deposition time of 5 seconds is sufficient for monolayer formation. Considering that the results from the underpotential deposition experiments indicate that the polycrystalline gold plug electrode is perfectly smooth (roughness factor = 0.96) which is not physically possible, it is concluded that lead underpotential deposition is not a reliable method for determining the 'real' surface area of the gold electrode employed. Hence, the surface area of 0.57 cm^2 obtained from the reduction of a monolayer of gold oxide is accepted as the electrochemically active surface area of the polycrystalline gold plug electrode used in this study.

7.3.1.3 Cyclic Voltammetry of Hydrogen Peroxide at a Solid Gold Electrode

The cyclic voltammogram of 1 mM H_2O_2 in PB (pH 7.4) at the reconstructed polycrystalline gold plug electrode is shown in Figure 7.8. This voltammogram is similar to that reported by Gerlache *et al.* for the electro-oxidation and reduction of 10 mM H_2O_2 in PB (pH 7.4) at a polycrystalline gold electrode.[21] In the current study, comparison with the scan recorded in blank electrolyte (0.04 M PB (pH 7.4) containing 0.1 M $NaClO_4$) allows the peaks at 0.84 (peak 2) and 0.45 V (peak 5) to be assigned to the formation and reduction of gold oxide respectively (refer to Section 7.3.1.1). The oxidation peak at 0.40 V (peak 1) is attributed to the oxidation of H_2O_2 to yield oxygen (equation 7.1). On the reverse scan, the oxygen generated is reduced back to H_2O_2 at -0.13 V (peak 3, reverse of equation 7.1) and the major reduction peak observed at -0.50 V (peak 4) is attributed to the reduction of H_2O_2 to water (equation 7.2). An oxidative current superimposed on the gold oxide reduction peak is also observed in the reverse scan. This unusual behaviour was

attributed by Gerlache *et al.* to H_2O_2 oxidation being inhibited by the formation of gold oxide, however, upon reduction of gold oxide the oxidation of H_2O_2 is favoured at potentials greater than 0.15 V.[21] The assignment of peak 4 to the reduction of oxygen generated during H_2O_2 oxidation was confirmed by the absence of this peak when a cyclic voltammogram was recorded from 0 to -0.80 V after degassing the solution with nitrogen.

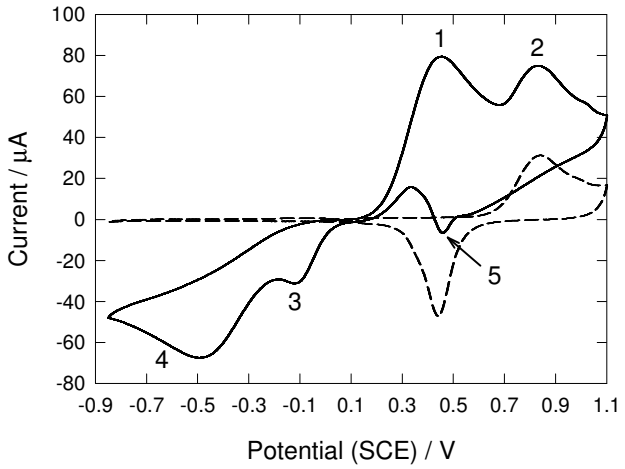

Figure 7.8. Cyclic voltammogram of 1 mM H_2O_2 in PB (pH 7.4) at a polycrystalline gold plug electrode (υ = 50 mV s^{-1}); in the absence (----) and presence (—) of 1 mM H_2O_2. Supporting electrolyte is 0.1 M $NaClO_4$. The voltammograms are initiated at 0 V and scanned in the positive potential direction first. Prior to recording the voltammograms, the gold electrode was electrochemically prepared by potential cycling between -0.20 V and 1.45 V at 50 mV s^{-1} in 0.01 M $HClO_4$ for 3 hours.

Comprehensive studies performed by Gerlache *et al.* regarding the electrochemical behaviour of H_2O_2 at a polycrystalline gold electrode revealed that the formation of the peak corresponding to the oxidation of H_2O_2 (peak 1) is dependent on the state of the electrode surface and is inhibited by the adsorption of adventitious impurities.[21] These workers proposed that formation of the first oxidation peak (peak 1) is favoured by the presence of a hydroxide layer physisorbed onto the gold surface.[21] Electrochemical cycling of the electrode removes a thin layer of gold to give a surface which is electrochemically favourable for the formation of a hydroxide layer which catalyses the oxidation of H_2O_2 and allows the reaction to occur at potentials less positive

than that for the formation of gold oxide. This catalytic behaviour is most likely due to hydrogen bonding between H_2O_2 and the physisorbed hydroxyl species.[21]

The reconstruction process used to pre-treat the solid gold electrode prior to recording the voltammograms shown in Figure 7.8 involves extensive cycling and is impractical for the development of a sensor to monitor H_2O_2 in the field in real time. Therefore, different pre-treatment procedures were investigated to understand the importance of the electrode surface state on the electrochemical detection of H_2O_2. These experiments were performed at a polycrystalline gold disk electrode constructed by sealing gold wire in Teflon (see Section 7.2.2). Cyclic voltammograms of 1 mM H_2O_2 were recorded after the gold electrode was polished with alumina slurries (1.0 and 0.05 μm) and after the electrode was electrochemically pre-treated by cycling between -0.40 and 1.20 V in PB (0.04 M, pH 7.4) for five successive cycles at 50 mV s^{-1} (Figure 7.9).

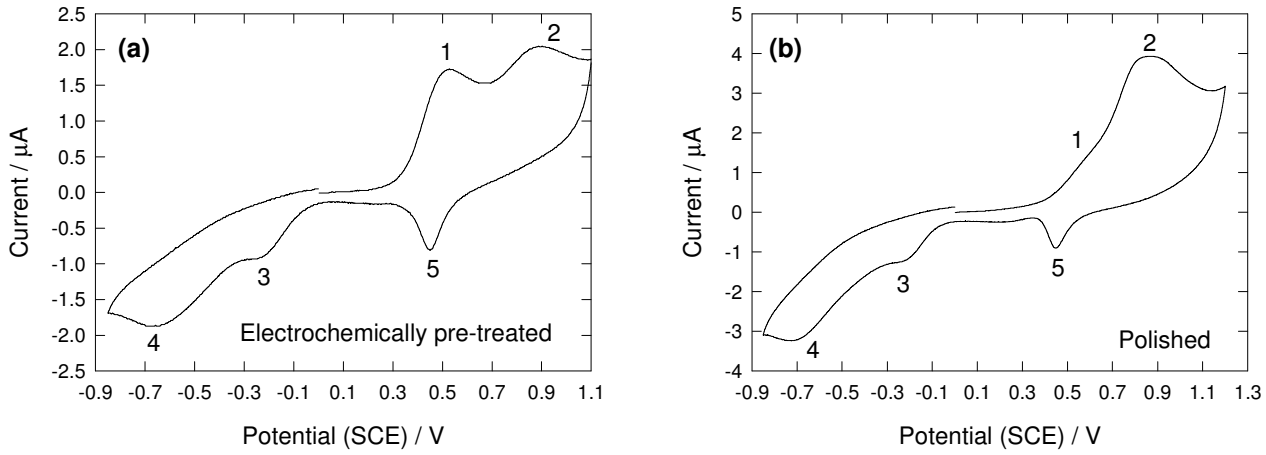

Figure 7.9. Cyclic voltammograms of 1 mM H_2O_2 in PB (pH 7.4) recorded at a polycrystalline gold disk electrode (υ = 50 mV s^{-1}) after (a) subjecting the electrode to potential cycling between -0.40 and 1.20 V in PB (pH 7.4) for five successive cycles and (b) after polishing with alumina slurries (1.0 and 0.05 μm). Supporting electrolyte is 0.1 M $NaClO_4$.

The response observed at the gold electrode electrochemically prepared by cycling in PB for five successive cycles is similar to that obtained at the electrode reconstructed in 0.01 M $HClO_4$ for 3 hours (compare Figure 7.8 and 7.9 (a)). Two oxidation peaks are observed at 0.53 (peak 1) and 0.90 V (peak 2) corresponding to the oxidation of H_2O_2 and the formation of gold oxide

respectively. The subsequent reduction of oxygen generated by the oxidation of H_2O_2 occurs at -0.23 V (peak 3) and H_2O_2 is reduced at -0.67 V (peak 4). Reduction of the gold surface oxide occurs at 0.44 V (peak 5). When the gold electrode is prepared by simply polishing with alumina the peak at 0.53 V (peak 1) appears as a small shoulder peak and the peak current for the second oxidation peak at 0.87 V (peak 2) is greater indicating that the oxidation of H_2O_2 and the formation of gold oxide are occurring at the same potential (Figure 7.9 (b)). Suppression of the first oxidation peak after polishing the gold electrode with alumina only is assumed to occur because polishing debris which remains adsorbed on the gold surface after rinsing with Milli-Q water inhibits the formation of a hydroxide layer and therefore the catalytic oxidation of H_2O_2. Hence, the process occurs at potentials similar to that observed for the formation of gold oxide. The cathodic processes attributed to the reduction of oxygen (peak 3) and H_2O_2 (peak 4) are not effected by polishing, although, a small shift to more negative potentials is observed.

Further studies were carried out to investigate the influence of H_2O_2 concentration on cyclic voltammograms obtained at a gold disk electrode which had been electrochemically prepared by cycling between -0.40 and 1.20 V in PB (pH 7.4) for five successive cycles at 50 mV s^{-1}. Aliquots of 0.147 M H_2O_2 (68 μL) solution were added successively to a solution of blank PB (pH 7.4, 10 mL) and cyclic voltammograms were recorded after each addition (Figure 7.10). The current associated with peaks 1 to 4 increases as the concentration of H_2O_2 increases from 1 to 4 mM. Consideration of the anodic peaks suggests that the oxidation of H_2O_2 occurs *via* the catalytic and non-catalytic mechanisms because the peak currents for both oxidation waves increase with H_2O_2 concentration. The shape of the cathodic peak corresponding to the reduction of gold oxide (peak 5) changes when a scan is recorded in a solution of 4 mM H_2O_2. A small oxidative current due to H_2O_2 oxidation is superimposed on the reduction current in the potential range of 0.25 to 0.55 V. This is assumed to have the same origins as discussed for the voltammograms obtained at the reconstructed surface of a gold plug electrode (Figure 7.8). It was found that the peak current associated with the first oxidation peak (peak 1) decreased when the H_2O_2 concentration increased above 6 mM (not shown) and became much smaller than the second oxidation peak (peak 2). However, when a cyclic voltammogram was recorded in a fresh solution of 6 mM H_2O_2 using a freshly prepared electrode, the first oxidation peak had a greater current than the second. It is proposed that the suppression of the first oxidation peak most likely occurred due to competitive adsorption between chloride ions (leached into solution from the SCE reference electrode) and hydroxide ions at the gold electrode.

This explanation is consistent with the results of Gerlache *et al.* who showed that when chloride ions are added to the H_2O_2 solution the first oxidation peak disappears.[21]

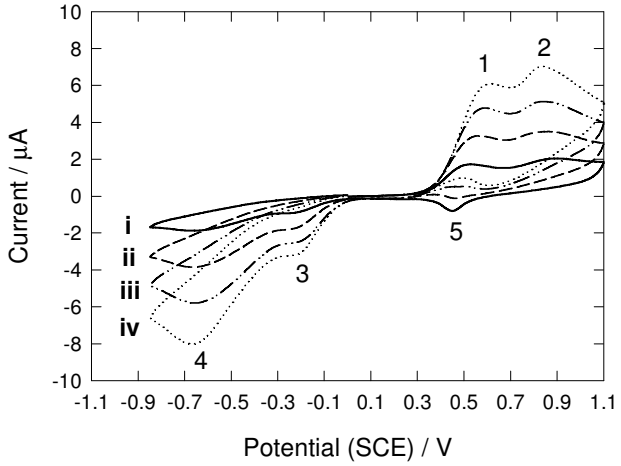

Figure 7.10. The influence of H_2O_2 concentration on cyclic voltammograms recorded at a polycrystalline gold disk electrode; (i) 1 mM, (ii) 2 mM, (iii) 3 mM and (iv) 4 mM H_2O_2 in PB (pH 7.4) (υ = 50 mV s^{-1}). Supporting electrolyte is 0.1 M $NaClO_4$. Prior to recording the voltammogram, the gold electrode was electrochemically prepared by potential cycling between -0.40 V and 1.20 V in PB (pH 7.4) for five successive cycles at 50 mV s^{-1}.

7.3.2 Electrochemical Detection of Hydrogen Peroxide at Gold Nanoparticle Electrodes

7.3.2.1 Preparation and Characterisation of Gold Nanoparticle Electrodes

The activity of gold nanoparticles towards the electro-oxidation and reduction of H_2O_2 was examined at electrodes fabricated using two different assembly methods: (1) electrostatic immobilisation of colloidal gold nanoparticles onto amine-modified glassy carbon surfaces and (2) electrodeposition of gold nanoparticles directly onto glassy carbon substrates.

Citrated-capped gold nanoparticles were assembled onto amine containing films by immersing ED-modified glassy carbon samples in as-prepared gold nanoparticle solution for 180 minutes followed by rinsing in Milli-Q water and drying with a gentle stream of nitrogen. For these experiments, ED-modified glassy carbon surfaces were prepared from

0.1 M $[Bu_4N]BF_4$-acetonitrile solution containing approximately 5 mM ED by cycling from 0 to 1.20 V for 6 cycles at 100 mV s^{-1}. The citrate-capped gold nanoparticles were synthesised using standard methods (see Section 7.2.3.1, Preparation I) and had an average diameter of 12 nm, a solution concentration of 1.77×10^{16} nanoparticles L^{-1} and a solution pH of 5.8. The assembly of gold nanoparticles onto the ED-film at pH 5.8 is controlled by electrostatic attraction between protonated amine groups in the film and the negative charge of the citrate-capping groups on the gold nanoparticles (Figure 7.11). The electrodes prepared using this method will be referred to as nanoAu/ED/GC.

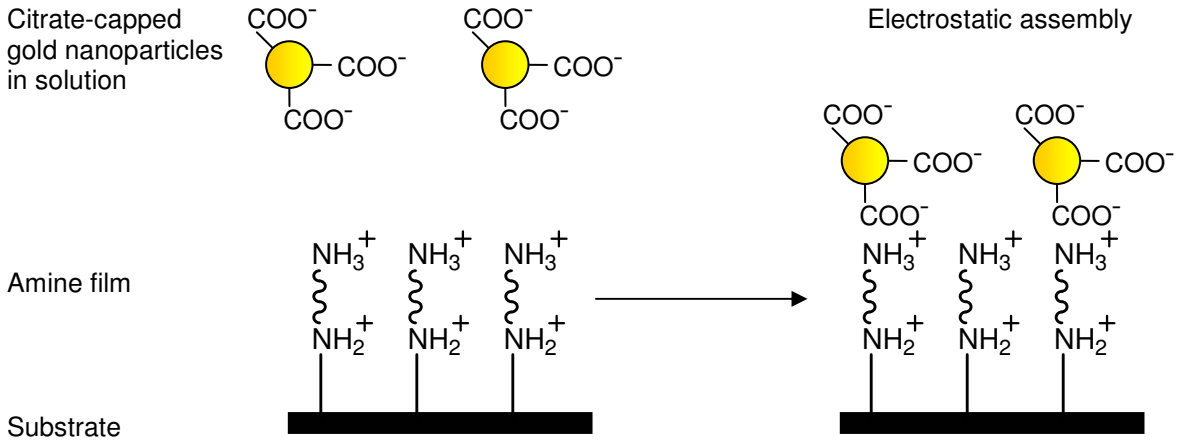

Figure 7.11. Assembly of colloidal gold nanoparticles onto an amine-modified surface *via* electrostatic interactions between protonated amine groups within the film and negatively charged citrate-capping groups on the gold nanoparticles.

Electrodes fabricated by electrochemically depositing gold nanoparticles directly onto the glassy carbon surface (referred to as nanoAu/GC) were also assessed for the electrochemical detection of H_2O_2. Established methods were used to deposit particles reported to have an average diameter of 10 nm.[94] This size was selected so that the activity of these electrodes towards H_2O_2 could be compared with those fabricated by assembling citrate-capped colloidal gold nanoparticles (average diameter 12 nm) onto amine-containing films *via* electrostatic interactions.

Scanning electron microscopy (SEM) was used to examine the size and density of the gold nanoparticles immobilised at the glassy carbon surface using the two assembly methods (Figure 7.12). The image obtained for the nanoAu/GC electrode showed that the electrodeposited gold forms islands on the surface that have an average diameter of 17 nm (note: the preparation conditions used in this work were reported to give particles with an average diameter of 10 nm) and are widely dispersed (Figure 7.12 (a)). The discrete island particle growth is consistent with reports in the literature regarding the electrodeposition of gold onto glassy carbon.[94,95,96] A detailed discussion of the mechanism for the electrochemical deposition of metals onto conductive substrates is given in Chapter 4. Immobilisation of citrate-capped gold nanoparticles onto ED-modified glassy carbon surfaces led to a dense-coating of gold nanoparticles (average diameter 12 nm) and gave a clearly visible gold colouration to the surface (Figure 7.12 (b-d)). Areas of 3-dimensional aggregates of gold nanoparticles were observed on top of an underlying gold nanoparticle layer. SEM analysis of a control sample prepared by immersing a polished glassy carbon surface in the as-prepared citrate-capped gold nanoparticle solution showed that the gold nanoparticles assemble onto the unmodified glassy carbon surface to a significantly lesser extent (Figure 7.12 (e)).

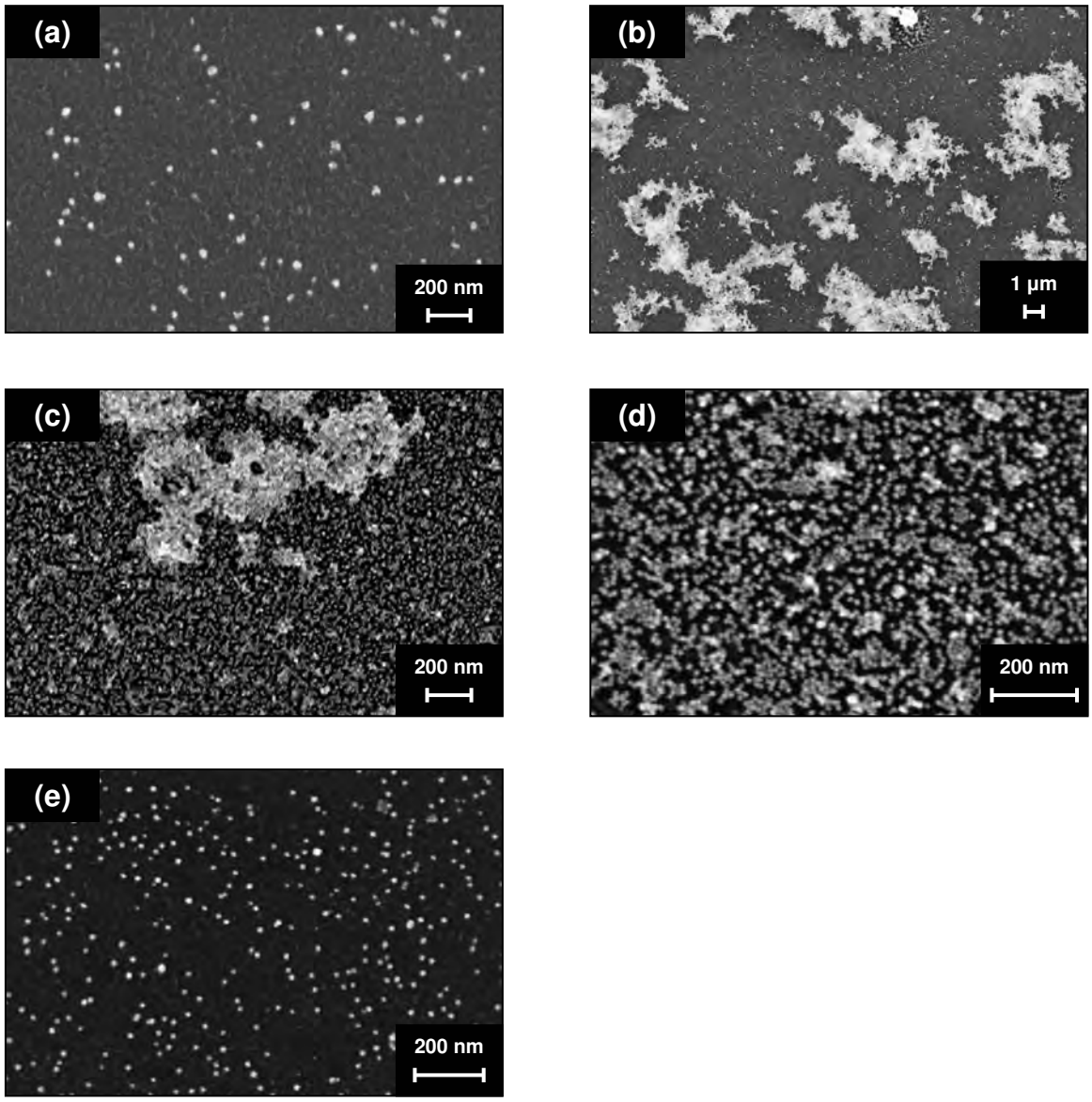

Figure 7.12. SEM images of gold nanoparticles immobilised onto glassy carbon surfaces: (a) gold nanoparticles were electrodeposited onto glassy carbon from a solution of 0.01 mM $KAuCl_4$ in 0.5 M H_2SO_4 by stepping the potential from 1.10 to 0 V for 5 seconds; (b-d) ED-modified and (e) unmodified glassy carbon surfaces after treatment with colloidal gold nanoparticle solution (1.77×10^{16} nanoparticles L^{-1}, immersion time = 180 minutes, pH 5.8).

Further characterisation of the nanoAu/ED/GC electrode was performed because this electrode showed the most promise for the electrochemical detection of H_2O_2 (see Section 7.3.2.2). Figure 7.13 shows the voltammetric response recorded at the nanoAu/ED/GC electrode in 0.01 M $HClO_4$. This voltammogram is comparable to that obtained at a solid gold electrode (Figure 7.3) and provides further evidence for the successful attachment of gold nanoparticles at the ED-modified glassy carbon surface. A similar voltammogram has also been reported for citrate-capped gold nanoparticles attached to a glassy carbon electrode through a sulfhydryl-terminated monolayer.[61] At the nanoAu/ED/GC electrode the small oxidation peak observed at 1.30 V corresponds to the formation of gold surface oxide and the well-defined reduction peak observed in the reverse scan at 0.75 V is attributed to the subsequent reduction of the surface oxide species. These peaks are assigned according to the reactions described in Section 7.3.1.1 for the formation and reduction of gold oxide.

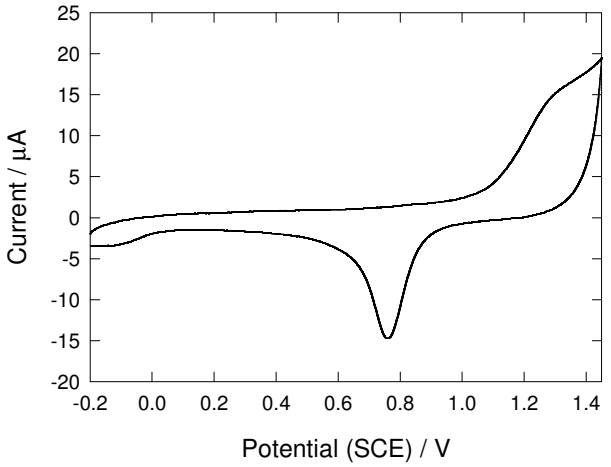

Figure 7.13. Cyclic voltammogram of a nanoAu/ED/GC electrode in 0.01 M $HClO_4$ (50 mV s^{-1}). NanoAu/ED/GC electrode preparation: an ED-modified glassy carbon surface was prepared from 0.1 M $[Bu_4N]BF_4$-acetonitrile solution containing approximately 5 mM ED by cycling from 0 to 1.20 V for 6 cycles at 100 mV s^{-1} and treated with as-prepared colloidal gold nanoparticle solution (average particle diameter 12 nm) for 180 minutes at pH 5.8.

The microcrystal structure of the gold nanoparticles assembled onto the ED-modified glassy carbon electrode was characterised by stripping underpotentially deposited lead from the gold nanoparticle surface. Lead was deposited onto the gold nanoparticles from a solution prepared by

dissolving 1 mM PbO in 0.01 M $HClO_4$ by stepping the potential from 0.20 V to -0.40 V for 5 seconds. The voltammogram corresponding to stripping of the underpotentially deposited monolayer of lead from the gold nanoparticle surface is shown in Figure 7.14. This voltammogram is comparable to that reported in the literature for the stripping of a layer of underpotentially deposited lead from gold nanoparticles electrochemically deposited on glassy carbon.[94] Two oxidative stripping peaks are observed; the sharp peak at -0.24 V is attributed to the stripping of lead from the Au(111) crystal plane and the broader wave at -0.02 V corresponds to stripping from the Au(110)/Au(100) crystal planes.[83,84,86,87,94] The recorded voltammogram is similar to that described in Section 7.3.1.1 for the stripping of underpotentially deposited lead from the surface of a polycrystalline solid gold electrode and suggests that the gold nanoparticles are polycrystalline consisting of a combination of Au(111), (110) and (100) sites. Control experiments were performed whereby polished glassy carbon and ED-grafted surfaces were subjected to the conditions for the underpotential deposition of lead. No lead stripping peaks were observed at either of the control surfaces demonstrating that lead is only deposited onto the surface of the gold nanoparticles at the nanoAu/ED/GC electrode.

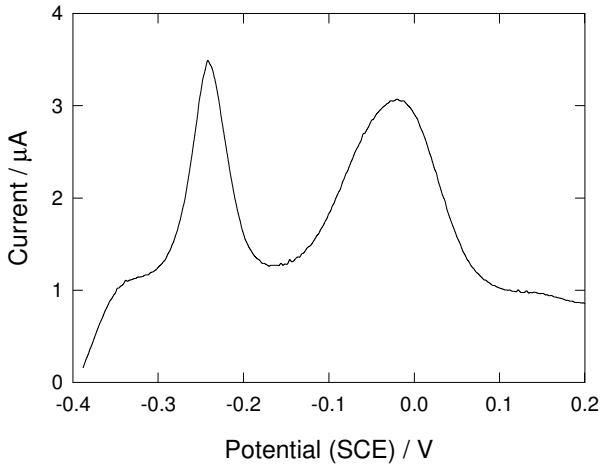

Figure 7.14. Stripping voltammogram recorded in a solution prepared by dissolving 1 mM PbO in 0.01 M $HClO_4$ for the oxidative desorption of a layer of lead underpotentially deposited onto a nanoAu/ED/GC electrode (υ = 50 mV s^{-1}). Lead was underpotentially deposited onto the gold nanoparticles from the solution of 1 mM PbO dissolved in 0.01 M $HClO_4$ by stepping the potential from 0.20 to -0.40 V for 5 seconds. The stripping voltammogram was initiated at -0.40 V. The nanoAu/ED/GC electrode was prepared using the conditions specified in Figure 7.13.

Additional experiments were performed to examine the effect of positive potential excursions on the stability of the nanoAu/ED/GC electrode. For this study, two nanoAu/ED/GC electrodes with different gold nanoparticle densities were employed and SEM was used to characterise the morphology of the gold nanoparticle surfaces before and after positive potentials were applied to the electrodes. Citrate-capped gold nanoparticles (average diameter 12 nm) were assembled onto ED-modified glassy carbon surfaces by immersing the samples in as-prepared gold nanoparticle solution for 60 or 180 minutes followed by rinsing and drying. The ED-modified glassy carbon surfaces were prepared from 0.1 M $[Bu_4N]BF_4$-acetonitrile solution containing approximately 5 mM ED by cycling from 0 to 1.20 V for 6 cycles at 100 mV s^{-1}. Figures 7.15 and 7.16 present two representative sets of SEM images for the nanoAu/ED/GC electrodes prepared by assembling gold nanoparticles for 60 and 180 minutes respectively. Comparison of the images obtained for the as-prepared gold nanoparticle surfaces prior to electrochemical analysis shows that the density of gold nanoparticles assembled onto the ED-film increases as the immersion time increases (compare Figures 7.15 and 7.16 (a, b)). At both nanoAu/ED/GC surfaces the coating of gold nanoparticles consists of areas of 3-dimensional aggregates on top of an underlying gold nanoparticle layer. The particles have a uniform size and shape and individual nanoparticles are observed in the 3-dimensional aggregates. The effect of positive potential excursions on the nanoAu/ED/GC electrodes was investigated in 0.01 M $HClO_4$ solution. Increasingly positive potentials ranging from 0.90 to 1.65 V (E_{app}) were applied to the surfaces for 90 seconds, after which time the surface oxide species formed at these potentials was subsequently reduced by scanning from E_{app} to 0 V at 50 mV s^{-1}. The morphology of the gold nanoparticles was examined using SEM after applying potentials of 1.10, 1.37, 1.50 or 1.55 and 1.65 V and reducing the gold oxide layer as specified in Figure 7.15 (c-m) and Figure 7.16 (c-j). These SEM images are representative of the nanoAu/ED/GC surfaces as it was not possible to image the same area of the electrode after each treatment. No significant changes are observed in the morphology of the gold nanoparticle surfaces after applying potentials between 0.90 and 1.10 V (Figures 7.15 and 7.16 (c,d)). However, upon application of more positive potentials, fusing of the individual nanoparticles is observed giving clusters which vary in size and shape (Figure 7.15 (e, f, h, i, k, and l) and Figure 7.16 (e, g and i). The size of the clusters increases as more positive potentials are applied. The resolution of the individual nanoparticles comprising the 3-dimensional aggregates is also lost due to fusing of the particles (Figure 7.15 (g, j, and m) and Figure 7.16 (f, h and j)).

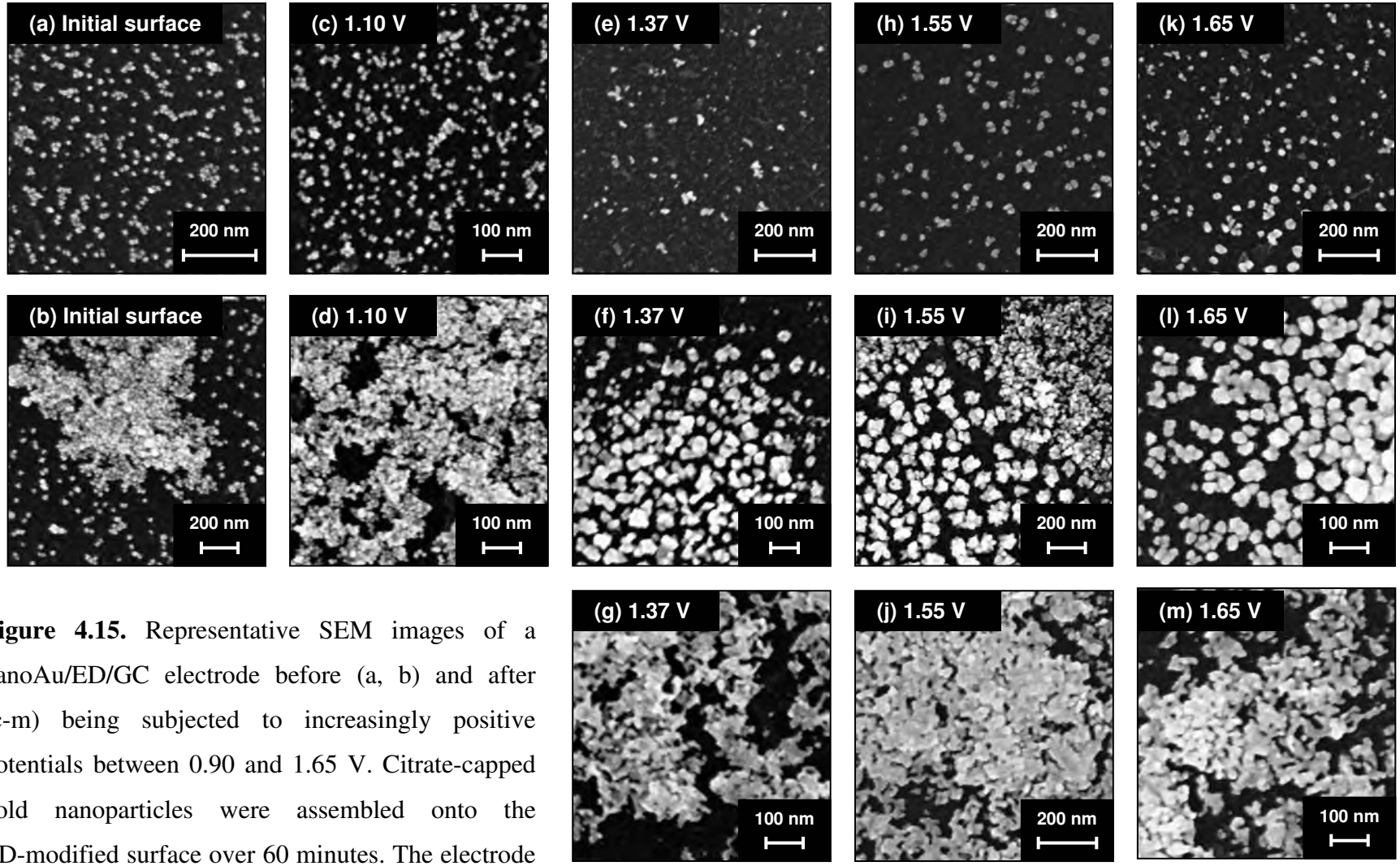

Figure 4.15. Representative SEM images of a nanoAu/ED/GC electrode before (a, b) and after (c-m) being subjected to increasingly positive potentials between 0.90 and 1.65 V. Citrate-capped gold nanoparticles were assembled onto the ED-modified surface over 60 minutes. The electrode was held at each potential (E_{app}) for 90 seconds in 0.01 M $HClO_4$ before the surface oxide species formed was subsequently reduced by scanning from E_{app} to 0 V at 50 mV s^{-1}. SEM images were obtained after applying potentials of 1.10 (c, d) 1.37 (e-g), 1.55 (h-j) and 1.65 V (k-m).

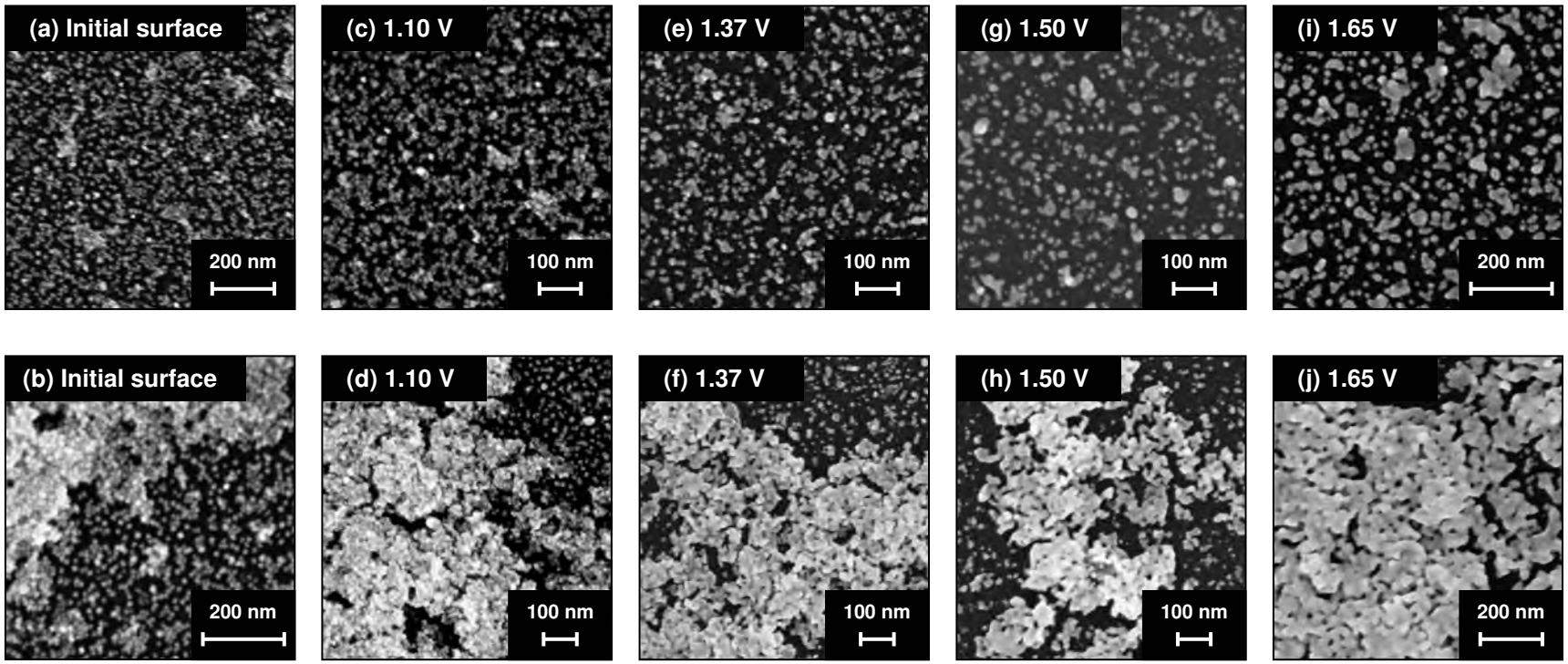

Figure 7.16. Representative SEM images of a nanoAu/ED/GC electrode before (a, b) and after (c-j) being subjected to increasingly positive potentials between 0.90 and1.65 V. Citrate-capped gold nanoparticles were assembled onto the ED-modified surface over 180 minutes. The electrode was held at each potential (E_{app}) for 90 seconds in 0.01 M $HClO_4$ before the surface oxide species formed was subsequently reduced by scanning from E_{app} to 0 V at 50 mV s^{-1}. SEM images were obtained after applying potentials of 1.10 (c,d) 1.37 (e, f), 1.50 (g,h) and 1.65 V (i, j).

Similar changes have been reported after polarisation at positive potentials for gold nanoparticles encapsulated with a shell of 1,9-nonanedithiol and assembled onto planar substrates.[97] Fusing of the gold nanoparticles was shown using AFM and this was attributed to the partial or complete removal of the 1,9-nonanedithiol shell upon application of oxidising potentials. The change in morphology observed using AFM was investigated further using an electrochemical quartz crystal nanobalance (EQCN) and infrared reflection spectroscopy (IRS). After polarisation at positive potentials a decrease in mass was detected for the gold nanoparticle electrode using EQCN, and IR spectra exhibited a reduction in absorbance for spectral features diagnostic of 1,9-nonanedithiol. In the current study, the uniform size and shape for individual gold nanoparticles observed after the nanoAu/ED/GC is prepared is due to electrostatic interactions between the negative charges of the citrate-capping groups repelling one another. Aggregation is known to occur under conditions where the charge on the colloidal gold nanoparticles is decreased due to desorption of citrate ions.[98] Hence, it is most likely that the fusing of particles after polarisation of the electrode at positive potentials is due to the removal of the citrate-capping groups. It has been shown that citrate adsorbed onto Au (111) electrodes is oxidised in acidic media at 1.30 V (*vs*. SCE).[99] This potential is similar to that applied to the nanoAu/ED/GC electrodes (1.37 V) following which an increase in particle size and shape, along with fusion of the individual gold nanoparticles comprising 3-dimensional aggregates, is first observed using SEM.

An attempt was made to determine the total active surface area of the gold nanoparticles comprising the nanoAu/ED/GC electrodes analysed using SEM, by evaluating the charges passed during the stripping of the gold oxide layer formed at each applied potential. However, due to the instability of the gold nanoparticles towards increasingly positive potentials, the potential at which a complete monolayer of gold oxide is formed could not be determined. Figure 7.17 shows plots of the potential applied to the nanoAu/ED/GC electrodes to form a layer of surface oxide *versus* the charge passed during the subsequent reduction of the gold oxide species. A well-defined plateau region corresponding to the complete formation of gold surface oxide was not observed at either surface. Instead, a steady increase in the charge passed during the stripping of the gold oxide layer formed between 0.90 and 1.50 or 1.55 V was observed. Application of more positive potentials caused a decrease in the charge associated with the reduction of gold oxide and at the low density particle surface no charge was observed for the reduction of the gold oxide layer formed at 1.65 V (Figure 7.17 (a)). The reason for the abrupt decrease in charge is unclear as no significant loss of

gold from the surface is observed for the SEM images taken after applying a potential of 1.65 V to the nanoAu/ED/GC surfaces (Figure 7.15 (k-m) and Figure 7.16 (i, j)). It has been suggested that the formation of surface oxide species on the gold nanoparticles may cause the effective isolation of particles and lead to a finite band gap.[97] This might explain the decrease in charge associated with the reduction of gold oxide at potentials greater than ~ 1.50 V.

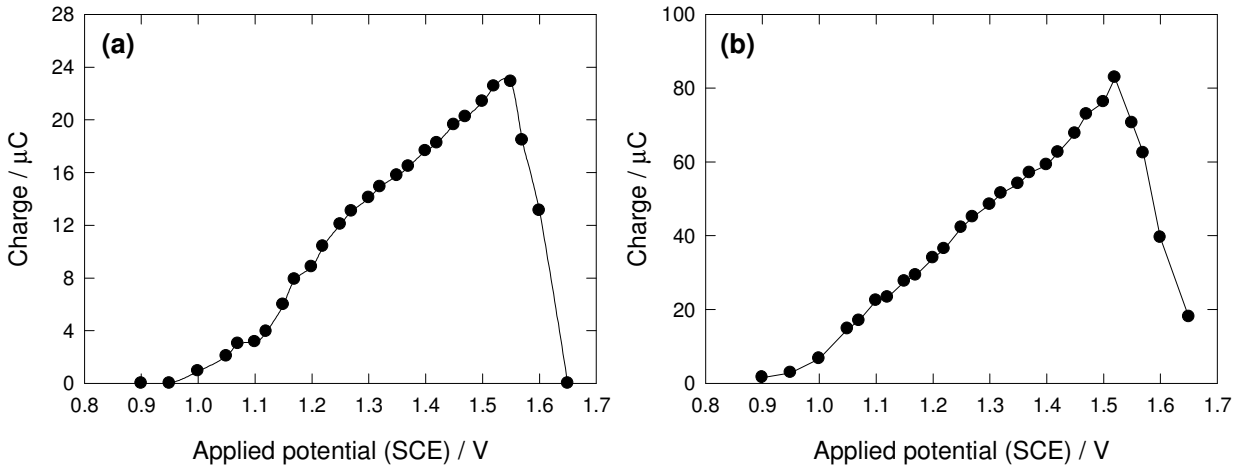

Figure 7.17. Plots of applied potential for gold oxide formation *versus* the charge passed during the subsequent reduction of the gold oxide layer at nanoAu/ED/GC electrodes prepared by immersing an ED-modified glassy carbon surface in as-prepared citrate-capped gold nanoparticle solution (average diameter 12 nm) for (a) 60 and (b) 180 minutes. The ED-modified glassy carbon surfaces were prepared from 0.1 M $[Bu_4N]BF_4$-acetonitrile solution containing approximately 5 mM ED by cycling from 0 to 1.20 V for 6 cycles at 100 mV s^{-1}. The nanoAu/ED/GC electrodes were held at each potential (E_{app}) for 90 seconds in 0.01 M $HClO_4$ before the surface oxide layer was reduced by scanning from E_{app} to 0 V at 50 mV s^{-1}.

Determining the total surface area of gold nanoparticles comprising the nanoAu/ED/GC electrodes using stripping of a monolayer of underpotentially deposited lead was not attempted because earlier experiments with a solid gold electrode showed that the results were unreliable (refer to Section 7.3.1.2). A similar conclusion was reached by McDermott *et al.* who attempted to determine the overall surface area of gold nanoparticles electrochemically deposited onto glassy carbon substrates using the stripping of underpotentially deposited lead.[94] Therefore, because the total surface area of the gold nanoparticles could not be estimated for the nanoAu/ED/GC

electrodes, the activities of different electrodes employed for the electro-oxidation and reduction of H_2O_2 in Sections 7.3.2.2 and 7.3.2.3 were compared by normalising the peak currents against geometric area. For the gold nanoparticle electrodes, the peak current densities were based on the geometric area of the glassy carbon support.

7.3.2.2 Electrochemical Detection of Hydrogen Peroxide at Gold Nanoparticle Electrodes

Cyclic voltammograms of 1 mM H_2O_2 in PB (pH 7.4) at nanoAu/ED/GC and nanoAu/GC electrodes are shown in Figure 7.18. The peak potentials and peak current densities (based on geometric area) measured from these voltammograms are given in Table 7.4. Voltammetric data for the electro-oxidation and reduction of H_2O_2 at solid gold electrodes electrochemically pre-treated by potential cycling in $HClO_4$ (0.01 M) or blank PB (0.04 M, pH 7.4) are also included for comparison (see Section 7.3.1.3). The gold nanoparticle electrodes were fabricated using the conditions described in Section 7.3.2.1 and used as-prepared. For the nanoAu/ED/GC electrode, citrate-capped gold nanoparticles were assembled onto the ED-modified surface by immersing the amine-containing surface in as-prepared gold nanoparticle solution for 180 minutes.

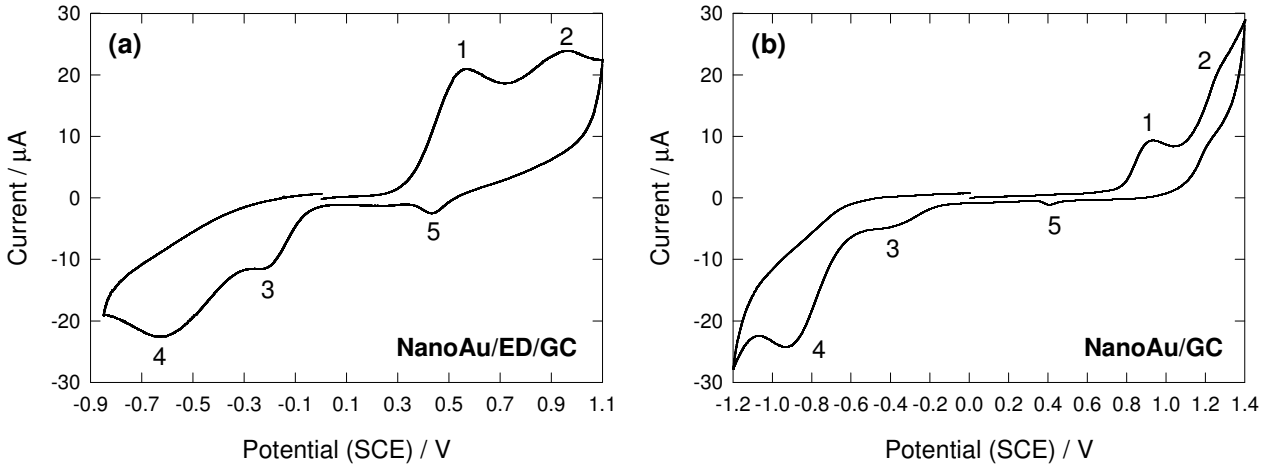

Figure 7.18. Cyclic voltammogram of 1 mM H_2O_2 in PB buffer (pH 7.4) at (a) nanoAu/ED/GC and (b) nanoAu/GC electrodes (υ = 50 mV s^{-1}). Supporting electrolyte is 0.1 M $NaClO_4$. The gold nanoparticle electrodes were prepared using the conditions specified in Table 7.4. Peaks 1 and 2 represent the oxidation of H_2O_2 and the formation of gold surface oxide whilst peaks 3 and 4 correspond to the reduction of oxygen and H_2O_2 respectively. Peak 5 is attributed to the reduction of gold surface oxide.

Table 7.4. Voltammetric data for the electrochemical detection of H_2O_2 at gold nanoparticle and solid gold electrodes. The experiment was performed at the solid gold plug electrode three times and the errors indicate the range of values observed.

Electrode	Cyclic voltammetry data for the electro-oxidation and reduction of H_2O_2[a]							
	E_p (V)				j_p (μA cm^{-2})[b]			
	Peak 1	Peak 2	Peak 3	Peak 4	Peak 1	Peak 2	Peak 3	Peak 4
Solid gold plug[c]	0.48 ± 0.03	0.85 ± 0.02	-0.13	-0.52 ± 0.02	152 ± 14	88 ± 17	38 ± 20	102 ± 7
Solid gold disk[d]	0.54	0.91	-0.24	-0.64	100	49	33	59
NanoAu/ED/GC[e]	0.58	0.97	-0.23	-0.64	122	33	47	85
NanoAu/GC[f]	0.90	1.28	-0.40	-0.91	85	[g]	16	113

[a] Cyclic voltammograms of 1 mM H_2O_2 were recorded over the potential ranges shown in Figures 7.8, 7.9 (a) and 7.18. The peaks correspond to (1) oxidation of H_2O_2, (2) formation of gold surface oxide, (3) reduction of oxygen and (4) reduction of H_2O_2.

[b] Based on the geometric area of the electrode.

[c] Electrochemically pre-treated by cycling between -0.20 and 1.45 V at 50 mV s^{-1} in 0.01 M $HClO_4$ for 3 hours.

[d] Electrochemically pre-treated by cycling between -0.40 and 1.20 V in blank PB (pH 7.4) for five cycles at 50 mV s^{-1}.

[e] ED-modified glassy carbon surfaces were prepared from 0.1 M $[Bu_4N]BF_4$-acetonitrile solution containing approximately 5 mM ED by cycling from 0 to 1.20 V for 6 cycles at 100 mV s^{-1} and treated with as-prepared colloidal gold nanoparticle solution (average particle diameter 12 nm) for 180 minutes at pH 5.8.

[f] Gold nanoparticles (average diameter 17 nm) were electrodeposited onto glassy carbon from a solution of 0.01 M $KAuCl_4$ in 0.5 M H_2SO_4 by stepping the potential from 1.10 to 0 V for 5 seconds.

[g] Could not be measured.

The responses observed for the electro-oxidation and reduction of H_2O_2 at the nanoAu/ED/GC and nanoAu/GC electrodes in Figure 7.18 are attributed to the gold nanoparticles as no response was observed at a bare glassy carbon electrode. The cyclic voltammogram recorded at the nanoAu/ED/GC electrode exhibits the same characteristic peaks observed at the solid gold electrodes in the presence of H_2O_2 (compare Figures, 7.8, 7.9 (a) and 7.18 (a)). In general, higher peak current densities are obtained at the nanoAu/ED/GC electrode compared to the solid gold disk electrode electrochemically prepared by cycling in PB for five successive cycles. However, these peak current densities are in most cases lower than those obtained at the solid gold plug electrode reconstructed in 0.01 M $HClO_4$ for 3 hours (Table 7.4). The peaks corresponding to the oxidation of H_2O_2 (peak 1, equation 7.1) and the formation of gold surface oxide (peak 2) are shifted to more

positive potentials at the nanoAu/ED/GC electrode compared to the reconstructed solid gold electrodes whilst the peaks attributed to the reduction of oxygen (generated by the oxidation of H_2O_2 (peak 3, equation 7.1)) and H_2O_2 (peak 4, equation 7.2) are shifted to more negative potentials (Table 7.4). The shift in peak potential indicates that the rate of electron transfer is slower at the nanoAu/ED/GC electrode compared to the solid gold plug electrode which has undergone extensive surface reconstruction. This is attributed to the ED-tether layer and layer of citrate-capping groups surrounding the gold nanoparticles increasing the distance of electron transfer between the glassy carbon electrode and the electroactive gold nanoparticles. No significant differences in peak potential are observed between the nanoAu/ED/GC electrode and the solid gold disk electrode electrochemically pre-treated by potential cycling in PB for five successive cycles.

At the nanoAu/GC electrode, only three main peaks are observed (Figure 7.18 (b)). These peaks correspond to the oxidation of H_2O_2 (peak 1, equation 7.1) and the reduction of oxygen (peak 3) and H_2O_2 (peak 4, equation 7.2) respectively. The small shoulder observed on the solvent limit at 1.28 V (peak 2) is attributed to the formation of gold surface oxide and the subsequent reduction of this oxide layer occurs at ~ 0.40 V (peak 5). In comparison to the responses obtained at the solid gold and nanoAu/ED/GC electrodes for the electro-oxidation and reduction of H_2O_2, the peak potentials measured at the nanoAu/GC electrode occur at less favourable potentials and the peak current densities are lower (except for the reduction of H_2O_2) (Table 7.4). The reason for the positive shift in oxidation peak potentials and the negative shift in reduction peak potentials compared with the nanoAu/ED/GC electrode is not clear. The nanoAu/GC electrode does not contain modifying layers on the glassy carbon or gold nanoparticle surface and therefore, a faster rate of electron transfer might be expected. It is possible that the larger size of the electrochemically deposited gold nanoparticles (17 nm compared to 12 nm for the colloidal gold nanoparticles) accounts for the less favourable potentials. The lower peak current densities obtained at the nanoAu/GC electrode compared to the nanoAu/ED/GC electrode are attributed to the low particle density for the nanoAu/GC electrode (Figure 7.12 (a)).

Low operating potentials and high peak current densities are desirable for the electrochemical detection of H_2O_2 in real samples. Of the gold electrodes examined for the electro-oxidation and reduction of H_2O_2, the best conditions are achieved at the solid gold plug electrode following potential cycling in 0.01 M $HClO_4$ for 3 hours (Table 7.4); however, the reconstruction

process is time-consuming and therefore, impractical for the development of a sensor to monitor H_2O_2 in real-time. Considering the other electrodes, nanoAu/ED/GC is the most promising electrode for the electrochemical detection of H_2O_2 as high currents are achieved at favourable potentials. Furthermore, the catalytic oxidation of H_2O_2 (peak 1) is observed at potentials less positive than that for the formation of gold oxide (peak 2) at the as-prepared nanoAu/ED/GC electrode. This is in contrast to the electro-oxidation of H_2O_2 at a solid gold electrode which has been polished but not electrochemically pre-treated. At such surfaces the formation of the first oxidation peak is suppressed by the adsorption of adventitious impurities, such as alumina, after polishing and electrochemical cycling of the solid gold electrode is required to form a hydroxide layer on the surface which favours the catalytic oxidation of H_2O_2 at low potentials (see Section 7.3.1.3). Comparison of the electro-oxidation and reduction of H_2O_2 at the gold nanoparticle electrodes shows that the nanoAu/ED/GC electrode performs better than the nanoAu/GC electrode. The preparation method of nanoAu/ED/GC electrodes has advantages over electrochemical deposition. By immobilising pre-synthesised colloidal gold nanoparticles onto an amine-modified surface the size of the gold nanoparticles can be selected independently of their density which is controlled by the number of amine functionalities on the surface. In comparison, the size and density of gold nanoparticles electrodeposited onto glassy carbon substrates is difficult to control independently of each other under the conditions used in this work as both these parameters increase with electrolysis time and furthermore, a broad size distribution is obtained.

7.3.2.3 Control of the Nano-Scale Architecture of Gold Nanoparticles Assembled on Amine-Modified Carbon Surfaces

Further studies were undertaken to investigate the effects of gold nanoparticle size and density on H_2O_2 oxidation and reduction. These experiments were carried out using nanoAu/ED/GC electrodes. Four solutions of citrate-capped gold nanoparticles were used in this work. These solutions were synthesised using standard methods (see Section 7.2.3.1) and the average particle diameter for each solution ranged from 2.8 to 12 nm. In initial experiments, the activity of nanoAu/ED/GC electrodes for the electrochemical detection of H_2O_2 was studied as a function of gold nanoparticle size. Citrate-capped gold nanoparticles were assembled onto ED-modified glassy carbon samples, electrografted as described in Section 7.3.2.1, by immersing the samples in the as-prepared gold nanoparticle solutions for 180 minutes followed by rinsing and drying. The effect

of gold nanoparticle size on the voltammetric response of the electrodes towards 1 mM H_2O_2 is shown in Table 7.5 and Figure 7.19. The results obtained at a solid gold plug electrode electrochemically prepared by cycling between -0.20 and 1.45 V in 0.01 M $HClO_4$ (50 mV s^{-1}) for 3 hours are included for comparison.

Table 7.5. Effect of gold nanoparticle size on the cyclic voltammetric response of nanoAu/ED/GC electrodes towards the electro-oxidation and reduction of 1 mM H_2O_2 in PB (pH 7.4).[a] Errors are reported for experiments that were replicated at least twice and indicate the range of values observed. All other experiments were only carried out once.

Particle size (nm)	Cyclic voltammetry data for the electro-oxidation and reduction of H_2O_2[b]							
	E_p (V)				j_p (µA cm^{-2})[c]			
	Peak 1	Peak 2	Peak 3	Peak 4	Peak 1	Peak 2	Peak 3	Peak 4
2.8	0.55	0.97	-0.20	-0.54	267	133	114	200
3.2	0.52 ± 0.01	0.98 ± 0.02	-0.18 ± 0.01	-0.50 ± 0.01	160 ± 6	96 ± 19	63 ± 8	113 ± 3
3.6	0.52 ± 0.02	0.97 ± 0.02	-0.18 ± 0.02	-0.54 ± 0.03	140 ± 30	121 ± 20	74 ± 14	107 ± 8
12.0	0.57	0.97	-0.22	-0.63	122	33	47	85
Solid Au[d]	0.48 ± 0.03	0.85 ± 0.02	-0.13	-0.52 ± 0.02	152 ± 14	88 ± 17	38 ± 20	102 ± 7

[a] ED-modified glassy carbon surfaces were prepared from 0.1 M $[Bu_4N]BF_4$-acetonitrile solution containing approximately 5 mM ED by cycling from 0 to 1.20 V for 6 cycles at 100 mV s^{-1} and treated with as-prepared colloidal gold nanoparticle solution for 180 minutes at pH 5-5.8.

[b] Cyclic voltammograms of 1 mM H_2O_2 were recorded over the potential ranges shown in Figures 7.9 (a) and 7.18 (a). The peaks correspond to (1) oxidation of H_2O_2, (2) formation of gold surface oxide, (3) reduction of oxygen and (4) reduction of H_2O_2.

[c] Based on the geometric area of the electrode.

[d] Electrochemically pre-treated by cycling between -0.20 and 1.45 V at 50 mV s^{-1} in 0.01 M $HClO_4$ for 3 hours.

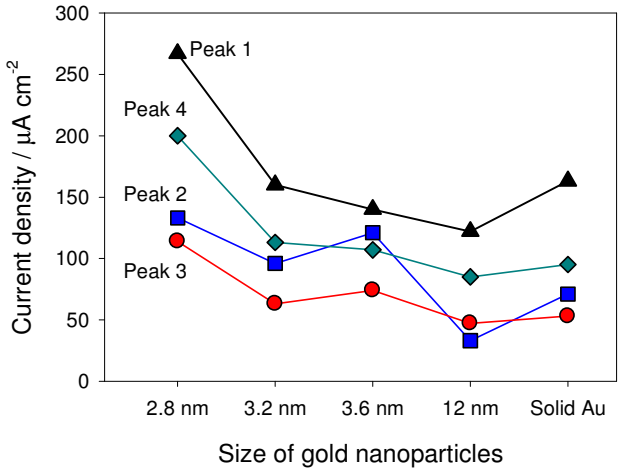

Figure 7.19. Plot of gold nanoparticle size *versus* the peak current densities measured at nanoAu/ED/GC electrodes for the electro-oxidation and reduction of 1 mM H_2O_2 in PB (pH 7.4). The nanoAu/ED/GC and solid gold disk electrodes were prepared using the conditions specified in Table 7.5. Peak 1 (▲) and peak 2 (■) represent the oxidation of H_2O_2 and the formation of gold surface oxide whilst peak 3 (●) and peak 4 (♦) correspond to the reduction of oxygen and H_2O_2 respectively.

The data presented in Table 7.5 and Figure 7.19 show that the peak current densities measured at the nanoAu/ED/GC electrodes (based on the geometric area of the glassy carbon electrode) increase as the size of the gold nanoparticles decrease. The nanoAu/ED/GC electrodes prepared using 2.8 and 3.2 nm gold nanoparticles exhibit greater peak current densities for the electro-oxidation and reduction of H_2O_2 than the solid gold plug electrode. The increased sensitivity at the gold nanoparticle electrodes is most likely due to the combined surface area of the gold nanoparticles being greater than that of the solid gold plug electrode. Evaluation of the peak potentials reveals only small shifts to less positive potentials for the oxidation peaks and less negative potentials for the reduction peaks at the nanoAu/ED/GC electrodes as the size of the gold nanoparticles decreases. The most favourable potentials for the electro-oxidation and reduction of H_2O_2 are obtained at the solid gold plug electrode.

Control experiments were performed by recording cyclic voltammograms of 1 mM H_2O_2 at unmodified glassy carbon electrodes treated with gold nanoparticle solution containing particles with an average size of 2.8 and 12nm. No response was observed at the electrode fabricated using 2.8 nm gold particles and only one oxidation peak was observed at 0.92 V in the presence of 12 nm gold particles. This peak was attributed to the oxidation of H_2O_2 and had a low current density (21 $\mu A\ cm^{-2}$) due to the low particle density observed by SEM for gold nanoparticles assembled on unmodified glassy carbon surfaces (Figure 7.12 (e)).

A simple method for controlling the density of gold nanoparticles assembled onto the amine-containing grafted film is to vary the immersion time of the grafted film in the nanoparticle solution.[100] Using gold nanoparticles with the optimum size of 2.8 nm, ED-modified surfaces were immersed in the as-prepared gold nanoparticle solution for 30, 60 or 180 minutes. A denser coating of gold nanoparticles is assembled on the ED-grafted surface as the immersion time increases (compare Figures 7.15 (a, b) and Figure 7.16 (a, b)) and this gave higher peak current densities for the electro-oxidation and reduction of H_2O_2 (Table 7.6 and Figure 7.20). As immersion time increased, a small shift to more favourable potentials was observed for all peaks (Table 7.6). The optimum immersion time (180 minutes) for assembling gold nanoparticles onto ED-modified glassy carbon surfaces was used for all subsequent experiments.

Table 7.6. Effect of assembly time for 2.8 nm gold nanoparticles on the cyclic voltammetric response of nanoAu/ED/GC electrodes towards the electro-oxidation and reduction of 1 mM H_2O_2 in PB (pH 7.4).[a]

Assembly time (min)	Cyclic voltammetry data for the electro-oxidation and reduction of H_2O_2[b]							
	E_p (V)				j_p (μA cm^{-2})[c]			
	Peak 1	Peak 2	Peak 3	Peak 4	Peak 1	Peak 2	Peak 3	Peak 4
30	0.62	0.89	-0.29	-0.72	19	48	24	94
60	0.62	0.98	-0.23	-0.63	81	57	48	105
180	0.55	0.97	-0.20	-0.54	267	133	114	200

[a] ED-modified glassy carbon surfaces were prepared from 0.1 M $[Bu_4N]BF_4$-acetonitrile solution containing approximately 5 mM ED by cycling from 0 to 1.20 V for 6 cycles at 100 mV s^{-1} and treated with as-prepared colloidal gold nanoparticle solution (average diameter 2.8 nm) for 30, 60 or 180 minutes at ~ pH 5.

[b] Cyclic voltammograms of 1 mM H_2O_2 were recorded over the potential ranges shown in Figure 7.18 (a). The peaks correspond to (1) oxidation of H_2O_2, (2) formation of gold surface oxide, (3) reduction of oxygen and (4) reduction of H_2O_2.

[c] Based on the geometric area of the glassy carbon electrode.

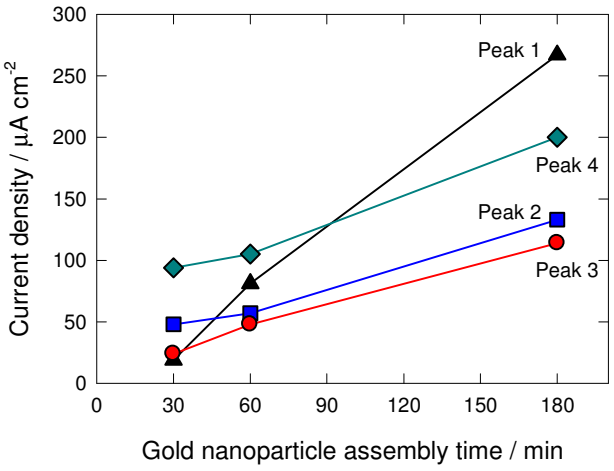

Figure 7.20. Plot of assembly time for 2.8 nm gold nanoparticles *versus* the peak current densities measured at nanoAu/ED/GC electrodes for the electro-oxidation and reduction of 1 mM H_2O_2 in PB (pH 7.4). The nanoAu/ED/GC electrodes were prepared using the conditions specified for Table 7.6. Peak 1 (▲) and peak 2 (■) represent the oxidation of H_2O_2 and the formation of gold surface oxide whilst peak 3 (●) and peak 4 (♦) correspond to the reduction of oxygen and H_2O_2 respectively.

An alternative strategy investigated to control the density of gold nanoparticles assembled on the ED film involved varying the amount of modifier attached to the surface through the choice of grafting conditions. Both the concentration of the modifier and the grafting time influence the amount of modifier grafted to the surface and the density of gold nanoparticles assembled.[100] ED-modified glassy carbon surfaces were prepared from 0.1 M $[Bu_4N]BF_4$-acetronitrile solution containing approximately 5 mM ED by cycling between 0 and 1.20 V at 100 mV s^{-1} for 1, 3 or 6 cycles. Citrate-capped gold nanoparticles with an average diameter of 3.2 nm were assembled on the ED films by immersing the samples in the as-prepared gold nanoparticle solution for 180 minutes. Comparison of the voltammetric data obtained at the nanoAu/ED/GC electrodes for the electro-oxidation and reduction of 1 mM H_2O_2 showed no significant shifts in peak potentials, however, the greatest peak current densities were observed at the nanoAu/ED/GC electrode containing the lowest surface concentration of ED and hence, (presumably) the lowest density of nanoparticles (Table 7.7, entries 1-3 and Figure 7.21). When the concentration of the ED modifying solution was decreased to 1 mM, reducing the surface concentration of ED and subsequently the nanoparticle density further, the nanoAu/ED/GC electrodes prepared by grafting films for 1 and 3 cycles gave lower peak current densities than the corresponding electrodes prepared from 5 mM ED (Table 7.7, compare entries 2-3 with 4-5 respectively). The decrease in peak current densities was coupled with a small shift to less favourable peak potentials. These results show that the most favorable nanoparticle density for optimising the catalytic activity of the nanoAu/ED/GC electrode towards H_2O_2 is obtained when the ED film is grafted for 1 cycle from a 5 mM ED solution. The decreased sensitivity of the nanoAu/ED/GC electrodes fabricated by grafting the ED film from a 1 mM modifier solution is attributed to the low density of gold nanoparticles assembled giving a smaller surface area. In contrast, for high density nanoAu/ED/GC electrodes, it is likely that aggregation of the gold nanoparticles causes a decrease in surface area which consequently reduces the current densities associated with the electro-oxidation and reduction of H_2O_2.

Table 7.7. The effect of changing the electrografting conditions for the preparation of amine-containing films on the assembly of 3.2 nm gold nanoparticles used for the electrochemical detection of H_2O_2. Errors indicate the range of values observed.[a]

	Film preparation			Cyclic voltammetric data for the electro-oxidation and reduction of H_2O_2[b]							
	Amine	Conc^{n} (mM)	Electrolysis conditions	E_p (V)				j_p (μA cm^{-2})[c]			
				Peak 1	Peak 2	Peak 3	Peak 4	Peak 1	Peak 2	Peak 3	Peak 4
1	ED	5	6 cycles	0.52 ± 0.02	0.98 ± 0.02	-0.18 ± 0.01	-0.5 ± 0.01	160 ± 8	96 ± 27	63 ± 11	113 ± 3
2	ED	5	3 cycles	0.49 ± 0.01	0.98 ± 0.00	-0.17 ± 0.01	-0.51 ± 0.01	193 ± 7	126 ± 11	79 ± 8	103 ± 4
3	ED	5	1 cycle	0.48 ± 0.01	0.93 ± 0.01	-0.17 ± 0.01	-0.54 ± 0.01	210 ± 1	90 ± 4	87 ± 5	112 ± 8
4	ED	1	3 cycles	0.53 ± 0.00	0.92 ± 0.02	-0.20 ± 0.01	-0.63 ± 0.04	129 ± 4	63 ± 9	65 ± 2	102 ± 4
5	ED	1	1 cycle	0.55 ± 0.02	0.89 ± 0.00	-0.20 ± 0.01	-0.66 ± 0.01	81 ± 10	64 ± 4	58 ± 10	87 ± 4
6	HD	5	1 cycle	0.53 ± 0.01	0.94 ± 0.01	-0.20 ± 0.01	-0.66 ± 0.02	157 ± 14	84 ± 16	88 ± 13	74 ± 3

[a] Amine-modified glassy carbon surfaces were prepared from 0.1 M $[Bu_4N]BF_4$-acetonitrile solution by cycling from 0 to 1.20 V at 100 mV s^{-1} and treated with as-prepared colloidal gold nanoparticle solution (average diameter 3.2 nm) for 180 minutes at ~ pH 5.

[b] Cyclic voltammograms of 1 mM H_2O_2 were recorded over the potential ranges shown in Figure 7.18 (a). The peaks correspond to (1) oxidation of H_2O_2, (2) formation of gold surface oxide, (3) reduction of oxygen and (4) reduction of H_2O_2.

[c] Based on the geometric area of the glassy carbon electrode.

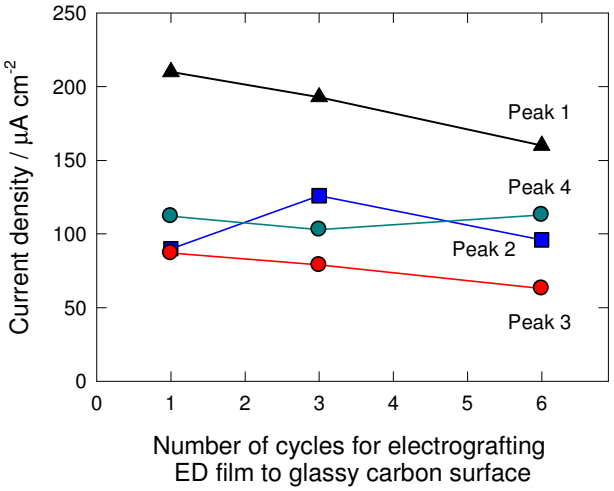

Figure 7.21. Plot of the number of cycles used to electrochemically graft ED to the glassy carbon substrate *versus* the peak current densities measured at nanoAu/ED/GC electrodes for the electro-oxidation and reduction of 1 mM H_2O_2 in PB (pH 7.4). The nanoAu/ED/GC electrodes were prepared using the conditions specified for entries 1-3 of Table 7.7. Peak 1 (▲) and peak 2 (■) represent the oxidation of H_2O_2 and the formation of gold surface oxide whilst peak 3 (●) and peak 4 (♦) correspond to the reduction of oxygen and H_2O_2 respectively.

Further studies were performed to examine the effect of the modifying diamine chain length on the activity of assembled gold nanoparticles for the electrochemical detection of H_2O_2. For these experiments, hexamethylene diamine (HD) was used and nanoAu/HD/GC electrodes were prepared using the optimised conditions for fabricating nanoAu/ED/GC electrodes. In brief, HD-modified glassy carbon electrodes were prepared from 0.1 M $[BuN_4]BF_4$-acetonitrile solution containing approximately 5 mM HD by cycling once from 0 to 1.20 V at 100 mV s^{-1}. Citrate-capped gold nanoparticles with an average size of 3.2 nm were assembled onto the amine-containing film by immersing the HD-modified glassy carbon surfaces into the as-prepared solution for 180 minutes followed by rinsing and drying. The nanoAu/HD/GC electrode was not as sensitive towards the electro-oxidation and reduction of H_2O_2 compared to the corresponding nanoAu/ED/GC electrode (Table 7.7, compare entries 3 and 6). Lower peak current densities were observed at the nanoAu/HD/GC electrode along with a small shift to less favourable potentials indicating that the rate of electron transfer is slower at the nanoAu/HD/GC electrode compared to at the

nanoAu/ED/GC electrode. This result is to be expected as the longer alkyl chain length of the HD modifier (six methylene units compared to two methylene units for ED) will increase the distance of electron transfer between the glassy carbon electrode and the gold nanoparticles.

7.3.3 Electrochemical Detection of Hydrogen Peroxide at a Solid Palladium Electrode

The response of a solid palladium electrode towards 1 mM H_2O_2 in PB (pH 7.4) is shown in Figure 7.22. All cyclic voltammograms were initiated at an oxide free surface and two successive scans were recorded (scan i and ii respectively) by scanning from an initial potential of 0.10 V in the negative (Figure 7.22 (a)) or positive potential direction first (Figure 7.22 (b)). The corresponding voltammograms recorded in blank electrolyte are shown for comparison (scan iii).

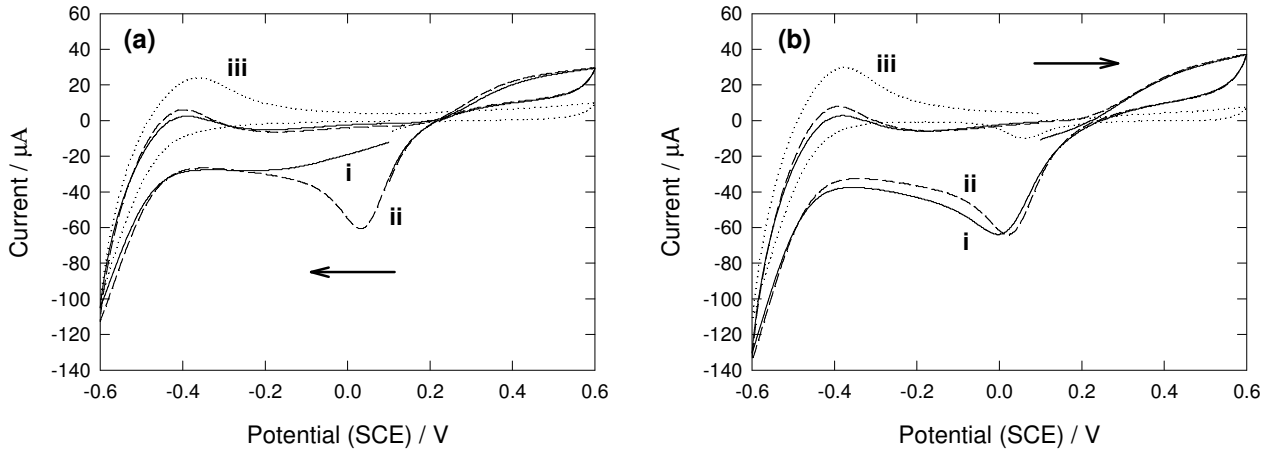

Figure 7.22. Cyclic voltammograms at a solid palladium electrode of PB (pH 7.4) in the presence (i and ii) and absence (iii) of 1 mM H_2O_2 (υ = 50 mV s^{-1}). Supporting electrolyte is 0.1 M $NaClO_4$. The voltammograms were initiated at 0.10 V and recorded by scanning in (a) the negative or (b) the positive potential direction as represented by the arrows.

A broad cathodic peak corresponding to the reduction of H_2O_2 is observed at -0.24 V in the first cyclic voltammogram recorded at a solid palladium electrode when scanning in the negative potential direction first (Figure 7.22 (a), scan i). By comparison with the scan recorded in blank electrolyte (Figure 7.22 (a), scan iii), the onset of hydrogen adsorption at the palladium surface occurs at -0.40 V and the oxidation peak observed at -0.38 V is attributed to the subsequent

desorption of hydrogen from the surface.[101,102] The increase in anodic current at potentials between 0.20 and 0.60 V corresponds to the oxidation of H_2O_2 (equation 7.1). For the second scan, a large reduction peak is observed at 0.026 V (Figure 7.22 (a), scan ii) and the shape of this peak is analogous to that observed when cyclic voltammograms of 1 mM H_2O_2 are recorded by scanning in the positive potential direction first (compare Figure 7.22 (a, scan ii) and (b, scans i and ii)) suggesting that the application of positive potentials prior to the reduction of H_2O_2 catalyses the reaction. This observation is consistent with studies reported in the literature regarding the electrochemistry of H_2O_2 at palladium containing surfaces which have shown that the oxidation and reduction of H_2O_2 is dependent on the condition of the palladium surface. In particular, it is the formation and reduction of a surface oxide layer which catalyses these reactions at a palladium electrode.[31,32,67]

In blank electrolyte, a small oxidation current corresponding to the formation of an oxide layer at the surface of the palladium electrode is observed at potentials positive of 0.20 V (equation 7.12) (Figure 7.22 (a) and (b), scan iii). It has been proposed that this surface oxide species catalyses the oxidation of H_2O_2 generating oxygen by the mechanism illustrated in Scheme 7.1.[31,32] Adsorbed H_2O_2 chemically reduces the oxidised palladium surface to give the metal (equation 7.13) which is then re-oxidised electrochemically (equation 7.12) giving rise to the increased oxidation current observed between 0.20 and 0.60 V in the presence of H_2O_2 (compare scans i and iii in Figure 7.22 (a) and (b)).

$$Pd + 2H_2O \longrightarrow Pd(OH)_2 + 2e^- + 2H^+ \qquad (7.12)$$

$$Pd(OH)_2 + H_2O_2 \longrightarrow Pd + 2H_2O + O_2 \qquad (7.13)$$

Hence, the overall reaction for the oxidation of H_2O_2 at a palladium electrode is represented by

$$H_2O_2 \longrightarrow O_2 + 2H^+ + 2e^-$$

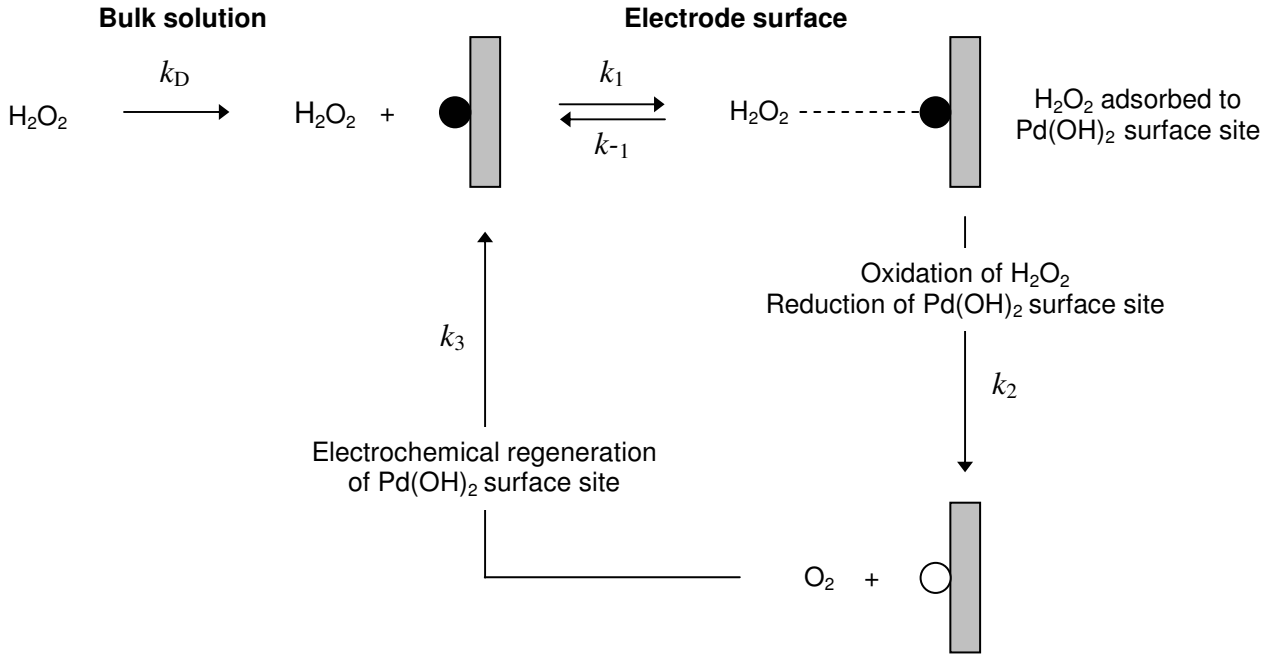

Scheme 7.1. Proposed mechanism for the oxidation of H_2O_2 at a palladium electrode. The symbols ● and ○ represent the oxidised and reduced forms of the palladium surface respectively. The following rate constants are defined as: k_D is the mass transfer constant for the diffusion of H_2O_2 from the bulk solution to the palladium electrode; k_1 and k_{-1} are the rate constants for the adsorption and desorption of H_2O_2 at the electrode surface respectively; k_2 is the rate constant for the charge transfer between adsorbed H_2O_2 and the oxidised palladium surface site and k_3 is the rate constant for electrochemical regeneration of the palladium surface oxide layer. Scheme adapted from reference 31.

The reduction of H_2O_2 is reported to be catalysed by electrochemical reduction of the palladium surface oxide species. Cai *et al.* showed that in the presence of H_2O_2, an enhancement in the peak current corresponding to the reduction of palladium oxide is observed when the voltammogram is initiated within the positive potential region where the palladium surface is oxidised.[67] These workers proposed that electrochemical reduction of the palladium surface oxide species generates an activated elemental form of palladium (equation 7.14) which catalyses the reduction of H_2O_2 *via* generation of hydroxy radicals at the electrode surface (equation 7.15). The palladium electrode is then re-oxidised by the hydroxy radicals (equation 7.16) and the oxide layer is electrochemically reduced again (equation 7.14) giving rise to the enhanced peak currents

observed at potentials similar to that for the reduction of palladium oxide in blank electrolyte (compare scans i and ii with scan iii, Figure 7.22 (b)).

$$Pd(OH)_{2,s} + 2H^+ + 2e^- \longrightarrow Pd_{s,a} + 2H_2O \quad (7.14)$$

$$H_2O_2 \xrightarrow{Pd_{s,a}} 2OH^{\bullet}_{s} \quad (7.15)$$

$$2OH^{\bullet}_{s} + Pd_{s,a} \longrightarrow Pd(OH)_{2,s} \quad (7.16)$$

In equations 7.14 to 7.16, subscripts ‘s’ and ‘a’ represent the groups of atoms forming part of the surface and the activated form of the palladium electrode respectively. The overall reaction for the reduction of H_2O_2 at a palladium electrode is represented by

$$H_2O_2 + 2H^+ + 2e^- \longrightarrow 2H_2O$$

It is noted that PdO has been proposed to be the surface oxide species involved in the catalytic reduction of H_2O_2 under alkaline conditions, however, in this thesis the surface oxide species has been represented as $Pd(OH)_2$ in equations 7.14 and 7.16 because it is considered that the hydroxide form is more likely to be present in alkaline or neutral media such as that employed in this research.

The reduction of oxygen to water at a palladium electrode has been shown to occur *via* hydrogen peroxide as an intermediate. In the presence of oxygen, the peak current associated with the reduction of H_2O_2 increases demonstrating that both species are reduced at the same or similar potentials and are indistinguishable.[31,32,67] Trace amounts of oxygen produced by the disproportionation of H_2O_2 at the electrode surface (equation 7.3) has also been reported to influence the electroreduction of H_2O_2 at gold and platinum electrodes.[19,26] Therefore, the reduction of oxygen generated by the oxidation of H_2O_2 at potentials positive of 0.20 V is also considered to contribute to the current observed for the reduction peak at 0.026 V (Figure 7.22 (a) scan ii and (b) scans i and ii).

Additional studies were carried out to investigate the influence of H_2O_2 concentration on the cyclic voltammograms obtained at a solid palladium electrode. Aliquots of 0.147 M H_2O_2 (68 μL) were added successively to a solution of blank PB (10 mL) (final H_2O_2 concentration, 6 mM) and cyclic voltammograms were recorded starting from 0.10 V by scanning in the positive potential direction first (Figure 7.23). An increase in the currents associated with the oxidation and reduction of H_2O_2 is observed as the concentration of H_2O_2 increases from 1 to 6 mM. For the reduction peak, a shift to more negative peak potentials is observed with the addition of each aliquot and two peaks are apparent when the concentration of H_2O_2 is increased to 4 mM and above. Similar behaviour was observed by Lingane and Lingane for the electroreduction of H_2O_2 at a platinum electrode where the peak observed in the reduction wave at less negative potentials was attributed to the direct reduction of oxygen and that occurring at more negative potentials corresponded to the reduction of H_2O_2.[19] It is likely that a similar mechanism is operating under the conditions used in this study and that the separation of the two processes occurs as a result of deactivation of the palladium electrode presumably caused by repetitive potential cycling.[101]

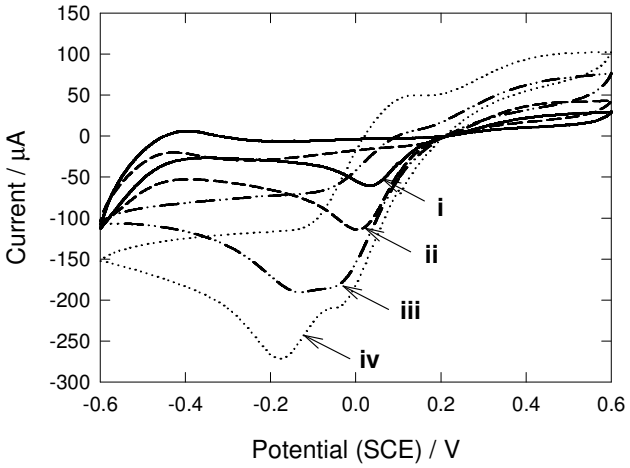

Figure 7.23. The influence of H_2O_2 concentration on cyclic voltammograms recorded at a solid palladium electrode; (i) 1 mM, (ii) 2 mM, (iii) 4 mM and (iv) 6 mM H_2O_2 in PB (pH 7.4) (υ = 50 mV s^{-1}). Supporting electrolyte is 0.1 M $NaClO_4$. The voltammograms were initiated at 0.10 V and scanned in the positive potential direction first.

For analytical applications, quantification of H_2O_2 by measurement of the oxidation current is more convenient since it is difficult to determine the current corresponding to the reduction of H_2O_2 in the presence of oxygen. Further studies were carried out to investigate the effect of different pre-treatment procedures on the oxidation of H_2O_2 at a solid palladium electrode. In addition, the reproducibility of the signal was also examined. Prior to recording cyclic voltammograms in a solution of 1 mM H_2O_2, the palladium electrode was polished with alumina slurries (1.0 and 0.05 μm) or electrochemically pre-treated by cycling between -0.10 and 1.35 V in 1 M H_2SO_4 at 50 mV s^{-1} for 30 minutes or until no change was observed in successive cycles. The oxidation of H_2O_2 showed poor reproducibility between successive scans at both the polished and electrochemically pre-treated surfaces (Figures 7.24 (a) and (b)). However, the shape (but not the current) of the broad oxidation peak was more reproducible after the palladium electrode was electrochemically pre-treated compared to when it was simply polished with alumina. The effect of polishing the palladium electrode between scans was also examined but greater variability in peak shape and current was observed (Figure 7.24 (c)).

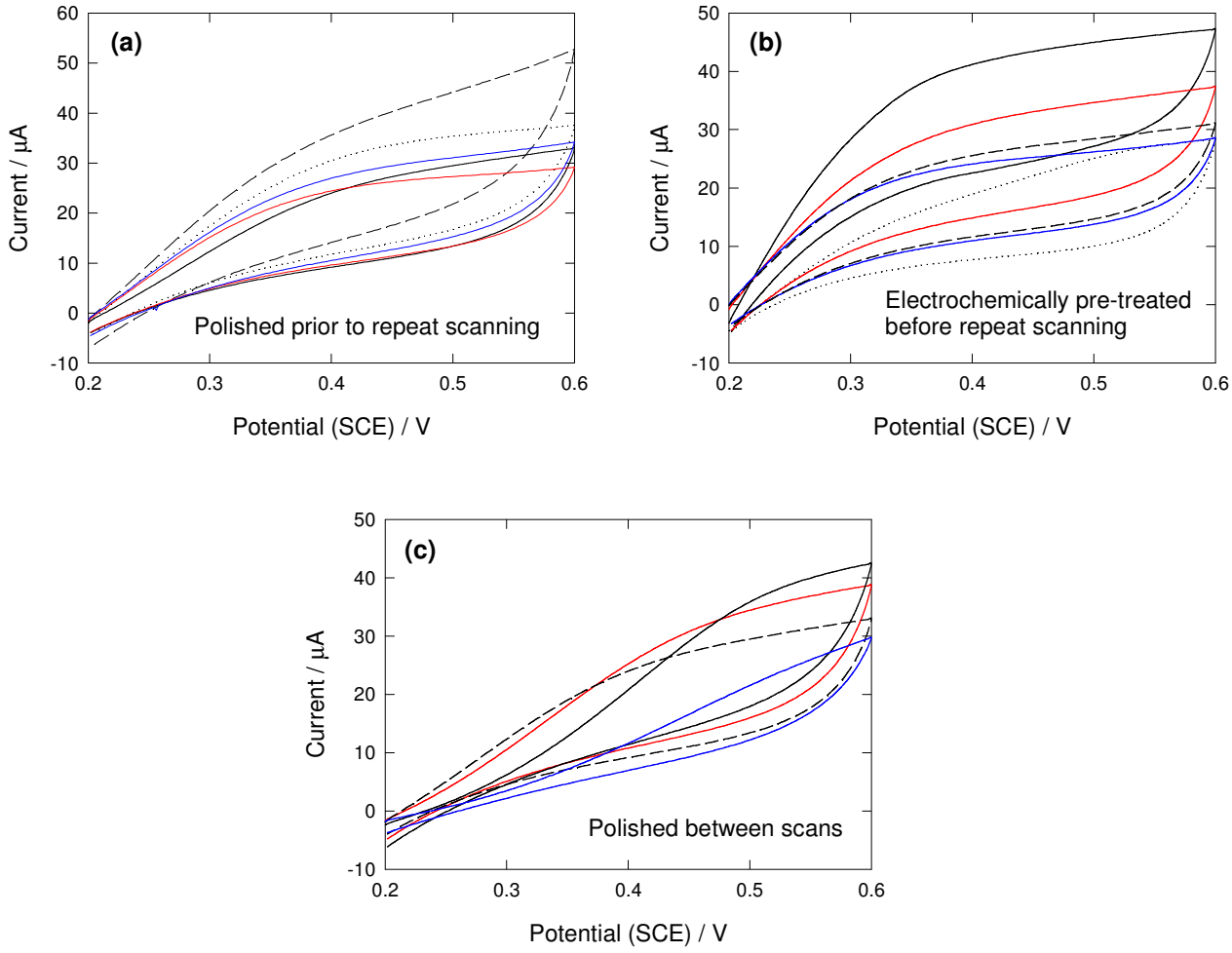

Figure 7.24. Reproducibility of the oxidation signal for 1 mM H_2O_2 in PB (pH 7.4) at a solid palladium electrode which was (a) electrochemically pre-treated or (b) polished with alumina prior to recording successive scans and (c) polished with alumina between each scan (υ = 50 mV s^{-1}); scan 1 (——), scan 2 (·····), scan 3 (----), scan 4 (——) and scan 5 (——).

7.3.4 Electrochemical Detection of Hydrogen Peroxide at Palladium Nanoparticle Assemblies Supported on Pyrolysed Photoresist Film

NanoPd/PPF electrodes were fabricated by Nano Cluster Devices Ltd by depositing palladium nanoparticles onto PPF substrates using a UHV-compatible cluster deposition system (Section 7.2.4). Palladium nanoparticles ranging in size from 2.4 to 7.8 nm were deposited to give nominal fractional surface coverages (θ_{Pd}) ranging from 0.2 to 2.0, as estimated from the total mass of metal deposited (measured using a quartz crystal film thickness monitor) and the nanoparticle size. It is noted that the fractional surface coverage is calculated as the fraction of the substrate surface covered by hemispherical nanoparticles of the given diameter (the area an individual nanoparticle occupies on the surface is referred to as the 'footprint' of the nanoparticle). Furthermore, the total surface area of the hemispherical nanoparticles is twice that of the 'footprint' as shown in equation 7.17, and is therefore directly proportional to the fractional surface coverage.

$$\frac{\text{Surface area of hemispherical nanoparticle}}{\text{'Footprint' of nanoparticle on PPF surface}} = \frac{2\pi r^2}{\pi r^2} = 2 \qquad (7.17)$$

A survey was conducted to examine the voltammetric response of the provided nanoPd/PPF surfaces towards the electro-oxidation and reduction 1 mM H_2O_2. The nanoPd/PPF electrodes were used as-prepared and two successive cyclic voltammograms were recorded at each surface between the potential limits shown in Figure 7.25. The voltammetric data obtained at each nanoPd/PPF electrode are summarised in Table 7.8. Control experiments investigating the electrochemistry of 1 mM H_2O_2 at a bare PPF surface showed no evidence of H_2O_2 oxidation or reduction and therefore, any response observed at the nanoPd/PPF electrodes must be related to the palladium nanoparticles.

The response of nanoPd/PPF electrodes fabricated by depositing 2.4 and 5.0 nm palladium nanoparticles onto PPF substrates to give a nominal fractional surface coverage of 0.2 are shown in Figure 7.25 and are representative of the responses observed at the range of surfaces examined. Well-defined cathodic peaks corresponding to the reduction of H_2O_2 were observed in the initial scans recorded at the nanoPd/PPF electrodes (see Figure 7.25, scan i). For the second scan, two

Table 7.8. The effect of palladium nanoparticle size and fractional surface coverage (θ_{Pd}) on the electrochemical detection of H_2O_2 at nanoPd/PPF electrodes. Cyclic voltammograms of 1 mM H_2O_2 in PB buffer (pH 7.4) were obtained at the nanoPd/PPF electrodes by scanning in the negative potential direction first using the limits shown in Figure 7.25 (υ = 50 mV s^{-1}).

Sample	Pd nanoparticles		Surface concentration of $Pd(OH)_2$ (mol cm^{-2})[a]	Cyclic voltammetry data for the electroreduction of H_2O_2[b]			Reproducibility of H_2O_2 oxidation signal
	Diameter (nm)	θ_{Pd}		E_{pc} (V)	i_{pc} (μA)	j_{pc}[c] (μA cm^{-2})	
1	2.40	0.2	Not observed	-0.40	35.4	114	Y
2	2.55	0.2	[d]	-0.42	23.7	76	[d]
3	2.55	0.2	7.18×10^{-11}	-0.23	61.6	199	Y
4	2.45	0.4	4.29×10^{-10}	-0.24	32.3	104	N
5	2.35	2.0	1.86×10^{-9}	-0.12	32.5	105	N
6	5.0	0.2	3.29×10^{-10}	-0.21	40.0	129	N
7	5.0	0.7	1.20×10^{-9}	-0.18	20.0	65	[d]
8	5.0	0.7	6.82×10^{-10}	-0.18	26.0	84	N
9	6.70	0.7	1.78×10^{-10}	-0.50	14.5	47	Y
10	7.80	0.7	1.89×10^{-9}	-0.08	33.8	109	[d]
Solid Pd	-	-	8.42×10^{-10}	-0.24	5.3	33	N

[a] Measured from the charge associated with the reduction of $Pd(OH)_2$ in blank PB solution.

[b] Cyclic voltammetry data taken from the initial scan.

[c] Based on the geometric area of the electrode.

[d] Not measured.

distinct cathodic behaviours were observed (scan ii). NanoPd/PPF surfaces prepared using small palladium nanoparticles (2.4 and 2.55 nm) deposited at a low nominal fractional surface coverage (0.2) exhibited two reduction peaks. This behaviour is represented in Figure 7.25 (a) (scan ii) which shows that oxygen reduction occurs at a less negative potential than H_2O_2 reduction (oxygen is generated by the oxidation of H_2O_2 at potentials between 0.20 and 0.60 V (equation 7.1)). Hence, this surface appears to be relatively inactive for H_2O_2 reduction. It is noted that this behaviour was also observed at the nanoPd/PPF surface containing 6.7 nm palladium nanoparticles deposited to give a nominal fractional surface coverage of 0.7. At all the other surfaces examined only one reduction peak was observed in the second scan as shown in Figure 7.25 (b) (scan ii) for 5 nm palladium nanoparticles deposited onto PPF to give a nominal fractional surface coverage of 0.2. In these cases, the reduction peak observed in the second scan occurred at less negative potentials compared to that for the reduction peak in the first scan. This behaviour is similar to that observed at the solid palladium electrode (see Section 7.3.3) and corresponds to simultaneous reduction of oxygen and H_2O_2.

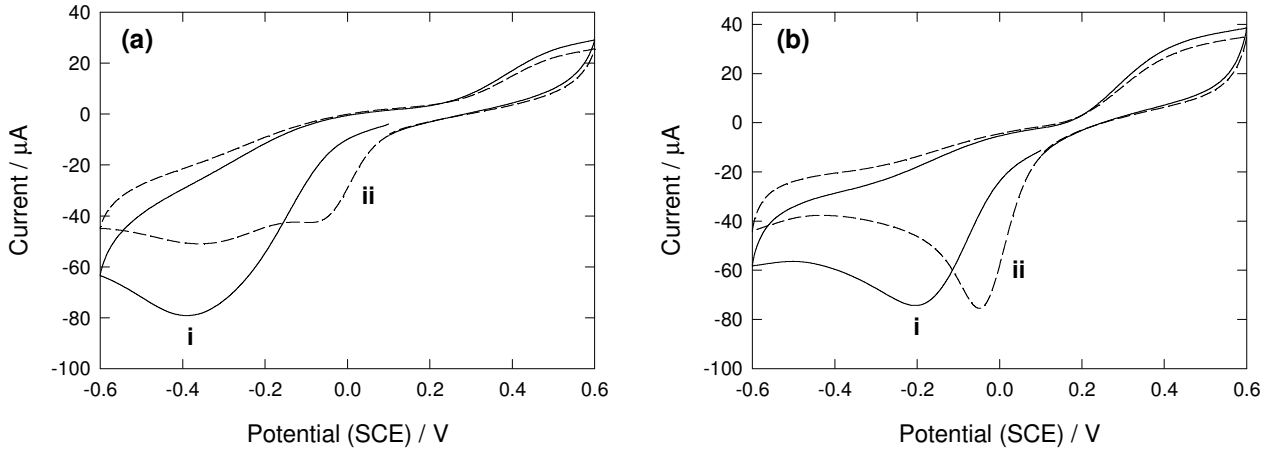

Figure 7.25. Cyclic voltammograms of 1 mM H_2O_2 at nanoPd/PPF electrodes fabricated by depositing (a) 2.4 and (b) 5.0 nm palladium nanoparticles onto PPF substrates to give a nominal fractional surface coverage of 0.2. The voltammograms were initiated at 0.10 V and scanned in the negative potential direction first (υ = 50 mV s^{-1}); (i) first scan, (ii) second scan.

The mechanism for the catalytic reduction of H_2O_2 is assumed to occur in an analogous fashion to that described for the reduction of H_2O_2 at a solid palladium electrode (refer to Section 7.3.3). Hence, the different cathodic behaviours observed for the reduction process at the range of nanoPd/PPF surfaces examined is most likely influenced by the amount of palladium oxide formed at positive potentials. The data shown in Table 7.8 was examined to determine the effect of palladium nanoparticle size and fractional surface coverage on the reduction of H_2O_2 and the influence of palladium surface oxide on the cathodic behaviour observed in the presence of oxygen (generated by the oxidation of H_2O_2). The following comments can be made:

1. The occurrence of the two cathodic behaviours observed for the reduction of H_2O_2 in the presence of oxygen is not related to nanoparticle size or the nominal fractional surface coverage but is related to the surface concentration of palladium oxide which can be formed at the surface. In general, for the nanoPd/PPF surfaces at which the reduction of H_2O_2 occurs at -0.40 V or a more negative potential and two separate reduction peaks are observed in the presence of oxygen, negligible amounts of palladium surface oxide are formed at the surface (entries 1, 2 and 9, Table 7.8) (note: for entry 9, a large surface concentration of palladium oxide is obtained). In comparison, for the nanoPd/PPF surfaces at which the reduction of H_2O_2 occurs at -0.24 V or a less negative potential and only one reduction peak is observed in the presence of oxygen, larger surface concentrations of palladium surface oxide are formed (entries 3-8 and 10, Table 7.8) and reduction of this layer is assumed to activate the palladium electrode for the reduction of H_2O_2.

2. The size of the palladium nanoparticles or the nominal fractional surface coverage does not appear to influence the potential at which H_2O_2 reduction occurs (E_{pc}).

3. No systematic relationship is observed for the current (i_{pc}) associated with the reduction of H_2O_2 with respect to nanoparticle size or fractional surface coverage.

The lack of the expected relationship between the nominal fractional surface coverage and the peak current associated with the reduction of H_2O_2 may be at least partly explained by the way the nanoPd/PPF samples were prepared. In most cases, the beam of clusters was not centered on the PPF substrates and therefore, the position of nanoparticles on the surface was unknown as they could not be observed by eye or by microscopy. Hence, the nominal fractional surface coverages

must be considered unreliable. Furthermore, these values are calculated assuming that the hemispherical particles form a monolayer before progressing to multilayer structures; however, this is unlikely to be the case. The surface concentration of palladium oxide formed at a nanoPd/PPF surface was considered to give a better estimate of the fractional surface coverage as this value should be proportional to the total surface area of palladium exposed to the solution at the surface. It is noted that the surface concentrations of palladium oxide determined for the nanoPd/PPF surfaces are reasonable compared to that measured for the solid palladium surface (Table 7.8) considering that the surface area of a hemisphere is twice that of its 'footprint' on the surface and the values corresponding to the surface concentration of palladium oxide are calculated using the geometric area of PPF.

As noted above, the amount of palladium surface oxide appears to determine the potential at which the H_2O_2 reduction peak occurs. However, as shown in Figure 7.26 (a) there is no relationship between the surface concentration of palladium oxide ($\Gamma_{Pd(OH)_2}$) and the current associated with the reduction of H_2O_2 (i_{pc}) (note: that the values for $\Gamma_{Pd(OH)_2}$ and i_{pc} were determined at the same position on the nanoPd/PPF surface). The relationship between the amount of palladium oxide and the nominal fractional surface coverage was also examined and is shown in Figure 7.26 (b). Again no trend is observed. The latter result is not surprising considering the uncertainty in the distribution of the nanoparticles on the surface. However, the lack of relationship between the surface concentration of palladium oxide and the H_2O_2 reduction peak current is unexpected. Furthermore, while it is generally accepted that smaller particles are more active, this is not evident for the range of nanoPd/PPF samples examined in this study.

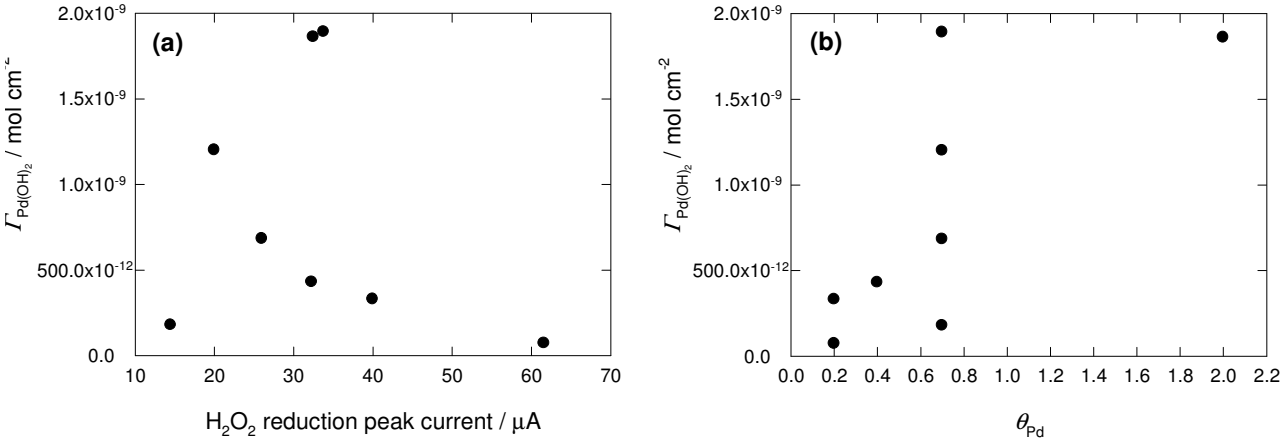

Figure 7.26. Plots of (a) H_2O_2 reduction peak current and (b) the nominal fractional surface coverage of palladium nanoparticles (θ_{Pd}) *versus* the surface concentration of palladium oxide ($\Gamma_{(Pd(OH)_2)}$) at nanoPd/PPF electrodes. Raw data and conditions under which the data were obtained are given in Table 7.8.

The oxidation of H_2O_2 at the nanoPd/PPF electrodes was examined in more detail. The potential region over which the oxidation of H_2O_2 occurs remains constant following successive scanning at all the nanoPd/PPF surfaces examined (refer to Figure 7.25 (a) and (b)). The greatest reproducibility was generally obtained for surfaces which showed two peaks for the reduction of H_2O_2 and oxygen, with the H_2O_2 reduction peak potential occurring at -0.40 V or a more negative potential (entries 1, 3 and 9, Table 7.8) (note: for entry 3, H_2O_2 reduction was observed at -0.23 V and only one reduction peak was observed in the presence of H_2O_2 and oxygen). This result is illustrated in Figure 7.27 which compares repeat scans recorded for the oxidation of 1 mM H_2O_2 at nanoPd/PPF surfaces fabricated by depositing palladium nanoparticles of 2.4 and 5.0 nm to give a nominal fractional surface coverage of 0.2. The surface containing 2.4 nm particles showed two peaks for the reduction of H_2O_2 after scanning in the positive potential region whilst only one reduction peak was observed at the surface containing 5 nm particles (Figure 7.25). Clearly, the reproducibility of repeat scanning is excellent at the surface consisting of 2.4 nm palladium particles and poor at the 5 nm particle surface (Figure 7.27).

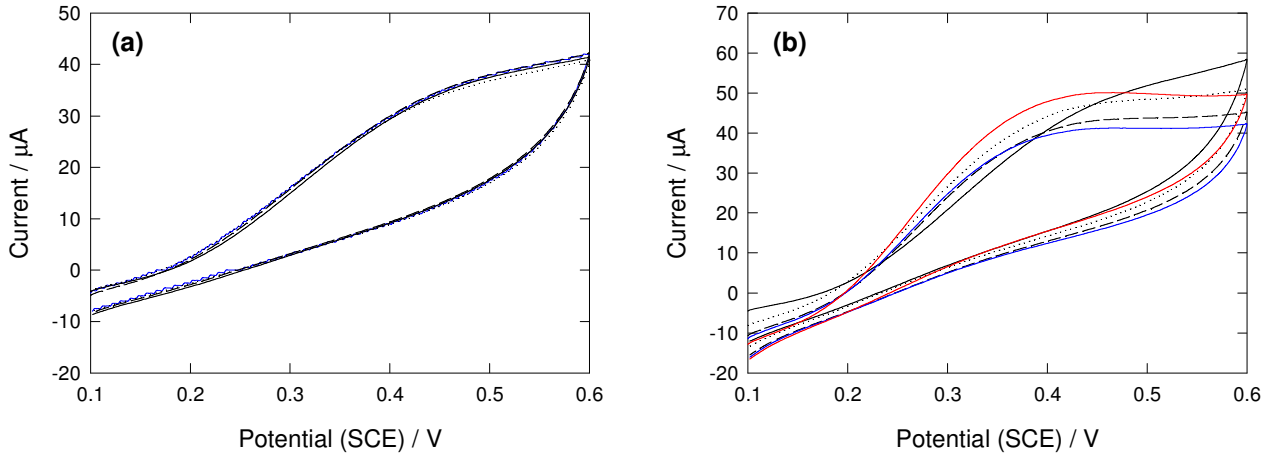

Figure 7.27. Reproducibility of the oxidation signal for 1 mM H_2O_2 in PB (pH 7.4) at nanoPd/PPF electrodes containing palladium nanoparticles of size (a) 2.4 and (b) 5.0 nm deposited to give a nominal fractional surface coverage of 0.2 (υ = 50 mV s^{-1}); scan 1 (——), scan 2 (·····), scan 3 (----), scan 4 (——) and scan 5 (——).

The influence of H_2O_2 concentration on the oxidation current recorded at nanoPd/PPF electrodes was investigated using hydrodynamic voltammetry. The nanoPd/PPF surfaces examined in this study were fabricated by depositing palladium nanoparticles with an approximate size of 2.0 or 5.0 nm to obtain nominal fractional surface coverages ranging from 0.2 to 2.0 as shown in Table 7.9. For comparison, the influence of H_2O_2 concentration on the oxidation current recorded at a solid palladium electrode was also investigated. An operating potential of 0.43 V was applied for all surfaces and increments of 0.25 mM H_2O_2 were added to blank PB solution at one minute intervals (final concentration, 5 mM). The steady-state current *versus* time plots shown in Figure 7.28 are representative of the responses observed at the range of surfaces examined. The insets show the resulting steady-state calibration curves with respect to H_2O_2 concentration. Compared to the response obtained at a solid palladium electrode, the nanoPd/PPF electrodes exhibited less noise (compare Figures 7.28 (a) and (b) with (c)). The best signal to noise ratio for the amperometric detection of H_2O_2 was observed at nanoPd/PPF surfaces with nominal fractional surface coverages of 0.2. A low signal to noise ratio is advantageous for analytical quantification of H_2O_2. The shape of the steady-state current *versus* time curves and the corresponding calibration plots are consistent with those reported in the literature for the oxidation response measured at thin

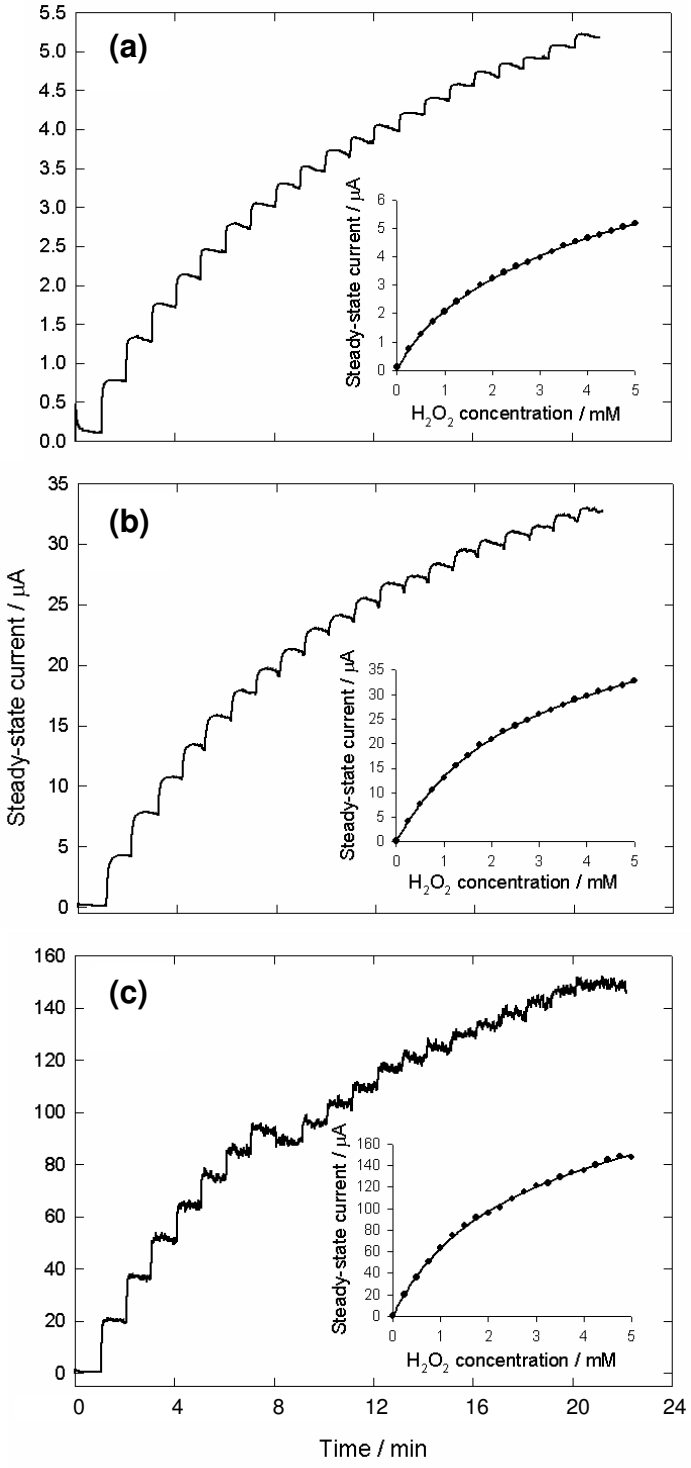

Figure 7.28. Steady-state current *versus* time responses for increments of 0.25 mM H_2O_2 recorded at (a, b) nanoPd/PPF and (c) solid palladium electrodes. Operating potential, 0.43 V. The resulting calibration plots are also shown (inset). The nanoPd/PPF electrodes consist of (a) 2.4 and (b) 5.0 nm palladium particles deposited to give a nominal fractional surface coverage of 0.2.

film gold/palladium electrodes[31] and platinum-dispersed carbon paste electrodes[68] towards increasing H_2O_2 concentration and is due to the oxidation of H_2O_2 occurring *via* a surface process. The steady-state calibration plots can be analysed according to the mechanism shown in Scheme 7.1 (Section 7.3.3) whereby it is assumed that the oxidation of H_2O_2 proceeds *via* adsorption of H_2O_2 onto oxidised palladium surface sites before electron transfer takes place. Following adsorption, H_2O_2 chemically reduces the palladium surface to give the metal and is itself oxidised to generate oxygen (equation 7.13). This mechanism leads to the expression given in equation 7.18,[31]

$$\frac{1}{j} = \frac{1}{k_2 N} + \frac{k_{-1} + k_2}{k_1 k_2 [\mathrm{H_2O_2}]_0 N} \qquad (7.18)$$

where j represents the flux of H_2O_2 molecules to the palladium electrode surface per cm^2 per second, N is the number of binding sites on the surface per cm^2, the term '$[H_2O_2]_0$' is the surface concentration of H_2O_2 which is related to the bulk concentration and the stirrer speed, k_1 and k_{-1} represent the rate constants for the adsorption and desorption of H_2O_2 at the palladium surface and k_2 is the charge transfer rate constant for the chemical reduction of the palladium surface oxide layer by H_2O_2. Equation 7.18 predicts that the double reciprocal plot of current *versus* H_2O_2 concentration will be linear with a positive gradient and a positive intercept equal to $1/k_2N$ which represents the maximum current that can be obtained when all surface sites are full.[31] Figure 7.29 shows linear double reciprocal plots corresponding to the steady-state calibration curves recorded at the range of nanoPd/PPF electrodes examined and at a solid palladium electrode. This observation demonstrates that the mechanism for H_2O_2 oxidation is the same at all the palladium surfaces analysed and is independent of palladium nanoparticle size or fractional surface coverage. A slight deviation from linearity is observed at high H_2O_2 concentrations for the nanoPd/PPF electrode consisting of 2.55 nm palladium particles deposited to give a fractional surface coverage of 0.2. This surface is considered to be the most likely nanoPd/PPF electrode to exhibit two separate peaks for the reduction of oxygen and H_2O_2 upon scanning to negative potentials indicating that the surface is relatively inactive towards H_2O_2 electrochemistry (refer to Figure 7.25). However, this was not confirmed as the nanoPd/PPF surfaces used in the steady-state experiments were not examined by cyclic voltammetry.

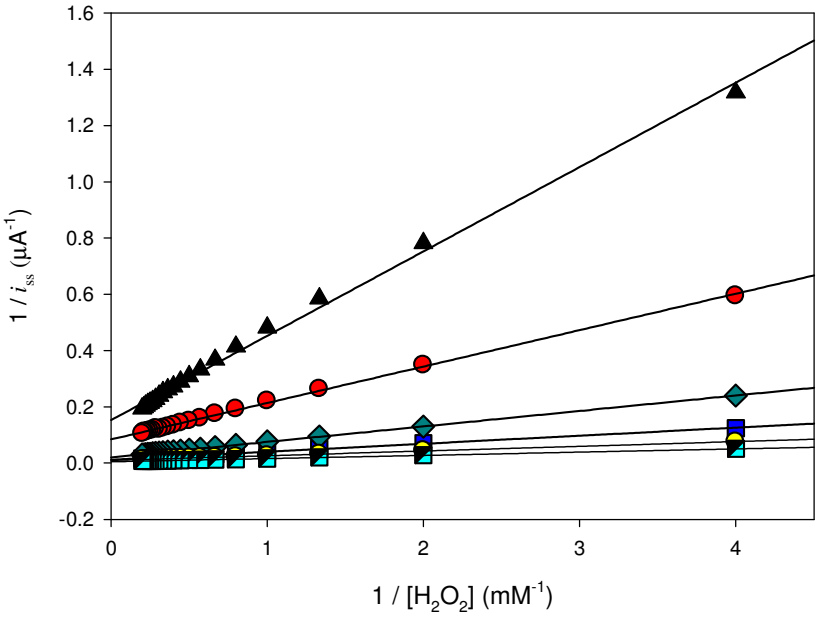

Figure 7.29. Double reciprocal plots for steady-state calibration curves recorded at nanoPd/PPF electrodes for the oxidation of H_2O_2. The steady-state calibration curves were recorded using the conditions given for Figure 7.28. The nanoPd/PPF surfaces examined consisted of palladium nanoparticles of size (▲) 2.55, (●) 2.45, (■) 2.35 and (♦, ●) 5.0 nm deposited to give nominal fractional surface coverages of (▲, ♦) 0.2, (●) 0.5, (■) 2 and (●) 0.7. The plot for the response at a solid palladium electrode is shown for comparison (◪).

Further analysis of the steady-state currents corresponding to the oxidation of 5 mM H_2O_2 recorded at each of the nanoPd/PPF surfaces examined showed no systematic relationship with respect to the size or nominal fractional surface coverage of the palladium nanoparticles (Table 7.9). These currents were also significantly less than that observed for the oxidation of H_2O_2 at a solid palladium electrode. The lack of the expected relationship between the fractional surface coverage and the H_2O_2 oxidation current is attributed to the uncertainty in the distribution of the nanoparticles on the surface (as discussed above).

Table 7.9. The effect of palladium nanoparticle size and fractional surface coverage on the steady-state current recorded at nanoPd/PPF electrodes for the electro-oxidation of 5 mM H_2O_2 in PB (pH 7.4) using hydrodynamic voltammetry. Amperometric detection was performed at 0.43 V.

Sample	Pd nanoparticles		Hydrodynamic voltammetry data for the electro-oxidation of 5 mM H_2O_2	
	Diameter (nm)	θ_{Pd}	i_{ss} (μA)	j_{ss} (μA cm^{-2})[a]
1	2.55	0.2	5.17	17
2	2.45	0.5	9.59	31
3	2.35	2.0	62.87	203
4	5.00	0.2	32.84	106
5	5.00	0.7	80.43	259
Solid Pd	-	-	147.47	1134

[a] Based on the geometric area of the electrode.

In summary, the nanoPd/PPF electrodes were less active compared to the solid palladium electrode for the electro-oxidation of H_2O_2. The cathodic behaviour observed for the reduction of H_2O_2 in the presence of oxygen was found to be indicative of electrode activity for this reaction. The nanoPd/PPF surfaces at which the reduction of H_2O_2 was observed at -0.24 V or a less negative potential behaved in an analogous fashion to the solid palladium electrode and exhibited only one peak corresponding to the simultaneous reduction of H_2O_2 and oxygen. In contrast, the nanoPd/PPF surfaces which exhibited two separate peaks in the presence of H_2O_2 and oxygen were less active than the solid palladium electrode as the H_2O_2 reduction peak occurred at more negative peak potentials. However, these surfaces may be advantageous in the development of electrochemical sensors for the quantification of H_2O_2 as the oxygen reduction peak is well-separated from that for H_2O_2 reduction.

The effect of palladium nanoparticle size and fractional surface coverage on the electrochemical detection of H_2O_2 could not be determined from this brief study. No systematic relationship was observed for the peak potentials or the currents associated with the oxidation and/or

reduction of H_2O_2 due to the uncertainty in the distribution of the nanoparticles on the surface. A considerably larger number of samples which are better characterised and include a better range of nanoparticle sizes and fractional surface coverages would be required to obtain an understanding of the effect (if any) that these parameters have on the electro-oxidation and reduction of H_2O_2.

7.4 Conclusions

The use of gold and palladium nanoparticle electrodes for the direct electrochemical detection of H_2O_2 has been examined along with the response obtained at the corresponding solid metal electrodes. Metal nanoparticle electrodes exhibited increased sensitivity towards H_2O_2 compared to the solid metal electrodes. In particular, palladium nanoparticles assembled onto PPF substrates by vapour deposition showed higher activity towards the electro-reduction of H_2O_2 whilst greater sensitivity was observed for both the electro-oxidation and reduction of H_2O_2 at gold nanoparticle electrodes fabricated by electrostatic immobilisation of colloidal gold nanoparticles onto an ED-modified glassy carbon electrode. Metal nanoparticles possess a high surface area-to-volume ratio and therefore, the increase in sensitivity is attributed to the nanoparticles having a greater combined surface area compared to that of the solid metal electrodes. Metal nanoparticle electrodes offer an efficient use of metal for the development of analytical applications as less material is required to achieve high sensitivity.

Small gold nanoparticles assembled *via* electrostatic interactions onto an ED-modified glassy carbon electrode at high density without aggregating are the most promising electrodes for the direct electrochemical detection of H_2O_2. These electrodes are advantageous for sensor developments as the catalytic oxidation of H_2O_2 at potentials less positive than that for the formation of gold oxide is observed at the as-prepared nanoAu/ED/GC electrodes. This is in contrast to the electro-oxidation of H_2O_2 at a solid gold electrode where the formation of the first oxidation peak is suppressed by the adsorption of adventitious impurities, such as alumina after polishing, and electrochemical cycling of the solid gold electrode is required to form a hydroxide layer on the surface which favours the catalytic oxidation of H_2O_2 at low potentials. Furthermore, in the presence of oxygen, the H_2O_2 reduction peak can be distinguished unlike at the palladium-containing electrodes. Electrochemical grafting of amine films is a versatile approach to the preparation of gold nanoparticle assemblies as

the assembly conditions can be adjusted to give the desired surface concentration of cationic amine sites and hence, density of electrostatically assembled nanoparticles, providing opportunities to tune the characteristics of the electrode. Further control of the nanoparticle assembly can be gained by varying the nanoparticle size and assembly time.

7.5 References for Chapter 7

1. Lund, H.; Pedersen, H. H.; Xu, H.; Luo, J. Enzymatic treatment of paper making pulps. U.S. Patent 20070119559, January 31, 2007.

2. Knittel, D.; Wei, Q. X.; Schollmeyer, E. Strategies for the development of a voltammetric sensor for the determination of hydrogen-peroxide at high-concentrations. *Fresenius Journal of Analytical Chemistry* **1994**, *348*, 820-824.

3. Schwake, A.; Ross, B.; Cammann, K. Chrono amperometric determination of hydrogen peroxide in swimming pool water using an ultramicroelectrode array. *Sensors and Actuators B-Chemical* **1998**, *46*, 242-248.

4. Vogna, D.; Marotta, R.; Napolitano, A.; Andreozzi, R.; d'Ischia, M. Advanced oxidation of the pharmaceutical drug diclofenac with UV/H_2O_2 and ozone. *Water Research* **2004**, *38*, 414-422.

5. Ksibi, M. Chemical oxidation with hydrogen peroxide for domestic wastewater treatment. *Chemical Engineering Journal* **2006**, *119*, 161-165.

6. Monteagudo, J. M.; Rodriguez, L.; Villasenor, J. Advanced oxidation processes for destruction of cyanide from thermoelectric power station waste waters. *Journal of Chemical Technology and Biotechnology* **2004**, *79*, 117-125.

7. Solvay hydrogen peroxide. http://solvayh2o2.com/index/0,5307,2216-_en,00.htm (accessed Oct 17, 2007).

8. Bromberg, S. E.; Bitowft, B. K.; Crane, E.; El-Sayed, M.; Huitt, D. A.; Nguyen, A.; deGopegui, R. R.; Shieh, D. S.; Smith, W. L.; Timberman, J. Antimicrobial product combination. U.S. Patent 20070227930, October 4, 2007

9. Say, J.; Tomasco, M. F.; Heller, A.; Gal, Y.; Aria, B.; Heller, E.; Plante, P. J.; Vreeke, M. S.; Friedman, K. A.; Colman, F. C. Analyte monitoring device and methods of use U.S. Patent 20070244380, June 21, 2007.

10. Dong, S.; Deng, Q.; Cheng, G. Cholesterol sensor based on electrodeposition of catalytic palladium particles. *Analytica Chimica Acta* **1993**, *279*, 235-240.

11. Hurdis, E. C.; Romeyn, H. Accuracy of determination of hydrogen peroxide by cerate oxidimetry. *Analytical Chemistry* **1954**, *26*, 320-325.

12. Şansal, U.; Somer, G. Detection of H_2O_2 in food samples by FTIR. *Food Chemistry* **1999**, *65*, 259-261.

13. Shiga, M.; Saito, M.; Kina, K. Highly sensitive enzymatic spectrophotometric determination of hydrogen-peroxide with water-soluble diphenylmethane-based derivatives. *Analytica Chimica Acta* **1983**, *153*, 191-197.

14. Clapp, P. A.; Evans, D. F.; Sheriff, T. S. S. Spectrophotometric determination of hydrogen-peroxide after extraction with ethyl-acetate. *Analytica Chimica Acta* **1989**, *218*, 331-334.

15. Matsubara, C.; Kawamoto, N.; Takamura, K. Oxo[5,10,15,20-tetra(4-pyridyl)porphyrinato]titanium(IV) - an ultra-high sensitivity spectrophotometric reagent for hydrogen-peroxide. *Analyst* **1992**, *117*, 1781-1784.

16. Nakashima, K.; Maki, K.; Kawaguchi, S.; Akiyama, S.; Tsukamoto, Y.; Imai, K. Peroxyoxalate chemiluminescence assay of hydrogen-peroxide and glucose using 2,4,6,8-tetrathiomorpholinopyrimido[5,4-d]-pyrimidine as a fluorescent component. *Analytical Sciences* **1991**, *7*, 709-713.

17. Price, D.; Fauzi, R.; Mantoura, C.; Worsfold, P. J. Shipboard determination of hydrogen peroxide in the western mediterranean sea using flow injection with chemiluminescence detection. *Analytica Chimica Acta* **1998**, *377*, 145-155.

18. Yamashiro, N.; Uchida, S.; Satoh, Y.; Morishima, Y.; Yokoyama, H.; Satoh, T.; Sugama, J.; Yamada, R. Determination of hydrogen peroxide in water by chemiluminescence detection, (i) flow injection type hydrogen peroxide detection system. *Journal of Nuclear Science and Technology* **2004**, *41*, 890-897.

19. Lingane, J. L.; Lingane, P. J. Chronopotentiometry of hydrogen peroxide with a platinum wire electrode. *Journal of Electroanalytical Chemistry* **1963**, *5*, 411-419.

20. Prabhu, V. G.; Zarapkar, L. R.; Dhaneshwar, R. G. Electrochemical studies of hydrogen-peroxide at a platinum disk electrode. *Electrochimica Acta* **1981**, *26*, 725-729.

21. Gerlache, M.; Senturk, Z.; Quarin, G.; Kauffmann, J. M. Electrochemical behavior of H_2O_2 on gold. *Electroanalysis* **1997**, *9*, 1088-1092.

22. Zhang, Y.; Wilson, G. S. Electrochemical oxidation of H_2O_2 on Pt and Pt + Ir electrodes in physiological buffer and its applicability to H_2O_2-based biosensors. *Journal of Electroanalytical Chemistry* **1993**, *345*, 253-271.

23. Hall, S. B.; Khudaish, E. A.; Hart, A. L. Electrochemical oxidation of hydrogen peroxide at platinum electrodes. Part 1. An adsorption-controlled mechanism. *Electrochimica Acta* **1998**, *43*, 579-588.

24. Gerlache, M.; Girousi, S.; Quarin, G.; Kauffmann, J. M. Pulsed electrochemical detection of H_2O_2 on gold. *Electrochimica Acta* **1998**, *43*, 3467-3473.

25. Brett, A. M. O.; Matysik, F. M.; Vieira, M. T. Thin-film gold electrodes produced by magnetron sputtering. Voltammetric characteristics and application in batch injection analysis with amperometric detection. *Electroanalysis* **1997**, *9*, 209-212.

26. Kolthoff, I. M.; Jordan, J. Oxygen induced electroreduction of hydrogen peroxide and reduction of oxygen at the rotated gold wire electrode. *Journal of the American Chemical Society* **1952**, *74*, 4801-4805.

27. Honda, M.; Kodera, T.; Kita, H. On the electrochemical-behavior of H_2O_2 at Ag in alkaline-solution. *Electrochimica Acta* **1983**, *28*, 727-733.

28. Appleby, A. J.; Savy, M. Kinetics of oxygen reduction reactions involving catalytic decomposition of hydrogen-peroxide - application to porous and rotating-ring-disk electrodes. *Journal of Electroanalytical Chemistry* **1978**, *92*, 15-30.

29. Wilshire, J.; Sawyer, D. T. Redox chemistry of dioxygen species. *Accounts of Chemical Research* **1979**, *12*, 105-110.

30. Abe, Y.; Yasuda, K. Electrochemical sensor capable of determining hydrogen peroxide concentration and analyser using the same. U.S. Patent 4525265, June 25, 1985.

31. Johnston, D. A.; Cardosi, M. F.; Vaughan, D. H. The electrochemistry of hydrogen peroxide on evaporated gold/palladium composite electrodes - manufacture and electrochemical characterisation. *Electroanalysis* **1995**, *7*, 520-526.

32. Gorton, L. A carbon electrode sputtered with palladium and gold for the amperometric detection of hydrogen peroxide. *Analytica Chimica Acta* **1985**, *178*, 247-253.

33. Karyakin, A. A. Prussian Blue and its analogues: Electrochemistry and analytical applications. *Electroanalysis* **2001**, *13*, 813-819.

34. Karyakin, A. A.; Karyakina, E. E. Prussian Blue-based 'artificial peroxidase' as a transducer for hydrogen peroxide detection. Application to biosensors. *Sensors and Actuators B-Chemical* **1999**, *57*, 268-273.

35. de Mattos, I. L.; Gorton, L.; Ruzgas, T.; Karyakin, A. A. Sensor for hydrogen peroxide based on Prussian Blue modified electrode: Improvement of the operational stability. *Analytical Sciences* **2000**, *16*, 795-798.

36. de Mattos, I. L.; Gorton, L.; Laurell, T.; Malinauskas, A.; Karyakin, A. A. Development of biosensors based on hexacyanoferrates. *Talanta* **2000**, *52*, 791-799.

37. de Mattos, I. L.; Gorton, L.; Ruzgas, T. Sensor and biosensor based on Prussian Blue modified gold and platinum screen printed electrodes. *Biosensors & Bioelectronics* **2003**, *18*, 193-200.

38. Garjonyte, R.; Malinauskas, A. Operational stability of amperometric hydrogen peroxide sensors, based on ferrous and copper hexacyanoferrates. *Sensors and Actuators B-Chemical* **1999**, *56*, 93-97.

39. Deng, Q.; Li, B.; Dong, S. J. Self-gelatinisable copolymer immobilised glucose biosensor based on Prussian Blue modified graphite electrode. *Analyst* **1998**, *123*, 1995-1999.

40. Ricci, F.; Gonçalves, C.; Amine, A.; Gorton, L.; Palleschi, G.; Moscone, D. Electroanalytical study of Prussian Blue modified glassy carbon paste electrodes. *Electroanalysis* **2003**, *15*, 1204-1211.

41. Garjonyte, R.; Malinauskas, A. Electrocatalytic reactions of hydrogen peroxide at carbon paste electrodes modified by some metal hexacyanoferrates. *Sensors and Actuators B-Chemical* **1998**, *46*, 236-241.

42. Fiorito, P. A.; Córdoba de Torresi, S. I. Optimised multilayer oxalate biosensor. *Talanta* **2004**, *62*, 649-654.

43. Eftekhari, A. Aluminum electrode modified with manganese hexacyanoferrate as a chemical sensor for hydrogen peroxide. *Talanta* **2001**, *55*, 395-402.

44. Liu, X. J.; Chen, T.; Liu, L. F.; Li, G. X. Electrochemical characteristics of heme proteins in hydroxyethylcellulose film. *Sensors and Actuators B-Chemical* **2006**, *113*, 106-111.

45. Dai, Z. H.; Xu, X. X.; Ju, H. X. Direct electrochemistry and electrocatalysis of myoglobin immobilised on a hexagonal mesoporous silica matrix. *Analytical Biochemistry* **2004**, *332*, 23-31.

46. Ferapontova, E. E. Direct peroxidase bioelectrocatalysis on a variety of electrode materials. *Electroanalysis* **2004**, *16*, 1101-1112.

47. Ruzgas, T.; Csöregi, E.; Emnéus, J.; Gorton, L.; Marko-Varga, G. Peroxidase-modified electrodes: Fundamentals and application. *Analytica Chimica Acta* **1996**, *330*, 123-138.

48. Ferapontova, E.; Gorton, L. Bioelectrocatalytical detection of H_2O_2 with different forms of horseradish peroxidase directly adsorbed at polycrystalline silver and gold. *Electroanalysis* **2003**, *15*, 484-491.

49. Sánchez, P. D.; Blanco, P. T.; Alvarez, J. M. F.; Smyth, M. R.; Okennedy, R. Flow-injection analysis of hydrogen-peroxide using a horseradish peroxidase-modified electrode detection system. *Electroanalysis* **1990**, *2*, 303-308.

50. Wollenberger, U.; Bogdanovskaya, V.; Bobrin, S.; Scheller, F.; Tarasevich, M. Enzyme electrodes using bioelectrocatalytic reduction of hydrogen peroxide. *Analytical Letters* **1990**, *23*, 1795-1808.

51. Sun, D. M.; Cai, C. X.; Li, X. G.; Xing, W.; Lu, T. H. Direct electrochemistry and bioelectrocatalysis of horseradish peroxidase immobilised on active carbon. *Journal of Electroanalytical Chemistry* **2004**, *566*, 415-421.

52. Wollenberger, U.; Wang, J.; Ozsoz, M.; Gonzalezromero, E.; Scheller, F. Bulk modified enzyme electrodes for reagentless detection of peroxides. *Bioelectrochemistry and Bioenergetics* **1991**, *26*, 287-296.

53. Morrin, A.; Moutloali, R. M.; Killard, A. J.; Smyth, M. R.; Darkwa, J.; Iwuoha, E. I. Electrocatalytic sensor devices: (I) cyclopentadienylnickel(II) thiolato schiff base monolayer self-assembled on gold. *Talanta* **2004**, *64*, 30-38.

54. Darder, M.; Takada, K.; Pariente, F.; Lorenzo, E.; Abruña, H. D. Dithiobissuccinimidyl propionate as an anchor for assembling peroxidases at electrodes surfaces and its application in a h2o2 biosensor. *Analytical Chemistry* **1999**, *71*, 5530-5537.

55. Wang, G. H.; Zhang, L. M. Using novel polysaccharide-silica hybrid material to construct an amperometric biosensor for hydrogen peroxide. *Journal of Physical Chemistry B* **2006**, *110*, 24864-24868.

56. Razola, S. S.; Ruiz, B. L.; Diez, N. M.; Mark, H. B.; Kauffmann, J. M. Hydrogen peroxide sensitive amperometric biosensor based on horseradish peroxidase entrapped in a polypyrrole electrode. *Biosensors & Bioelectronics* **2002**, *17*, 921-928.

57. Xu, Y.; Peng, W.; Liu, X.; Li, G. A new film for the fabrication of an unmediated H_2O_2 biosensor. *Biosensors and Bioelectronics* **2004**, *20*, 533-537.

58. Wang, G.; Thai, N. M.; Yau, S. T. Preserved enzymatic activity of glucose oxidase immobilised on an unmodified electrode. *Electrochemistry Communications* **2006**, *8*, 987-992.

59. Ruan, C. M.; Yang, F.; Lei, C. H.; Deng, J. Q. Thionine covalently tethered to multilayer horseradish peroxidase in a self-assembled monolayer as an electron-transfer mediator. *Analytical Chemistry* **1998**, *70*, 1721-1725.

60. Li, J.; Xiao, L. T.; Liu, X. M.; Zeng, G. M.; Huang, G. H.; Shen, G. L.; Yu, R. Q. Amperometric biosensor with HRP immobilised on a sandwiched nano-Au polymerised m-phenylenediamine film and ferrocene mediator. *Analytical and Bioanalytical Chemistry* **2003**, *376*, 902-907.

61. Zhang, L.; Jiang, X. U.; Wang, E. K.; Dong, S. J. Attachment of gold nanoparticles to glassy carbon electrode and its application for the direct electrochemistry and electrocatalytic behavior of hemoglobin. *Biosensors & Bioelectronics* **2005**, *21*, 337-345.

62. Lei, C. X.; Wang, H.; Shen, G. L.; Yu, R. Q. Immobilisation of enzymes on the nano-Au film modified glassy carbon electrode for the determination of hydrogen peroxide and glucose. *Electroanalysis* **2004**, *16*, 736-740.

63. Gu, H. Y.; Yu, A. M.; Chen, H. Y. Direct electron transfer and characterisation of hemoglobin immobilised on a Au colloid-cysteamine-modified gold electrode. *Journal of Electroanalytical Chemistry* **2001**, *516*, 119-126.

64. Welch, C. M.; Banks, C. E.; Simm, A. O.; Compton, R. G. Silver nanoparticle assemblies supported on glassy-carbon electrodes for the electro-analytical detection of hydrogen peroxide. *Analytical and Bioanalytical Chemistry* **2005**, *382*, 12-21.

65. Wu, S.; Zhao, H. T.; Ju, H. X.; Shi, C. G.; Zhao, J. W. Electrodeposition of silver-DNA hybrid nanoparticles for electrochemical sensing of hydrogen peroxide and glucose. *Electrochemistry Communications* **2006**, *8*, 1197-1203.

66. Yamamoto, Y.; Shiigi, H.; Nagaoka, T. Characterisation of Au nanoparticle film electrodes prepared on polystyrene. *Electroanalysis* **2005**, *17*, 2224-2230.

67. Cai, X. H.; Kalcher, K.; Kolbl, G.; Neuhold, C.; Diewald, W.; Ogorevc, B. Electrocatalytic reduction of hydrogen-peroxide on a palladium-modified carbon-paste electrode. *Electroanalysis* **1995**, *7*, 340-345.

68. Wang, J.; Naser, N.; Angnes, L.; Wu, H.; Chen, L. Metal-dispersed carbon paste electrodes. *Analytical Chemistry* **1992**, *64*, 1285-1288.

69. Wang, J.; Liu, J.; Chen, L.; Lu, F. Highly selective membrane-free, mediator-free glucose biosensor. *Analytical Chemistry* **1994**, *66*, 3600-3603.

70. Grabar, K. C.; Freeman, R. G.; Hommer, M. B.; Natan, M. J. Preparation and characterisation of Au colloid monolayers. *Analytical Chemistry* **1995**, *67*, 735-743.

71. Brown, K. R.; Walter, D. G.; Natan, M. J. Seeding of colloidal Au nanoparticle solutions. 2. Improved control of particle size and shape. *Chemistry of Materials* **2000**, *12*, 306-313.

72. Reichel, R.; Partridge, J. G.; Dunbar, A. D. F.; Brown, S. A.; Caughley, O.; Ayesh, A. Construction and application of a UHV compatible cluster deposition system. *Journal of Nanoparticle Research* **2006**, *8*, 405-416.

73. Von Issendorff, B.; Palmer, R. E. A new high transmission infinite range mass selector for cluster and nanoparticle beams. *Review of Scientific Instruments* **1999**, *70*, 4497-4501.

74. Angerstein-Kozlowska, H.; Conway, B. E.; Hamelin, A.; Stoicoviciu, L. Elementary steps of electrochemical oxidation of single-crystal planes of Au .2. A chemical and structural basis of oxidation of the (111) plane. *Journal of Electroanalytical Chemistry* **1987**, *228*, 429-453.

75. Hamelin, A. Cyclic voltammetry at gold single-crystal surfaces .1. Behaviour at low-index faces. *Journal of Electroanalytical Chemistry* **1996**, *407*, 1-11.

76. Hamelin, A.; Martins, A. M. Cyclic voltammetry at gold single-crystal surfaces .2. Behaviour of high-index faces. *Journal of Electroanalytical Chemistry* **1996**, *407*, 13-21.

77. Tremiliosi-Filho, G.; Dall'Antonia, L. H.; Jerkiewicz, G. Growth of surface oxides on gold electrodes under well-defined potential, time and temperature conditions. *Journal of Electroanalytical Chemistry* **2005**, *578*, 1-8.

78. Trasatti, S.; Petrii, O. A. Real surface-area measurements in electrochemistry. *Pure and Applied Chemistry* **1991**, *63*, 711-734.

79. Piela, B.; Wrona, P. K. Capacitance of the gold electrode in 0.5 m H_2SO_4 solution - ac-impedance studies. *Journal of Electroanalytical Chemistry* **1995**, *388*, 69-79.

80. Doescher, M. S.; Evans, U.; Colavita, P. E.; Miney, P. G.; Myrick, M. L. Construction of a nanowell electrode array by electrochemical gold stripping and ion bombardment. *Electrochemical and Solid State Letters* **2003**, *6*, C112-C115.

81. Juodkazis, K.; Juodkazyte, J.; Šebeka, B.; Lukinskas, A. Cyclic voltammetric studies on the reduction of a gold oxide surface layer. *Electrochemistry Communications* **1999**, *1*, 315-318.

82. Juodkazis, K.; Juodkazyte, J.; Juodiene, T.; Lukinskas, A. Determination of Au (III) in the surface layers formed anodically on the gold electrode. *Journal of Electroanalytical Chemistry* **1998**, *441*, 19-24.

83. Hamelin, A. Lead adsorption on gold single-crystal stepped surfaces. *Journal of Electroanalytical Chemistry* **1979**, *101*, 285-290.

84. Engelsmann, K.; Lorenz, W. J.; Schmidt, E. Underpotential deposition of lead on polycrystalline and single-crystal gold surfaces .1. Thermodynamics. *Journal of Electroanalytical Chemistry* **1980**, *114*, 1-10.

85. Engelsmann, K.; Lorenz, W. J.; Schmidt, E. Underpotential deposition of lead on polycrystalline and single-crystal gold surfaces .2. Kinetics. *Journal of Electroanalytical Chemistry* **1980**, *114*, 11-24.

86. Hamelin, A. Underpotential deposition of lead on single-crystal faces of gold .1. The influence of crystallographic orientation of the substrate. *Journal of Electroanalytical Chemistry* **1984**, *165*, 167-180.

87. Hamelin, A.; Lipkowski, J. Underpotential deposition of lead on gold single-crystal faces .2. General discussion. *Journal of Electroanalytical Chemistry* **1984**, *171*, 317-330.

88. Melroy, O.; Kanazawa, K.; Gordon, J. G.; Buttry, D. Direct determination of the mass of an underpotentially deposited monolayer of lead on gold. *Langmuir* **1986**, *2*, 697-700.

89. Walczak, M. M.; Alves, C. A.; Lamp, B. D.; Porter, M. D. Electrochemical and X-ray photoelectron spectroscopic evidence for differences in the binding-sites of alkanethiolate monolayers chemisorbed at gold. *Journal of Electroanalytical Chemistry* **1995**, *396*, 103-114.

90. Kirowa-Eisner, E.; Bonfil, Y.; Tzur, D.; Gileadi, E. Thermodynamics and kinetics of upd of lead on polycrystalline silver and gold. *Journal of Electroanalytical Chemistry* **2003**, *552*, 171-183.

91. Shimazu, K.; Hashimoto, Y.; Kawaguchi, T.; Tada, K. Construction of mixed mercaptopropionic acid/alkanethiol monolayers on polycrystalline gold electrodes using underpotentially deposited lead as the control element. *Journal of Electroanalytical Chemistry* **2002**, *534*, 163-169.

92. Bard, A. J.; Faulkner, L. R., *Electrochemical methods: Fundamentals and applications;* (2nd ed.); John Wiley & Sons Inc.: New York, NY, USA, 2001; p 166-168.

93. Vidakovic, T. *Kinetics of methanol electrooxidation on PtRu catalysts in a membrane electrode assembly*. Ph.D. Thesis, Otto von Guericke University of Magdeburg, Germany, 2005.

94. Finot, M. O.; Braybrook, G. D.; McDermott, M. T. Characterisation of electrochemically deposited gold nanocrystals on glassy carbon electrodes. *Journal of Electroanalytical Chemistry* **1999**, *466*, 234-241.

95. Li, Y. G.; Lasia, A. Electrodeposition of hard gold from acidic solution - the influence of substrates. *Journal of the Electrochemical Society* **1997**, *144*, 1979-1988.

96. Schmidt, U.; Donten, M.; Osteryoung, J. G. Gold electrocrystallisation on carbon and highly oriented pyrolytic graphite from concentrated solutions of LiCl. *Journal of the Electrochemical Society* **1997**, *144*, 2013-2021.

97. Luo, J.; Maye, M. M.; Lou, Y. B.; Han, L.; Hepel, M.; Zhong, C. J. Catalytic activation of core-shell assembled gold nanoparticles as catalyst for methanol electrooxidation. *Catalysis Today* **2002**, *77*, 127-138.

98. Turkevich, J. Collodial gold. Part II: Colour, coagulation, adhesion, alloying and catalytic properties. *Gold Bulletin* **1985**, *18*, 125-131.

99. Floate, S.; Hosseini, M.; Arshadi, M. R.; Ritson, D.; Young, K. L.; Nichols, R. J. An in-situ infrared spectroscopic study of the adsorption of citrate on Au(111) electrodes. *Journal of Electroanalytical Chemistry* **2003**, *542*, 67-74.

100. Downard, A. J.; Tan, E. S. Q.; Yu, S. S. C. Controlled assembly of gold nanoparticles on carbon surfaces. *New Journal of Chemistry* **2006**, *30*, 1283-1288.

101. Burke, L. D.; Nagle, L. C. Anomalous electrochemical behaviour of palladium in aqueous solution. *Journal of Electroanalytical Chemistry* **1999**, *461*, 52-64.

102. Burke, L. D.; Casey, J. K. An examination of the electrochemical-behavior of palladium in base. *Journal of the Electrochemical Society* **1993**, *140*, 1292-1298.

Chapter 8

Conclusions and Future Directions

The work described in this thesis was firstly aimed at using electrochemical techniques to develop an alternative approach to the process of wool setting which has a lower impact on the environment than conventional chemical methods. Efficient electrochemical methods for reducing the disulfide bonds of cystine and 2-HED to generate thiol reducing agents for cleaving wool disulfide bonds during wool setting were developed by surveying the direct electroreduction of cystine and 2-HED in alkaline media (pH 8.0-9.0) at a range of electrode surfaces including mercury, gold, silver, platinum, lead, nickel, copper, stainless steel, and glassy carbon. Transition metal phthalocyanine complexes containing cobalt, iron and manganese metal centers immobilised onto glassy carbon electrodes were also investigated as mediators for disulfide reduction. Of these surfaces, gold and silver were identified as the most practical electrodes for the reduction of cystine and 2-HED respectively. Cleavage of the disulfide bond occurred at the highest potentials, more positive than hydrogen evolution, and high currents were obtained. Although greater currents were achieved using mercury, lead and FePc/GC electrodes, the toxic nature of mercury and lead rendered them unsuitable for use in industrial wool processing and the molecular catalyst FePc was impractical due to progressive loss of the catalyst from the electrode surface.

Due to the high cost involved with using large-scale metal electrodes in industrial processes, high surface area gold and silver electrodes were fabricated by electrochemically depositing metal nanoparticles onto carbon substrates. The single step deposition procedure involving reduction of the metal salt makes electrodeposition a convenient, fast and low-cost method for the preparation of metal nanoparticles on cheap conductive substrates on an industrial scale. Gold and silver nanoparticles were deposited onto glassy carbon electrodes and the metal loading could be easily optimised by controlling the deposition time. The optimised metal nanoparticle electrodes, nanoAu/GC and nanoAg/GC, had advantages over the solid metal electrodes for the electroreduction of cystine and 2-HED as in most cases the disulfide bonds were cleaved at more positive potentials which could represent a small energy saving. The most promising electrode for the electroreduction of cystine and 2-HED was nanoAu/GC as the peak potentials for cleavage of the S–S bond were

more positive compared to the response obtained at nanoAg/GC. The electroreduction of cystine at nanoAu/GC occurred at the most positive potential overall and was recognised as the most efficient system for generating the thiol reducing agent, cysteine, to cleave wool disulfide bonds in the process of wool setting.

The ability of a small amount of catalytically generated cysteine to reduce wool disulfide bonds was successfully demonstrated using large surface area nanoAu/CF electrodes. Cysteine concentrations 10 times less than the amount of sodium metabisulfite used in conventional chemical setting processes were used to mediate the reduction of wool disulfide bonds. Treatment of subsequent batches of wool showed that the degree of setting could be maintained when the cysteine setting agent was regenerated by electrochemically reducing solution-based cystine (produced as a result of the wool setting reaction) at the nanoAu/CF electrode until the electrode became blocked due to fouling. In the absence of electrolysis, the degree of setting was not maintained due to depletion of the cysteine setting agent. Further research directed at reducing fouling of the nanoAu/CF electrode to increase the turnover of cystine to cysteine during wool setting is recommended.

The application of electrochemical methods to industrial wool setting processes is advantageous as lower levels of reagents are required and a degree of controllability is added to the reaction whilst being environmentally friendly. At present, the wool processing industry is not ready to adopt this technology and the organisation sponsoring this research, Canesis Network Ltd, have adopted a strategy for protecting the intellectual property in the interim. Nevertheless, before this technology could be taken up by industry, optimisation of the process with consideration of technical parameters needs to be carried out, and the efficiency of the developed process needs to be calculated to establish economic feasibility. In this research, electrochemical methods were applied to impart twist into woolen yarns which increases yarn strength but these methods may also be useful for imparting other desirable properties into yarn. For example, stretching of wool fibres to reduce fibre diameter allows coarse wool to be used in high value applications such as apparel and bulking of wool is advantageous for producing lighter clothing which is still warm. In addition, bulking of wool is also attractive when manufacturing carpets to ensure cut carpet tufts fill space.

Expanding on the research directed at fabricating high surface area metal nanoparticle electrodes, further studies were carried out to investigate methods for the controlled preparation of metal nanoparticle assemblies and their potential use in electroanalysis was examined by studying the electro-oxidation and reduction of H_2O_2. Gold nanoparticles were immobilised directly onto glassy carbon electrodes using electrochemical deposition procedures and an alternative method was developed whereby pre-synthesised citrate-capped gold nanoparticles were electrostatically assembled onto amine-films attached to glassy carbon surfaces. The gold nanoparticle electrodes had advantages over solid gold electrodes for detecting H_2O_2 *via* its oxidation as no electrochemical pretreatment was required in order to observe the catalytic oxidation of H_2O_2 at potentials less positive than that for the formation of gold oxide. This is in contrast to the electro-oxidation of H_2O_2 at a solid gold electrode where the formation of the catalytic oxidation peak is suppressed by the adsorption of adventitious impurities and electrochemical cycling of the solid gold electrode is required to form a hydroxide layer on the surface which favours the catalytic oxidation of H_2O_2 at low potentials.

Electrostatic assembly of citrate-capped gold nanoparticles onto ED tether layers attached to glassy carbon substrates provided a greater degree of control over the nanoscale architecture. By immobilising pre-synthesised colloidal gold nanoparticles onto an amine-modified surface the size of the gold nanoparticles could be selected independently of their density. Electrochemical grafting of ED films proved to be a versatile approach to the preparation of gold nanoparticle assemblies as the assembly conditions were easily adjusted to give the desired surface concentration of cationic amine sites and hence, density of electrostatically assembled nanoparticles. This provided opportunities to tune the characteristics of the electrode. Additional control of the nanoparticle assembly was gained by varying the nanoparticle size and assembly time. Independent control of the size and density of gold nanoparticles electrodeposited directly onto glassy carbon substrates was difficult to achieve under the conditions used in this work as both parameters increased with electrolysis time and furthermore, a broad size distribution was obtained.

The ED tether film was strongly attached to the surface by a C–N bond and the structure of these films along with their stability in solution was derived from electrochemical, AFM and XPS studies. The combined results of these studies showed that the films have a loosely-packed structure and are stable in solution. Redox probe studies revealed that the ED films are responsive to their

environment. In aqueous buffer solution at pH 7.4, the films adopted an open film structure allowing probe molecules to access pinholes and to permeate into the film for faster electron-transfer by tunneling. However, the film remains compact and electron-transfer across the film is slowed after exposure to acetonitrile. In order to fully characterise the stability of the ED tether films, additional studies investigating the effect of applied potential on the film need to be carried out. Positive potential excursions appeared to cause aggregation of individual nanoparticles to form clusters which vary in shape and increase in size as more positive potentials are applied. Further research investigating the stability of gold nanoparticle tethered electrodes to negative potential excursions and the effect of different media is also of interest.

The optimum response towards the electro-oxidation and reduction of H_2O_2 achieved using the tethered gold nanoparticle assemblies was gained by electrostatically assembling a high density of small, non-aggregated citrate-capped gold nanoparticles onto a thin ED-film attached to glassy carbon. These gold nanoparticle assemblies exhibited greater currents for the electrochemical detection of H_2O_2 than solid gold due to a greater combined surface area of the gold nanoparticles. Electroanalysis of H_2O_2 in real samples may be possible *via* electroreduction because the H_2O_2 reduction peak is well separated from that for oxygen reduction. However, these gold nanoparticle assemblies are not practical for the direct electrochemical detection of low concentrations of H_2O_2 *via* its oxidation in real samples because large overpotentials are required, increasing the potential for interference from common electro-oxidisable species such as ascorbic acid or uric acid. The use of a permselective coating to repel the anionic interfering species could be investigated for improving the selectivity of the gold nanoparticle tethered electrodes. Studies confirming the lack of interference by oxygen are also recommended.

Nanostructured palladium electrodes were also fabricated using vapour deposition methods to immobilise palladium nanoparticles ranging in size from 2.4 to 7.8 nm directly onto carbon substrates. The utility of these electrodes for the electroanalysis of H_2O_2 was of interest, however, poor characterisation of nanoparticle size and coverage meant that the full potential of these electrodes was not realised. No systematic relationship was observed between nominal nanoparticle size or fractional surface coverage and the peak potentials or currents associated with the electro-oxidation and reduction of H_2O_2. AFM, SEM and TEM are techniques commonly used to characterise nanomaterials, however, these techniques suffer from some drawbacks for determining

the size and/or coverage of very small palladium nanoparticles immobilised on carbon substrates. For example, TEM cannot be used to characterise palladium nanoparticles assembled on a solid support because this technique is based on the transmission of a beam of electrons through a sample. In contrast, AFM and SEM are capable of producing images of the sample surface. SEM images are advantageous in that they allow surfaces to be imaged in 3-dimensions and are useful for judging surface structure. In the current research, the resolution limit of the SEM instrument used was inadequate for resolving particle diameters less than 10 nm. However, it may be possible to characterise smaller particles using a higher resolution SEM instrument. AFM is most likely the best method for characterising very small nanoparticles immobilised on the carbon substrate. The smallest feature that can be resolved using AFM depends on the radius of the imaging tip. Commercially available high resolution tips have an end radius of curvature of 1 nm and therefore, it should be possible to resolve features down to this size using a high quality AFM instrument. Alternatively, AFM tips functionalised with nanotubes could also be used for high resolution imaging. Imaging would need to be performed under vacuum to avoid water droplets from atmospheric condensation between the tip and the sample from blurring the image and strict vibration-control would also be required. With better control of palladium nanoparticle deposition and full characterisation of the resulting surfaces, further investigations of the electrochemical activity of the palladium nanoparticle electrodes would be of interest.

Appendix A

^{1}H NMR Data to Determine the Species Present After Bulk Electrolysis of Cystine

Cysteine: ^{1}H NMR (500 MHz) (D_2O), δ 2.88 (1H, dd, *J* = 15, 4.5 Hz, C<u>H</u>HSH), 2.96 (1H, dd, *J* = 15, 5.5 Hz, CH<u>H</u>SH), 3.84 (1H, dd, *J* = 5.5, 4 Hz, C<u>H</u>(CO_2H)NH_2).

Cysteic acid: ^{1}H NMR (500 MHz) (D_2O), δ 3.31 (1H, dd, *J* = 15, 3.5 Hz, C<u>H</u>HSO_3H), 3.44 (1H, dd, *J* = 15, 8.5 Hz, CH<u>H</u>SO_3H), 4.32 (1H, dd, *J* = 8.5, 3.5 Hz, C<u>H</u>(CO_2H)NH_2).

Cystine: ^{1}H NMR (500 MHz) (D_2O), δ 3.02 (2H, dd, *J* = 15, 9.5 Hz, C<u>H</u>HS-S<u>H</u>HC), 3.20 (2H, dd, *J* = 15, 11 Hz, CH<u>H</u>S-SH<u>H</u>C), 3.93-3.94 (2H, m, NH_2(CO_2H)C<u>H</u>CH_2S-SCH_2C<u>H</u>(CO_2H)NH_2).

Product of the auto-oxidation of cysteine: ^{1}H NMR (500 MHz) (D_2O), δ 2.91-2.92 (2H, m, C<u>HH</u>SH), 3.05 (2H, dd, *J* = 15, 8 Hz, C<u>H</u>HS-S<u>H</u>HC), 3.25 (2H, dd, *J* = 15, 3.5 Hz, CH<u>H</u>S-SH<u>H</u>C), 3.79 (1H, app. t, *J* = 9.5 Hz, C<u>H</u>(CO_2H)NH_2), 3.96 (2H, dd, *J* = 8, 5 Hz, NH_2(CO_2H)C<u>H</u>CH_2S-SCH_2C<u>H</u>(CO_2H)NH_2).

Product of the bulk electrolysis of cystine: ^{1}H NMR (500 MHz) (D_2O), δ 2.87-2.91 (2H, m, C<u>HH</u>SH), 3.05 (2H, dd, *J* = 15, 8.5 Hz, C<u>H</u>HS-S<u>H</u>HC), 3.24 (2H, dd, *J* = 15, 11 Hz, CH<u>H</u>S-SH<u>H</u>C), 3.78-3.80 (1H, m, C<u>H</u>(CO_2H)NH_2), 3.95 (2H, dd, *J* = 8, 5 Hz, NH_2(CO_2H)C<u>H</u>CH_2S-SCH_2C<u>H</u>(CO_2H)NH_2).

Appendix B

Statistics

The following methods for determination of sample size and detection of outliers were applied to the Crink Angle Test used in Chapter 5 to assess the degree of setting in treated wool samples.

B.1 Determination of Sample Size

For reasons of greater speed and scope, information regarding the degree of setting in treated wool samples was obtained by a "sample survey". Population parameters such as the mean μ and standard deviation σ can be estimated using a random sample of size *n*, sample mean $\bar{x}$ and sample standard deviation *s*.[1,2] Sample parameters $\bar{x}$ and *s* were taken as estimates of population parameters μ and σ respectively. It was also assumed that distribution of all sample means $\bar{x}_i$ about the unknown population mean μ follow a normal distribution.[1]

The number of samples required for analysis is dependent on the required confidence interval for the mean and the desired relative standard deviation.[2] For a given confidence interval, an expression can be written for the number of sampling units (*n*) required to give a sample mean $\bar{x}$ that will lie within ± the desired confidence interval of the unknown population mean μ at some stated probability level (equation B.1).[2] The sample standard deviation *s* is used to estimate the population standard deviation σ and the *t* statistic from the Students *t*-distribution is used.[2,3] The term σ_r represents the relative uncertainty that is tolerable at the given confidence level.

$$n = \frac{t^2 s^2}{\bar{x}^2 \sigma_r{}^2} \qquad \text{(B.1)}$$

The calculation of the appropriate sample size (n) using equation B.1 is an iterative process since the value assigned to t itself depends on the yet unknown value of n. In practice, the equation is solved using an initial (chosen) value for n and the corresponding value for t. A second value for n is then calculated and the process is repeated until no significant improvement in n is achieved.[1,2]

To determine the sample size required for the Crink Angle Test to be representative of the degree of setting in the population wool samples, a pilot survey was performed whereby 30 V-shaped segments of treated wool were analysed using the Crink Angle Test (Table B.1) to gain some prior knowledge of the population parameters μ and σ.

Table B.1. Crink angles measured to assess the degree of setting for wool treated with cysteine (6 mM, 150 mL) at 85 °C for 5 minutes. The Crink Angle Test was performed by immersing V-shaped wool segments (n = 30) into Milli-Q water (200 mL) overnight at room temperature.

Crink Angle (°)									
34	48	49	51	52	53	57	58	58	59
60	60	61	61	61	62	63	64	66	67
67	69	76	78	79	79	79	80	81	82

From the data shown in Table B.1, the sample parameters of $\bar{x}$ and s were calculated to be 64° and 12° respectively. For this study, a relative uncertainty of 10 % and a confidence level of 95 % were chosen. Therefore, by substituting these numbers into equation B.1, and assuming an infinite number of samples, which gives a value of t of 1.960, the calculated number of samples required is 10. Two more iterations were performed based on the calculated value of n and were found to converge with an n value of 12.5. Hence, the number of samples for analysis required to obtain a relative standard deviation of 10 % at the 95 % confidence level is 13 samples. However, for the sample parameters to be representative of the population parameters, the data needs to be normally distributed and sample parameters $\bar{x}$ and s need to provide estimates of the population parameters μ and σ respectively. These assumptions are not necessarily true for small sample sizes and hence, the large sample size used for the pilot survey (n = 30) was used as the minimum number

of samples for analysis in all subsequent Crink Angle Tests. A sample size of 30 corresponds to a relative standard deviation of 7 %.

B.2 Detection of Outliers

An outlier is defined as an observation (or measurement) that is unusually large or small relative to the other values in a data set and can often be attributed to the following causes: (1) the measurement is observed, recorded or entered into the computer incorrectly, (2) the measurement comes from a different population or (3) the measurement is correct, but represents a rare (chance) event.[3] When analysing a data set it is sometimes important to identify inconsistent or unusual measurements as they can significantly affect the sample mean and, therefore, the final estimate of the population mean.[4] However, when the reason for the appearance of the outlier is unknown, rejection of the outlier measurement should be based on reliable statistical measurement.[4]

Dixon's Q test has been adopted by many modern statistical treatises and textbooks for analytical chemistry as the primary method for testing whether a suspected outlier should be retained or rejected.[2,4-7] In using this test, knowledge of the population mean and standard deviation is not required and it is assumed that the data is normally distributed.[7] To identify potential outliers, the data points are ranked in order of increasing size.

$$X_1 < X_2 < X_3 < \ldots\ldots\ldots < X_{n-2} < X_{n-1} < X_n$$

The criterion used to assess suspected outliers depends on the number of data points in the set.[4,7] For quantitative analysis of the degree of wool setting using the Crink Angle Test (see Chapter 5, Sections 5.2.4.1 and 5.3.1 to 5.3.4), a minimum sample size of 30 V-shaped wool segments is used and hence, the criterion for calculating the critical Dixon ratio is:[4]

$$Q = \frac{X_3 - X_1}{X_{n-2} - X_1} \qquad \text{when } X_1 \text{ is the suspected outlier}$$

$$Q = \frac{X_n - X_{n-2}}{X_n - X_3} \qquad \text{when } X_n \text{ is the suspected outlier}$$

To determine whether the suspected outlier should be rejected or retained, the calculated ratio (Q) is compared with critical values of Q (Q_{crit}). If Q is greater than Q_{crit} then the suspected outlier is rejected with the indicated degree of confidence. For this study, Dixon's Q test was applied as a two-tailed test (*i.e.*, outlier values were tested at both the upper and lower ends of the data set) using a 95 % confidence level as recommended by Rorabacher.[4]

Example

The use of Dixon's Q test for determining whether a suspected outlier should be retained or rejected is illustrated using the crink angle measurements shown in Table B.1. After ranking the data in increasing size,

$$34° < 48° < 49° < X_4 < \ldots\ldots.. < X_{27} < 80° < 81° < 82°$$

it is apparent that the value of 34° is a potential outlier. The critical Dixon ratio is calculated for the situation where X_1 as the suspected outlier:

$$Q = \frac{X_3 - X_1}{X_{n-2} - X_1} = \frac{49° - 34°}{80° - 34°} = 0.324$$

For a sample size of 30, Q_{crit} is equal to 0.414 at the 95 % confidence level.[4] Comparison of the calculated Q value (0.324) with Q_{crit} shows that $Q < Q_{crit}$ and therefore, the value should be retained.

B.3 References for Appendix B

1. Taylor, M. C. *Podzols: Aspects of their chemistry and development*. Ph.D. Thesis, University of Canterbury, Christchurch, New Zealand, 1980.

2. Skoog, D. A.; West, D. M.; Holler, F. J.; Crouch, S. R., *Fundamentals of analytical chemistry;* (8th ed.); Thomson-Brooks/Cole: Belmont, CA, USA, 2004; p 110-117, 167-169.

3. McClave, J. T.; Sincich, T., *Statistics;* (9th ed.); Prentice Hall: Upper Saddle River, NJ, USA, 2003.

4. Rorabacher, D. B. Statistical treatment for rejection of deviant values: Critical values of dixon's "*Q*" Parameter and related subrange ratios at the 95 % confidence level. *Analytical Chemistry* **1991**, *63*, 139-146.

5. Miller, J. C.; Miller, J. N., *Statistics for analytical chemistry;* Ellis Horwood Limited: Chichester, West Sussex, England, 1984; p 60-62.

6. Werimont, G. T., *Use of statistics to develop and evaluate analytical methods;* Association of Official Analytical Chemists: Arlington, VA, USA, 1985; p 96-97, 156.

7. Taylor, J. K.; Cihon, C., *Statistical techniques for data analysis;* (2nd ed.); Chapman & Hall/CRC: Boca Raton, FL, USA, 2004; p 102-104, 239.